Models of large-scale structure formation in cosmology

Michael Kopp

München 2014

Models of large-scale structure formation in cosmology

Michael Kopp

Dissertation
an der Fakultät für Physik
der Ludwig–Maximilians–Universität
München

vorgelegt von
Michael Kopp
aus München

München, den 30. Juni 2014

Erstgutachter: Prof. Jochen Weller
Zweitgutachter: Prof. Stefan Hofmann
Tag der mündlichen Prüfung: 28. Juli 2014

Zusammenfassung

Wenn wir all das Wissen kombinieren, welches wir bisher über Ursprung, Entwicklung und heutigen Zustand des Universum gesammelt haben, kommen wir unweigerlich zu dem Schluss, dass 95% der Materiedichte des Universums aus unbekannten Substanzen besteht, die man dunkle Materie und dunkle Energie nennt. Diese Dissertation beschäftigt sich mit verschiedenen Aspekten der Entstehung der größten Strukturen im Universum und entwickelt neue Methoden diese Strukturen, bestehend aus dem kosmischen Netz, Galaxienhaufen und Galaxien zu modellieren. Diese Strukturen hängen sehr sensibel von den Eigenschaften der dunklen Materie und dunklen Energie ab, insbesondere von ihren relativen und absoluten Mengen, sowie der Zustandsgleichung der dunklen Energie und einer eventuell von ihr vermittelten neuen Wechselwirkung. Aktuell durchgeführte und zukünftige Vermessungen der größten Strukturen kartographieren diese mit zunehmender Präzision und in immer größeren Volumen. Um die kosmologischen Parameter bestmöglich aus den Daten zu extrahieren, benötigen wir akkurate Modelle der Strukturbildung und der Prozesse, die das Licht auf seinem Weg zum Beobachter beeinflussen. Nur so können wir zuverlässig die kosmologischen Parameter rekonstruieren und die Modelle für dunkle Materie und dunkle Energie identifizieren die von den Daten bevorzugt werden. Somit trägt die Dissertation zu den Bemühungen bei, die Natur der dunklen Materie und dunklen Energie zu enthüllen.

Kapitel 2 untersucht ein Modell für dunkle Energie, welche eine “fünfte Kraft” vermittelt, die jedoch die Newtonsche Gravitationskraft auf Grund des Chamäleon-Mechanismus lediglich auf großen Skalen verstärkt und eine Expansionsgeschichte verursacht, die nicht vom einfachsten Fall zu unterscheiden ist, bei dem die dunkle Energie eine kosmologische Konstante ist. Deswegen stehen die einzigen Beobachtungsgrößen, welche die Modelle zu unterscheiden vermögen im Zusammenhang mit Strukturbildung. Wir untersuchen mit semi-analytischen Methoden die Häufigkeit von dunkle-Materie-Halos pro Halo-Masse und erhalten für diese eine Fitfunktion, die vom Wert des neuen Modellparameters abhängt, welcher die Reichweite und Stärke der fünften Kraft bestimmt. Wir finden eine gute Übereinstimmung der auf diese Weise bestimmten theoretischen Massenfunktion mit denjenigen bestimmt aus Monte-Carlo und N-Teilchen Simulationen. Die von uns gefundene Fitfunktion vermag das Modell durch Beobachtungen von Galaxienhaufen zu testen und kann dazu dienen nach den charakteristischen Signaturen des Chamäleon-Mechanismus in den Beobachtungsdaten zu suchen.

In Kapitel 3 und 4 zeigen wir, dass die Newtonsche Gravitationstheorie anstelle der Allgemeinen Relativitätstheorie auf allen Längenskalen verwendet werden kann, um akkurat die Entstehung der größten Strukturen zu beschreiben, sofern das Universum von kalter dunkler Materie und einer kosmologischen Konstante dominiert wird.

In Kapitel 5 zeigen wir, dass ein komplexes Skalarfeld, welches die Schrödinger-Poisson-

Gleichung erfüllt, in der Lage ist kollisionsfreie selbstgravitierende dunkle Materie mit der selben Zahl an Freiheitsgraden zu beschreiben wie das weitverbreitete Staubmodell. Im Gegensatz zum Staubmodell ist das Skalarfeldmodell frei von Singularitäten, weswegen es analytische und numerische Studien von komplett nichtlinearen Prozessen wie Halo-Entstehung erlaubt.

In Kapitel 6 untersuchen wir die Clusterung von Halos, oder die Halo-Korrelationsfunktion, wie sie im Rotverschiebungsraum beobachtet wird. Dazu entwickeln wir ein verbessertes Modell für die Dynamik von Halos, welches auf einer Körnung des Staubmodells und einer Verallgemeinerung des Gaussian-Streaming-Modells auf beliebige Phasenraumfunktionen beruht. Wir vergleichen unsere Resultate mit Messgrößen aus einer N-Teilchen-Simulation und finden, dass das granulierte Modell die Genauigkeit der vorhergesagten Korrelationsfunkionen im Rotverschiebungsraum wesentlich verbessert.

Summary

Combining all knowledge we have gathered about the origin, evolution and current state of the universe it appears indisputable that 95% of the mass-energy density in today's universe is comprised of unknown substances called dark matter and dark energy. This thesis explores different aspects of and develops models for the formation of the largest structures we observe in the universe, because these structures – the cosmic web made of dark matter halos, clusters of galaxies and galaxies – sensitively depend on properties of dark matter and dark energy, in particular on their abundances, the equation of state of and possible new interactions mediated by dark energy. Current and upcoming surveys map the large scale structure (LSS) with increasingly higher precision and in larger volumes. In order to optimally extract cosmological parameters we need to build accurate models for LSS formation that also describe how LSS is perceived by real observers trough processes affecting light propagation. Only then can we reliably reconstruct the cosmological parameters and identify the models for dark matter and dark energy preferred by the data. Therefore this thesis contributes to the endeavor to ultimately uncover the nature of dark matter and dark energy.

Chapter 2 studies a dark energy model which mediates a "fifth force" enhancing Newtonian gravity only on large scales due to the chameleon mechanism, but leads to an expansion history indistinguishable from the case where dark energy is a cosmological constant. Hence the only observables that can discriminate them are related to structure formation. We study the abundance of dark matter halos per halo mass with semi-analytical techniques to find a fit function depending on the model parameter responsible for the range and strength of the fifth force. We find good agreement with Monte-Carlo and N-body simulations of the mass function. Our result is a fit function for the halo mass function that can be used to constrain this model and to look for signatures of the chameleon effect in observations of galaxy of clusters.

In Chapters 3 and 4 we show why it is justified to use Newtonian gravity instead of General Relativity on all scales to accurately describe LSS formation in a universe governed by a cosmological constant and cold dark matter.

In Chapter 5 we show that a complex scalar field solving the Schrödinger-Poisson equation is able describe collisionless selfgravitating dark matter with the same number of degrees of freedom as the popular dust fluid. In contrast to the dust model it does not suffer from singularities and thus allows the analytical and numerical study of fully nonlinear effects like halo formation.

In Chapter 6 we study the clustering of halos as observed in redshift space, by developing an improved model for the halo dynamics based on a coarse grained dust model and by extending the so called Gaussian streaming model to general phase space distribution functions. We compare our results to a N-body simulation halo catalog and find that the coarse grained dust model significantly improves the accuracy of theoretical redshift space correlation functions.

Acknowledgements

I am very obliged and grateful to my supervisors Jochen Weller and Stefan Hofmann who made this thesis possible on so many different levels; for countless discussions and the opportunity to collaborate with both their groups, for their guidance but also for the freedom they gave me to follow my own ideas and last but not least for financing my work for which I am equally thankful to the DFG cluster of excellence "Origin and Structure of the Universe."

I would like to warmly thank my collaborators which besides Stefan Hofmann and Jochen Weller include Stephen Appleby, Ixandra Achitouv, Cora Uhlemann and Thomas Haugg, who all contributed to this thesis through many fruitful discussions and with their own work. In particular I have to mention Stephen Appleby's $f(R)$ spherical collapse PDE solver described in Section 2.3.4 and Ixandra Achitouv's mass function and Monte Carlo runs in Section 2.4, Cora Uhlemann's meticulous derivations of various results in Sections 5.2, 5.3 and 6.7 and Thomas Haugg's implementation of 6.7 into Lile Wang's publicly available CLPT code. A special thanks goes to Cora Uhlemann for proofreading large parts of the thesis.

I would like to thank Marco Baldi and Ewald Puchwein for providing the mass function data of their $f(R)$-N-body simulation that allowed me to check the main result of Chapter 2 in Fig. 2.14, and Juhan Kim, Changbom Park, Graziano Rossi, Sang Min Lee, J.Richard Gott III for making their Horizon Run II halo catalog public, which allowed me to check the accuracy of the main results of Chapter 6.

I want to thank Marco Bruni, Ram Brustein, Juhan Kim, Tsz Yan Lam, Lucas Lombriser, Cornelius Rampf, Syksy Räsänen, Antonio Riotto, Dominik Schwarz and Ravi Sheth for discussions and feedback to various parts of this thesis.

I also benefited from many inspiring discussions with Felix Berkhahn, Ben Hoyle, Katarina Markovic, Florian Niedermann, Tehseen Rug, Dennis Schimmel, Robert Schneider and many other colleges and friends at the LMU.

I am grateful to my GR and cosmology teachers Slava Mukhanov and Sergei Winitzki for their superb lectures and to Charles Misner, Kip Thorne and John Archibald Wheeler for writing the most beautiful and inspirational textbook in the world: *Gravitation*, which makes them largely responsible for me ending up in cosmology.

I am deeply grateful to my parents Inge Lihotzky-Kopp and Manfred Kopp, my grandparents Helga and Kurt Bergmann, and my partner Andreas Fackler for their encouragement and support.

Another special thanks goes to Jochen Weller for taking me to many skiing conferences and trips and to Stefan Hofmann and Kerstin Paech for introducing me into the art of baking bread.

Contents

Notation

Here we list some conventions and the meaning of some symbols that are shared between different quantities.

- The metric of spacetime is chosen to be "mostly plus" $(-1,+1,+1,+1)$ such that its spatial part would reduce to a flat positive definite euclidean metric in the absence of curvature.
- Euclidean 3d vectors are denoted by bold, italic letters like Eulerian position $\boldsymbol{x}$, Lagrangian position $\boldsymbol{q}$ or Fourier-space wave vectors $\boldsymbol{p}$, $\boldsymbol{k}$.
- The middle Roman letters $i, j, \ldots$ are used for indices of 3d quantities like x^i, δ_{ij}, σ_{ij}. The 3d partial derivative is denoted by a comma $V_{,i} = \partial_i V$ or as a Euclidean vector ∇V.
- Greek letters $\mu, \nu, \ldots$ are used as indices for 4d-components of spacetime tensors. The 4d covariant derivative is denoted by a semicolon: $T_{\mu\nu;\varrho}$.
- Symmetrization brackets ( ) of indices are defined by $T_{(\mu\nu)} = T_{\mu\nu} + T_{\mu\nu}$.
- C is used for the cumulants of the phase space distribution f, and for the connected n-point correlation functions of density δ and displacement fields $\boldsymbol{\Psi}$.
- f is used for the phase space distribution function $f(\boldsymbol{x}, \boldsymbol{p})$ and for the multiplicity function $f(\sigma)$ that defines the halo mass function as well as for the $f(R)$ function entering the modified gravity model. It is also for the linear growth function $f(z)$.
- j denotes the components j^i of the normalised momentum field $\boldsymbol{j}$, which in Chapter 4 is defined as $\boldsymbol{j} = (1+\delta)\boldsymbol{v}$ but in Chapter 5 is defined as $\boldsymbol{j} = (1+\delta)\boldsymbol{u}$.
- Φ is used as metric perturbation in Poisson gauge. The upright version Φ is used as gauge invariant metric perturbation.
- ϕ is used as metric perturbation and as phase of the wavefunction ϕ and as velocity potential. φ is the $f(R)$-scalar field.
- Ψ is used as metric perturbation in Poisson gauge and as component Ψ_i of the displacement vector $\boldsymbol{\Psi}$. The upright version Ψ is used as gauge invariant metric perturbation.
- ψ is used as metric perturbation and as wave function.

- σ is used as the variance of density perturbations and is used for the velocity dispersion σ_{ij}, the pairwise velocity dispersion σ_{12} and as phase space smoothing scales σ_x and σ_p.
- V is used as Newtonian potential. The upright V is used as gauge invariant scalar velocity perturbation.
- $\boldsymbol{v}$ is the peculiar velocities with components v^i. The spatial component of the 4D velocity u_μ are denoted by u_i and are also used as a 3D vector $\boldsymbol{u}$ in the Newtonian limit, where it is related to $\boldsymbol{v} = \boldsymbol{u}/a$.
- w is a scalar metric perturbation and denotes the components w^i of the vorticity vector $\boldsymbol{w} = \boldsymbol{\nabla} \times \boldsymbol{v}$, it is also used as general relativistic γ-factor.

"Φύσις κρύπτεσθαι φιλεί"

Heraklitus

"Die Natur der Dinge ist in der Gewohnheit sich selbst zu verbergen!"

Eugen Egner, Der Notfall erfordert alles

1 Introduction

In this chapter we set the stage for the topics of this thesis by giving a brief summary of the status of cosmology. We intersperse this overview with references to important articles, introductions and textbooks, as well as to chapters of this thesis.

1.1 The big picture

Physics without astrophysical and cosmological observations would be quite boring. Because without those observations we could pretend that all natural phenomena within the solar system neatly fit into the following "effective theory of everything" [Car13]

$$\overbrace{\int_{k<k_{\text{cut-off}}} [Dg][DA][D\psi]D[\Phi]}^{\text{quantum mechanics}} \exp\left\{\frac{i}{\hbar}\int d^4x \overbrace{\sqrt{-g}\Big[\frac{R}{16\pi G}}^{\text{gravity}} \overbrace{-\frac{1}{4}F^a_{\mu\nu}F^{a\mu\nu}}^{\text{electro-weak and strong forces}} + \underbrace{+i\bar{\psi}^i \not{D}\psi^i + \left(\bar{\psi}^i_{\text{L}} V_{ij}\psi^j_{\text{R}}\Phi + \text{h.c}\right)}_{\text{quarks and leptons}} \underbrace{- D_\mu\Phi D^\mu\Phi^\dagger - V(\Phi)}_{\text{Higgs}}\Big]\right\}. \tag{1.1}$$

All solar-system-bound phenomena can be described through quantum mechanics in its relativistic incarnation taking the special form of the Standard Model (SM) and General Relativity (GR), combined in (1.1). The SM describes all particles and their electro-weak and strong interactions in terms of quantum fields, while GR is a classical field theory that describes gravity through a dynamical metric coupled to all the other fields, see [Sre07, MTW73] for introductions. Of course, in almost all circumstances using (1.1) to calculate those phenoma is impractical and

there are new effective laws emerging on the ladder of complexity and we have a patchwork of effective theories each with its small regime of applicability. This is the very reason why science works at all.

If we also take into account information arriving from outside the solar system by means of astrophysical and cosmological observations, it appears that 95% of the mass-energy content of today's Universe is in form of unknown substances dubbed "dark matter" $\Omega_{\text{dm}} = 27\%$ and "dark energy" $\Omega_{\text{de}} = 68\%$ [PAA+13]. Only the remaining $\Omega_{\text{b}} = 4.9 \pm 0.1\%$ can be attributed to particles or fields described by the SM which is accurately tested without hints for new physics [Ell13]. On the other hand also Einstein's GR, the standard theory of gravity has withstood nearly 100 years of scrutiny [Ein15, Wil06]. The extraordinary claim that 95% of the energy budget of the universe cannot be described by the SM is based on the assumption that GR is still valid on the large scales probed by those cosmological observations. In any case, (1.1) is just a piece of a larger puzzle.

Believing in 95% darkness

Let us briefly describe some important observations that have lead to this picture, assuming that GR is correct.

Velocities inside galaxies and clusters The velocity distribution within galaxies and galaxy clusters requires 20 times more non-luminous "dark matter" in form of large spherical halos in which the luminous matter composed of gas and stars is embedded [Zwi37].

Supernovae and Hubble diagram On scales larger than the separation to neighbouring galaxies the universe expands isotropically according to the Hubble law, which is in accord with GR if the universe is homogeneous and isotropic as is observed on large scales. Measuring the distance-redshift relation, or Hubble diagram, using the apparent luminosity of "standardizable candles" type Ia supernovae [RFC+98, PAG+99, KBC+09], revealed that the expansion of the universe is accelerating, which requires 70% of the energy budget of the universe to be in the form of "dark energy" with large negative effective pressure. While the remaining 30% of the budget is effectively pressureless matter consistent with being a mixture of luminous and non-luminous matter as is learned from velocities with galaxies and clusters.

CMB and Big Bang Nucleosynthesis The discovery of the cosmic microwave background (CMB) [PW65] proved the Big Bang theory that posits that the universe was in a dense, hot and nearly homogeneous state some 14 billion years ago. The COBE satellite showed with FIRAS that the CMB has the energy spectrum of a black body radiation with $T = 2.72548 \pm 0.00057\,\text{K}$ [FCC+94, Fix09] that is isotropic after subtracting a Doppler dipole. From the observed temperature one can calculate using (1.1)[1] the fractional amount of light elements forged during Big Bang nucleosynthesis (BBN) as a function of the baryon energy budget Ω_b. It is is consistent

[1] All the interactions are in fact necessary to compute this!

with 5%, which we obtained already from just measuring the Hubble diagram as well as studying galaxies and clusters. However in addition, we have the crucial extra information that the dark matter (DM) cannot be comprised of baryons, otherwise they would have affected the BBN.

CMB temperature fluctuations Although the CMB seems to hold the record of being the most accurate realization of a Planck spectrum found in nature, it is actually the angular fluctuations in the temperature with an amplitude 20 times smaller than the FIRAS error bar 0.00057 K, which contain the most valuable information. COBE established the existence of these fluctuations with variance $\langle(\delta T/T)^2\rangle \simeq 10^{-10}$ heralding the advent of the era of "precision cosmology"; the fluctuations were subsequently mapped by various telescopes and by two other satellites, WMAP [KSD+11] and Planck [PAA+13] to a much higher precision and smaller angular resolution. When taking into account the full power spectrum measured by Planck, the energy budget is measured with a fractional error of only 1%! There are 3 main features of the angular fluctuations and its power spectrum.

i) The power spectrum features a series of oscillations with a prominent first peak at about 1° on the sky followed by a smaller second and equally small third peak.

ii) The fluctuations are Gaussian distributed within the measurement uncertainties (after subtraction of known contaminants).

iii) The power spectrum is nearly scale invariant with an amplitude of approximately 10^{-10} at large angles with slightly more power on large scales, or red spectral tilt.

The physical origin of the oscillations *i*) are small-amplitude sound waves developing from the initially nearly scale invariant, adiabatic and Gaussian primordial density perturbations, whose origin we describe in the last paragraph. The primordial plasma of coupled photons and baryons evolves under the influence of its own gravity and pressure as well as the gravity of cold dark matter (CDM) until the universe becomes cold enough for hydrogen to recombine, see [Hu95, Whi99] for an introduction. During this period of recombination the radiation is released and freely streams with the tiny temperature fluctuations imprinted, and with the peaks in its temperature power spectrum corresponding to the harmonics of the plasma sound waves. The first peak location corresponds to the angular size of the sound horizon of the plasma at recombination. Its intrinsic size is a standard ruler depending on the baryon to radiation fraction and its observed extent on the sky depends on the expansion history, in particular today's energy budget and the spatial geometry, which turns out to be flat. The relative heights of the peaks depend on the budget of baryons and CDM.

It is also true that given the observed amplitude of fluctuations during the time of recombination, there would not have been enough time to form the large-scale structure we observe today if it were not for CDM preserving the primordial gravitational potential wells into which the baryons could quickly fall after recombination to form galaxies. There is much more to learn from the CMB than the energy budget [Muk05]. The information about cosmological parameters is also encoded in other aspects of the CMB, e.g. polarization and secondary anisotropies.

Large-scale structure and BAO In GR the spacetime curvature caused by the energy density of dark matter strongly affects the overall expansion rate of the Universe and the formation of the large-scale structure of the Universe (LSS) – the cosmic web, along which dark matter and galaxies are distributed. Many different observations of the LSS tell us that dark matter must be "cold" dark matter (CDM), in the sense that the initially small particle velocities can be approximated by a smooth vector field and that it must be collisionless, such that their selfinteraction as well interaction with SM sector is so weak that they can be assumed to interact purely gravitationally. This excludes SM neutrinos, since they behave as hot dark matter. Galaxies and clusters of galaxies form in CDM halos such that the halo distribution can be inferred from galaxy surveys, e.g. [EWA+11, DES, PS, LAA+11]. Direct methods of mapping DM, like gravitational lensing, that probes spacetime curvature directly, give consistent results [HGH+13]. The halo power spectrum therefore contains information about linear and nonlinear gravitational growth and thus is sensitive to DE and DM budget, as DE slows down gravitational clustering [RSW+12]. We will see in Chapter 6 how the nonlinear halo correlation function can be accurately modelled and only give a sneak preview here:

As mentioned in the beginning of the introduction it is in most cases impractical to calculate physical processes using the most fundamental model at hand. Therefore throughout the whole thesis the goal will be to model the physical situation as simple as possible while trying to capture the most relevant physics. For instance in order to model the nonlinear halo correlation function we will assume Newtonian gravity. We justify this by showing that Newtonian gravity can be mapped to GR in all relevant situations in a ΛCDM cosmology if there is no backreaction, see Chapters 3 and 4.

The ingredients of the model for halo correlations are *(a)* the initial distribution of proto-halos $n(\boldsymbol{q}|z, M)$ encoding the halo bias, where a proto-halo is a cloud in the initial conditions whose particles are at time z part of a halo of mass M and *(b)* the trajectories connecting the initial proto-halo position $\boldsymbol{q}$ and the final halo position $\boldsymbol{x}$, the displacement field $\boldsymbol{\Psi}(\boldsymbol{q}, z)$, which encodes the gravitational dynamics between proto-halos.

The halo distribution $n(\boldsymbol{x}, z|M)$ at the observation time z is then simply obtained by displacing the proto-halo density field $n(\boldsymbol{x}, z|M) = \int d^3q\, n(\boldsymbol{q}|z, M)\delta_{\rm D}[\boldsymbol{x} - \boldsymbol{q} - \boldsymbol{\Psi}^s(\boldsymbol{q}, z)]$, where $\boldsymbol{\Psi}^s$ takes into account that observed positions along the line of sight $\hat{\boldsymbol{z}}$, when inferred via redshift z, appear to be displaced by an additional amount $\hat{\boldsymbol{z}} \cdot \dot{\boldsymbol{\Psi}}\hat{\boldsymbol{z}}/H$ [Kai87]. The simplest quantity characterizing the cosmic web is the two-point redshift-space correlation of halos forming at the same time with the same mass $\langle n(\boldsymbol{x}, z|M)n(\boldsymbol{x}+\boldsymbol{r}, z|M)\rangle$. It can be inferred from galaxy surveys upon further modelling the halo occupation by galaxies [RSW+12]. Having an accurate and physically transparent model for the LSS including redshift space distortions is very important in the quest of constraining cosmological parameters and searching for new physics that might hide in the combined dynamics of the dark matter and dark energy.

Baryon acoustic oscillations (BAO) in the power spectrum of CDM, halos and therefore galaxies and clusters are one of the most important observables in galaxy surveys. Like the oscillations in the CMB temperature power spectrum, BAO were imprinted by the very same acoustic waves long before galaxies formed. We will see in Chapter 6 that the BAO feature is deformed by nonlinear gravitational dynamics and by redshift space distortions which we will both accurately model, such that these correlation functions contain a "standardizable ruler"

allowing a measurement of the Hubble diagram [AAB+12]. In addition redshift space distortions depend on the velocity field which is a sensitive to dark energy.

It should be clear now that *the existence of non-baryonic dark matter and dark energy composing 95% of the total energy density of today's universe is a scientific fact.*[2] We are thus challenged to extend our "effective theory of everything" (1.1) and include the ingredients that are supposed to fill up the remaining 95%.

Inflation Before we investigate how to modify (1.1), we consider the initial conditions for the sound waves *ii*), *iii*) as well as the flatness of space and the problem of why thousands of seemingly causally disconnected 1° patches of the sky have nearly the same temperature. All these aspects can be explained – in the case of *ii*), *iii*) even predicted – with the help of a crazy sounding but ingenious idea called inflation [Muk05]. Recenlty *ii*), *iii*) were confirmed by Planck [PAA+13] such that inflation is widely accepted as the most likely scenario to explain those features. We simply add a scalar field ϕ, the inflaton, similar to the Higgs, to (1.1), but with very weak coupling to the SM fields. We can choose the potential $V(\phi) = 1/2m^2\phi^2$, $m \ll m_{\rm Pl}$ and prepare the field in a special initial state $\phi_{\rm ini} \simeq m_{\rm Pl}$ where its potential energy $V_{\rm ini} \simeq (10^{16}\,{\rm GeV})^4$ is much larger than $\partial_\mu\phi_{\rm ini}\partial^\mu\phi_{\rm ini}$ within a tiny patch of space with size at least $(G\,V_{\rm ini})^{-1/2} = 10^{-14}\,{\rm GeV}^{-1} = 10^5 l_{\rm Pl}$. The subsequent dynamics of metric and inflaton are such that the inflaton slowly rolls down its potential because of the friction the nearly exponentially expanding space exerts. This slow roll inflation will turn the tiny speck of space into an enormously large, flat and nearly homogeneous and isotropic universe of which our observable universe is only a tiny part. When inflation ends, after the inflaton has approached $\phi = 0$ and $\partial_\mu\phi\partial^\mu\phi$ becomes important, it decays into particles and radiation giving rise to the hot homogeneous Big Bang. During slow roll inflation quantum fluctuations of the inflaton are continuously created and stretched by the nearly exponential expansion, giving rise to the nearly scale invariant and gaussian spectrum of density fluctuations which are then turned into the adiabatic initial conditions during the hot Big Bang, see [Muk05].

1.2 How to extend the SM+GR

Without worrying too much about fundamental physics, all three new concepts imposed upon us by cosmology: inflation, CDM and DE can be modelled using scalar fields. Therefore it is very simple to find phenomenological models; by just adding three scalar fields to (1.1) with suitably chosen potentials. We could make a patchwork and append to the expression in curly brackets of (1.1)

$$-\left(\partial_\mu\phi_{\rm dm}\partial^\mu\phi_{\rm dm} + V_{\rm dm}(\phi_{\rm dm})\right) - \left(\partial_\mu\phi_{\rm infl}\partial^\mu\phi_{\rm infl} + V_{\rm infl}(\phi_{\rm infl})\right) - \left(\partial_\mu\phi_{\rm de}\partial^\mu\phi_{\rm de} + V_{\rm de}(\phi_{\rm de})\right)\,. \quad (1.2)$$

[2] As any scientific fact, it could be false [JB03]. But one has to appreciate the long history of independent discoveries and improved measurements and the physically very different methods that constrain the same parameters, which tell a consistent story. In addition, at the time of writing, there is no alternative that can tell a similarly consistent story and does not require DM and DE.

Dark matter It is interesting to note that if $\phi_{\rm dm}$ is complex and its potential is given by $1/2m_{\rm dm}^2|\phi_{\rm dm}|^2$ then the dynamics of this scalar with carefully chosen initial conditions can accurately model collective dynamics of many collisionless selfgravitating dark matter particles. We show this in Chapter 5 and explore that this property can be used to replace cosmological N-body simulations with scalar field simulations.[3] More importantly the scalar can replace the commonly used pressureless fluid model for CDM dynamics, which contains pathological singularities.

If one sought for a more fundamental model of CDM there are many candidates that have a deeper physical motivation and justification to be added to (1.1). For instance axions could not only comprise the CDM [DGL+14], but also solve the riddle of a seemingly missing term in (1.1) [PQ77]. Another alternative is that CDM is composed of supersymmetric particles, which happens to be a stable fermion in minimally supersymmetric extensions of the SM [EHN+84].

Inflation There are many inflation models motivated by fundamental physics, see [BM14] for a review. String theory and grand unified theories try to replace the curly brackets in (1.1) altogether by a more fundamental theory.

Dark energy It seems that the hardest part is DE, although it is in some sense the simplest. One might say it is the simplest problem to solve, because instead of introducing a scalar field one can simply modify (1.1) without introducing any new degrees of freedom by adding a cosmological constant to the Ricci scalar : $(R-2\Lambda)/(16\pi G)$. The resulting combined model of SM, GR, CDM and Λ is called ΛCDM model and is consistent with nearly[4] all observations. The big and old problem with Λ is to understand why it is so small: Various *physically distinct* contributions like SM phase transitions or vacuum fluctuations add to any Λ that we put in by hand and each of them is about 45 to 55 orders of magnitudes larger than the value observed, such that they must cancel each other out to incredible accuracy if GR is assumed to be correct, see the review by [Mar12]. At the same time we are very certain about the existence of the electroweak phase transition through the discovery of the Higgs boson [CKS+12] and about the effects of classical vacuum energies on the expansion rate through the success of the inflationary paradigm [PAA+13], that recently got further support trough the tentative discovery of primordial gravitational waves [BAA+14]. This motivates to modify the otherwise so successful GR and to look for signs beyond the ΛCDM model in observations. It feels like we are on the verge of learning something deeply profound about nature.

Although currently, there is no modified gravity model that can solve this problem, it makes sense to study alternatives to GR+Λ. In particular it is phenomenologically interesting to look for models that have not only a dynamical DE, but where DE also modifies the gravitational force giving rise to a "5th force". In Chapter 2 we will study the Hu-Sawicki-Starobinski (HSS) [HS07, Sta07] model where gravity and DE are described by $(R+f(R,\Lambda,\epsilon))/(16\pi G)$. In particular we derive the abundance $n(M,\epsilon)$ of DM halos of mass M, related to cluster counts, and analyze how this observable is changed compared to GR+Λ. The ϵ can be used to interpolate between

[3] The flip-book animation in the right corner is such a simulation, showing how a cold phase space distribution evolves.

[4] Neutrino masses and baryon asymmetry require further extensions in addition to inflation.

GR+Λ, where $\epsilon = 0$, and models that show a very strong 5th force. Therefore these models can be already ruled out by observations of the large scale structure and ϵ can be observationally constrained. The HSS model also exhibits the so called chameleon mechanism [KW04a], which is one of a few mechanisms that can locally turn off the 5th force close to dense environments like the Solar System, Galaxy or the early Universe in which GR has withstood precision tests such that these models are tuned to agree with GR under these conditions. The reason why the HSS model is so extensively studied in the literature is that it is a working example of the chameleon mechanism, a mechanism whose observational signatures should not be particularly sensitive to details of the model and if detected would be a clear sign of new physics.

2

Spherical collapse and halo mass function in $f(R)$ theories

This chapter is published as an article [KAAW13], and arose in collaboration with Stephen Apply, Ixandra Achitouv and Jochen Weller. We compute the critical density of collapse for spherically symmetric overdensities in a class of $f(R)$ modified gravity models. For the first time we evolve the Einstein, scalar field and non-linear fluid equations, making the minimal simplifying assumptions that the metric potentials and scalar field remain quasi-static throughout the collapse. Initially evolving a top hat profile, we find that the density threshold for collapse depends significantly on the initial conditions imposed, specifically the choice of size and shape. By imposing 'natural' initial conditions, we obtain a fitting function for the spherical collapse δ_c as a function of collapse redshift, mass of the overdensity and $f_{\rm R0}$, the background scalar field value at $z = 0$. By extending δ_c into a drifting and diffusing barrier within the context of excursion set theory, we obtain a realistic mass function that might be used to confront this class of scalar-tensor models with observations of dark matter halos. The proposed analytic formula for the halo mass function was tested against Monte Carlo random walks for a wide class of moving barriers and can therefore be applied to other modified gravity theories.

2.1 Introduction

Einstein's theory of General Relativity (GR) [Ein15] has withstood nearly one century of experimental testing. Many of its predictions have been confirmed through high precision laboratory and solar system experiments, and more recently with astrophyiscal and cosmological data (see [Wil06] for a review). Testing GR on the largest scales is a field still in its infancy, as probing cosmological distances is technically challenging. However current and future surveys mapping the

large-scale structure of the universe already provide a powerful tool to constrain gravity models [EWA+11, DES, PS, LAA+11].

In spite of its success, there are theoretical reasons to believe that GR is not a fundamental theory of gravity. In particular one expects corrections to the Einstein-Hilbert action through 1-loop corrections induced by matter [DFCB77]. In addition, there are puzzling cosmological observations such as the recently discovered accelerated expansion [RFC+98, PAG+99, ABC+06] which, although still consistent with GR and a cosmological constant term, might require a new gravity theory or the existence of an exotic form of matter known as dark energy.

In [Sta80] it was noticed that the local 1-loop corrections to the Einstein-Hilbert action are quadratic in curvature, and lead to a period of inflation in the very early universe. This motivates the introduction of additional functions of the curvature invariants, that allow for a dynamical late time acceleration [Cap02, Sta07] without the need for additional scalar fields or cosmological constant Λ. The observed value of the cosmological constant $\Lambda_{\rm obs} \simeq (10^{-4}\,{\rm eV})^4$ is so extraordinarily small that one needs a finely tuned bare cosmological constant $\Lambda_{\rm obs} = \Lambda_{\rm bare} + \Lambda_{1-{\rm loop}} + \Lambda_{\rm vev}$ in the Einstein Hilbert action in order to cancel the large quantum vacuum energy $\Lambda_{1-{\rm loop}} \geq E_{\rm ew}^4 \simeq (100\,{\rm GeV})^4$ and classical contributions related to Standard Model phase transitions $\Lambda_{\rm vev} \simeq \mathcal{O}(E_{\rm ew}^4, E_{\rm QCD}^4)$. This severe "old" cosmological constant problem [Wei89] is not resolved in $f(R)$ theories. In this chapter we assume that effectively $\Lambda_{\rm bare} = \Lambda_{1-{\rm loop}} = \Lambda_{\rm vev} = 0$ due to some other physical process possibly acting at the scale $\Lambda_{\rm obs} \simeq (10^{-4}\,{\rm eV})^4$ such that $\Lambda_{\rm obs}$ enters the modified gravity theory naturally. In addition, the unknown physics leading to the removal of the vacuum energy might be accompanied by an effective scalar degree of freedom. There exist some ideas of screening [DHK07, dDH+08, BDH+11] and relaxing [Dol85, CCPS11, EK11, BSS10] the vacuum energy.

In this work we focus on a simple class of modified gravity models, so called $f(R)$ gravity, where an arbitrary function of the Ricci scalar is introduced into the standard Einstein Hilbert action. It is well known that certain $f(R)$ functional forms can give rise to an expansion history that exactly mimics a Universe governed by a cosmological constant Λ and cold dark matter (ΛCDM). However even for such models, the modified gravity contribution will still affect the growth of structure, both in the linear and nonlinear regime via a fifth force mediated by a scalar degree of freedom, the "scalaron" [Sta80] .

To be consistent with local and astrophysical gravity tests, $f(R)$ functions must be used that essentially approach a constant value (usually $\Lambda_{\rm obs}$) in regions of high curvature. This ensures that in these high curvature regions the local scalaron mass becomes large enough to shut down the fifth force on much smaller scales. This effect is called the chameleon mechanism [KW04a, BvD+04]. At high curvature, such as in regions with deep potential wells in the late universe, e.g. galaxies and the solar system or in the early universe, at recombination, these $f(R)$ theories are pushed towards GR. However at small curvature, typically well after matter-radiation-equality and on large scales, detectable deviations from GR are possible and still allowed observationally. This is exactly the regime where linear and non-linear large-scale structure formation takes place. While $f(R)$ theories should not be viewed as fundamental theories of gravity, they offer a self-consistent tool to scrutinize GR and look for new physics signatures like the chameleon effect in the currently mapped large-scale structure. In order to avoid large quantum corrections and loss of predictability, the scalaron mass cannot become ar-

bitrary large [UHK12]. The formal limit of taking the scalaron mass to infinity, and therefore to recover GR, crosses a strong coupling regime and cannot be faithfully described by a classical theory. Fortunately, for the specific $f(R)$ theory we will specify in the next section, the scalaron mass can be chosen large enough to still allow to tune the model between "basically GR" and a model with fifth force.

In [OLH08, MMM+11] a constraint on $f(R)$ theories using the galaxy power spectrum was calculated, where it was found that the chameleon mechanism surpresses deviations from GR on small scales where perturbations become nonlinear. However the formation of galaxy clusters involves both linear and nonlinear growth and is thus better suited to probe both the fifth force and the chameleon effects present in scalar-tensor theories [LH11].

The aim of this chapter is to predict the number density of dark matter halos $n(M, z, f_{R0})$ with a given mass M and observed redshift z as a function of the model parameter f_{R0} of the Hu-Sawicki-Starobinsky $f(R)$ model [HS07, Sta07]. Building on the work of [CA11b, ARSC12], we employ the spherical collapse model to obtain a critical density contrast δ_c, from which we construct a realistic mass function. Similar semi-analytical formalisms were already applied to $f(R)$ theories in previous works [SLOH09, BRS10, BJZ11, LE11, LL12b, LL12a, LLKZ13], see [CCL13] for voids. In [SLOH09] only two limiting cases were considered: either the collapsing overdensity was considered to be fully chameleon screened or fully unscreened. As these two cases correspond to spherical collapse in ΛCDM with a rescaled Newton constant in the unscreened case, an initial top-hat density profile retains its shape during collapse. This allowed the authors to study the spherical collapse of a top-hat profile by simply comparing the evolution of a closed patch of Friedmann-Robertson-Walker (FRW) spacetime. However comparison to N-body simulations showed that this model was too simple and missed the interesting regime between the two limiting cases [SLOH09].

The above restrictions were dropped in [BJZ11], where the collapse of the top-hat was studied numerically by solving the modified gravity field equations. An important result of this work was the discovery that a top-hat profile develops shell crossing during its evolution. In order to alleviate this problem, a smooth transition region between the top-hat and the 'background' FRW spacetime was introduced. However the resulting values of δ_c showed dependence on the shape of the transition region, and did not lie in the expected range obtained in [SLOH09].

In this chapter we improve the spherical collapse calculation for $f(R)$ models by using as initial condition the average density profile around a density peak. This is completely determined by the input cosmology, thus removing any ambiguity in the choice of initial profile and making the spherically symmetric setup as physically accurate as possible. The profile is calculated using peaks theory [BBKS86] and the linear matter transfer function [LCL00].

The chapter is organized as follows. In Section 2.2 and 2.3 we review and obtain the relevant equations for spherical collapse in $f(R)$ theories and explain the method of their numerical solution. Here special care is taken of the initial conditions and applicability of the quasistatic approximation, which is crucial due to the breakdown of Birkhoff's theorem. We exhibit one of the main results of this work; a fitting function for the critical overdensity $\delta_c(M, z, f_{R0})$ which the linearly extrapolated matter density has to reach in order to form a halo of mass M at redshift z within the model parameter range $10^{-7} < f_{R0} < 10^{-4}$. In Section 2.4 we review the excursion set formalism and extending $\delta_c(M, z, f_{R0})$ into a drifting and diffusing barrier, modeling this way

aspherical collapse, in order to obtain a realistic mass function $n(M, z, \delta_c, f_{\rm R0})$ in terms of the collapse redshift z, mass of the object M and modified gravity parameter $f_{\rm R0}$. The accuracy of this mass function function is checked against Monte Carlo random walks and a mass function from N-body simulations in Section 2.4 and we conclude in Section 2.5.

2.2 Review of the Hu-Sawicki-Starobinsky $f(R)$ model

The $f(R)$ action is given by

$$S = S_m + \frac{1}{2\kappa^2}\int d^4x\sqrt{-g}\,(R + f(R))\,, \tag{2.1}$$

where $\kappa^2 = 8\pi G$ and S_m a minimally coupled matter action. Variation with respect to the metric gives the Einstein field equations

$$G_{\mu\nu} = e^{-\varphi}\left(\kappa^2 T_{\mu\nu} - \frac{1}{2}g_{\mu\nu}V(\varphi) + (e^{\varphi})_{;\mu\nu} - g_{\mu\nu}\Box e^{\varphi}\right)\,, \tag{2.2}$$

with energy momentum tensor $T_{\mu\nu}$ and Einstein tensor $G_{\mu\nu} = R_{\mu\nu} - Rg_{\mu\nu}/2$. We have introduced the notation

$$e^{\varphi} \equiv 1 + f_{,R}\,, \qquad V(\varphi) \equiv Re^{\varphi} - R - f\,, \tag{2.3}$$

where writing $V(\varphi)$ requires a form of f such that $e^{\varphi} = 1 + f_{,R}$ can be inverted to give $R(\varphi)$. The condition $1 + f_{,R} > 0$ is required to ensure that the $f(R)$ model remains ghost free [Sta07]. Using (2.3), the trace of the field equations

$$3\Box e^{\varphi} = -2V + V_{,\varphi} + \kappa^2 T \tag{2.4}$$

allows us to interpret the fourth order differential equations for $g_{\mu\nu}$, Eqs. (2.2) and (2.3), as second order field equation (2.2) plus a second order equation (2.4) for the scalar φ. One can view this procedure as a first step in the direction of a Hamiltonian formulation [OS11, SH11, DSY09]. It is also possible to make the replacement (2.3) already in the action (2.1)

$$S = S_m + \frac{1}{2\kappa^2}\int d^4x\sqrt{-g}\,(e^{\varphi}R - V(\varphi))\,, \tag{2.5}$$

where variation with respect to $g_{\mu\nu}$ and the scalar φ leads to (2.2) and (2.3). The action (2.5) is kown as O'Hanlon theory [O'H72], which is a subclass of the most general scalar field theory giving rise to second order field equations [Hor74]. Since matter is minimally coupled, the energy momentum tensor of matter $T_{\mu\nu}$ is conserved

$$T^{\mu}{}_{\nu;\mu} = 0\,, \tag{2.6}$$

implying that the Euler and continuity equation for a perfect fluid take the same form as in GR. The same is true for the geodesic equation and thus for the general relativistic virial theorem

[Jac70].[1] In the following we consider only cold dark matter in the single-stream approximation, such that the energy momentum tensor takes the form of pressureless perfect fluid

$$T_{\mu\nu} = \varrho u_\mu u_\nu \,, \quad u_\mu u^\mu = -1 \,, \quad T = -\varrho \,, \tag{2.7}$$

with energy density ϱ and four velocity u^μ. This is justified as we only consider times well after matter radiation equality and choose initial conditions where shell crossing does not occur.

The functional form of $f(R)$ is strongly restricted due to theoretical and phenomenological constraints [HS07, ADF10], meaning that the resulting theory is free of classical and quantum instabilities and consistent with all known gravity experiments and observations. We will consider the class of $f(R)$ functions proposed by Hu and Sawicki [HS07] and also Starobinsky [Sta07]

$$f(R) = -2\Lambda + \frac{\epsilon}{n}\frac{(4\Lambda)^{n+1}}{R^n} \tag{2.8}$$

$$\simeq -\frac{2\Lambda}{1 + 2\epsilon/n\ (4\Lambda/R)^n} \tag{2.9}$$

$$\simeq -2\Lambda + 2\Lambda\left(1 + \left[\frac{(n/2)^{1/n}}{\epsilon}\frac{R}{4\Lambda}\right]^2\right)^{-n/2} , \tag{2.10}$$

which can fulfill the above-mentioned constraints and are in this sense viable. In the cosmologically important region $R > 4\Lambda$ the three models above exhibit essentially the same behaviour. The Hu-Sawicki model (2.9) and the Starobinsky model (2.10) interpolate between $f = 0$ and $f = -2\Lambda$, where steepness is controlled by n and the position of the transition is at $\epsilon^{1/n}4\Lambda$. Here Λ is a constant energy scale whose value coincides with the measured value $\Lambda = \Lambda_{\rm obs} = 3H_0^2\Omega_\Lambda$ and $\epsilon \ll 1$ is a small positive deformation parameter which is related to the more commonly used $f_{\rm R0}$, via

$$f_{\rm R0} \equiv |f_{,R}(R_0)| = \epsilon\left(1 + \tfrac{1}{4}\left(\Omega_\Lambda^{-1} - 1\right)\right)^{-(n+1)} . \tag{2.11}$$

Galactic rotation curves require $\epsilon \lesssim 10^{-6}$ and cepheids $\epsilon \lesssim 0.5 \times 10^{-6}$, such that viable $f(R)$ theories and ΛCDM have virtually indistinguishable expansion histories [HS07, JVS12]. Stability of the de Sitter vacuum together with solar system tests demands $n \gtrsim 1$ [CT08]. Using the expansion history and baryon acoustic oscillations (BAO) gives complementary constraints on n [MMM+11]. Enforcing $\epsilon \ll 1$ effectively introduces two additional energy scales; Λ/ϵ and $\Lambda\epsilon$. As we will see, $\Lambda\epsilon$ is the range over which the effective potential of φ varies and Λ/ϵ is the squared mass of the scalaron, corresponding to small fluctuations ($\ll \epsilon$) around the background field $\bar{\varphi} = -\epsilon$ during the cosmic late time acceleration. Interestingly there exists also lower bounds on ϵ, to ensure that φ can be treated as a classical field [UHK12].

Now we derive the explicit form of $V(\varphi)$ for model (2.8), which will be assumed in the rest of this chapter. For this we note first that

$$f_{,R} = -\epsilon\left(\frac{4\Lambda}{R}\right)^{n+1} , \tag{2.12}$$

[1] Eq. (8) of [Jac70] applies unchanged to metric $f(R)$ theories. In order to estimate the virial radius within the context of spherical collapse one needs in addition to the virial theorem some form of energy conservation. This however does not exist in general $f(R)$ theories [CCHO09].

such that in and after matter domination

$$|f_{,R}| \leq \epsilon \ll 1 \qquad \Rightarrow \qquad f_{,R} \simeq \varphi \,. \tag{2.13}$$

From Eqs. (2.12) and (2.13) it follows

$$R = 4\Lambda \left(\frac{|\varphi|}{\epsilon}\right)^{-\frac{1}{n+1}} , \qquad f = -2\Lambda + \frac{\epsilon}{n} 4\Lambda \left(\frac{|\varphi|}{\epsilon}\right)^{\frac{n}{n+1}} . \tag{2.14}$$

Finally $V = \varphi R - f$ becomes

$$V = 2\Lambda \left(1 - 2\epsilon \frac{n+1}{n} \left(\frac{|\varphi|}{\epsilon}\right)^{\frac{n}{n+1}}\right) . \tag{2.15}$$

We can write the scalar equation (2.4) as

$$V^{\rm eff}_{,\varphi} \equiv -e^{-\varphi} \frac{1}{3} \left(2V + \kappa^2 \varrho - V_{,\varphi}\right) = \Box\varphi \,, \tag{2.16}$$

where $V^{\rm eff}$ is the effective potential the scalar φ tries to minimize. Using $|\varphi| \ll 1$ it is given by

$$V^{\rm eff} = \epsilon \frac{4\Lambda}{3} \left(\left(1 + \frac{\kappa^2 \varrho}{4\Lambda}\right) \frac{|\varphi|}{\epsilon} - \frac{n+1}{n} \left(\frac{|\varphi|}{\epsilon}\right)^{\frac{n}{n+1}}\right) . \tag{2.17}$$

The minimum of $V^{\rm eff}$ is at the field value $\varphi_{\rm min}$,

$$\varphi_{\rm min} = -\epsilon \left(1 + \frac{\kappa^2 \varrho}{4\Lambda}\right)^{-(n+1)} , \tag{2.18}$$

which approaches zero $\varphi_{\rm min} \to 0$ for $\kappa^2 \varrho \gg \Lambda$, see Fig 2.1. If φ occupies the minimum in this limit then GR is restored: the effective Newtonian constant $e^{-\varphi}\kappa^2 \to \kappa^2$ returns to its GR value and the potential becomes $V \to 2\Lambda$. For small fluctuations around $\varphi_{\rm min}$, the scalaron has a mass

$$m^2 \equiv V^{\rm eff}_{,\varphi\varphi} = \frac{4}{3(n+1)} \frac{\Lambda}{\epsilon} \left(\frac{|\varphi|}{\epsilon}\right)^{-\frac{n+2}{n+1}} , \tag{2.19}$$

which diverges at the General Relativistic limit $m(\varphi = 0) \to \infty$.[2] In this limit the fifth force is turned off since the effective interaction range of a Yukawa type interaction is given by the Compton wavelength $1/m$.

Whether φ actually sits at the potential minimum in high density regions depends on the magnitude of spatial gradients [KW04b]. For galaxy clusters, if the forming cluster is too small or ϵ to large, φ-gradients cost too much energy and φ will stay near its background value $\bar{\varphi} = \bar{\varphi}_{\rm min}$

[2] Adding a $R^2/6M^2$ to (2.8) removes this infinity amongst other pathologies [ABS10], but leaves the late time cosmology unaffected provided the energy scale M is large enough.

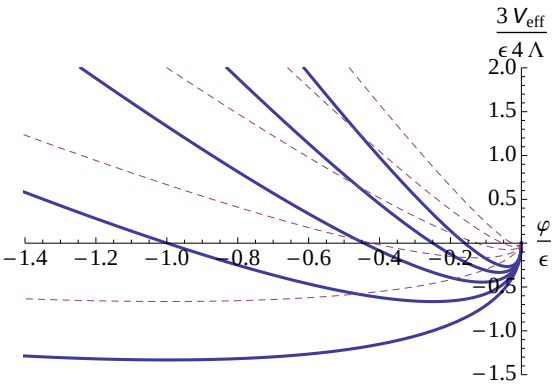

FIGURE 2.1: $V_{\rm eff}$ for model (2.8) with $n = 1$, *full* lines, and $n = 2$, *dashed* lines. From bottom to top $\kappa^2\varrho/4\Lambda = 10^{-3}, 1, 2, 3$ and 4.

even within the cluster, preventing the chameleon mechanism from operating. Large clusters and small ϵ on the other hand leave enough space for the scalar to change from $\bar{\varphi}$ to $\varphi_{\rm min}^{\rm cluster}$ and hence the chameleon mechanism becomes active above a certain cluster mass scale. A necessary condition for the chameleon mechanism to activate is that the Compton wavelength $1/m_{\rm min}$ must be much smaller than the size of the overdensity [HS07]. In this case there is only a "thin shell" at the edge of the object that can mediate a large distance fifth force, from which the interior is unaffected and thus behaves like a typical overdensity in GR.

For overdensities of different magnitude and shape, and for different values of the $f(R)$ model parameters (n, ϵ) we encounter a time dependent mixture of all the above cases.

2.3 Spherical collapse

The spherical collapse model [Pee67, GG72] is a deterministic criterion which allows one to map an initially small, spherically symmetric overdensity to the formation of a virialized dark matter halo. More concretely this spherical collapse of an initial density profile $\delta(z_i, r)$ allows one to estimate the formation time $z_c(\delta_i)$ of a halo as function of the initial density amplitude $\delta_i \equiv \delta(z_i, r = 0)$, which can be inverted to give the threshold

$$\delta_i(z_c) \equiv \delta(z_i, r = 0|z_c) \tag{2.20}$$

for the initial density profile to collapse at redshift z_c. Spherical collapse in an Einstein-de Sitter or ΛCDM universe can be modeled analytically by assuming that the density is homogeneous within the perturbation. Due to Birkhoff's theorem, the inner part is not influenced by the transition region and simply behaves as a closed FRW universe. The redshift z_c of collapse of this patch measured in the flat exterior FRW then approximately equals the formation time of a bound virialized object [JFW+01].

In the case of $f(R)$ theories we actually need to solve the full field equations since Birkoff's theorem does not apply. There are further complications which hamper the calculation in $f(R)$ models. It was noticed in [LH11] that halos are actually composed of subhalos, and this will

increase the chameleon effect as screened subhalos attract each other less strongly than particles in a homogeneous dust cloud. Another environmental effect arises due to the fact that the forming cluster is itself a subcluster of a larger sized over/underdensity, enhancing/diminishing the chameleon effect [LE11, LLKZ13] by diminishing/enhancing field gradients. In this work we do not consider these two effects, although part of the environmental dependence of the collapse threshold is taken into account by using the average density profile around a peak, which only depends on linear power spectrum $P(z_i, k)$. We comment further on the environment in 2.3.3 and 2.5.

As will be reviewed in Section 2.4 the halo mass function depends on the spherical collapse derived quantity $\delta_i(z_c)$ via

$$\nu_c \equiv \frac{\delta_i(z_c)}{\sigma(z_i, R)}\,, \tag{2.21}$$

which is z_c-independent for an Einstein de Sitter universe and slightly z_c-dependent in an ΛCDM universe. The standard deviation $\sigma(z_i, R)$ is given by the linear matter power spectrum $P(z_i, k)$ and filter function W

$$\sigma(z_i, R)^2 = \int \frac{d^3k}{(2\pi)^3} W(kR)^2 P(z_i, k)\,. \tag{2.22}$$

For convenience one usually considers

$$\delta_c(z_c) \equiv D(z_c, z_i)\delta_i(z_c)\,, \tag{2.23}$$

which defines the collapse threshold at redshift z_c. This quantity is the linearly extrapolated density field, where the linear growth function $D(z_c, z_i) = D(z_c)/D(z_i)$ was used to evolve from z_i to z_c, where and where $D \propto H(a)\int_0^a da'(a'H(a'))^{-3}$ is given by

$$D(z) = \frac{\sqrt{\Omega_m(1+z)^3 + 1 - \Omega_m}\ {}_2F_1[\frac{5}{6}, \frac{3}{2}, \frac{11}{6}, \frac{1-\Omega_m^{-1}}{(1+z)^3}]}{(1+z)^{5/2}\ {}_2F_1[\frac{5}{6}, \frac{3}{2}, \frac{11}{6}, 1-\Omega_m^{-1}]}\,. \tag{2.24}$$

The introduced time evolution has no physical meaning but is convenient as $\delta_c(z_c) = 1.686$ is constant in an Einstein-de Sitter universe, and only weakly dependent on z_c in ΛCDM. The approximate z_c- and R-independence of δ_c leads to the universality of halo mass function if written as a function of $\sigma(z_c, R) = D(z_c, z_i)\sigma(z_i, R)$. Despite the artificial time evolution introduced in the definition of (2.23), it is the collapse criterion (2.20) defined at the initial time that one should have in mind both for GR and $f(R)$ gravity: the halo mass function is determined within the initial conditions and the information about formation time only enters via (2.20). Due to the practically identical expansion histories in ΛCDM and the assumed $f(R)$ model (2.8), the initial conditions can be assumed to be equivalent for both models. In particular $\sigma(z_i, R)$ is identical in both models if z_i is chosen such that all relevant scales are still linear. Therefore in Eq. (2.21) only $\delta_i(z_c)$ should be adjusted when we consider $f(R)$ models.

Since the collapse criterion (2.20) is the quantity we wish to calculate, we can trivially rewrite the definition (2.21) of $\nu_c(z_c, R)$ using the ΛCDM growth function D

$$\nu_c \equiv \frac{\delta_i(z_c, R)}{\sigma(z_i, R)} = \frac{\delta_i(z_c, R)D}{\sigma(z_i, R)D} = \frac{\delta_c(z_c, R)}{\sigma(z_c, R)}\,. \tag{2.25}$$

This expression holds for both $f(R)$ and ΛCDM, however as we will see in Section 2.4, $f(R)$ theories predict a δ_c that is a function of both z_c and R. This is already the case for ellipsoidal collapse in GR [ST02].

As a final point, let us emphasize that using the scale dependent $f(R)$ linear growth factor instead of the GR equivalent $D(z)$ in Eq. (2.25) would be both incorrect and inconvenient. Incorrect since linear growth in $f(R)$ is scale dependent and therefore not multiplicative, and inconvenient as $\delta_c(z_c, R)$ would no longer encode all of the $f(R)$-dependent deviations; instead one would need to provide $\nu_c(z_c, R)$. $\delta_c(z_c, R)$ as defined in (2.20) and (2.23) is a convenient way to provide $\nu_c(z_c, R)$. Another convenient way would be to fix $\delta_c(z_c, R) \equiv \delta_c^\Lambda(z_c)$ and to fold all the $f(R)$-dependence into a modified $\sigma^{f(R)}(R)$ [LH11].

2.3.1 Quasistatic equations

To obtain δ_c, we must calculate the collapse of a spherically symmetric pressureless matter distribution in an asymptotic FRW spacetime, such that the 3+1 dimensional problem simplifies to a 1+1 dimensional one. In GR the calculation is much simpler. Due to Birkhoff's theorem an initially homogeneous ("top-hat") overdensity retains its shape during collapse. This allows us to treat the size of the homogeneous overdense region as the scale factor of a closed FRW universe [Wei08].

In $f(R)$ theories the additional scalar degree of freedom φ allows for monopole radiation [Sex66], thus Birkoff's theorem no longer applies. Another, more severe, problem is that in the linear regime of collapse the gravitational force is scale dependent due to mass of $\bar{\varphi}$ fluctuations. Finally, since the energy density becomes sufficiently large during collapse for the chameleon mechanism to take effect, the gravitational force will depend on the local density. As a result of these effects, an initial top-hat overdensity will not retain its shape during collapse and we cannot use a closed FRW to describe its collapse. Rather, we must solve the spherically symmetric $f(R)$ field equations.

A spacetime which a admits a spherically symmetric spatial slicing has a metric which can written in the form [MTW73]

$$ds^2 = -e^{2\Phi}dt^2 + a^2 e^{-2\Psi}(dr^2 + r^2 d\Omega^2)\,, \tag{2.26}$$

where both Φ and Ψ are functions of r and t. For convenience we factor out $a(t)$, which will be the scale factor of the asymptotic flat FRW spacetime, where we choose $a(t_0) = 1$ without loss of generality. Note that this metric is fully nonperturbative. We present the nonlinear field equations in Appendix 2.A and derive the conditions under which one can assume that Φ, Ψ and φ remain small even when the density becomes non-linear $\delta \equiv \varrho/\bar{\varrho} > 1$. Under these conditions, the set of relevant field and fluid equations reduces to the
Poisson equation

$$a^{-2}\Delta\Phi = \frac{2}{3}\kappa^2\bar{\varrho}\delta - \frac{1}{6}\delta V_{,\varphi}\,, \tag{2.27a}$$

the nonlinear scalar field equation

$$a^{-2}\Delta\varphi = \frac{1}{3}(\delta V_{,\varphi} - \kappa^2\bar{\varrho}\delta)\,, \tag{2.27b}$$

the energy conservation

$$\dot{\delta} + \frac{1}{ar^2}\partial_r\left(r^2(1+\delta)v\right) = 0 \tag{2.27c}$$

and the Euler equation

$$\dot{v} + vH + \frac{v}{a}v' = -\frac{1}{a}\Phi' , \tag{2.27d}$$

with $v \equiv v^r \equiv au^r/u^0$ as the radial velocity and $\delta V_{,\varphi} \equiv V_{,\varphi} - \bar{V}_{,\varphi}$ the perturbation in the Ricci curvature. Note that we cannot assume $\delta V_{,\varphi} = \bar{V}_{,\varphi\varphi}\delta\varphi$ in (2.27b) since we would then miss the effect of the chameleon mechanism. It is important to treat (2.27b) as a nonlinear partial differential equation, even though $\delta\varphi \equiv \varphi - \bar{\varphi} \leq \epsilon \ll 1$. This non-linearity makes solving the system (2.27) a nontrivial task. We explain details of the numerical methods in Section 2.3.4.

2.3.2 Initial conditions

In addition to the relevant dynamical equations, we must also specify the initial conditions of the problem. Well after matter-radiation equality and well before the late time accelerated expansion, the Universe is in a state that is well described by a linearly perturbed Einstein-de Sitter spacetime on all scales relevant for large-scale structure formation. At such early times modified gravity effects due to the scalar field φ are completely negligible due to the temporal chameleon effect as seen in Fig. 2.1.

We choose $z_i = 500$ as our initial time for the spherical collapse. At this redshift, radiation is already sub-dominant relative to matter by a factor of order $\sim \mathcal{O}(0.1)$. Also the subhorizon assumption implicit in eq. (2.29) at z_i is acceptable; the largest masses considered in this work are ~ 0.1 of the horizon size.[3] Note that at this initial redshift, the radiation component is subdominant to matter but non-negligible. To evade any potential problems with normalisation of the power spectrum, we use CAMB [LCL00] to obtain $\sigma(z{=}0, R)$ with the choice of cosmological parameters

$$\begin{aligned} \sigma_8 &= 0.8\,, \\ \Omega_m &= 0.27\,, \\ h &= 0.7\,, \\ n_s &= 0.96 \end{aligned}$$

and then evolve the general relativistic growth equation to obtain $\sigma(z_c, R) = D(z_c)\sigma(z{=}0, R)$ to the collapse redshift, neglecting radiation. Throughout this chapter, we stress that all quantities calculated using linear theory are obtained from the standard general relativistic equations.

We discuss our choice of the initial density profile $\delta_i(r)$ in the following section. Given $\delta_i(r)$, we can use the constraint and Poisson equations

$$2\Phi' H = -\kappa^2\bar{\varrho}(1+\delta)av \tag{2.28}$$

[3] The largest clusters have masses $\sim 10^{15}\,M_\odot$ and they entered the horizon $aH/k = 1$ at around $a = 3\cdot 10^{-5}$. In order to estimate the sizes at $z_i = 500$ and today we assume a matter dominated universe, thus $Ha \sim a^{-1/2}$ and we find $aH/k|_{z=0} \sim \mathcal{O}\left(10^{-3}\right)$ and $aH/k|_{z=500} \sim \mathcal{O}(0.1)$, which is well inside the horizon.

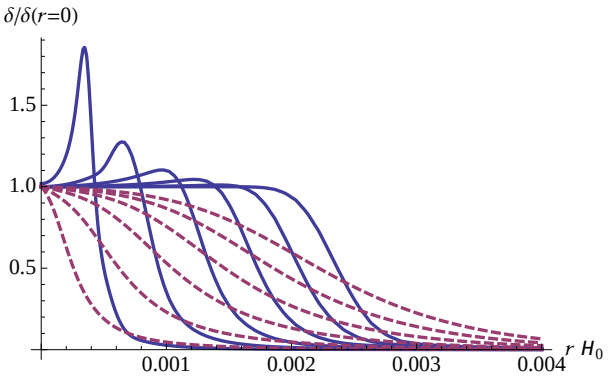

FIGURE 2.2: Comparison of density profiles (2.31) with $s = 0.05$, *full* lines, and $s = 0.4$, *dashed* lines for $n = 1$ and $\epsilon = 10^{-5}$. The plot shows the normalized density profile at different instances during collapse, from left to right $a = 0.24, 0.34, 0.44, 0.54, 0.64, 0.73$.

$$2a^{-2}\Delta\Phi = \kappa^2\bar{\varrho}\delta \tag{2.29}$$

to obtain $\Phi_i(r)$ and $v_i(r)$ at $z = z_i$;

$$v_i(r) = -\frac{a_i H_i}{r^2}\int_0^r \delta_i(r')r'^2 dr' \,. \tag{2.30}$$

We use the the following natural boundary conditions at all times; $\Phi' = \Psi' = \varphi' = 0$ at $r = 0$, and $\Phi = \Psi = 0$ at the outer boundary $r \to \infty$.

2.3.3 Density profile

It was observed in [BJZ11] that the shape of an initial tophat density profile will evolve in $f(R)$ theories, in contrast to the shape preserving evolution obtained in GR. Specifically, they found that a tophat profile develops a large spike near the boundary between the overdensity and background FRW spacetime. We confirmed this behaviour when using the initial density profile

$$\delta_i(r) = \frac{\delta_{i,0}}{2}\left(1 - \tanh\left(\frac{r/r_b - 1}{s}\right)\right) , \tag{2.31}$$

where r_b is the size of the tophat-like function and $0 < s < 1$ determines the steepness of the transition, with $s \to 0$ leading to $\delta_i(r) = \delta_{i,0}\theta(r - r_b)$. Decreasing s has the effect of forming a steeper spike at an earlier redshift. Fig. 2.2 shows the normalized density profiles for two different steepness parameters but same r_b at different instances during collapse.

The formation of a spike, which signals shell crossing, prohibits the use of tophat like functions for numerical studies. More importantly, it is clear that the shape of the density profile can dictate whether the chameleon mechanism becomes active; this is indicated in Fig .2.3. Depicted here are the potential V_{eff} and field φ at different times and positions. We see that the minimum of the effective potential φ_{min} only determines the position of φ far outside the overdensity $rH_0 = 1$,

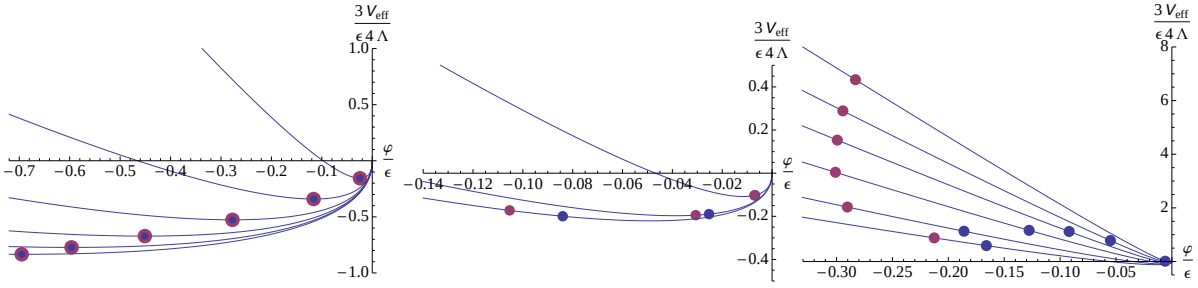

FIGURE 2.3: Comparison of $\varphi(r)$ for density profiles (2.31) with $s = 0.05$, *blue* dots, and $s = 0.4$, *red* dots using $n = 1$ and $\epsilon = 10^{-5}$. In the left plot the effective potential $V_{\rm eff}$ (*full* line) is evaluated for $\varphi(a, rH_0 = 1)$ at different instances during collapse, from top to bottom $a = 0.24, 0.34, 0.44, 0.54, 0.64, 0.73$. The middle and right plot show $V_{\rm eff}$ evaluated at the center $\varphi(a, r = 0)$ at $a = 0.24, 0.34, 0.44$ from top to bottom and $a = 0.54, 0.64, 0.69, 0.72, 0.73$ from bottom to top.

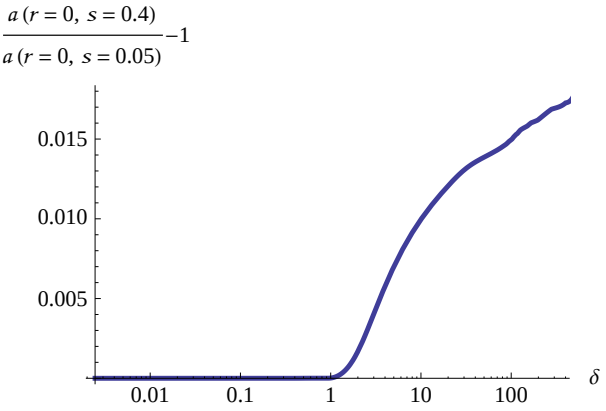

FIGURE 2.4: Ratio of of the scale factor written as function of the central overdensities for $s = 0.05$ and $s = 0.4$ using the density profile (2.31) ($n = 1$ and $\epsilon = 10^{-5}$)

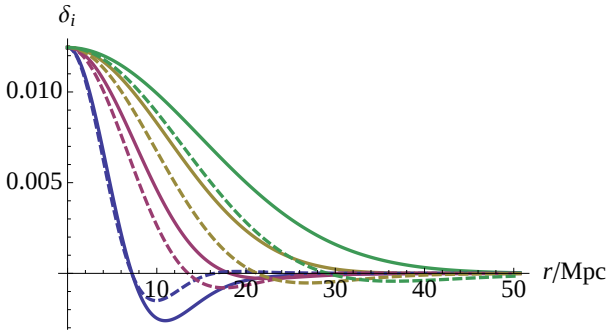

FIGURE 2.5: Comparison between primordial (*dashed* lines) and transferred (*full* lines) density profile (2.91) for $\nu = 1.5, 2, 2.5, 3$ from left to right corresponding to smoothing lengths $R = 11.1, 8.6, 6.0, 3.9\,\mathrm{Mpc}/h$ is the smoothing length.

where gradients are always small. In the center $r = 0$ it is prevented from settling into the minimum because the necessary field gradients are energetically too costly. However for the steep profile (blue dots), $\varphi(r = 0)$ finally turns around and moves to the potential minimum. Hence the collapse time of an overdensity with fixed M and δ_i will depend on the shape of the density profile. Fig. 2.4 shows that the growth rates of the two profiles start to deviate once δ becomes nonlinear. While the scalaron is nearly screened for $s = 0.05$, it remains unscreened for $s = 0.4$, enhancing the growth. It is thus clear that the collapse time z_c depends on the shape of the initial profile.

Due to the above subtleties, in our numerical calculations we use a physically motivated mean density profile around a peak of height $\nu \equiv \delta_{i,0}/\sigma_i(R)$

$$\delta_i(r, R) = \langle \delta(z_i, \mathbf{x}, R) | \text{peak}, \nu \rangle \tag{2.32}$$

which is completely determined by the gaussian statictics of the smoothed linear density field

$\delta(z_i, \mathbf{x}, R)$ [BBKS86]. In Appendix 2.C we derive and display the explicit shape function, and in Fig. 2.5 we exhibit the function for various initial ν values but fixed $\delta_{i,0}$. The mass contained in a spherical tophat

$$M = \frac{4\pi}{3}\varrho_0 R^3\,, \tag{2.33}$$

is used to define the mass M of the final halo, where $\varrho_0 = \bar{\varrho}(z=0)$ is the dark matter density at the present time.

The physical reason for the above mentioned shape dependence of spherical collapse is the same as the environment dependence taken into account in [LE11, LL12a, LL12b, LLKZ13]. In both cases the effectiveness of the chameleon mechanism is influenced by size of gradients in φ, which in turn depends on the density profile and its environment. The mean density profile (2.32) is an approximate way to take into account both effects: the actual mean shape close to the "size" $r \simeq R$ of the collapsing protohalo and its mean environment for $r > R$.

2.3.4 Numerical method

To numerically evolve the system of equations we start from the initial time slice $z_i = 500$ and evolve the energy conservation and Euler equations over a single timestep, where we use e-foldings $N \equiv \ln[a]$ as our time variable with a staggered leapfrog method to decompose the temporal and spatial derivatives. For sufficiently small ΔN and coarse grained radial coordinate (we define $\bar{R} = \ln[r/r_{\rm scale}]$ as the radial coordinate, with $r_{\rm scale} = 1\,$Mpc) the simple finite difference scheme remains stable. Between z_i and $z = 10$, we set the timesteps to be relatively large; $\Delta N = 2 \times 10^{-3}$, but for $z < 10$ we refine the timesteps to $\Delta N = 2 \times 10^{-4}$ to ensure that we can accurately model the effect of the chameleon mechanism.

Once we have evolved the fluid equations to the next timestep, we solve the φ equation (2.27b) using a very similar relaxation algorithm as outlined in [BJZ11]; decomposing the non-linear equation into discretized form and Taylor expanding around the previous timestep. By solving the resulting large, yet sparse matrix equation, we update the solution and repeat until convergence is achieved. Once the field φ is calculated on the new timestep, its contribution as a source in the Poisson equation equation is evaluated, and the metric potential Ψ is obtained by a simple numerical integration. The process is then repeated until collapse is reached. We cannot evolve the system of equations formally to collapse. Here we simply evolve our system to an arbitrary high value in the non-linear over density; $\Delta_{\rm cut-off} = 10^4$. Once the collapse redshift z_c has been determined, we use Eqs. (2.20) and (2.23) to obtain δ_c.

To test that the solution obtained with our code is accurate, we check (completely independently of the code) that the data output δ, φ, Ψ, v solves the redundant momentum constraint and Newtonian gauge equations as given in Eqs. (2.79*b*, 2.79*d*). We also test our code by attempting to reproduce the standard General Relativistic values of $\delta_c(z)$ (by using the algebraic relation $R = -8\pi G T$ as opposed to solving the non-linear $f(R)$ equation). We find an error of less than 0.3% in $\delta_c^{\rm GR}$ for collapsing objects in the redshift range $z_c = (0, 2.5)$. Finally, we test that the code is unaffected by modifying the number of points used in the Poisson equation integration, changing the asymptotic boundary and decreasing the timesteps by a factor of ten. All tests produced a deviation of less than 0.5% in the resulting δ_c.

We perform over 1000 runs of the code, varying over initial density δ_i, field value f_{R0} and scale of the perturbation R, choosing δ_i such that the overdensity collapses between $z = (0, 2.5)$ and R such that the mass of the object lies in the range relevant to clusters, $M = (10^{13}, 10^{15})M_\odot$.

2.3.5 Spherical collapse threshold for $f(R)$ gravity

The main results of this work are the $f(R)$ collapse threshold δ_c and a realistic halo mass function $n(M)$ as a function of f_{R0}, z and M, which we present in the following sections. In Section 2.3.5 we will obtain δ_c as a fit function to our numerical results, and in Section 2.4 we use this δ_c adding a drifting and diffusing barrier in the excursion set theory to obtain a realistic mass function $n(M)$.

The threshold for collapse will be a non-linear function of the $f(R)$ model parameters n and f_{R0}, and also the initial density δ_i (or correspondingly the collapse redshift z_c), and the mass of the overdensity M (or equivalently the size of the overdensity, fixed by R as discussed in section 2.3.3). We wish to construct a fitting function for δ_c using as input data the $N_{\rm code} = 1000$ values of δ_c obtained from our numerical simulations. In what follows we fix $n = 1$ for simplicity.

We exhibit the behaviour of δ_c as a function of R, z_c and f_{R0} in Fig. 2.6. These figures are instructive as a qualitative check of the influence of modified gravity on collapse. Each panel corresponds to runs with fixed f_{R0} and each set of data points of the same color/shape correspond to runs with the same average collapse redshift. We observe a clear linear dependence between δ_c and $\log_{10}[M/(M_\odot h^{-1})]$ for small M and a redshift and f_{R0}-dependent break in this behaviour. This break is determined by $m_b = 0$ from eq. (2.34). The dashed vertical line shows the mass as defined in (2.36) for which $m_b = 0$ at $z = 0$. We also observe an approach to the GR value δ_c^Λ for increasing z_c. Similarly, for f_{R0} field values close to the General Relativistic limit $f_{R0} = 0$, we find the correct limit $\delta_c \to 1.686$. The full lines show the fit function (2.34). We clearly observe a non-trivial R and z_c dependence and a return to GR for large objects and those with a high collapse redshift. An approximately linear relationship between δ_c and $\log[M/M_\odot]$ is observed for large values of $f_{R0} \gtrsim 10^{-5}$, in agreement with the results of [LE11, LLKZ13].

To quantify the effect of modified gravity we provide an interpolation function to fit the data. From Fig. 2.6 we can impose the following ansatz for δ_c

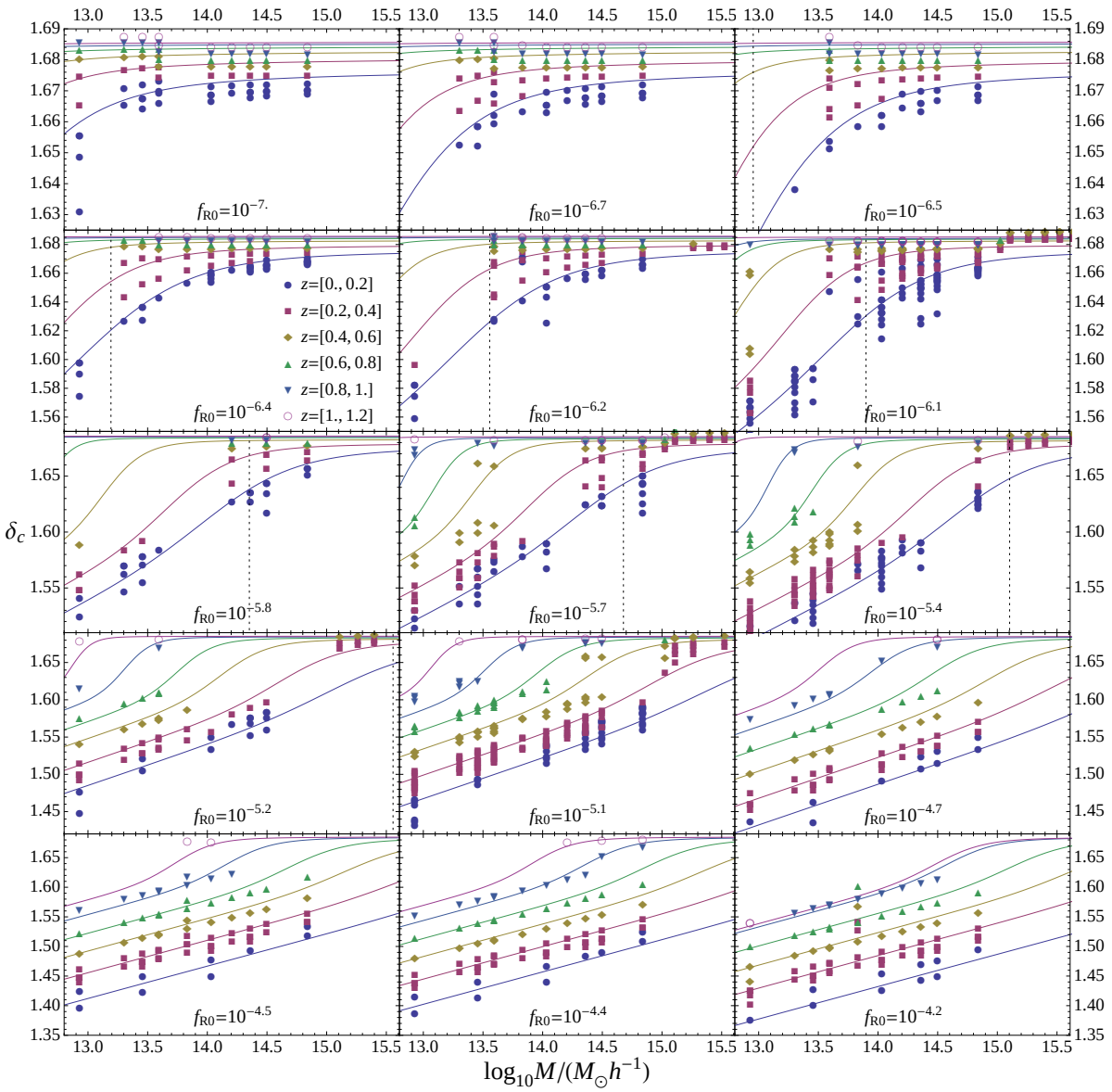

FIGURE 2.6: δ_c as a function of $\log_{10}[M/(M_\odot h^{-1})]$. Each panel corresponds to spherical collapse runs with fixed f_{R0} and each set of data points of the same color/shape corresponds to runs which collapse within the same redshift bin, which can be inferred from the legend. The full lines show the fitting function Eq. (2.34) evaluated at the mean redshift within each of the redshift bins.

$$\begin{aligned}
\delta_c(z, M, f_{R0}) &= \delta_c^{\Lambda}(z)\Bigg\{1 + b_2(1+z)^{-a_3}\left(m_b - \sqrt{m_b^2+1}\right) + \\
&\qquad + b_3(\tanh m_b - 1)\Bigg\} \qquad (2.34)\\
m_b(z, M, f_{R0}) &= (1+z)^{a_3}\left(\log_{10}[M/(M_\odot h^{-1})] - m_1(1+z)^{-a_4}\right)\\
m_1(f_{R0}) &= 1.99\log_{10} f_{R0} + 26.21\\
b_2 &= 0.0166\\
b_3(f_{R0}) &= 0.0027\cdot(2.41 - \log_{10} f_{R0})\\
a_3(f_{R0}) &= 1 + 0.99\exp\left[-2.08(\log_{10} f_{R0} + 5.57)^2\right]\\
a_4(f_{R0}) &= (\tanh[0.69\cdot(\log_{10} f_{R0} + 6.65)] + 1)\,0.11
\end{aligned}$$

The fit function converges separately for $M \to \infty$ and $z \to \infty$ to its GR limit $\delta_c^{\Lambda}(z)$, which can be approximated by [NS97]

$$\delta_c^{\Lambda}(z) \simeq \frac{3(12\pi)^{2/3}}{20}\left(1 - 0.0123\log_{10}\left[1 + \frac{\Omega_m^{-1}-1}{(1+z)^3}\right]\right). \qquad (2.35)$$

We obtained our result (2.34) by considering a_3, a_4, b_2, b_3, m_1 as independent fit parameters for each f_{R0} value. For instance the various best fit parameters m_1 suggest a linear dependence on $\log_{10} f_{R0}$, see Fig. 2.7. In a similar fashion we obtain the other functional forms of b_2, b_3, a_3, a_4. The parameter m_1 is of particular interest since it determines the position of the chameleon transition at $z = 0$, where $\delta_c(M)$ changes its behavior from a linear growth in $\log M$ to a constant; see Fig. 2.6. Therefore roughly speaking the halo mass function at $z = 0$ approaches ΛCDM for masses larger than

$$M_1 = 10^{14.2}\left(\frac{f_{R0}}{10^{-6}}\right)^2 M_\odot h^{-1} \qquad (2.36)$$

due to the chameleon mechanism.

2.4 Halo Mass function: prediction for $f(R)$ gravity and deviation from GR

Dark matter halos result from the non-linear collapse of initial density perturbations. The abundance of these virialized structures depends on both the properties of the initial matter density field and the collapse threshold which leads to their formation. Following the seminal work of [PS74], the excursion set approach [BCEK91] computes the abundance of dark matter halos as a function of their mass. The method involves smoothing the initial density field over different filter scales and positing that once the overdensity enclosed in a smoothing region is above a

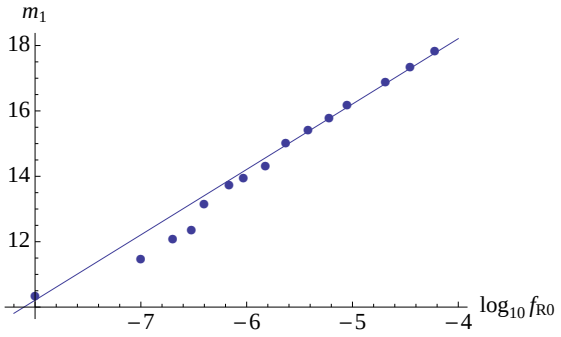

FIGURE 2.7: Fit parameter m_1 (*dots*) as function of f_{R0} suggests a linear relation $m_1 = c_1 \log_{10} f_{R0} + c_2$. The combined fit with 9 other fit parameters contained in the definitions of b_2, b_3, a_3, a_4 gives $c_1 = 1.99$ and $c_2 = 26.2$ (*full line*).

threshold criteria, the region will belong to a collapsed at some later time. The key assumption is then to equate the fraction of collapsed comoving volume per filter scale to the comoving density of halos $n(M)$. Thus the number density of haloes in the mass range $[M, M + dM]$, the halo mass function $n(M)$, is given by

$$n(M) = f(\sigma)\frac{\varrho_0}{M^2}\frac{d\ln\sigma^{-1}}{d\ln M}\,, \tag{2.37}$$

where ϱ_0 is the comoving background dark matter density and $f(\sigma)$ is related to fraction of collapsed volume. The fundamental quantity, which contains all information on the non-linear collapse dynamics, is $f(\sigma)$. In what follows we first review the analytic derivation of $f(\sigma)$ in case of spherical GR collapse. We then extend this calculation to $f(R)$ models with realistic collapse parameters. Having constructed the multiplicity function $f(\sigma)$ for these modified gravity models, we can provide an estimate of $f(R)$ signatures in the cluster abundance. Note that our methodology is different to existing approaches in the literature [LL12a, LL12b, LLKZ13]. In this work $f(R)$ effects are taken into account by averaging the barrier over environments of the initial Lagrangian perturbations.

2.4.1 Uncorrelated random walk and generic barrier

To estimate the fraction of collapsed volume, one has to compute the probability $\Pi(R,\delta)$ of having an overdensity δ smoothed on a scale R. In the original Press-Schechter (PS) approach [PS74], assuming Gaussian initial conditions, the fraction of collapsed regions can be calculated analytically; it is given by

$$F(R) = \int_B^\infty \Pi(\delta, \sigma(R))d\delta\,, \tag{2.38}$$

where B is the collapse threshold and the probability density function (PDF) is $\Pi(\delta,\sigma(R)) = e^{-\delta^2/(2\sigma^2)}/\sqrt{2\pi\sigma^2}$. However the PS approach suffers from the so called cloud in cloud problem: it requires an ad-hoc normalization of the mass function due to an incorrect counting of collapsed

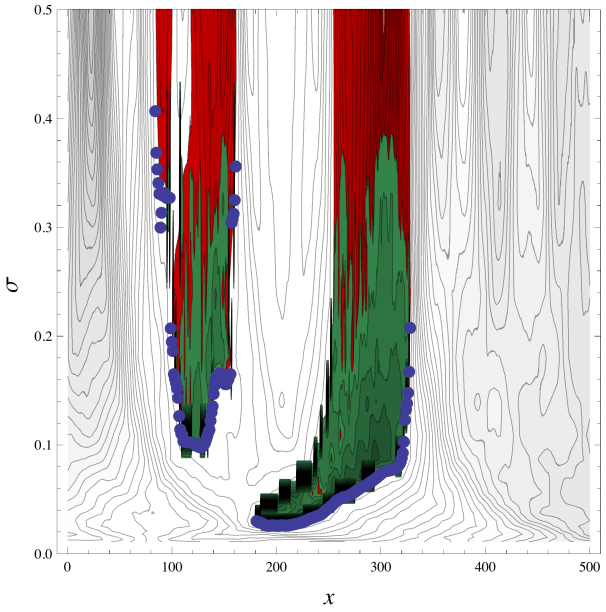

FIGURE 2.8: Illustration of the Press-Schechter $\mathcal{F}_{\rm PS} = dF_{\rm PS}/dS$, Eq. (2.38) (*green* spiky contours) and excursion set $\mathcal{F}_{\rm Exc} = dF_{\rm Exc}/dS$, Eq. (2.44) (*blue* dots) for some random field $\delta(x, R)$ (*black* smooth contours) and a constant barrier B (*red* area, partially obscured by the *green* spiky contours). Instead of the smoothing scale R we use $\sigma(R)$ on the y-axis. The barrier B cuts through the random field $\delta(x, R)$ at a fixed hight $B = \delta_c(z)$, with everything above colored *red*, which can be envisioned as the "dry land", while the barrier B is the "ocean", see [BCEK91]. The $\mathcal{F}_{\rm Exc}$ is proportional to the number of *blue* dots per σ and only takes into account regions that first up-cross exactly at the hight B and therefore $\mathcal{F}_{\rm Exc}$ counts only structures that survive and form at redshift z. The blue dots are the "shore line" facing the "open ocean" located at $\sigma \to 0$. On the other hand although $\mathcal{F}_{\rm PS}$ also counts mostly regions that first upcross (large green spikes where also the number density of blue dots is largest), it prominently counts down-crossing regions (e.g. around $x = 200, \sigma = 0.05$, "inbound shores") and therefore double counts objects. It also counts the *light green* parts inside the red region, the "dry land", and therefore counts objects above the barrier where $\delta(x, R) > \delta_c(z)$. These regions correspond to objects that form at times larger than z but actually get destroyed or incorporated later on (at the *blue* dots).

regions. To understand where the problem occurs let us review the standard excursion set procedure. We start by re-writing the smoothed overdensity on a scale R at any random position as

$$\delta(R) = \frac{1}{(2\pi)^3} \int d^3k \; W(k, R) \; \tilde{\delta}(z, k) \,, \tag{2.39}$$

where W and $\tilde{\delta}$ are the Fourier transforms of the filter function and and the linearly extrapolated δ respectively. Since $\delta(R)$ is a random variable, it was shown in [BCEK91] that its evolution follows a Langevin equation. Once we fix the filter, there is a one to one relationship between the smoothing scale R, the mass of the halos $M(R)$, see Eq. (2.33) and the variance defined as

$$S \equiv \sigma^2(z, R) = \frac{1}{2\pi^2} \int dk \; k^2 P(z, k) \; W^2(k, R). \tag{2.40}$$

In the case of a sharp-k filter $W(k,R) = \theta(1/R - k)$ and Gaussian initial conditions, the Langevin equation takes the form

$$\frac{\partial \delta}{\partial S} = \eta_\delta(S)\,, \tag{2.41}$$

where η_δ is white Gaussian noise completely specified by its mean $\langle \eta_\delta \rangle = 0$ and variance $\langle \eta_\delta(S)\eta_\delta(S')\rangle = \delta_{\rm D}(S - S')$. According to these equations, $\delta(R)$ performs a random walk and its evolution between two scales S and S' is determined by its previous step only. Since the system does not keep memory of previous steps, the dynamics corresponds to a Markovian random walk and the PDF follows a simple Fokker-Planck equation

$$\frac{\partial \Pi}{\partial S} = \frac{1}{2}\frac{\partial^2 \Pi}{\partial \delta^2}\,. \tag{2.42}$$

The PDF is fully specified by two initial conditions. At $S = 0$, which corresponds to very large scales, the homogeneity of the universe implies that $\Pi(\delta, S = 0) = \delta_{\rm D}(\delta)$. If one does not enforce a second condition then one solution of Eq. (2.42) is a Gaussian PDF corresponding to the original PS prediction.

In the excursion set approach, when random walks cross the collapse threshold B at scale S a halo of mass $M(S)$ is assumed to form. However, random walks can cross B more than once at different smoothing scales, and this can lead to double counting of halos, see Fig 2.8. In this illustration of a one-dimensional random field $\delta(R(\sigma), x)$ a random walk happens along $x = $const starting at $\sigma = 0$ and ends at the blue dot where it first up-crosses the red barrier. To evade this cloud-in-cloud problem, one must remove walks when they cross B for the first time. This can be encoded in an absorbing boundary condition; the PDF of uncollapsed objects is given by the solution of Eq. (2.42) with the second "final" condition $\Pi(\delta{=}B, S) = 0$. An exact analytic solution for a barrier that is a generic function of the smoothing scale does not exist. However for a constant spherical collapse barrier the exact solution is given by [BCEK91, Red01]:

$$\Pi(\delta, S) = \frac{1}{\sqrt{2\pi S}}\left(e^{-\delta^2/(2S)} - e^{-(2\delta_c - \delta)^2/(2S)}\right)\,, \tag{2.43}$$

where the first term on the right hand side is the previous Gaussian solution while the second term is known as the 'anti-Gaussian'. The fraction of collapsed volume is then

$$F(S) = 1 - \int_{-\infty}^{\delta_c} d\delta \Pi(\delta, S). \tag{2.44}$$

The first-crossing rate is given by $\mathcal{F}(S) = dF(S)/dS$. From the definition of the multiplicity function $f(\sigma) = 2\sigma^2\mathcal{F}(\sigma^2)$ it follows

$$f(\sigma) = \sqrt{\frac{2}{\pi}} e^{-\delta_c^2/(2\sigma^2)}\frac{\delta_c}{\sigma}\,, \tag{2.45}$$

which is the original PS prediction with the correct normalisation.

The above calculation corresponds to spherically collapsing overdensities; the situation is considerably more complicated in the real Universe. The dynamics of collapse is aspherical and

small over-dense regions require additional matter to collapse [SMT01] since they are significantly affected by the surrounding shear field. Using ellipsoidal collapse in the excursion set approach introduces a stochastic barrier; this motivates the study of a generic barrier. In the ΛCDM case a simple Gaussian distribution for the barrier B with a mean value $\bar{B}$ which drifts linearly as function of the variance S is sufficient to reproduce the N-body halo mass function with high accuracy [CA11b, CA11a, AC12a, AC12b]. Furthermore this barrier is consistent with the overdensity required to collapse measured in the initial condition [ARSC12] and has the advantage of admitting an exact solution for Markovian multiplicity function.

For $f(R)$ gravity we have shown in Section 2.3.5 that spherical collapse cannot be modeled using a linear barrier. To obtain an analytical prediction for $f(\sigma)$ using a generic barrier, we start by introducing the variable $Y = B - \delta$ and assume that the barrier is described by a Gaussian PDF with mean value $\bar{B}(S)$ and variance $D_B S$, with constant D_B. In such a scenario the Fokker-Planck equation for the Y variable is given by

$$\frac{\partial \Pi(Y,S)}{\partial S} = \frac{1+D_B}{2}\frac{\partial^2 \Pi(Y,S)}{\partial Y^2} - \frac{d\bar{B}}{dS}\frac{\partial \Pi(Y,S)}{\partial Y} \tag{2.46}$$

In the special case where $\bar{B} = \delta_c + \beta S$, the exact solution for $\Pi(Y,\delta)$ is [CA11b, CA11a]

$$f(\sigma) = \sqrt{\frac{2a_B}{\pi}} e^{-a_B \bar{B}^2/(2\sigma^2)} \frac{\delta_c}{\sigma} \tag{2.47}$$

with $a_B = 1/(1+D_B)$. For generic $\bar{B}(S)$, the solution of the Fokker-Planck equation without the absorbing boundary condition is simply given by a Gaussian with mean $\bar{B}$ and variance $(1+D_B)S$. The crossing rate in this case would be given by

$$\mathcal{F}(S) = -\frac{d}{dS}\int_0^\infty \sqrt{\frac{a_B}{2\pi S}} e^{-a_B (Y-\bar{B})^2/(2S)}\,, \tag{2.48}$$

leading to

$$f(\sigma) = \sqrt{\frac{2a_B}{\pi}} e^{-a_B \bar{B}^2/(2\sigma^2)} \frac{1}{2\sigma}\left(\bar{B} - 2S\frac{d\bar{B}}{dS}\right)\,. \tag{2.49}$$

However, this expression does not have the correct normalisation since we did not solve the equations using an absorbing boundary condition. For constant barrier, one could correct this expression by multiplying by an ad-hoc factor two, however for a linear drift this would not be sufficient to recover the exact solution since there is no factor of two multiplying the first derivative of $\bar{B}$. In fact one can show that the factor of two in front of the first derivative of $\bar{B}$ cancels once we add the anti-Gaussian term [CA11a]. Thus the exact solution for a constant and linear barrier is given by

$$f(\sigma) = \sqrt{\frac{2a}{\pi}} e^{-a_B \bar{B}^2/(2\sigma^2)} \frac{1}{\sigma}\left(\bar{B} - S\frac{d\bar{B}}{dS}\right). \tag{2.50}$$

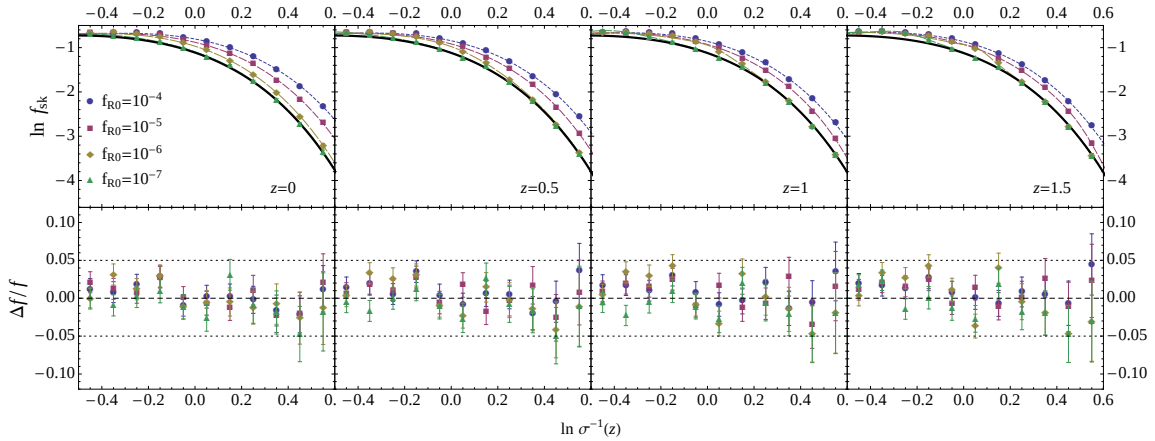

FIGURE 2.9: Monte Carlo (dot) and theory (line) prediction for the $f(R)$ halo mass function at different redshift using spherical collapse barrier and sharp-k filter on the upper panel. Black line show the GR prediction while the colours line are for different f_{R0}. Lower panel shows the relative difference between the exact Monte Carlo solution and theory.

Note that this expression matches the first two terms of [dMR11a] which are equivalent to [ST02] for $D_B = 0$. In [ST02] it was proposed that the additional correction for a generic barrier is given by

$$f_{\rm ST}(\sigma) = \sqrt{\frac{2}{\pi}} e^{-\bar{B}^2/(2\sigma^2)} \frac{1}{\sigma} \left(\sum_{n=0}^{5} \frac{(-\sigma^2)^n}{n!} \frac{d\,\bar{B}^n}{d(\sigma^2)^n} \right) , \tag{2.51}$$

see also [dMR11b] for the problems regarding the upper end of the sum.
In what follows we will use Eq. (2.50) to model the spherical collapse barrier of $f(R)$. Although our barrier is not linear in S, this procedure will justified a posteriori by comparing it to Monte-Carlo random walks.

In the absence of N-body simulations, one way to evaluate the effect of $f(R)$ gravity on the halo mass function is to use spherical collapse (ie: $D_B = 0, \beta = 0$) and measure the ratio between the GR and $f(R)$ prediction for an uncorrelated walk (ie: sharp-k filter). For that purpose we first need an accurate prediction for $f(R)$ gravity. We run Monte Carlo walks for various f_{R0} parameters to test the accuracy of Eq. (2.50).

In Fig 2.9 we observe the halo mass function corresponding to the exact Monte Carlo solution (dot) and our prediction (full line) Eq. (2.50) with $\beta = 0$, $D_B = 0$ and δ_c given by Eq. (2.34). On the lower panel we show the relative difference between the Monte Carlo and theoretical prediction. We see that the difference is of order $\sim 5\%$, confirming that Eq. (2.50) provides an excellent fit. The colours correspond to the different model parameters we test: blue, red, yellow and green correspond to $\log_{10} f_{R0} = -4$, $\log_{10} f_{R0} = -5$, $\log_{10} f_{R0} = -6$ and $\log_{10} f_{R0} = -7$ respectively and black is the GR spherical collapse prediction. The deviation between GR and

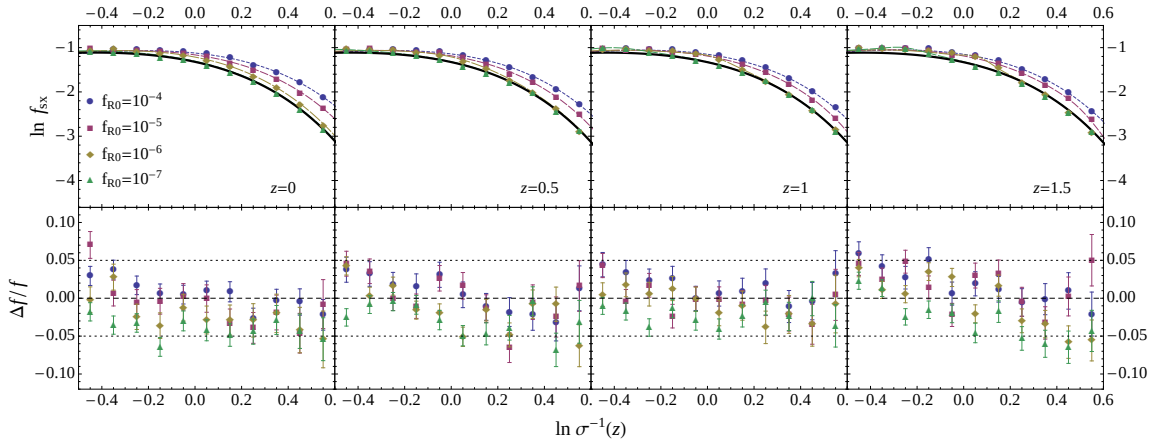

FIGURE 2.10: Monte Carlo (dot) and theory (line) prediction for the $f(R)$ halo mass function at different redshift using a drifting diffusing barrier and sharp-x filter on the upper panel. Black line show the GR prediction while the colours line are for different f_{R0}. Lower panel shows the relative difference between the exact Monte Carlo solution and theory.

$f(R)$ gravity is explored further in section 2.4.3.

2.4.2 Realistic mass function from correlated random walks

In the previous section we predicted the $f(R)$ multiplicity function using two simple assumptions: one is related to the filtering procedure which we took to be sharp-k and the other to the spherical dynamics of collapse. In fact, the Fokker-Planck equation (2.46) is only valid in the special case where there is no absorbing boundary [MR10a] or if the random walk is Markovian. This is the case only when δ is smoothed with a sharp$-k$ filter in Eq. (2.39). The choice of filter is important as it defines the relationship between the mass of the halos and the variance of the field. Assuming that the mass of a halo is given by $M(R) = \varrho_0 V_{\rm sp}$ where $V_{\rm sp}(R)$ is the volume of a sphere, then one should actually consider a real-space top-hat filter (ie: sharp$-x$), where the Lagrangian radius of the halo is related to the variance $\sigma(R)^2$ in Eq. (2.40), which we normalise to $\sigma_8 = 0.8$. In this case there is no exact analytical solution for the PDF.

In [MR10a] a path integral approach to compute the non-Markovian corrections induced by a sharp$-x$ filter has been developed. The magnitude of the correction is given by κ, which depends on the linear matter power spectrum. For a standard ΛCDM Universe, $\kappa \sim 0.65$. In [MR10b] this formalism was applied to a stochastic barrier with Gaussian distribution and in [CA11b, CA11a] the solution was extended to a diffusive barrier with mean $\delta_c + \beta S$. Such a barrier encapsulates the main features of ellipsoidal collapse. In such a case, the multiplicity function to first order in κ is given by

$$f(\sigma) = f_0(\sigma) + f^{m-m}_{1,\beta=0}(\sigma) + f^{m-m}_{1,\beta^{(1)}}(\sigma) + f^{m-m}_{1,\beta^{(2)}}(\sigma)\,, \tag{2.52a}$$

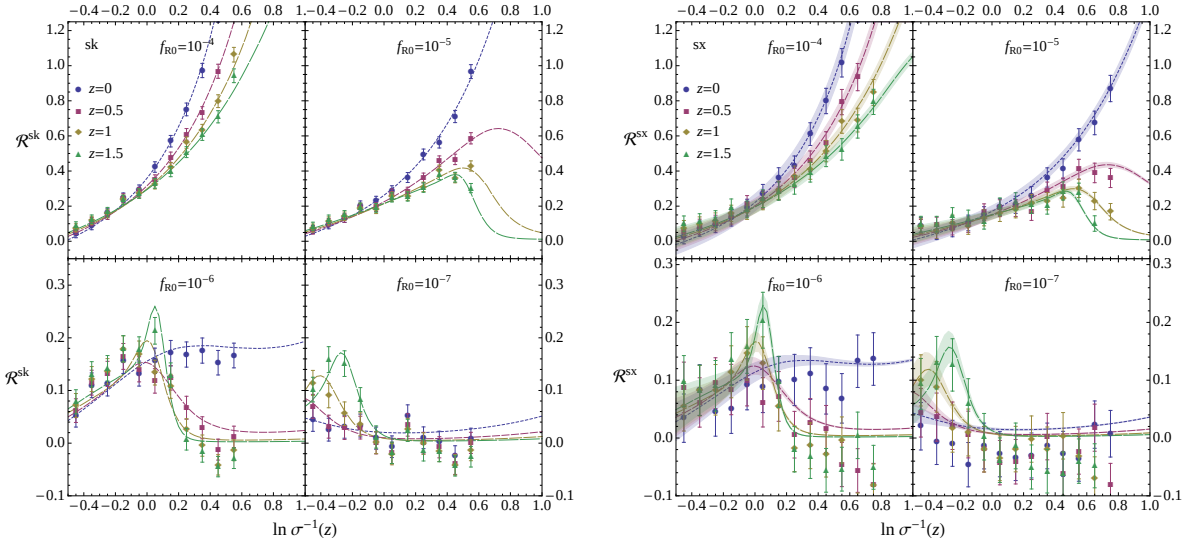

FIGURE 2.11: Multiplicity function ratio $\mathcal{R}$ between GR and $f(R)$ gravity over different redshift and f_{R0} parameters for naive spherical collapse with sharp-k filter (left panel), see Eq. (2.58) and using a drifting diffusive barrier with sharp-x filter (right panel), see Eq. (2.57). Colored bands in the rights panel show variations in D_B and β, see Eq. (2.57). Dots show the Monte Carlo runs for $f(R)$ gravity.

where

$$f_0(\sigma) = \frac{\delta_c}{\sigma}\sqrt{\frac{2a_B}{\pi}}\,\exp\left(-\frac{a_B}{2\sigma^2}(\delta_c+\beta\sigma^2)^2\right), \tag{2.52b}$$

$$f^{m-m}_{1,\beta=0}(\sigma) = -\tilde{\kappa}\frac{\delta_c}{\sigma}\sqrt{\frac{2a_B}{\pi}}\left[\exp\left(-\frac{a_B\delta_c^2}{2\sigma^2}\right)-\frac{1}{2}\Gamma\left(0,\frac{a_B\delta_C^2}{2\sigma^2}\right)\right], \tag{2.52c}$$

$$f^{m-m}_{1,\beta^{(1)}}(\sigma) = -a_B\,\delta_c\,\beta\left[\tilde{\kappa}\,\mathrm{Erfc}\left(\delta_c\sqrt{\frac{a_B}{2\sigma^2}}\right)+f^{m-m}_{1,\beta=0}(\sigma)\right], \tag{2.52d}$$

$$f^{m-m}_{1,\beta^{(2)}}(\sigma) = -a_B\,\beta\left[\frac{\beta}{2}\sigma^2 f^{m-m}_{1,\beta=0}(\sigma)+\delta_c\,f^{m-m}_{1,\beta^{(1)}}(\sigma)\right]. \tag{2.52e}$$

In [ARSC12] it was shown that the first order approximation in κ is sufficient to reproduce the exact solution to $\sim 5\%$ accuracy, using parameter values $\beta = 0.12$, $D_B = 0.4$. This effective barrier can match the N-body halo mass function with accuracy $\sim 5\%$ and is also consistent with the collapse threshold measured in the initial conditions, suggesting that β, D_B are parameters that should depend on physics of the collapse dynamics. For $f(R)$ spherical collapse we find that we recover the general relativistic prediction for massive halos, however for small mass objects the threshold of collapse decreases as function of the variance. Such behaviour can be roughly approximated by a negative drift coefficient β which would counteract the expected $\beta > 0$ behaviour associated with GR ellipsoidal collapse. Thus it is not clear how $f(R)$ gravity will effect the collapse of an aspherical patch. However, we can reasonably assume that for $f_{R0} \to 0$ one should recover the GR limits. As an initial step we can therefore fix β and D_B to their GR values

and run MC walks for the sharp-x filter, with δ_c given by (2.34). In what follows we exhibit the resulting halo mass functions, and end the section by estimating the sensitivity of our results to our choice of (β, D_B).

In order to predict the multiplicity function for $f(R)$ gravity we begin by noting that the sharp-x multiplicity function can be rewritten as the sharp-k function with a correction in κ. Hence the ratio between the GR and $f(R)$ predictions is given by

$$\frac{f^{f(R),\mathrm{sx}}}{f^{\mathrm{GR,sx}}} = \frac{f^{f(R),\mathrm{sk}} + f^{f(R)}_{\kappa=1} + \theta(\kappa^2)}{f^{\mathrm{GR,sk}} + f^{\mathrm{GR}}_{\kappa=1} + \theta(\kappa^2)} \,. \tag{2.53}$$

Therefore

$$f^{f(R),\mathrm{sx}}(\sigma) = \frac{f^{\mathrm{GR,sx}}}{f^{\mathrm{GR,sk}}}\left[f^{f(R),\mathrm{sk}} + \left(f^{f(R)}_{\kappa=1} - f^{\mathrm{GR}}_{\kappa=1}\right) + \theta(\kappa^2)\right] , \tag{2.54}$$

where $f^{\mathrm{GR,sk}}$ is given by Eq. (2.52b), $f^{\mathrm{GR,sx}}$ by Eq. (6.64), $f^{f(R),\mathrm{sk}}$ by Eq. (2.50), $f^{\mathrm{GR}}_{\kappa=1}$ by Eq. (2.52c-2.52e) and $f^{f(R)}_{\kappa=1}$ is the first order non-Markovian corrections due to the sharp-x filter. Since this correction is also proportional to κ, it seems reasonable that the difference $f^{f(R)}_{\kappa=1} - f^{\mathrm{GR}}_{\kappa=1}$ should be negligible. In fact one could rewrite $f^{f(R)}_{\kappa=1}$ as an expansion around the GR spherical collapse solution, in which case the first order term would be given by Eq. (2.52c) as for the GR case (ie: $\beta = 0$) and the first non-vanishing term in the difference would be proportional to $a_B\,\kappa\,\beta \sim 0.05$. Thus we assume in what follows that

$$f^{f(R),\mathrm{sx}}(\sigma) \simeq f^{\mathrm{GR,sx}}(\sigma)\frac{f^{f(R),\mathrm{sk}}}{f^{\mathrm{GR,sk}}} \,. \tag{2.55}$$

We test Eq. (2.55) by comparing with the exact Monte Carlo solution. The result is shown in Fig. (2.10), where we use the GR parameters for (β, D_B). In the upper panel we see the Monte Carlo solution (dots) and Eq. (2.55) for different redshift and f_{R0} parameters. On the bottom panel we show the relative difference between Monte Carlo runs and equation (2.55). Once again, the fractional difference is of order $\sim 5\%$ confirming the validity of Eq. (2.55). Hence we adopt this simple prescription to define the multiplicity function for $f(R)$ gravity. The halo mass function can obtained from Eq. (2.55) via

$$n(M, z, f_{\mathrm{R0}}) = f^{f(R),\mathrm{sx}}(\sigma)\frac{\varrho_0}{M^2}\frac{d\,\ln\sigma^{-1}}{d\,\ln M} \,, \tag{2.56}$$

where $\sigma(z, R) = D(z)\,\sigma(z{=}0, R)$ is calculated from ΛCDM linear growth $D(z)$ and the linear power spectrum $P(z{=}0, k)$ obtained from CAMB as described in Sec. 2.3.

2.4.3 Realistic prediction for $f(R)$ gravity and deviation from GR

For completeness we test whether there is a significant modified gravity imprint on the $f(R)$ mass function Eq. (2.56). To evaluate the sensitivity of our results to our choice of collapse parameters, we consider the ratio of the $f(R)$ and GR predictions using different values of (β, D_B).

One might reasonably assume that if the spherical collapse deviation with respect to GR is

$$\eta \equiv (\delta_c^{f(R)} - \delta_c^{\rm GR})/\delta_c^{\rm GR}$$

then the drift term β should also exhibit deviations of order η. Since the diffusive term D_B appears as $\delta_c/\sqrt{2S(1+D_B)}$ in the mass function, we estimate that $\sqrt{D_B}$ will also be modified on the order of η. We therefore define

$$\begin{aligned}
\mathcal{R}^{\rm sx} &= \frac{f^{f(R),{\rm sx}}(\delta_c^{f(R)}, \beta^{\rm GR}, D_B^{\rm GR})}{f^{\rm GR,sx}} - 1 \\
\mathcal{R}^{\rm sx}_{+} &= \frac{f^{f(R),{\rm sx}}(\delta_c^{f(R)}, \beta^{+}, D_B^{+})}{f^{\rm GR,sx}} - 1 \\
\mathcal{R}^{\rm sx}_{-} &= \frac{f^{f(R),{\rm sx}}(\delta_c^{f(R)}, \beta^{-}, D_B^{-})}{f^{\rm GR,sx}} - 1
\end{aligned} \tag{2.57}$$

where $f^{f(R),{\rm sx}}$ is given by Eq. (2.55), $f^{\rm GR,sx}$ is given by Eq. (6.64) with $D_B^{\rm GR} = 0.4, \beta^{\rm GR} = 0.12$ and $\beta^{\pm} \equiv \beta^{\rm GR}(1 \pm \eta)$ while $D_B^{\pm} \equiv D_B^{\rm GR}(1 \pm \eta^2)$.

In left panel of Fig.(2.11) we exhibit the ratios between the $f(R)$ and GR halo mass functions using the naive sharp-k and spherical collapse for four model parameters using Eq. (2.50) in section 2.4.1:

$$\mathcal{R}^{\rm sk} \equiv \frac{f^{f(R),{\rm sk}}(\delta_c^{f(R)}, \beta = 0, D_B = 0)}{f^{\rm GR,sk}} - 1. \tag{2.58}$$

On the right panel we show the ratio $\mathcal{R}^{\rm sx}$ as lines and $\mathcal{R}^{\rm sx}_{+}, \mathcal{R}^{\rm sx}_{-}$ as shaded strips. First note that for a given scale S, $\mathcal{R}^{\rm sx}$ and $\mathcal{R}^{\rm sk}$ differ significantly, implying that a simple spherical collapse model in the excursion set framework with a sharp-k filter should not be used to measure departures from GR. However both $\mathcal{R}^{\rm sx}$ and $\mathcal{R}^{\rm sk}$ share the same qualitative features. Our second important conclusion is that varying D_B and β over the range we might expect in $f(R)$ gravity does not significantly modify the departure from GR. Indeed, the width of the strip does not appreciably change for the multiplicity function.

Finally, we use Eq. (2.55) in Eq. (6.63) to study how the number count of halos changes for $f(R)$ gravity compared to GR. For this we note that from Eq. (2.56) follows that

$$\mathcal{R}^{\rm sx} = \frac{n^{f(R),{\rm sx}}(\delta_c^{f(R)}, \beta^{\rm GR}, D_B^{\rm GR})}{n^{\rm GR,sx}} - 1\,. \tag{2.59}$$

In Figs. 2.12 we show the number count ratio for various $f_{\rm R0}$ values and the evolution at different redshifts. It is clear from this figure that the $f(R)$ signature strongly depends on redshift. In Fig. 2.13 we exhibit the redshift evolution of the $f(R)$-GR halo mass function ratio for various mass bins and $f_{\rm R0}$ values. There is a distinctive signature in both the mass and time dependence of the halo mass function due to the chameleon effect. The lower panels of Figs. (2.12,2.13) correspond to field values $f_{\rm R0} = 10^{-7}$. Modified gravity effects are suppressed for models so close to GR, suggesting a floor $f_{\rm R0} \sim O(10^{-7})$ below which cluster counts will not competitively probe non-standard physics.

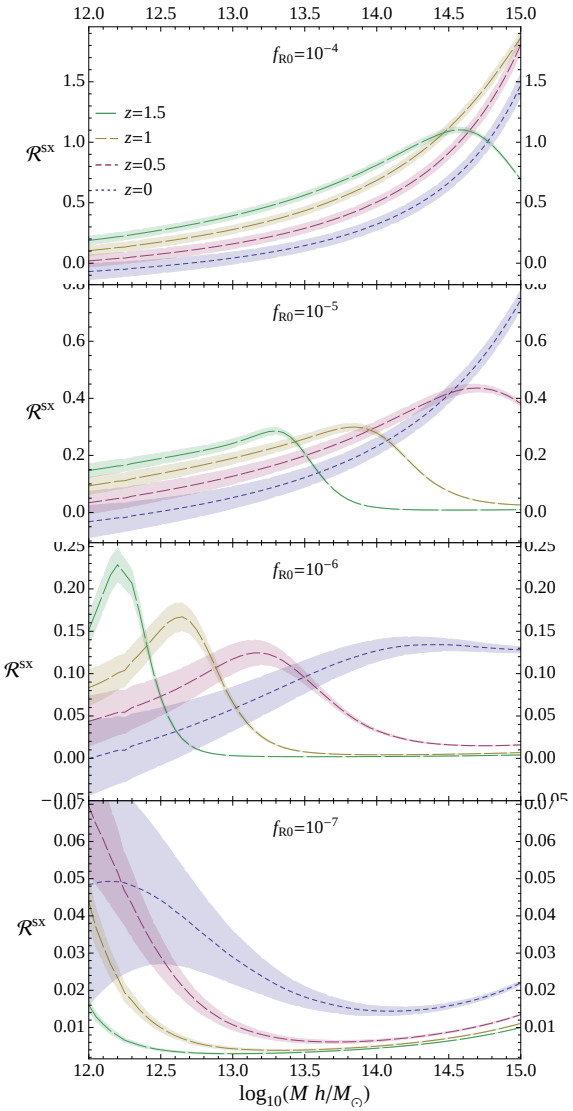

FIGURE 2.12: The panels from top to bottom show the halo mass function ratios (2.57) for different f_{R0}. Within each panel different lines show different collapse redshifts (see the legend in the first panel).

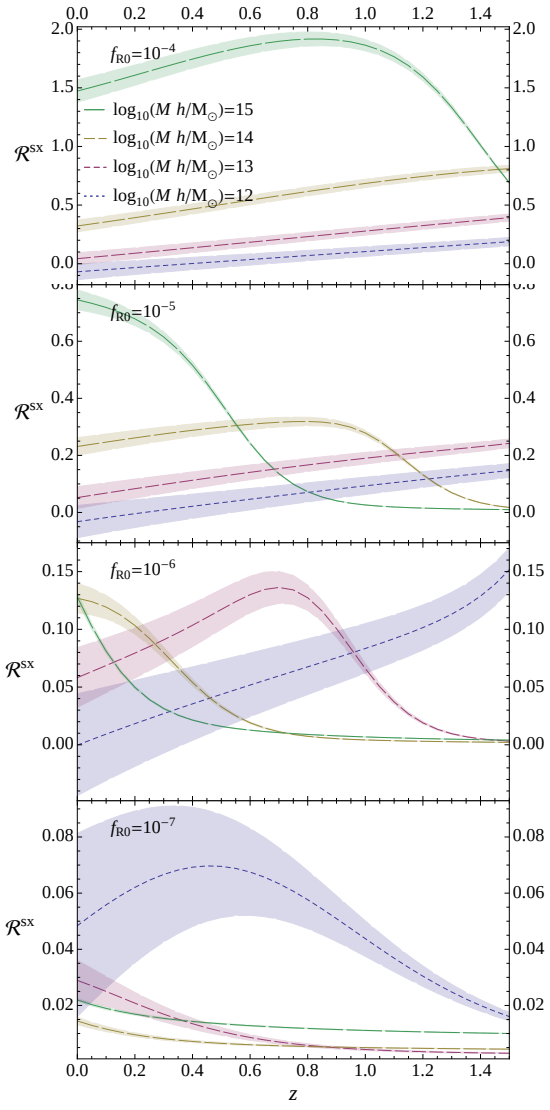

FIGURE 2.13: The panels from top to bottom show the redshift evolution of the halo mass function ratio (2.57) for different f_{R0}. Within each panel the different lines show different halo masses (see the legend in the first panel).

Improvements to our results could be made by testing the abundance of halos by using N-body $f(R)$ simulations [PBS13]. Especially low mass halos will allow us to further study aspherical collapse which could ameliorate the uncertainties that exist in our numerical results (shown by the shaded regions in our figures). As a final check of our analysis we compare our mass function to a mass function measured in a $f(R)$ N-body simulation [PBS13]. The simulation

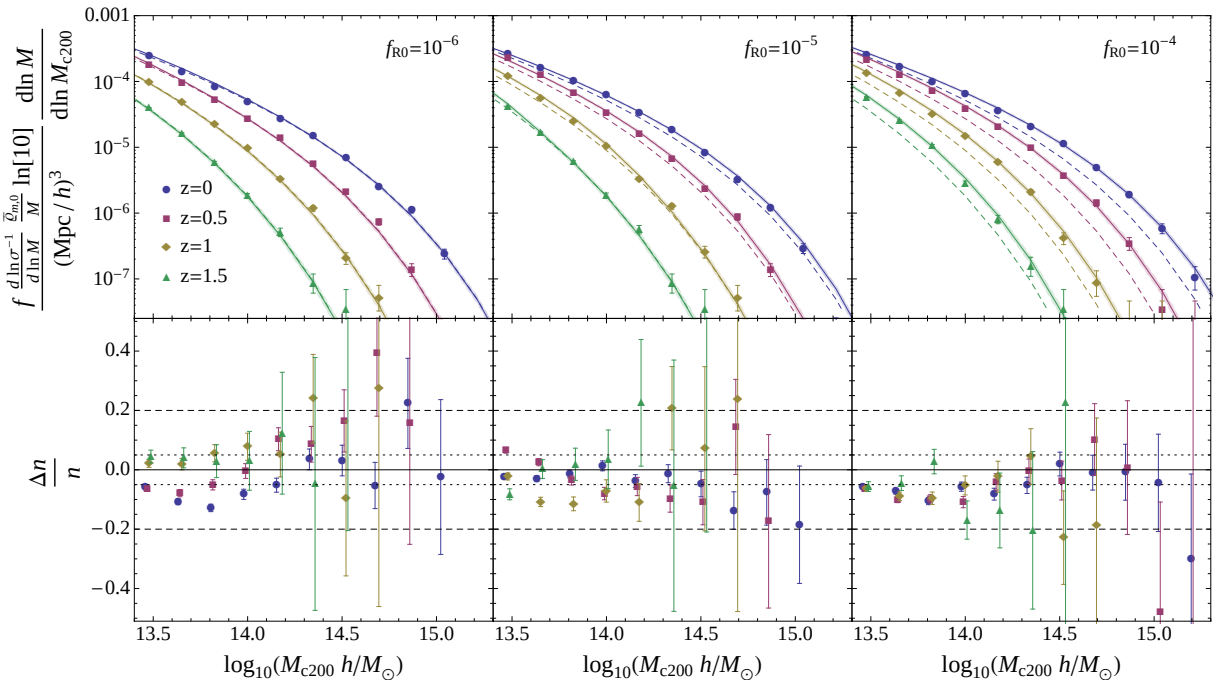

FIGURE 2.14: The upper panels from left to right show the mass function $n(\log_{10}(M_{200c}/h))$ in units $(\mathrm{Mpc}/h)^3$ for $f_{R0} = 10^{-6}, 10^{-5}, 10^{-4}$. Each panel shows 4 different redshifts $z = 0, 0.5, 1, 1.5$. The data points are courtesy of Marco Baldi and Ewald Puchwein [PBS13]. The thick line is the fit function (2.56), with thickness given by (2.59). The dashed lines show the GR prediction (2.52). The lower panels show the ratio between the fit function and the N-body mass function. The dotted line and dashed line signal 5% and 20% deviations.

was described in [PBS13], but the mass function is preliminary and was measured by Marco Baldi and Ewald Puchwein, who also kindly provided us with the data, which allows us a preliminary check of the mass function (2.56). In order to compare the mass function it is crucial to convert our virial masses into M_{200c} used to define halo masses by Baldi & Puchwein according to Appendix of [JSW+07]. In Fig. 2.14 we compare the results and find reasonable agreement.

As was shown in [JVS12] looking for local variations of physical properties induced by the environment-dependent chameleon effect puts the strongest constraints on f_{R0}. In the context of spherical collapse, taking into account local variations would require the use of initial density profiles conditioned on the desired environment. For instance one could use as initial condition for spherical collapse the mean shape not only conditioned on the height and mass of the peak (see Eq. (2.87)), but also conditioned on value of the density at a relevant scale; the environmental density $\delta_{\rm env}$.

The resulting conditional spherical collapse threshold $\delta_c(z, M, f_{R0}, \delta_{\rm env})$ would then allow the construction of a conditional halo mass function [LZK11, LE11, LL12a, LL12b, LLKZ13]. This has not been done for the above mentioned physically motivated profile conditioned on $\delta_{\rm env}$.

2.5 Conclusion

Confronting modified gravity models with cosmological data sets is a highly non-trivial task. Even a seemingly straightforward physical process such as the collapse of a spherically symmetric overdensity becomes a problem fraught with complications. In this work we have calculated numerically the linear threshold for collapse δ_c for one of the simplest modified gravity models in the literature; $f(R)$ gravity. By solving the full modified Einstein and fluid equations, we were able to construct an approximate functional form for $\delta_c(z_c, M, f_{\rm R0})$, which depends on both the initial size and shape of the overdensity and also the modified gravity parameter. A number of subtleties were encountered, such as the choice of initial conditions and the applicability of the linearization procedure.

Using the spherical collapse δ_c of $f(R)$ gravity and a drifting diffusing barrier in the excursion set approach, we constructed a physically motivated halo mass function using the formalism first introduced in [MR10b, CA11b]. This method has been shown to accurately reproduce the general relativistic halo mass function, and we expect that it is also robust for a wide variety of modified gravity models. It was shown in Section 2.4 that our ansatz for $n(M, z, f_{\rm R0})$ is in excellent agreement with our numerical Monte Carlo random walk simulations, and can be applied to generic barriers that are algebraic functions of the variance.

Whilst the collapse threshold that we obtain is based upon the $f(R)$ spherical collapse barrier, we have gone beyond simple spherical collapse when calculating $n(M, z, f_{\rm R0})$. Our ansatz introduces two parameters; β takes into account deviations from spherical collapse and D_B quantifies the scatter around it. In addition we have shown that our results are relatively insensitive to possible deviations to these parameters induced by modified gravity. The existence of substructure in the halo progenitor environment [LH11], which is partially accounted for in our work, and substructure within the halo progenitor, see [LE11], influences the chameleon effect and further complicates the computation of the halo mass function. Therefore more work is required to fully understand aspherical collapse and all effects of modified gravity on the multiplicity function. The next step in this direction would be to directly compare our approach with modified gravity N-body simulations [PBS13] and measure the parameters of collapse following [ARSC12].

Appendix 2

2.A Nonlinear equations

We introduce the following notation. K is the trace of the extrinsic curvature

$$K = 3e^{-\Phi}(\dot{\Psi} - H)\,, \tag{2.60}$$

$H = \dot{a}/a$ is the Hubble constant of the asymptotic FRW and Δ is the flat space Laplacian. The general relativistic version of the γ-factor, w, is given by

$$w = e^{\Phi}u^0 = \frac{1}{\sqrt{1 - v^2 e^{-2(\Phi+\Psi)}}}\,, \tag{2.61}$$

and $v \equiv v^r \equiv au^r/u^0$ is the radial coordinate speed times a. The velocities u_r and v are related via

$$u_r = vwae^{-2\Psi-\Phi}\,. \tag{2.62}$$

The "momentum"[4] of φ is denoted by

$$\Pi \equiv e^{-\Phi}\dot{\varphi}\,. \tag{2.63}$$

The Einstein equations can be decomposed into energy constraint $(-\,{}^0_0)$

$$\frac{1}{3}K^2 - K\Pi + e^{2\Psi}a^{-2}\left(\Delta(2\Psi - \varphi) - \Psi'^2 + \Psi'\varphi' - \varphi'^2\right) = e^{-\varphi}\left(\kappa^2\varrho w^2 + \frac{1}{2}V\right)\,, \tag{2.64a}$$

momentum constraint $(e^{-\Phi}\cdot\,{}_{0r})$

$$\frac{2}{3}K' - \left(\Pi' + \Pi\varphi' + \frac{1}{3}K\varphi'\right) = -e^{-\varphi}\kappa^2\varrho w u_r\,, \tag{2.64b}$$

evolution equation $({}^j_j)$

$$\begin{aligned} &e^{-\Phi}(2\dot{K} - 3\dot{\Pi}) - K^2 + 2K\Pi - 3\Pi^2 - 2e^{2\Psi}a^{-2}\Delta(\Psi - \Phi - \varphi) - \\ &\quad -2e^{2\Psi}a^{-2}\left(-\Phi'^2 - \frac{1}{2}\Psi'^2 + \Phi'\Psi' - \varphi'^2 + \Psi'\varphi' - \frac{3}{2}\Phi'\varphi'\right) = -\,e^{-\varphi}\left(\kappa^2\varrho(1 - w^2) + \frac{3}{2}V\right)\,, \end{aligned} \tag{2.64c}$$

[4] This is not the canonical momentum of φ, see [DSY09]

and Newtonian gauge condition $({}_{rr} - 1/3\,{}^{j}{}_{j})$

$$\Delta(\Psi - \Phi - \varphi) - \frac{3}{r}(\Psi' - \Phi' - \varphi') + \Psi'^2 - \Phi'^2 - \varphi'^2 - 2\Psi'\Phi' - 2\Psi'\varphi' = 0\,. \tag{2.64d}$$

The spatial trace of the Einstein equation (2.64c) provides the evolution equation for K, and (2.64d) is the evolution equation for the traceless part of the extrinsic curvature, which is constrained to vanish in the chosen Newtonian coordinate system. The trace of the Einstein equations gives the equation of motion (2.4) for the scalar field φ. In terms of Π (using Eq. (2.63)) and the metric (2.26), the equation is given by

$$e^{-\Phi}\dot{\Pi} + \Pi^2 - K\Pi - e^{2\Psi}a^{-2}\left(\Delta\varphi + \varphi'^2 - \varphi'(\Psi' - \Phi')\right) = e^{-\varphi}\frac{1}{3}\left(2V + \kappa^2\varrho - V_{,\varphi}\right)\,. \tag{2.65}$$

The fluid equation $T^{\mu}{}_{\nu;\mu} = 0$ determines ϱ and v, and depends on the metric potenials Ψ and Φ. It splits into energy conservation

$$\partial_t\left(we^{-3\Psi}a^3\varrho\right) + \frac{1}{ar^2}\partial_r\left(r^2we^{-3\Psi}a^3\varrho v\right) = 0 \tag{2.66}$$

and Euler equation

$$\dot{u}_r + \frac{v}{a}u_r' = -e^{\Phi}\left(w\Phi' + \frac{w^2-1}{w}\Psi'\right)\,. \tag{2.67}$$

2.B Double expansion

In the context of cosmological perturbation theory one encounters two types of linearization in the literature. The first [KS84, MFB92] is predicated upon three assumptions; (i) perturbations in the metric are small $\Phi, \Psi \ll 1$, (ii) energy momentum tensor perturbations are small $\delta, v \ll 1$ and (iii) the Einstein and fluid equations are linearized around a background FRW spacetime. This is an excellent approximation in the very early universe, where both fluid and metric perturbations are small. However during structure formation the Newtonian gauge density contrast δ becomes large

$$\delta \equiv \frac{\varrho}{\bar{\varrho}} - 1 > 1\,. \tag{2.68}$$

In spite of this breakdown of assumption (ii) at late times, a miraculously working and seemingly inconsistent second linearization scheme is used on subhorizon scales. The metric is assumed to be a Newtonian gauge linearly perturbed FRW metric (i) with $\Phi, \Psi \ll 1$, but (ii) the density contrast δ is allowed to become non-perturbatively large $\delta > 1$, while the velocity v is assumed to remain small $v \ll 1$. The field and fluid (iii) equations are then expanded according to the following scheme, which in case of GR and spherical symmetry can be expressed solely in terms of the Newtonian metric perturbation, see [IW06] and Chapter 4

$$\Phi \ll 1\,, \quad \dot{\Phi} \ll \Phi_{,i}/a\,, \quad \Phi_{,i}\Phi_{,j} \ll \Phi_{,ij} \sim \delta \gtrsim 1\,. \tag{2.69}$$

Applying (2.69) to the Einstein and fluid equations is a procedure known as the quasistatic approximation. It is mixture of expanding in the smallness of Φ and the smallness of Ha/k on subhorizon scales, the smallness of the velocity v and the smallness of $\dot{\Phi} \lesssim H\Phi$ [Ras11]. We thus linearize all equations with respect to $\Phi, \dot{\Phi}, \varphi, \dot{\varphi}, v$ and $\dot{v}$, but not with respect to spatial derivatives of these quantities. We say more on this in Chapter 4.

2.B.1 Choice of gauge

Before we examine the fully non-linear equations to see why this expansion indeed works in the Newtonian gauge, we first consider the scalar part of the linearized comoving synchronous gauge metric [MB95]

$$ds^2 = -dt^2 + a^2 \left(\delta_{ij} - 2\psi_S \delta_{ij} + 2h_{S,ij}\right) dx^i dx^j \,. \tag{2.70}$$

Evaluting the continuity equation in synchronous gauge S we find $\delta_S' + \Delta h_S' = 0$, see Eq. (3.6b). We thus observe that the linearized metric written in synchronous gauge (2.70) becomes non-linear as soon as the density contrast δ_S does. This scenario is what one would naively expect, but we will see that a special feature of the Newtonian coordinates is that the expansion (2.69) is consistent.

2.B.2 Newtonian gauge discussion

In the case of standard GR, small velocities v and initially small Newtonian gauge potentials $\Phi \equiv \phi_N$ and $\Psi \equiv \psi_N$, it can be shown using the Lemaître-Tolman-Bondi metric [Van08] that the solution to the metric-linearized, quasistatic spherically symmetric field equations also solves the fully nonlinear equations. This means that the linearized metric in the Newtonian gauge accurately describes the geometry of spacetime even if density perturbations become large and the spacetime curvature becomes non-linearly distorted. If we accept this, it is clear that the Newtonian coordinates belong to a class which make the approximate FRW symmetry of the metric manifest. One might question whether this property survives if we drop the assumption of spherical symmetry. The answer would appear to be in the affirmative; Φ and Ψ are small for all practical purposes in the entire universe (except near Black Holes and Neutron stars). Assuming (2.69), the Newtonian coordinates have proved very useful without spherical symmetry to model nonlinear structure formation [BR11a] and estimating the effect of backreaction of nonlinear structures on the FRW background [GW11].

It is important to note that a spacetime is not necessarily close to FRW just because the metric is close to FRW. This is because the curvature contains second derivatives of the metric and they are known to become large in the Newtonian gauge $\Delta\Phi \sim \delta$. Two spacetimes can differ significantly despite their metrics being related by a small deformation. Also, even in a spacetime in which the metric is close to FRW and there is negligible backreaction [GW11], there can still be a large effect on observables, as photons probe both the metric and the curvature [EMR09, Ras11] and Chapters 3 and 4.

2.B.2.1 General relativity

We now examine the full non-linear equations (2.64) with $\varphi = 0$, and show why the quasistatic expansion is successful. We do this as preparation for the $f(R)$ case, where no exact LTB like solution is known and hence no comparison between the Newtonian linearized and exact solution can be performed[5]. Subtracting the background equations

$$3H^2 = \bar{\varrho}\,, \qquad 6\dot{H} + 9H^2 = 0\,, \tag{2.71}$$

and writing $K = \delta K - 3H$ and $\varrho = \bar{\varrho}(1+\delta)$, the fully non-linear Einstein equations (2.64) are given by

$$\frac{1}{3}\delta K^2 - H\delta K + 2e^{2\Psi}a^{-2}\left(\Delta\Psi - \frac{1}{2}\Psi'^2\right) = \kappa^2\bar{\varrho}\left((w^2-1) + w^2\delta\right) \tag{2.72a}$$

$$\frac{2}{3}\delta K' = -\kappa^2\bar{\varrho}(1+\delta)wu_r \tag{2.72b}$$

$$\begin{aligned} 2e^{-\Phi}\delta\dot{K} + 9(e^{-\Phi}-1)H^2 - \delta K^2 + 6H\delta K - \\ -2e^{2\Psi}a^{-2}\left(\Delta(\Psi-\Phi) - \Phi'^2 - \frac{1}{2}\Psi'^2 + \Phi'\Psi'\right) = \bar{\varrho}(1+\delta)(w^2-1) \end{aligned} \tag{2.72c}$$

$$\Delta(\Psi-\Phi) - \frac{3}{r}(\Psi'-\Phi') + \Psi'^2 - \Phi'^2 - 2\Psi'\Phi' = 0\,. \tag{2.72d}$$

Using the background energy conservation $\bar{\varrho}a^3 =$const, the fluid equations reduce to

$$\partial_t\left(we^{-3\Psi}(1+\delta)\right) + \frac{1}{ar^2}\left(r^2we^{-3\Psi}(1+\delta)v\right)' = 0 \tag{2.73}$$

$$\dot{u}_r + \frac{v}{a}u_r' = -e^{\Phi}\left(w\Phi' + \frac{w^2-1}{w}\Psi'\right)\,. \tag{2.74}$$

If Φ, Ψ are small initially and we can estimate their spatial derivatives as $a^{-1}\Phi' \sim \Phi/L$, where L is the physical size of the perturbation, then we can infer from (2.72d) that $\Psi - \Phi = \mathcal{O}(\Phi^2)$. Inspecting Eq. (2.72c) it is then easy to see that if v, Φ, Ψ and δK are small initially, then all source terms for $\delta\dot{K}$ are also small. This prevents

$$\delta K = -3(e^{-\Phi}-1)H + 3e^{-\Phi}\dot{\Psi} \tag{2.75}$$

and thus also Ψ and Φ from growing significantly, as long as v remains non-relativistic. Specifically we require $(HL)^2(1+\delta)v^2 \sim \mathcal{O}(\Phi^2)$ and $HL^2\delta K \sim (HL)^3(1+\delta)v \sim \mathcal{O}(\Phi^2)$ in Eq. (2.72c), where we used (2.72b). Subject to these conditions, the quasistatic approximation

[5]This comparision was performed in the case of GR in [Van08].

will be a consistent expansion and the metric will remain linearly perturbed away from the background, even if δ becomes nonlinear. We thus arrive at the following equations:

$$2a^{-2}\Delta\Phi = \kappa^2\bar{\varrho}\delta \tag{2.76a}$$

$$\dot{\delta} + \frac{1}{ar^2}\partial_r\left(r^2(1+\delta)v\right) = 0 \tag{2.76b}$$

$$\dot{v} + vH + \frac{v}{a}v' = -\frac{1}{a}\Phi' . \tag{2.76c}$$

They are sufficient to determine Φ, δ and v from initial data. At the initial time we have to ensure that the constraint (2.72b)

$$\frac{2}{3}\delta K' = 2\Phi' H + 2\dot{\Phi}' = -\kappa^2\bar{\varrho}(1+\delta)av \tag{2.77}$$

is fulfilled, such that the subsequent evolution of δK and thus (2.72c) is irrelevant. Note that quasistatic approximation and metric linearization break down near the final stages of the collapse, where a Black Hole will form. We stop our simulations well before this time, making the reasonable assumption that the duration of the final stage of collapse is negligible.

2.B.2.2 $f(R)$

We now apply a similar argument to the fully nonlinear $f(R)$ Einstein equations (2.64). Again subtracting the background equations

$$3H(H+\bar{\Pi}) = e^{-\bar{\varphi}}(\kappa^2\bar{\varrho} + \frac{1}{2}\bar{V}) \tag{2.78a}$$

$$2\dot{H} + 3H^2 + \dot{\bar{\Pi}} + \bar{\Pi}^2 + 2H\bar{\Pi} = \frac{1}{2}e^{-\bar{\varphi}}\bar{V} \tag{2.78b}$$

$$\dot{\bar{\Pi}} + \bar{\Pi}^2 + 3H\bar{\Pi} = e^{-\bar{\varphi}}\frac{1}{3}\left(2\bar{V} + \kappa^2\bar{\varrho} - \bar{V}_{,\varphi}\right) , \tag{2.78c}$$

and defining $\delta\varphi \equiv \varphi - \bar{\varphi}$, $\delta V \equiv V - \bar{V}$ and $\delta V_{,\varphi} \equiv V_{,\varphi} - \bar{V}_{,\varphi}$, the modified Einstein equations (2.64) take the following form.

Energy constraint

$$\begin{aligned}\frac{1}{3}\delta K^2 - H\delta K - \delta K\bar{\Pi} + 3H\delta\Pi - \delta K\delta\Pi + \\ + e^{2\Psi}a^{-2}\left(\Delta(2\Psi-\varphi) - \Psi'^2 + \Psi'\varphi' - \varphi'^2\right) = e^{-\varphi}\left(\kappa^2\bar{\varrho}\left((w^2-1)+w^2\delta\right) + \frac{1}{2}\delta V\right) \\ - e^{-\bar{\varphi}}\left(\kappa^2\bar{\varrho} + \frac{1}{2}\bar{V}\right)(1-e^{-\delta\varphi}) ,\end{aligned} \tag{2.79a}$$

momentum constraint

$$\frac{2}{3}\delta K' - \left(\delta\Pi' + (\bar{\Pi}+\delta\Pi)\varphi' + \frac{1}{3}\delta K\varphi' - H\varphi'\right) = -e^{-\varphi}\kappa^2\bar{\varrho}(1+\delta)wu_r , \tag{2.79b}$$

evolution equation

$$e^{-\Phi}(2\delta\dot{K}-3\delta\dot{\Pi})+3(1-e^{-\Phi})(2\dot{H}+\dot{\bar{\Pi}})+6H\delta K-\delta K^2+2\delta K\bar{\Pi}- \\ -6H\delta\Pi+2\delta K\delta\Pi-6\bar{\Pi}\delta\Pi-3\delta\Pi^2-2e^{2\Psi}a^{-2}\Delta(\Psi-\Phi-\varphi)- \\ -2e^{2\Psi}a^{-2}\left(-\Phi'^2-\frac{1}{2}\Psi'^2+\Phi'\Psi'-\varphi'^2+\Psi'\varphi'-\frac{3}{2}\Phi'\varphi'\right) \\ =(1-e^{-\delta\varphi})e^{-\bar{\varphi}}\frac{3}{2}\bar{V}-e^{-\varphi}\left(\kappa^2\varrho(1-w^2)+\frac{3}{2}\delta V\right), \quad (2.79c)$$

Newtonian gauge condition

$$\Delta(\Psi-\Phi-\varphi)-\frac{3}{r}(\Psi'-\Phi'-\varphi')+\Psi'^2-\Phi'^2-\varphi'^2-2\Psi'\Phi'-2\Psi'\varphi'=0\,. \quad (2.79d)$$

and scalar field equation

$$e^{-\Phi}\delta\dot{\Pi}+\delta\Pi^2-\delta K\delta\Pi+2\delta\Pi\bar{\Pi}-\delta K\bar{\Pi}+3H\delta\Pi-e^{2\Psi}a^{-2}\left(\Delta\varphi+\varphi'^2-\varphi'(\Psi'-\Phi')\right) \\ =(e^{-\delta\varphi}-1)e^{-\bar{\varphi}}\frac{1}{3}\left(2\bar{V}+\kappa^2\bar{\varrho}-\bar{V}_{,\varphi}\right)+e^{-\varphi}\frac{1}{3}(2\delta V+\kappa^2\bar{\varrho}\delta-\delta V_{,\varphi})\,. \quad (2.79e)$$

The argument for using the quasistatic approximation in the $f(R)$ field equations contains additional caveats. The reason is the following. Some of the source terms for $\delta\dot{\Pi}$ in (2.79e) are known to become large during the evolution, namely $\Delta\varphi$, δ and $\delta V_{,\varphi}$, hence it is not a priori clear that $\delta\dot{\Pi}$ will remain small (and similarly $\delta\dot{K}$). However if $\delta\varphi$, Ψ and Φ are small initially, and relations such as $a^{-1}\Phi'\sim\Phi/L$ hold for all three variables individually, then from (2.79d) we can deduce that $\Psi-\Phi-\varphi\sim\mathcal{O}(\Phi^2)$. If in addition v, δV, $\delta\Pi$ and δK are small then the evolution equation (2.79c) tells us that the combination $2\delta\dot{K}-3\delta\dot{\Pi}$ will also be small. However we cannot infer that $\delta\Pi$ and δK both remain small individually, so we can make no definite statement regarding the magnitudes of $\delta\varphi$, Ψ and Φ. We can argue that it is plausible that if the combination $2\delta\dot{K}-3\delta\dot{\Pi}$ is small then $\delta\dot{K}$ and $\delta\dot{\Pi}$ are small separately, unless there is some form of cancelation. With this extra assumption we can write down the relevant equations. Subject to $v,\delta V\ll 1$, (2.79a) and (2.79e) become

$$a^{-2}\Delta(2\Phi+\varphi)=e^{-\bar{\varphi}}\kappa^2\bar{\varrho}\delta\,, \quad (2.80a)$$

$$-a^{-2}\Delta\varphi=e^{-\bar{\varphi}}\frac{1}{3}(\kappa^2\bar{\varrho}\delta-\delta V_{,\varphi})\,. \quad (2.80b)$$

and again we need to enforce the constraint equation

$$\frac{2}{3}\delta K'-\left(\delta\Pi'+(\bar{\Pi}+\delta\Pi)\varphi'+\frac{1}{3}\delta K\varphi'-H\varphi'\right) \\ =-e^{-\varphi}\kappa^2\bar{\varrho}(1+\delta)av\,, \quad (2.81)$$

on the initial time slice.

The $f(R)$ model that we are using (2.8) allows for further simplifications. The background value of the scalar field today is of order $\bar{\varphi} \simeq -\epsilon$. This makes $\bar{\varphi}$ itself quasistatic for $\epsilon \ll 1$ and we can neglect $\bar{\Pi}$, $\dot{\bar{\Pi}}$ compared to H and $\dot{H}$ respectively in (2.78). Using $V \simeq R\varphi - f \simeq 2\Lambda$, the relevant background equations reduce to ΛCDM

$$3H^2 = \kappa^2\bar{\varrho} + \Lambda \tag{2.82a}$$

$$2\dot{H} + 3H^2 = \Lambda\,. \tag{2.82b}$$

If we take initial conditions during matter domination, all $f(R)$ terms in (2.81) are negligible such that we can use the GR momentum constraint (2.77). In addition, since $\dot{\Phi} = 0$ during the matter era, the initial velocity v must satisfy the GR condition

$$2\Phi' H = -\kappa^2\bar{\varrho}(1+\delta)av \tag{2.83}$$

Eqs. (2.80) together with the fluid equations (2.76b) and (2.76c) completely determine the non-linear spherical collapse provided all quantities are initially perturbative and subject to the conditions; (i) δV is comparably small to $v^2(1+\delta)$ and (ii) $v \sim HL$. This involves the extra assumption that $2\delta K - 3\delta\Pi \simeq 6\dot{\Psi} - 3\dot{\varphi}$ has the same order of magnitude as both $\delta K \simeq 6\dot{\Psi}$ and $\delta\Pi \simeq \dot{\varphi}$. So the full set of relevant equations is

$$a^{-2}\Delta\Phi = \frac{2}{3}\kappa^2\bar{\varrho}\delta - \frac{1}{6}\delta V_{,\varphi}\,, \tag{2.84a}$$

$$a^{-2}\Delta\varphi = \frac{1}{3}(\delta V_{,\varphi} - \kappa^2\bar{\varrho}\delta) \tag{2.84b}$$

$$\dot{\delta} + \frac{1}{ar^2}\partial_r\left(r^2(1+\delta)v\right) = 0 \tag{2.84c}$$

$$\dot{v} + vH + \frac{v}{a}v' = -\frac{1}{a}\Phi'\,. \tag{2.84d}$$

Note that one could replace equation (2.84a) or (2.84b) by

$$(2\Phi + \varphi)'H + (2\dot{\Phi} + \dot{\varphi})' = -\kappa^2\bar{\varrho}(1+\delta)av \tag{2.85}$$

which is the simplified (2.81) valid in the quasistatic approximation. One advantage of (2.85) compared to (2.84b) is that only the former is linear in φ.

The assumptions made above regarding the size of $\dot{\Phi}$ and $\dot{\varphi}$ may be unjustified in situations where the effective potential of φ suddenly changes, such as during the onset of the chameleon mechanism (see Fig. 2.3). Another example might be the oscillation of φ during the emission of monopole radiation. In these situations Φ may compensate the time dependence of φ such that the combination $2\Phi + \varphi$ might remain quasi-static, but it is not clear that any of the assumptions made will continue to hold. Since we cannot say anything definite about the validity of equations (2.84), we check during the numerical solution of the equations that all neglected terms stay much smaller than the terms appearing in (2.84), and also that the neglected equation (2.79d) is satisfied.

While performing these checks we noticed that $\dot{\Phi} \ll \Phi'/a$ is never satisfied well within and far outside the density perturbation; rather we find $\dot{\Phi} \gg \Phi'/a$ in these regions. This is not an $f(R)$ artifact, but is simply a consequence of the boundary conditions at $r = 0$ and $r = \infty$, where all spatial derivatives approach zero. It seems that $\dot{\Phi} \ll \Phi'/a$ is not globally required to ensure a quasistatic evolution.

2.C Peaks theory shape function

Consider a gaussian random field $\delta(z_i, \mathbf{x}, R)$ smoothed with a window function $W(kR)$ over the comoving scale R. The properties of this field are completely determined by its two-point correlation function $\xi(r = |\mathbf{x}-\mathbf{y}|, R)$, or equivalently its Fourier transfrom, the power spectrum $P(k, R) = W(kR)^2 P(k)$. The mean shape

$$\delta_i(r, R) = \langle \delta(z_i, \mathbf{x}, R) | \text{peak}, \nu \rangle \tag{2.86}$$

around a peak of height $\nu = \delta_{i,0}/\sigma(z_i, R)$ can be expressed in terms of the autocorrelation function $\xi(r, R)$ and its first, second and forth derivative with respect to r. Following Appendix A-D and Section VII of [BBKS86] we arrive at[6]

$$\delta_i(r, R) = \frac{\nu}{1-\gamma^2}\left(\frac{\xi}{\sigma_0} + \frac{\gamma}{\sigma_2}\Delta\xi - \frac{\langle x|\text{peak}, \nu\rangle}{\nu}\left(\gamma\frac{\xi}{\sigma_0} + \frac{1}{\sigma_2}\Delta\xi\right)\right) \tag{2.87}$$

with variance $\sigma \equiv \sigma_0$ and the first two moments σ_1, σ_2 are given by

$$\sigma_i = \int_0^\infty \frac{k^2 dk}{2\pi^2} P(k, R) k^{2i}\,, \tag{2.88}$$

and with $x \equiv -\Delta\delta|_{\mathbf{x}=0}/\sigma_2$ and $\gamma \equiv \sigma_1^2/(\sigma_0\sigma_2)$. The mean central curvature x of a peak is approximately given by eq. (6.13) and (6.14) of [BBKS86]

$$\langle x|\text{peak}, \nu\rangle = \gamma\nu + \theta \tag{2.89}$$

$$\theta = \frac{3(1-\gamma^2) + (1.216 - 0.9\gamma^4)\exp[-\gamma/2\,(\gamma\nu/2)^2]}{[3(1-\gamma^2) + 0.45 + (\gamma\nu/2)^2]^{1/2} + \gamma\nu/2}\,. \tag{2.90}$$

Rather than applying the actual power spectrum $P_i \sim k^{n_s} T_\mathrm{N}(k)^2$ at redshift $z_i = 500$ to the peaks theory shape formula (2.87), we use the primordial powerspectrum $P_0 \sim k^{n_s}$ to calculate the mean shape at very early times on superhorizon scales and use the transfer function $T_\mathrm{N}(k)$ to evolve this shape to subhorizon scales after matter radiation equality. $T_\mathrm{N}(r)$ is the post-recombination transfer function in the Newtonian gauge, related to the synchronous gauge function $T_\mathrm{S}(k)$ via $T_\mathrm{N}(k) = (1 + 3a^2H^2/k^2)T_\mathrm{S}(k)$. Here $T_\mathrm{N}(k)$ is normalized as $T_\mathrm{N}(k{=}0) = 1$. Note that the primordial amplitude of $P(k)$ and its linear growth is irrelevant here, as the k- and

[6] Note that eq. (D6) and (7.10) of [BBKS86] do in fact coincide with each other and with (2.87) after rescaling the radial coordinate. We thank Ravi Sheth for pointing this out to us. Eq. (2.87) was be obtained by averaging over x, y and z in eq. (D3) of [BBKS86].

a-dependence factorise in linear perturbation theory and we are free to choose our initial ν at z_i. With a gaussian filter $W = \exp(-k^2R^2/2)$ and primordial spectrum $P_0(k) \sim k^{n_s}$, the mean shape $\delta_i(r, R)$ is given by

$$\delta_i(r, R) = \int_0^\infty dk k^2 \delta_0(k, R) \frac{\sin kr}{kr} T_{\rm N}(k)\,, \tag{2.91a}$$

$$\delta_0(k, R) = \delta_{i,0} \frac{1}{2}(n_s + 5) R^3 e^{-k^2R^2} (kR)^{n_s} \times \left\{ \frac{\sqrt{\frac{n_s+3}{n_s+5}}}{\nu \Gamma\left(\frac{n_s+5}{2}\right)} \left[\frac{e^{-\frac{1}{8}\left(\frac{n_s+3}{n_s+5}\right)^{3/2}\nu^2} \left((12n_s + 60) e^{\frac{1}{8}\left(\frac{n_s+3}{n_s+5}\right)^{3/2}\nu^2} + (0.632n_s + 13.52)n_s + 44.6 \right)}{(n_s + 5)^2 \left(2\sqrt{\frac{(0.25n_s+0.75)\nu^2+0.45n_s+8.25}{n_s+5}} + \sqrt{\frac{n_s + 3}{n_s + 5}}\nu \right)} \right.\right.$$
$$\left.\left. + \sqrt{\frac{n_s + 3}{n_s + 5}}\nu \right] \left(2k^2R^2 - n_s - 3\right) + \frac{(n_s + 3)\left(-2k^2R^2 + n_s + 3\right)}{2\Gamma\left(\frac{n_s+7}{2}\right)} + \frac{4}{(n_s + 5)\Gamma\left(\frac{n_s+3}{2}\right)} \right\}, \tag{2.91b}$$

where Γ is the Gamma function.

3

Mapping between Newtonian gravity and GR on all linear scales

This chapter is available as preprint [HHK12], and arose in collaboration with Thomas Haugg and Stefan Hofmann. We show that Newtonian N-body simulations and other Newtonian gravity based techniques to describe collisionless cold dark matter in a ΛCDM background are compatible with general relativity on all scales where linear perturbation theory applies, ranging from small scales well inside the horizon, where Newtonian nonlinearities are still subleading, up to arbitrary large scales, even larger than the horizon. In addition we show that the Newtonian approximation can be used to make exact general relativistic predictions. This verdict is based on four facts. (1) The system of linearized Einstein equations and conservation laws is well-posed in the gauge invariant formulation and physically meaningful. (2) Comparing general relativity with its Newtonian approximation at a given order in perturbation theory is only meaningful at the level of observables. (3) Observables for the dust fluid can be chosen such that their general relativistic dynamics and its Newtonian approximation agree at the linear level. Any disagreement for observables on the lightcone is well-known, of which the most dominant is the Kaiser effect and gravitational lensing. (4) Large curvature fluctuations contribute significantly only to gravitational lensing and Kaiser effect. Therefore, these fluctuations are not in conflict with Newtonian N-body simulations and other Newtonian techniques. They are encoded in the Newtonian velocity of the source and the Newtonian potential and can be used to calculate the effect on a light ray connecting source and observer.

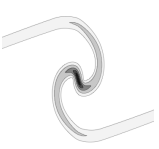

3.1 Introduction

Although there is still debate on whether nonlinear structure formation can backreact on the expansion of the Universe [IW06, BNSZ12a, Buc11, Ber12, BR12], there seems to be little doubt that the gravitational formation of structures on scales deep inside the Hubble volume is accurately described by Newtonian gravity, with general-relativistic effects entering at subleading level in the perturbative description. Nevertheless it was claimed [FS12] recently that effects in cosmological perturbation theory become dominant over 2nd order effects in the Newtonian approximation on scales larger than 10 Mpc.

In greater detail the argument was based on the following. The evolution of cosmological perturbations was calculated in a particular coordinate system, called the *Newtonian matter gauge* (NM), in which the linear density contrast $\delta_{\rm NM}$ and the peculiar velocity $v_{\rm NM}$ coincide with the corresponding quantities $\delta_{\rm N} = \delta_{\rm NM}$, $v_{\rm N} = v_{\rm NM}$ in the Newtonian (N) approximation. It was found that fluctuations in the local Hubble parameter $\delta^H_{\rm NM} \equiv -1 - K_{\rm NM}/(3H)$, where $K_{\rm NM}$ denotes the extrinsic curvature, are of order $\mathcal{O}(\delta_{\rm NM})$. The significance of this observation was evaluated by comparing $\delta^H_{\rm NM}$ to the size of second order corrections $\delta^{(2)}_{\rm N}$ in the Newtonian approximation. For comoving scales k and redshifts z with

$$\delta^H_{\rm NM} \geq \delta^{(2)}_{\rm N} \qquad \text{and} \qquad \delta^{(2)}_{\rm N} \ll \delta_{\rm N} < 1 \,, \tag{3.1}$$

it was argued that relativistic effects linear in cosmological fluctuations dominate over nonlinear Newtonian effects well within the domain of validity of perturbation theory. Based on this criterion, the authors of [FS12] found that linear cosmological perturbations on an Einstein-de Sitter background dominate over Newtonian nonlinearities for scales $k^{-1} > 10$ Mpc during the redshift interval $z \in [0.4, 750]$, from which they concluded that Newtonian N-body simulations cannot be trusted on these scales during the specified redshift interval. Note that this would not only invalidate the use of Newtonian N-body simulations but also the use Newtonian dust fluid model for collisionless cold dark matter (CDM) that is widely employed to model nonlinear structure formation, and central ingredient of this thesis. It is there for crucially important to understand the issue raised by [FS12].

Since by choice of gauge, $\delta_{\rm N} = \delta_{\rm NM}$, $v_{\rm N} = v_{\rm NM}$, while the fluctuations in the Hubble parameter are absent in the Newtonian approximation, and thus in N-body simulations, it is interesting to ask how these fluctuations become manifest in observables? It might be expected [FS12] that fluctuations in the Hubble parameter cause additional redshift space distortions, because the observed redshift depends on $K_{\rm NM}$ integrated along the line of sight between observer and source, in addition to the peculiar velocities of observer and source, $v^{\rm O}_{\rm NM}$ and $v^{\rm S}_{\rm NM}$, respectively. We find indeed that these fluctuations contribute considerably to redshift space distortions, however, only via gravitational lensing, which is well known as *lensing magnification*, e.g [Gun67, KS87, YFZ09, Yoo10, Mat00b, BD11, CL11]. These lensing induced distortions can be taken into account in N-body simulations using ray tracing technology [WCO98, HWHS07, HHWS09].

Cosmological perturbation theory can be compared to its Newtonian approximation in a meaningful way only by comparing observables. Observables are by definition gauge invariant combinations of the perturbations. The set of observables should be specified before a choice

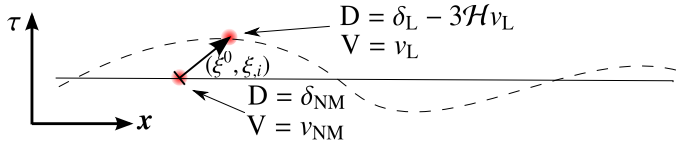

FIGURE 3.1: D and V agree on different hypersurfaces (*full* Newton matter gauge and *dashed* longitudinal gauge) evaluated at the same coordinate values in their respective coordinate systems. This means that although the physical interpretation of D and the way D is measured are different in the two depicted hypersurfaces, the hypothetical observers attached to these hypersurfaces still measure the same values for D.

of gauge is implemented, after the gauge redundancies have been removed it is impossible to identify observables. However, once the observables have been identified, gauge freedom is not sacrosanct and can either be removed or, equivalently, used to rewrite the theory using gauge invariant variables. Both procedures are perfectly valid. A comparison of observables using gauge invariant perturbations has been performed in [NH12] and was criticized in [FS12] as follows: "The initial conditions must be specified on a spatial Cauchy hypersurface, which in the context of cosmological perturbation theory corresponds to a particular foliation of space-time, i.e., to a hypothetical observer who is able to determine physical quantities on a spatial hypersurface. The relativistic-Newtonian correspondence mixes the quantities defined on different spatial hypersurfaces and thus no hypothetical observer in the Einsteinian world could actually determine these combined quantities."

This is a misconception that requires immediate clarification. Although gauge invariant variables might have a simple physical interpretation only in one specific gauge, they present observables in all other coordinate systems and, in particular, different hypersurfaces, as well. For instance, let D be a gauge invariant variable which reduces to the linear density contrast $\delta_{\rm S}$ in synchronous (S) gauge, measured by an observer at rest with respect to synchronous coordinates. Let V denote a gauge invariant variable which reduces to the peculiar velocity $v_{\rm L}$ as measured by an observer at rest relative to the longitudinal coordinate system. This is the situation referred to "defined on different spatial hypersurfaces" in the above quote. However, (D,V) are defined in all possible coordinate systems related by a linear gauge transformation $x^\mu \to x^\mu + \xi^\mu$ and observers adopted to different and arbitrary coordinate systems can measure D and V and will find the same numerical values for them. By construction, it is not the definition of gauge invariant variables that is tied to certain hypersurfaces, but it is their physical interpretation. This is why any smart observer will construct the set of observables before choosing a particular gauge to measure them, because even if not all observables have a convenient physical interpretation in the observer's coordinate frame, they still resemble the only meaningful quantities for any other observer. The only reasonable academic debate between observers adopted to different coordinate systems is about the physical interpretation of the gauge invariant variables.

As an example, consider an observer who is adopted to a longitudinal (L) coordinates system. This observer will interpret D as $\mathrm{D}_{\rm L} = \delta_{\rm L} - 3\mathcal{H}v_{\rm L}$. Although the observer has a physical interpretation for the gauge dependent quantities $(\delta_{\rm L}, v_{\rm L})$, (s)he understands the necessity to construct gauge invariant combinations involving $(\delta_{\rm L}, v_{\rm L})$, rather than assuming any other observer adopted to an arbitrary coordinate system would agree on the values of the gauge dependent quantities.

The observer adopted to the longitudinal frame can measure (δ_L, v_L) on a hypersurface, set up the initial value problem for an appropriate evolution equation involving (D,V) and finally solve for them, instead of (δ_L, v_L), see Fig. 3.1.

The plan for the rest of this chapter is as follows. In Section 3.2 it is shown explicitly that the hypothetical observables (δ_N, v_N) of linearized Newtonian gravity and (D,V) of linearized Einsteinian gravity obey the same evolution equations on a flat ΛCDM background (in [FS12] only $\Lambda = 0$ has been considered). This was expected since (D,V) reduce to (δ_{NM}, v_{NM}) for observers at rest in the Newtonian matter coordinate system.

However, a real observer cannot measure (D,V) on a hypersurface, because (s)he can only observe the light cone associated with (her) him via light rays, which get affected by curvature perturbations. This induces a feedback of general relativistic effects on the inference of (D,V), although (D,V) still coincide with (δ_{NM}, v_{NM}) on each hypersurface. Note that the status of (D,V) as observables is not challenged by the practical obstacles that prevent any observer from measuring them on the entire hypersurface.

Section 3.3 is devoted to investigate the impact of Hubble parameter fluctuations on the linear density contrast observed along a light cone. This is a well-known example highlighting the fact that δ^H_{NM} in particular, and any curvature perturbation in general, contributes significantly only to gravitational lensing. The strongest correction to the observed density flucutation in addition to redshift space distortions is due to gravitational lensing [Gun67, KS87, YFZ09, Yoo10, Mat00b, BD11, CL11] which indeed depends on δ^H_{NM} (and more generally on extrinsic and intrinsic curvature, see Section 3.3). The gauge invariant lensing term, of course, does not depend on the gauge the observer preferred. An observer adopted to the longitudinal gauge finds a negligible contribution from δ^H_L to gravitational lensing.

Our main result is that Newtonian N-body simulations and other Newtonian methods are compatible with cosmological perturbation theory and are not threatened by relativistic effects at the linear level although relativistic effects can become significant. We give a practical dictionary for using Newtonian quantities (δ_{NM}, v_{NM}) to evaluate these relativistic corrections.

3.2 Compatibility of linear observables on a hypersurface

In this section we show that a pressureless fluid in a universe with ΛCDM background geometry can be characterized by observables (D,V) in 1st-order cosmological perturbation theory that obeys evolution equations identical to those governing the evolution of (δ_N, v_N).

Restricting attention solely to scalar perturbations, the conformal evolution equations for (ϕ_N, δ_N, v_N) in the Newtonian approximation are given by

$$\Delta\phi_N = \tfrac{3}{2}\mathcal{H}^2\Omega_m\delta_N\,, \tag{3.2a}$$

$$\delta'_N + \Delta v_N = 0\,, \tag{3.2b}$$

$$v'_N + \mathcal{H}v_N = -\phi_N\,, \tag{3.2c}$$

with $\mathcal{H}$ denoting the conformal expansion rate of the background determined by Friedmann

equations

$$3\mathcal{H}^2 = 8\pi G(\bar{\varrho}_{\rm m} + \varrho_\Lambda)a^2 \,, \tag{3.3a}$$

$$4\pi G a^2 \bar{\varrho}_{\rm m} \equiv \frac{3}{2}\Omega_{\rm m}\mathcal{H}^2 = a^2(\mathcal{H}^2 - \mathcal{H}') \,, \tag{3.3b}$$

where $\bar{\varrho}_{\rm m} \propto a^{-3}$ and $\Omega_{\rm m}$ denotes the background matter density relative to the critical density.

The Newtonian perturbation variables $(\delta_{\rm N}, v_{\rm N})$ are defined by the matter density $\varrho_{\rm m} = \bar{\varrho}_{\rm m}(1+\delta_{\rm N})$ and the peculiar velocity $\boldsymbol{v}_{\rm N} = \nabla v_{\rm N}$. The triple $(\phi_{\rm N}, \delta_{\rm N}, v_{\rm N})$ constitutes the set of observables relevant for the discussion.

The corresponding description in general relativity requires a background metric around which the geometry fluctuates. Restricting attention again solely to scalar metric fluctuations, (ϕ, w, ψ, h), the total metric field is give by

$$\begin{aligned} {\rm d}s^2 = a^2\Big[&-(1+2\phi)\,({\rm d}\tau)^2 + 2w_{,i}\,{\rm d}\tau{\rm d}x^i + \\ &+ [(1-2\psi)\delta_{ij} + 2h_{,ij}]{\rm d}x^i{\rm d}x^j\Big] \,. \end{aligned} \tag{3.4}$$

The total pressureless source is encoded in $T_{\mu\nu} = \varrho_{\rm m}u_\mu u_\nu$, with $\varrho_{\rm m} = \bar{\varrho}_{\rm m}(1+\delta)$ and $u^\mu = (1-\phi, v^i)/a$. Altogether the dynamical degrees of freedom $(\phi, \psi, w, h, \delta, v)$ are the gauge dependent metric, density and velocity perturbations, see [Bar80, Muk05, FS12] for how they transform under gauge transformations $x^\mu \to x^\mu + \xi^\mu$.

Observables can be constructed by the following gauge invariant linear combinations, the so-called Bardeen variables [Bar80]:

$$\Phi = \phi + [(w-h')a]'/a \,, \tag{3.5a}$$

$$\Psi = \psi - \mathcal{H}(w-h') \,, \tag{3.5b}$$

$${\rm D} = \delta - 3\mathcal{H}(v+w) \,, \tag{3.5c}$$

$${\rm V} = v + h' \,. \tag{3.5d}$$

The perturbed Einstein and conservation equations then yield evolution equations [Mat00a, NH12] for the gauge invariant quantities $(\Phi, \Psi, {\rm D}, {\rm V})$:

$$\Delta\Phi = \tfrac{3}{2}\mathcal{H}^2\Omega_{\rm m}{\rm D} \,, \tag{3.6a}$$

$${\rm D}' + \Delta{\rm V} = 0 \,, \tag{3.6b}$$

$${\rm V}' + \mathcal{H}{\rm V} = -\Phi \,, \tag{3.6c}$$

where the background equations (3.3) and the linearized $(0j)$- and (ij)-Einstein equations have been used:

$$\mathcal{H}\Phi + \Psi' = -\tfrac{3}{2}\mathcal{H}^2\Omega_{\rm m}{\rm V} \,, \tag{3.7a}$$

$$\Phi = \Psi \,. \tag{3.7b}$$

Comparing (3.6) with the Newtonian approximation (3.2) it is evident that the evolution equations are identical in form. In addition, $(\Phi, {\rm D}, {\rm V})$ constitute the triple of observables relevant for

this discussion. Of course, any linear combination of these gauge invariant variables constitutes an equally legitimate observable. The triple (Φ, D, V) is favored only to establish directly the correspondence between relativistic observables and observables in the Newtonian approximation at the linear level.

Note that Φ and Ψ have the same quasi-static dynamics as $\phi_{\rm N}$, which allow us to qualify relativistic corrections to Newtonian observables, e.g. (3.8) below, as large or small in comparison to 2nd order corrections in the Newtonian approximation (3.1).

Let us emphasize again that there is no gauge G in which simultaneously

$$\Phi = \phi_{\rm G}, \quad \Psi = \psi_{\rm G}, \quad {\rm D} = \delta_{\rm G}, \quad {\rm V} = v_{\rm G} \; .$$

Different observers simply assign different physical meaning to these gauge invariant variables. For instance, in longitudinal, synchronous and Newtonian matter gauge the following physical interpretations hold:

Gauge	Φ	Ψ	D	V
L	$\phi_{\rm L}$	$\psi_{\rm L}$	$\delta_{\rm L} - 3\mathcal{H}v_{\rm L}$	$v_{\rm L}$
S	$-h''_{\rm S} - h'_{\rm S}\mathcal{H}$	$\psi_{\rm S} + h'_{\rm S}\mathcal{H}$	$\delta_{\rm S}$	$h'_{\rm S}$
NM	$w'_{\rm NM} + w_{\rm NM}\mathcal{H}$	$\psi_{\rm NM} - w_{\rm NM}\mathcal{H}$	$\delta_{\rm NM}$	$v_{\rm NM}$

3.3 Linear observables on the lightcone

A physical observer is in practice not able to measure (D,V) everywhere on any hypersurface. Instead, a physical observer can only learn about (D,V) by employing light rays traveling along (her) his respective light cone. As a consequence of such an observation campaign, (D,V) become subject to relativistic effects that have no Newtonian counterpart. In particular, the light rays will be gravitationally lensed and these lensing effects will be attributed to (D,V). Since gravitational lenses are absent in the Newtonian approximation, the dictionary $(\Phi, {\rm D}, {\rm V}) \leftrightarrow (\phi_{\rm N}, \delta_{\rm N}, v_{\rm N})$ is challenged. It is important to realize that the existence of geometry flucutations in GR and their absence in the Newtonian approximation does not imply that Newtonian N-body simulations are inaccurate to explore GR at linear scales, as it was claimed in [FS12]. We show here how to make these two theories compatible.

As an example, consider within the linear general relativistic framework the density fluctuation observable $\mathcal{D}(\boldsymbol{n}, z, \tau_{\rm O}, \boldsymbol{x}_{\rm O})$, where $(\tau_{\rm O}, \boldsymbol{x}_{\rm O})$ is the observer's space-time position, z is the density fluctuation's observed redshift and $-\boldsymbol{n}$ its direction on the sky. It is given by the gauge invariant expression [BD11]

$$\begin{aligned} \mathcal{D}(\boldsymbol{n}, z) \;=\; & {\rm D} - \frac{1}{\mathcal{H}}\partial_r^2 {\rm V} - \frac{1}{r_S}\int_0^{r_S} d\lambda \frac{r_S - r}{r}\Delta_\Omega(\Phi + \Psi) + \\ & + \left(\frac{\mathcal{H}'}{\mathcal{H}^2} + \frac{2}{r_S\mathcal{H}}\right)\left(\Psi - \partial_r {\rm V} + \int_0^{r_S} d\lambda (\Phi + \Psi)'\right) \\ & + \frac{1}{\mathcal{H}}\Phi' + 3\mathcal{H}{\rm V} - 2\Phi + \Psi + \frac{2}{r_S}\int_0^{r_S} d\lambda (\Phi + \Psi) \; , \end{aligned} \tag{3.8}$$

where all functions are evaluated along the unperturbed light cone $\boldsymbol{x} = \boldsymbol{x}_{\rm O} - \boldsymbol{n}r(z)$ and $\tau = \tau_{\rm O} - r(z)$, with $r(z) = \int_0^z dz'/(H(z')a_{\rm O})$, the unperturbed affine parameter $\lambda = r$ and S denotes the source. Δ_Ω is the angular part of the Laplacian in spherical coordinates. Detailed derivations of (3.8) can be for instance found in [YFZ09, BD11, CL11].

The Newtonian approximation of gravity is void of the light cone concept. Moreover, the gravitational potential couples only to massive bodies, in particular, there is no coupling to light rays. In other words, light rays cannot probe $\phi_{\rm N}$. The assumption that there is a light cone embedded in the background cosmology, albeit an artificial point of view, allows to obtain the first and second term of (3.8) in the Newtonian approximation, $\mathcal{D}_{\rm N}(\boldsymbol{n}, z) = \delta_{\rm N} - \mathcal{H}^{-1}\partial_r^2 v_{\rm N}$. The second term is known as *Kaiser-effect* [Kai87] and is the dominant volume distortion for small redshifts [BD11]. Moreover, let us assume that light couples to $\phi_{\rm N}$ such that its bending around the Sun conforms to actual observations. Including the lensing contribution,

$$\mathcal{D}_{\rm N}(\boldsymbol{n}, z) = \delta_{\rm N} - \mathcal{H}^{-2}\partial_r^2 v_{\rm N} - \frac{1}{r_S}\int_0^{r_S} d\lambda \frac{r_S - r}{r}\Delta_\Omega \phi_{\rm N} \,. \tag{3.9}$$

Well inside the horizon, in particular around 10 Mpc, this formula is a very good approximation to (3.8) [CL11, BD11]. The lensing contribution can be the leading redshift space distortion, which can even dominate over $\delta_{\rm N}$ [CL11, BD11] for sufficiently distant sources.

For a more transparent treatment, let us define a Newtonian observable $\mathcal{D}_{\rm N}(\boldsymbol{n}, z)$ through the following replacements in the relativistic quantity (3.8):

$$\mathcal{D}_{\rm N}(\boldsymbol{n}, z) \equiv \mathcal{D}(\boldsymbol{n}, z)\Big|_{\rm D\to\delta_N, V\to v_N, \Phi=\Psi\to\phi_N} \,. \tag{3.10}$$

Using the results from the last section it follows that $\mathcal{D}_{\rm N}(\boldsymbol{n}, z) = \mathcal{D}(\boldsymbol{n}, z)$ at all scales where linear perturbation theory applies. As a consequence, *N-body simulations can be used directly to extract relativistic observables* when scalar dust fluctuations on a ΛCDM background are considered at the linear level. It should be also emphasized that the compatibility of the general relativistic equations (3.6) and the Newtonian approximation Eq. (3.2) only holds on a LCDM background. Any other background, like a dynamical dark energy or radiation component and the presence of other fluctuating fields precludes such an exact compatibility.

Let us comment on why fluctuations $\delta^H_{\rm NM}$ in the Hubble parameter $\bar{K} = -3H$,

$$\begin{aligned} \delta^H &\equiv -\frac{\delta K/3}{\mathcal{H}/a} \\ &= \frac{-1}{\mathcal{H}}\left(\psi' + \mathcal{H}\phi + \tfrac{1}{3}\Delta(w - h')\right) \,, \end{aligned} \tag{3.11}$$

are, in fact, strongly contributing only to the lensing term and, therefore, were identified correctly in [FS12] as a major source of correction to density observables.

Clearly, large fluctuations in the Hubble parameter do not imply that Newtonian N-body simulations cannot be trusted. Instead it implies that either (3.9) or (3.10) (or, better, an expression including nonlinear effects) should be used to compare numerical experiments based on the Newtonian approximation to observations, which was well known [Gun67, KS87, YFZ09, Yoo10, Mat00b, BD11, CL11] before the work [FS12].

From the gauge invariance of formula (3.8) alone [KS87, BD11], it follows that $\mathcal{D}(\boldsymbol{n}, z)$ is constructed from Hubble parameter fluctuations δ^H, intrinsic curvature $R^{(3)} = 4\Delta\psi/a^2$, anisotropic extrinsic curvature $A_{ij} = a(\partial_i\partial_j/\Delta - \delta_{ij}/3)\Delta(w - h')$, and the divergence of the hypersurface observer acceleration $\boldsymbol{a} = \boldsymbol{\nabla}\ln[a(1+\phi)]$ in such a way that arguing about the size of δ^H adapted to various gauges is meaningless. In certain gauges δ^H might qualify as large (NM and S), while in others it qualifies as small (L), but this does not matter at all.

Any change in δ^H induced by a transition between coordinate systems must be compensated for by corresponding changes in

$$\delta^R \equiv \Delta\psi, \quad \delta^a \equiv \Delta\phi \quad \text{and} \quad \delta^A \equiv \Delta(w - h')\,.$$

In order to proof that a large $\delta^H_{\rm NM}$ can strongly effect only the lensing term, note that on the smallest scales where the linear approximation still applies, second spatial derivatives of $\psi_{\rm NM}$ and $w_{\rm NM}$ can become large through the Poisson equation (3.6a), while $\psi_{\rm NM}$ and $w_{\rm NM}$ remain small due to the quasistatic evolution of Φ and Ψ, preserving their initially small amplitude and the smallness of the velocity $\boldsymbol{\nabla}v_{\rm NM}$. Except close to neutron stars and black holes, see [GW11, HW98], Φ and Ψ are evolving very slowly even if the density becomes nonlinear. Provided that all relevant scales are inside the Hubble radius and the peculiar velocity $\boldsymbol{\nabla}v_{\rm NM}$ is non-relativistic it was shown in [BR11b] that Φ freezes once $\delta > 1$, see however Chapter 4 for a more careful derivation. In the spherically symmetric case it was proven in [Van08] that the solution obtained using these approximations solves the fully nonlinear Einstein equations. Therefore these second derivatives are the sole reason for why $\delta^H_{\rm NM}$ becomes as large as $\delta_{\rm NM}$ and why only the Kaiser and lensing terms in (3.8) will add large corrections to D at those scales. Since the lensing term $\Delta(\Phi + \Psi)$ is the single term in (3.8) that contains second derivatives of $\psi_{\rm NM}$ and $w_{\rm NM}$ it is only here that the second derivative terms of $\delta^H_{\rm NM}$ can contribute. Therefore all other terms in the second and third line of (3.8) can depend on $\delta^H_{\rm NM}$ only through the combination $\mathcal{H}\delta^H_{\rm NM} + \delta^A_{\rm NM}/3 = -\psi'_{\rm NM}$, which is small and quasistatic. Note that the Kaiser term retains its physical meaning in Newtonian matter gauge because $\mathrm{V} = v_{\rm NM}$. More generally the second and third line of (3.8) containing only Ψ, Φ, as well as their conformal time derivatives, V and $\partial_r\mathrm{V}$ remain much smaller than the first line of (3.8) on scales well inside the Hubble radius.

On top of that bear in mind that in a strict sense

$$\Delta(\Phi + \Psi) = \delta^R + \delta^a + \delta^{A'} \tag{3.12}$$

does not depend on δ^H. However in linear theory a large $\delta^H_{\rm NM}$ implies a large δ^A. Similary a large $\Delta(\Phi + \Psi)$ implies a large lensing term $\Delta_\Omega(\Phi + \Psi)$. In this sense we have shown that a large $\delta^H_{\rm NM}$ contributes only to the well known lensing term. Note also that there is nothing special about $\delta^H_{\rm NM}$ compared to $\delta^R_{\rm NM}$, $\delta^a_{\rm NM}$, $\delta^A_{\rm NM}$; all of these curvature perturbations are similarly large and all of them are absent in Newtonian gravity.

The discussion outlined for $\mathcal{D}(\boldsymbol{n}, z)$ applies quite generally to any observable. A constructive algorithm for an arbitrary observable is the following: (*i*) construct the general relativistic gauge invariant observable and express it in terms of (D,V) and Φ. (*ii*) Use the quasi-static evolution of Φ to determine which contributions qualify as large on small but still linear scales. If one

can identify large contributions that are not reflected in the corresponding Newtonian observable, then these contributions will have a genuine relativistic origin. (*iii*) Employ the dictionary $(\mathrm{D}, \mathrm{V}, \Phi) \to (\delta_\mathrm{N}, v_\mathrm{N}, \phi_\mathrm{N})$ to extract relativistic observables using Newtonian N-body simulations or any other technique based on Newtonian gravity. This has been worked out in much greater in detail in [CZ11, GW12].

3.4 Conclusion

In summary, we have shown that fluctuations in the Hubble parameter and other curvature fluctuations do not give rise to a new type of redshift space distortions or other important relativistic effects. Those linear curvature perturbations do however contribute to important relativistic corrections, but only in form of the well-known Kaiser effect and lensing magnification. Therefore expanding on the findings of [FS12], Newtonian N-body simulations *are* the appropriate numerical experiments to extract relativistic observables on all scales where 1st order perturbation theory applies.

In Section 4 we will see that on small and even fully nonlinear scales another mapping between GR and Newtonian gravity exists. Combined, this means that in order to study the dynamics of collisionless cold dark matter we can fully rely on Newtonian gravity on all scales. If we want to know how the CDM dynamics appears on the light cone, we need to include the most important effects; redshift space distortions and gravitational lensing, which can be reconstructed from the Newtonian CDM dynamics.

4

Mapping between Newtonian gravity and GR on nonlinear scales

This chapter is published as an article [KUH14], and arose in collaboration with Cora Uhlemann and Thomas Haugg. We investigate the relation between the standard Newtonian equations for a pressureless fluid (dust) and the Einstein equations in a double expansion in small scales and small metric perturbations. We find that parts of the Einstein equations can be rewritten as a closed system of two coupled differential equations for the scalar and transverse vector metric perturbations in Poisson gauge. It is then shown that this system is equivalent to the Newtonian system of continuity and Euler equations. Brustein and Riotto [BR11b] conjectured the equivalence of these systems in the special case where vector perturbations were neglected. We show that this approach does not lead to the Euler equation but to a physically different one with large deviations already in the 1-loop power spectrum. We show that it is also possible to consistently set to zero the vector perturbations which strongly constrains the allowed initial conditions, in particular excluding Gaussian ones such that inclusion of vector perturbations is inevitable in the cosmological context. In addition we derive nonlinear equations for the gravitational slip and tensor perturbations, thereby extending Newtonian gravity of a dust fluid to account for nonlinear light propagation effects and dust-induced gravitational waves.

4.1 Introduction

In [BR11b], a new method to study the evolution of nonlinear cosmological matter perturbations was presented in which the nonlinear Einstein equations were employed to deduce a single equation for the Newtonian potential. The key advantage of this approach is to provide a closed and non-perturbative equation for the gravitational potential instead of a coupled fluid system for

density and velocity. This allows to study directly the Newtonian potential which remains always small, even if density perturbations become large. The framework presented for the gravitational potential was shown to bear close resemblance to the Newtonian fluid formulation with regard to perturbative and mean field solutions and therefore their equivalence was conjectured.

Following closely [BR11b], we derive a coupled system for the Newtonian potential and a transverse vector field from the Einstein equations for a dust fluid by performing a small scale expansion and an expansion in the smallness of metric perturbations in Poisson gauge. Hereby taking vector perturbations ω_i of the metric explicitly into account we are able to prove the equivalence of parts of the Einstein equation and the Newtonian pressureless fluid equations. The remaining parts of the Einstein system yield nonlinear equations for tensor perturbations χ_{ij} and the 'slip' $\Psi - \Phi$ thereby naturally extending Newtonian gravity of dust to allow for a consistent description of Einsteinian effects like light propagation and gravitational waves. Similar to Ψ, the quantities $\Phi, \omega_i, \chi_{ij}$ are therefore already encoded in the Newtonian dynamics of a dust fluid and can be extracted from it. This fact was recently observed in [BTW13],[1] where ω_i was measured from a Newtonian N-body simulation. Although ω_i turned out to be sub-leading compared to Ψ and therefore consistent with the double expansion scheme, it was on average 10 times larger than expected from a perturbative calculation [BTW13].

We will furthermore show that restricting attention to scalar metric perturbations leads to a constraint equation that amounts to considering fine-tuned initial conditions. On the other hand, ignoring this constraint as done in [BR11b] modifies the Euler equation. Both approaches for vanishing vector perturbations therefore have serious ramifications. Most notably, discarding the constraint on the initial conditions leads to disagreement with known standard perturbation theory results, which remained unacknowledged in [BR11b]. We re-derive perturbation theory including vector perturbations in Appendix 4.B and compare numerical results for the 1-loop matter and momentum power spectrum in Section 4.4.

4.2 Evolution equation in the presence of vector perturbations

We assume that the metric is perturbatively close to a flat Friedmann-Robertson-Walker (FRW) metric written in Poisson gauge and conformal time τ with scale factor $a(\tau)$

$$ds^2 = a^2(\tau)\left[-e^{2\Phi}d\tau^2 + 2\omega_i d\tau dx^i + \left(e^{-2\Psi}\delta_{ij} + \chi_{ij}\right)dx^i dx^j\right], \tag{4.1}$$

where Φ and Ψ are assumed to be first order perturbation quantities in the initial conditions and at later times ω_i and χ_{ij} are secondarily induced, with $\omega_{i,i} = \chi_{ij,j} = \chi_{ii} = 0$. The physical justification for this is that throughout the universe, except very close to black holes and neutron stars, Φ and Ψ are quasistatic and remain at their primordially small value, typically $\Phi, \Psi = \mathcal{O}(\epsilon) \simeq 10^{-5}$. In addition any primordial ω_i and χ_{ij} will have decayed quickly such that we will assume that they vanish in the initial conditions and are only induced with size $\mathcal{O}(\epsilon^2)$

[1] We would like to thank Marco Bruni for making us aware of this work.

later on. The vector perturbation ω_i grows slowly, and although χ_{ij} are constantly emitted they are weak and decay quickly.

Although the metric is perturbatively close to a FRW metric, spacetime curvature is not assumed to be perturbatively close to FRW on small scales. Spatial gradients $\nabla_i = \partial_i$ of metric perturbations, determining curvature, can become much larger. For example, in the quasilinear regime of structure formation, typically even if $\Psi \simeq 10^{-5}$ we have that $\Psi_{,i}/\mathcal{H} \simeq v^i \simeq 10^{-3}$ and $\Delta\Psi/\mathcal{H}^2 \simeq \delta \simeq 1$, where $1/\mathcal{H} = a/a'$ is the comoving Hubble radius, v^i matter velocity and δ the matter density contrast. We therefore introduce another small bookkeeping quantity η and estimate spatial derivatives by assigning $\mathcal{H}^{-1}\partial_i = \mathcal{O}(\eta^{-1})$ and assuming that $\Delta\Psi/\mathcal{H}^2 = \mathcal{O}(\epsilon/\eta^2) \simeq \mathcal{O}(1)$. In Fourier space this means $k \gg \mathcal{H}$, and the expansion parameter η is the ratio between the typical length scale of perturbations and the size of the Universe. We will see later in Eq. (4.5b) that the dynamical equations suggest that $\omega_i = \mathcal{O}(\epsilon^2/\eta)$ and therefore vector perturbations are a little bit more important than originally assumed. Recovering Newtonian gravity imposes this as a consistency requirement. In particular this implies that $\Delta\omega_i/\mathcal{H}^2 = \mathcal{O}(\epsilon^2/\eta^3) = \mathcal{O}(\epsilon/\eta)$ and $\omega_{i,j}/\mathcal{H} = \mathcal{O}(\epsilon)$.

Performing this expansion scheme on the Einstein tensor calculated from the perturbed FRW metric (4.1), see for example Eqs. (A.9)-(A.11) in [BMR07], one can easily recover the result obtained in [BR11b], see Eqs. (4.2) below. In the 00-component the leading order terms are $\mathcal{O}(1)$, the $0i$-component is $\mathcal{O}(\epsilon/\eta)$ and the ij-component order $\mathcal{O}(\epsilon)$. Therefore we assume a priori $\Delta(\Psi - \Phi)/\mathcal{H}^2 = \mathcal{O}(\epsilon)$. This means that one can set $\Phi = \Psi$ everywhere except where the $\mathcal{O}(\eta^2\epsilon)$ correction is not subleading, which happens only for $\Delta\Phi$ in the ij-component. Note also that for gravitational waves χ_{ij}, time derivatives are as important as spatial derivatives, because they travel with the speed of light. Therefore we have a priori $\chi''_{ij}/\mathcal{H}^2 = \mathcal{O}(\Delta\chi_{ij}/\mathcal{H}^2) = \mathcal{O}(\epsilon^2/\eta^2) = \mathcal{O}(\epsilon)$. Taking into account all the aforementioned assumptions, that have to be checked a posteriori, the Einstein tensor takes the following form when keeping in each component only the leading orders in ϵ and η:

$$G_{00} = 3\mathcal{H}^2 + 2\Delta\Psi\,, \tag{4.2a}$$

$$G_{0i} = 2\Psi'_{,i} + 2\mathcal{H}\Psi_{,i} - \frac{1}{2}\Delta\omega_i\,, \tag{4.2b}$$

$$\begin{aligned} G_{ij} = {} & \left[\left(\mathcal{H}^2 - 2\frac{a''}{a}\right)(1-4\Psi) + 2\Psi'' + 6\mathcal{H}\Psi' + (\nabla\Psi)^2 - \Delta\left(\Psi - \Phi\right)\right]\delta_{ij} - \\ & - 2\Psi_{,i}\Psi_{,j} + \nabla_i\nabla_j\left(\Psi - \Phi\right) - \mathcal{H}(\omega_{i,j} + \omega_{j,i}) - \frac{1}{2}(\omega'_{i,j} + \omega'_{j,i}) + \\ & + \frac{1}{2}\left(\chi''_{ij} - \Delta\chi_{ij}\right)\,. \end{aligned} \tag{4.2c}$$

The following projectors

$$(\mathcal{P}_{\mathrm{L}})^{ij} = \frac{\nabla_i\nabla_j}{\Delta}\,, \qquad (\mathcal{P}_{\mathrm{V}})^{ij}_{k} = \left(\delta^j_k - \frac{\nabla_k\nabla_j}{\Delta}\right)\nabla_i\,, \tag{4.3}$$

applied to $G_{ij} = T_{ij}$ will be used in the following to derive closed equations of motion for the scalar Ψ and vector ω_i. We use units where $8\pi G = 1$ and $c = 1$.

Master equations Considering a dust fluid of density ϱ and four-velocity u_μ with energy momentum tensor $T_{\mu\nu} = \varrho u_\mu u_\nu$ one can write its ij-component in terms of the 00 and $0i$-components: $T_{ij} = T_{0i}T_{0j}/T_{00}$. One can then employ the Einstein equations $G_{\mu\nu} = T_{\mu\nu}$ to write a closed form equation for the metric

$$G_{ij} = \frac{G_{0i}G_{0j}}{G_{00}}\,, \tag{4.4}$$

thus eliminating ϱ and u_μ from the equation. The system of interest then consists of the longitudinal $(\mathcal{P}_\mathrm{L})^{ij}$ and the vector $(\mathcal{P}_\mathrm{V})^{ij}_k$ projections of Eq. (4.4) with Einstein tensor components (4.2), in which Φ and χ_{ij} drop out automatically. Assuming that the Friedmann equations of an Einstein-de Sitter universe with average density $\bar{\varrho}$ hold separately, the master system takes the form

$$\Psi'' + 3\mathcal{H}\Psi' + \frac{1}{2}(\nabla\Psi)^2 = (\mathcal{P}_\mathrm{L})^{ij}S_{ij}\,, \tag{4.5a}$$

$$\frac{1}{4}\Delta\omega_i' + \frac{1}{2}\Delta\omega_i\mathcal{H} = (\mathcal{P}_\mathrm{V})^{km}_i S_{km}\,, \tag{4.5b}$$

where we defined the source tensor $S_{ij} := \Psi_{,i}\Psi_{,j} + \frac{1}{2}G_{0i}G_{0j}/G_{00}$, whose explicit form is

$$S_{ij} = \left(\Psi_{,i}\Psi_{,j} + \frac{2}{3\mathcal{H}^2}\left\{\frac{\left[(\Psi' + \mathcal{H}\Psi)_{,i} - \frac{1}{4}\Delta\omega_i\right]\left[(\Psi' + \mathcal{H}\Psi)_{,j} - \frac{1}{4}\Delta\omega_j\right]}{1 + \frac{2}{3\mathcal{H}^2}\Delta\Psi}\right\}\right)\,. \tag{4.5c}$$

Contrary to what one might naively expect, vector perturbations are crucial in order to recover Newtonian gravity [BTW13]. We will prove this for the case of a pressureless fluid in Section 4.3.

The master system (4.5) does not contain all information present in Eq. (4.4). The remaining bits can be extracted similarly by applying

$$(\mathcal{P}_\mathrm{TT})^{km}_{ij} = \left(\delta_{im} - \frac{\nabla_i\nabla_m}{\Delta}\right)\left(\delta_{jk} - \frac{\nabla_j\nabla_k}{\Delta}\right) - \frac{1}{2}\left(\delta_{km} - \frac{\nabla_k\nabla_m}{\Delta}\right)\left(\delta_{ij} - \frac{\nabla_i\nabla_j}{\Delta}\right)\,, \tag{4.6a}$$

$$(\mathcal{P}_\mathrm{TL})^{ij} = \delta_{ij} - 3\frac{\nabla_i\nabla_j}{\Delta} \tag{4.6b}$$

to Eq. (4.4). The resulting equations determine χ_{ij} and Φ as

$$\Delta(\Psi - \Phi) = (\mathcal{P}_\mathrm{TL})^{ij}S_{ij}\,, \tag{4.7a}$$

$$\frac{1}{4}(\chi_{ij}'' - \Delta\chi_{ij}) = (\mathcal{P}_\mathrm{TT})^{km}_{ij}S_{km}\,. \tag{4.7b}$$

Since χ_{ij} and Φ do not influence the dynamics of Ψ and ω_i, we do not consider these equations in the following. The equations (4.7) can be applied to calculate nonlinear light propagation effects, like estimating nonlinear corrections to gravitational lensing and the Sachs-Wolfe effect, or the gravitational waves induced by nonlinear structure formation. All metric perturbations Ψ, Φ, ω_i

and χ_{ij} are in general generated by nonlinearities and necessary to calculate light propagation, see [RMKB96] for perturbative treatment. In [BTW13] the effect of $\boldsymbol{\omega}$ on weak gravitational lensing was estimated from $\boldsymbol{\omega}$ determined via Eq. (4.20) by measuring $\boldsymbol{\nabla}\times[(1+\delta)\boldsymbol{v}]$ in a N-body simulation.

Finally let us note that it is straightforward to include a cosmological constant by simply replacing $G_{00}\to G_{00}-\Lambda a^2$ and $G_{ij}\to G_{ij}+\Lambda a^2(1+2\Psi)\delta_{ij}$ in Eq. (4.2), see App. 4.C.

4.3 Equivalence of fluid and Einstein systems

In [BR11b] the possible equivalence of (4.5a) with $\boldsymbol{\omega}=0$ and the nonlinear Newtonian pressureless fluid equations was mentioned. However, this issue has not been investigated further nor been resolved in a conclusive manner. The goal of this section is to show that the set of Newtonian fluid equations is indeed equivalent to the Einsteinian Eqs. (4.5). As we will point out in the next section, the constraint arising from forcing $\boldsymbol{\omega}\equiv 0$, which was not taken into account in [BR11b], is incompatible with general initial conditions. In this section we therefore keep the transverse vector $\boldsymbol{\omega}$ unconstrained, apart from the original assumption that $\boldsymbol{\omega}=\mathcal{O}(\epsilon^2/\eta)$.

Fluid equations Introducing the momentum $\boldsymbol{j}=(1+\delta)\boldsymbol{v}$, the curl-free non-relativistic fluid equations (which also follow from $\nabla^\mu G_{\mu\nu}=\nabla^\mu(\varrho u_\mu u_\nu)$, with $G_{\mu\nu}$ from Eq. (4.2),[2] $\varrho=3\mathcal{H}^2(1+\delta)$, $u_0=-a$ and $u_i=av^i$ and the aforementioned assumptions) can be written as

$$\delta'+\boldsymbol{\nabla}\cdot\boldsymbol{j}=0\,, \tag{4.8a}$$

$$\boldsymbol{j}'+\mathcal{H}\boldsymbol{j}+\boldsymbol{\nabla}\cdot\left(\frac{\boldsymbol{j}\boldsymbol{j}}{1+\delta}\right)+(1+\delta)\boldsymbol{\nabla}\Psi=0\,, \tag{4.8b}$$

$$\boldsymbol{\nabla}\times\boldsymbol{v}=0\,. \tag{4.8c}$$

The Poisson equation supplements both the fluid equations and the master system

$$\delta=\frac{2}{3\mathcal{H}^2}\Delta\Psi\,. \tag{4.9}$$

Equivalence

(4.5) $\Rightarrow$ (4.8) The Euler equation (4.8b) can be derived easily from the master equation by taking the time derivative of

$$\boldsymbol{j}:=-\frac{2}{3\mathcal{H}^2}\left[\boldsymbol{\nabla}(\Psi'+\mathcal{H}\Psi)-\frac{1}{4}\Delta\boldsymbol{\omega}\right] \tag{4.10}$$

[2] Note that the Bianchi identity $\nabla^\mu G_{\mu\nu}=0$ does not hold anymore for the $G_{\mu\nu}$ with components (4.2) and ∇^μ, the covariant derivative within the ϵ,η expansion scheme, see Eqs. (A.8) of [BMR07]. However $\nabla^\mu G_{\mu\nu}=\nabla^\mu T_{\mu\nu}$, consistently expanded in ϵ and η leads to the correct Newtonian equations (4.8).

and replacing Ψ'' and $\Delta\omega'$ according to (4.5a) and (4.5b), respectively. For details see App. 4.A.1. The continuity equation (4.8a) is obtained by taking the time derivative of the Poisson equation and making use of the definition of $\boldsymbol{j}$, Eq. (4.10). Note that (4.8) is obtained with built-in condition $\nabla \times \boldsymbol{v} = 0$. This is because $\boldsymbol{\omega}$ in the Einstein system (4.5) is a second order quantity and therefore initially $\boldsymbol{v} = \boldsymbol{j}$. But the fluid equations then imply $\nabla \times \boldsymbol{v} = 0$ for all later times since the Euler equation (4.8b) for $\boldsymbol{w} := \nabla \times \boldsymbol{v}$ implies

$$\boldsymbol{w}' + \mathcal{H}\boldsymbol{w} - \nabla \times (\boldsymbol{v} \times \boldsymbol{w}) = 0\,, \tag{4.11}$$

and guarantees that if $\boldsymbol{w} = 0$ initially, it remains so. Note that the initial condition $\boldsymbol{w} = 0$ does not constrain δ and $\theta := \nabla \cdot \boldsymbol{v}$. It is also important to note that $\boldsymbol{w} = 0$ does not imply $\boldsymbol{\omega} = 0$ since

$$\boldsymbol{w} = \frac{\nabla \times \Delta\boldsymbol{\omega}}{6\mathcal{H}^2(1+\delta)} - \frac{\nabla\delta}{(1+\delta)^2} \times \boldsymbol{j}\,. \tag{4.12}$$

(4.8) $\Rightarrow$ (4.5) To derive the coupled master system (4.5) from the fluid equations (4.8), one has to define a transverse vector $\boldsymbol{\omega}$ according to (4.10). The longitudinal ∇_i/Δ and transverse part $(\delta_{ij} - \nabla_i\nabla_j/\Delta)$ of the Euler equation (4.8b) can then be used to derive (4.5a) and (4.5b), respectively with the help of (4.9) and (4.8a). For details see App. 4.A.

Remarks We would like to point out that the equivalence might break down after shell-crossing infinities $\delta \to \infty$ occur in the fluid system (4.8). These infinities are an artifact of the assumed single streaming pressureless fluid and seem to be harmless in the master system (4.5) since they simply correspond to regions where the matter source term (the curly brackets in (4.5c)) vanishes. This vanishing happens only if the numerator of the matter source remains finite at shell crossings, which might not be the case. It would be interesting to extend the framework of [BR11b] to include multi-streaming effects, which would allow to describe dark matter dynamics at even smaller scales and times after shell crossings. However, simply adding a shear term to the energy momentum tensor $T_{\mu\nu} \to \varrho u_\mu u_\nu + \sigma_{\mu\nu}$ requires either an additional dynamical equation for $\sigma_{\mu\nu}$ or to postulate $\sigma_{\mu\nu}$ to be a functional of G_{00} and G_{0i}. In Chapter 5 will show that an ansatz like this exists that allows to describe collisionless dark matter in the single- and multi-stream regime using a complex scalar field instead of perfect fluid. In App. 4.C we show how to derive the corresponding master equation in the special case where $\sigma_{\mu\nu} = p(T_{00}, T_{0i})(u_\mu u_\nu + g_{\mu\nu})$ and outline the case of shear viscosity.

One might wonder why Poisson gauge equipped with the assumptions about the metric and its derivatives only, leads exactly to the Newtonian limit. The reason is that these assumptions imply for the Einstein tensor $G_{ij} \ll G_{0i} \ll G_{00}$ and therefore via Einstein equations $T_{ij} \ll T_{0i} \ll T_{00}$, which together with small metric perturbations $\chi_{ij}, \omega_i \ll \Psi = \Phi \ll 1$ defines a Newtonian source. Therefore the η-ϵ-expansion seems to be equivalent to the post-Friedmann expansion proposed in [BTW13, TBW14].

It should be also noted that the recently described [Ram13] cosmological frame dragging effect on dust disappears in the double expansion scheme used here. Although a nonzero $\boldsymbol{\omega}$ is generated in our case, it leaves the dynamics of dust unchanged from the Newtonian case.

$\boldsymbol{\omega}$ encodes the miss-alignment of directions of the Newtonian $\nabla\delta$ and $\boldsymbol{v}$, see Eq. (4.12). This was already mentioned in [BTW13] and means that considering vanishing vector perturbations $\boldsymbol{\omega} = 0$ enforces the constraint $\nabla \times \varrho\boldsymbol{v} = 0$, which was described in [BTW13] as unphysical.

It is also interesting to note that the Newtonian system (4.8) manifestly contains only two scalar degrees of freedom δ and θ, because $\boldsymbol{w} = 0$ is a constant of motion. The fact that if $\boldsymbol{\omega} = 0$, (4.5a) contains only the two scalar degrees of freedom Ψ and Ψ' is suggestive for considering the case of $\boldsymbol{\omega} = 0$, which will be done in the next section.

4.4 Problems with $\boldsymbol{\omega_i = 0}$

The special case of vanishing vector perturbations (setting $\boldsymbol{\omega} \equiv 0$) leads to the following system of differential equations

$$\Psi'' + 3\mathcal{H}\Psi' + \frac{1}{2}(\nabla\Psi)^2 = (\mathcal{P}_{\mathrm{L}})^{ij} S_{ij}[\boldsymbol{\omega} = 0]\,, \tag{4.13a}$$

$$0 = (\mathcal{P}_{\mathrm{V}})_i^{km} S_{km}[\boldsymbol{\omega} = 0]\,, \tag{4.13b}$$

with $S_{ij}[\boldsymbol{\omega}=0]$ from Eq. (4.5c). Translating the system (4.13) into the fluid language, we observe that Eqs. (4.8) are still implied but that in addition to $\nabla\times\boldsymbol{v} = 0$ also $\nabla\times\boldsymbol{j} = 0$ is enforced during time evolution. This puts strong constraints on the initial conditions of δ and $\boldsymbol{v}$. Constraint (4.13b) is equivalent to the requirement that $\nabla\delta$ is aligned with the velocity $\boldsymbol{v}$,

$$\nabla\delta \times \boldsymbol{v} = 0\,, \tag{4.14}$$

see Eq. (4.12). While ignoring the constraint (4.13b) is inconsistent, keeping the constraint has unwanted physical consequences for the allowed initial conditions of Ψ. In [BR11b], only Eq. (4.13a) without the accompanying constraint was obtained due to a mistake in going from Eq. (2.11) to Eq. (2.12) in [BR11b].[3] The master equation Eq. (4.13a) considered in [BR11b] is equivalent to the following non-perturbative fluid-like system of equations

$$\delta' + \nabla\cdot\boldsymbol{j} = 0\,, \tag{4.15a}$$

$$\nabla\cdot\left(\boldsymbol{j}' + \mathcal{H}\boldsymbol{j} + \nabla\cdot\left(\frac{\boldsymbol{jj}}{1+\delta}\right) + (1+\delta)\nabla\Psi\right) = 0\,, \tag{4.15b}$$

$$\nabla\times\boldsymbol{j} = 0\,, \tag{4.15c}$$

see App. 4.A.2. These equations are only equivalent to the fluid equations (4.8) if $\nabla\delta\times\boldsymbol{v} = 0$. If this constraint is not satisfied, then although $\nabla\times\boldsymbol{v} = 0$ holds initially it is not conserved during time evolution.

[3] While the left hand sides of the $0i$ and ij Einstein equations, Eqs. (2.5) and (2.6) in [BR11b], were projected onto their longitudinal parts, the right hand sides were not projected. The wrong Eq. (2.5) was then used in Eq. (2.11), leading to the master equation Eq. (2.13), or our Eq. (4.13a) without the constraint (4.13b).

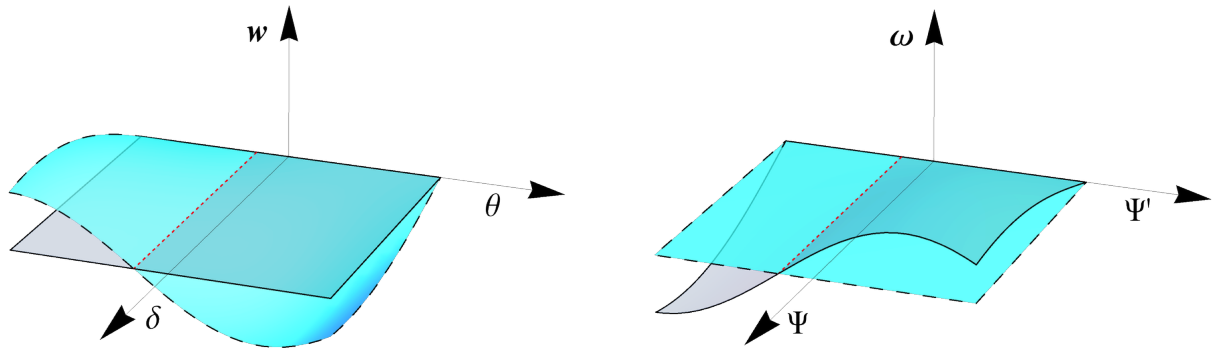

FIGURE 4.1: A sketch of the configuration space of two scalars and one transverse vector, *left*: in the basis $\delta, \theta, \boldsymbol{w}$, *right*: in the basis $\Psi, \Psi', \boldsymbol{\omega}$. The solution space with initial conditions $\boldsymbol{w} = \boldsymbol{\omega} = 0$ is indicated by the two surfaces. The surface with the continuous boundary line corresponds to the solution space of Newtonian fluid equations (4.8) or (4.5) for which $\boldsymbol{w} = 0$ holds during time evolution. The surface with dashed boundary corresponds to the solution space of (4.15) or (4.13a) for which $\boldsymbol{\omega} = 0$ holds during time evolution, discarding (4.14) or (4.13b), respectively. The dotted line – the intersection of the two planes – corresponds to the solution space of (4.13) or (4.14,4.15) in which $\boldsymbol{w} = \boldsymbol{\omega} = 0$ holds during time evolution. For instance, spherically symmetric solutions lie in this subspace.

As we will see next, the solution to Eqs. (4.15) are not a good approximation to the solution of the Newtonian fluid system Eqs. (4.8) in perturbation theory. Hence, results obtained from (4.13a), corresponding to Eq. (2.13) from [BR11b], should be reconsidered carefully using the full master system (4.13). We summarize the three approaches of describing nonlinear dust dynamics in Fig. 4.1.

Perturbation theory If one wants to solve the $\boldsymbol{\omega} = \boldsymbol{w} = 0$ system Eq. (4.13) up to order n in perturbation theory, one is forced to fine-tune $\delta_1, .., \delta_{n-1}$ and $\theta_1, ..., \theta_{n-1}$, such that the constraint is satisfied to order n. In particular, it can be easily shown that constraint (4.14) is incompatible with Gaussian initial conditions for Ψ_1 determining $\delta_1 \propto \Delta\Psi_1$ and $\boldsymbol{v}_1 \propto \nabla\Psi_1$. To this end we show that the expectation value of $|\nabla\delta_1 \times \boldsymbol{v}_1|$ is nonzero:

$$0 \neq \langle |\nabla\delta_1 \times \boldsymbol{v}_1| \rangle \tag{4.16a}$$

$$\Leftrightarrow \quad 0 \neq \langle (\nabla\delta_1)^2 (\boldsymbol{v}_1)^2 - (\nabla\delta_1 \cdot \boldsymbol{v}_1)^2 \rangle \tag{4.16b}$$

$$\Leftrightarrow \quad 0 \neq \left(\int_0^\infty k^4 P_1(k)\, dk \right) \left(\int_0^\infty P_1(p)\, dp \right) - \left(\int_0^\infty k^2 P_1(k) dk \right)^2 , \tag{4.16c}$$

where we used the definition of the linear power spectrum $\langle \delta_1(\boldsymbol{k}) \delta_1(\boldsymbol{p}) \rangle = (2\pi)^3 \delta_{\rm D}(\boldsymbol{k} + \boldsymbol{p}) P_1(k)$ and Wick's theorem.
On the other hand if one considers the $\boldsymbol{\omega} = 0$ system Eq. (4.13a) as was done in [BR11b], one obtains a wrong result for the perturbation theory kernels $F_{n\geq 3}$ defined as

$$\delta_n(\boldsymbol{p}) = \int \frac{d^3k_1}{(2\pi)^3} ... \frac{d^3k_n}{(2\pi)^3} (2\pi)^3 \delta_{\rm D}(\boldsymbol{k}_1 + ... + \boldsymbol{k}_n - \boldsymbol{p}) F_n(\boldsymbol{k}_1, ..., \boldsymbol{k}_n) \delta_1(\boldsymbol{k}_1) ... \delta_1(\boldsymbol{k}_n) \,. \tag{4.17}$$

Indeed contrary to what was claimed in [BR11b], the symmetrized perturbation kernel F_3 calculated from the master equation (4.13a), see Eqs. (3.19-20) in [BR11b] and our Appendix 4.B,

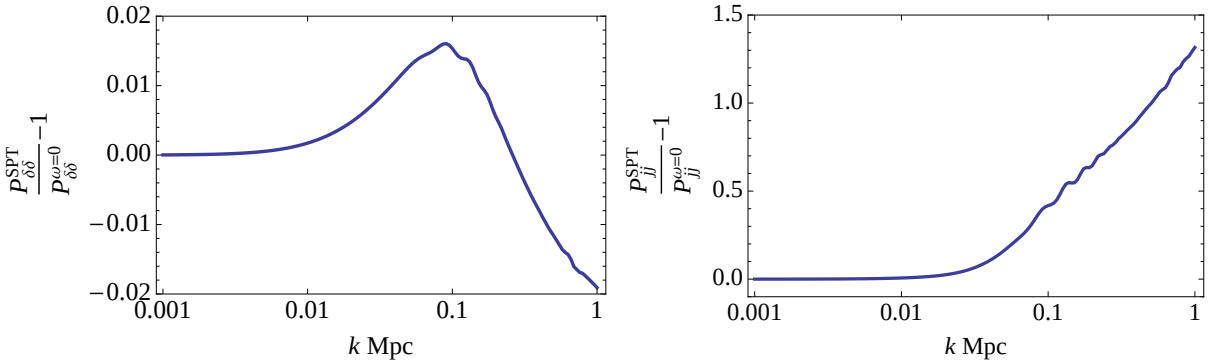

FIGURE 4.2: *Left*: Comparison between one-loop matter power spectra $P_{\delta\delta}$ obtained using (4.18a) and (4.18b), respectively. *Right*: Comparison between one-loop momentum power spectra P_{jj} obtained using (4.21). By SPT we denote results obtained from the master system (4.5) including a growing mode for ω, which we checked to be equivalent to SPT results based on (4.8). The $\omega = 0$ labeled power spectra are obtained from (4.13a), neglecting (4.13b).

is not equivalent to the symmetrized kernel F_3 found in the standard literature, see for example (A3) in [GGRW86]. Since this kernel directly affects $P_{13,\delta\delta}$, defined by $2\langle\delta_1(\boldsymbol{k})\delta_3(\boldsymbol{p})\rangle = (2\pi)^3\delta_{\rm D}(\boldsymbol{k}+\boldsymbol{p})P_{13,\delta\delta}(k)$, this leads to a discrepancy with results obtained for one-loop power spectrum $P_{\delta\delta} = P_1 + P_{22,\delta\delta} + P_{13,\delta\delta}$, using standard perturbation theory [MSS92] based on Eqs. (4.8) and Gaussian statistics

$$P^{\omega=0}_{13,\delta\delta}(k) = \frac{k^3}{252\cdot 4\pi^2}P_1(k)\int_0^\infty dr\ P_1(kr)\left\{\frac{40}{r^2} - \frac{614}{3} + \frac{440}{3}r^2 - 70r^4 + \right. \tag{4.18a}$$
$$\left. + \frac{5}{r^3}(r^2-1)^3(7r^2+4)\ln\left|\frac{1+r}{1-r}\right|\right\},$$

$$P^{\rm SPT}_{13,\delta\delta}(k) = \frac{k^3}{252\cdot 4\pi^2}P_1(k)\int_0^\infty dr\ P_1(kr)\left\{\frac{12}{r^2} - 158 + 100r^2 - 42r^4 + \right. \tag{4.18b}$$
$$\left. + \frac{3}{r^3}(r^2-1)^3(7r^2+2)\ln\left|\frac{1+r}{1-r}\right|\right\}.$$

If we had used statistics that guarantee Eq. (4.13b), both expressions would be identical.[4] Numerical results obtained on the basis of (4.18) indicate that the differences for $P_{13,\delta\delta}$ are of order unity and relevant only on large scales, which results in a quite small percent-level deviation on scales below 50 Mpc for the 1-loop matter power spectrum $P_{\delta\delta} = P_1 + P_{22,\delta\delta} + P_{13,\delta\delta}$ with

[4] See also [RR13, BHMW13] for another situation in which non-Gaussian initial conditions are required in order to fulfill a relativistic constraint.

standard values of the cosmological parameters, see Fig. 4.2, left.[5] One might therefore hope that ignoring the constraint arising from $\boldsymbol{\omega} = 0$, although inconsistent leads to physically acceptable results also in the non-perturbative regime for which Eq. (4.13b) was devised in [BR11b]. Unfortunately, the fact that the matter power spectrum in perturbation theory is close to SPT seems to be accidental, because, as we will show next, the momentum power spectrum shows much larger deviations. We therefore must conclude that the master equation Eq. (4.13b) cannot serve as an approximation to the full system Eqs. (4.5) in the nonlinear regime.

To see this, we first note that setting $\boldsymbol{\omega} = 0$ gives rise to vorticity $\boldsymbol{\nabla} \times \boldsymbol{v}_2 \neq 0$ in second order perturbation theory, unless one takes the constraint (4.13b), at second order into account. From Eq. (4.10), see also Eq. (4.39):

$$v_2^i \supset \Delta\Psi_1\Psi_{1,i} \overset{(4.13b)}{=} \frac{\nabla^i\nabla^j}{\Delta}(\Delta\Psi_1\Psi_{1,j})\,. \tag{4.19}$$

Therefore assuming $\boldsymbol{\omega} = 0$ and discarding the constraint $\boldsymbol{\nabla}\delta \times \boldsymbol{v} = 0$ introduces not only deviations in the matter power spectrum at third order but also a curl in the velocity field in second order perturbation theory. This curl has a large impact on the momentum power spectrum, see Fig. 4.2, right. The momentum $\boldsymbol{j}$, (4.10) can be rewritten with the help of the Poisson equation as

$$\boldsymbol{j} = -\frac{\boldsymbol{\nabla}\delta'}{\Delta} + \frac{1}{6\mathcal{H}^2}\Delta\boldsymbol{\omega}. \tag{4.20}$$

The momentum power spectrum is defined via $\langle \boldsymbol{j}(\boldsymbol{k}) \cdot \boldsymbol{j}(\boldsymbol{p})\rangle = (2\pi)^3\delta_{\mathrm{D}}(\boldsymbol{k}+\boldsymbol{p})P_{jj}(k)$ and takes the following form in second order perturbation theory

$$P_{jj}^{\omega=0}(k) = \frac{\mathcal{H}^2}{k^2}\left(P_1(k) + 4P_{22,\delta\delta}(k) + 3P_{13,\delta\delta}^{\omega=0}(k)\right) \tag{4.21a}$$

$$P_{jj}^{\mathrm{SPT}}(k) = \frac{\mathcal{H}^2}{k^2}\left(P_1(k) + 4P_{22,\delta\delta}(k) + 3P_{13,\delta\delta}^{\mathrm{SPT}}(k)\right) + P_{22,\omega\omega}^{\mathrm{SPT}}(k) \tag{4.21b}$$

$$P_{22,\omega\omega}^{\mathrm{SPT}}(k) = \frac{\mathcal{H}^2 k}{2\cdot 4\pi^2}\int_0^\infty dr \int_{-1}^1 dx\; P_1(k\sqrt{1-2rx+r^2})P_1(kr)\frac{(1-x^2)(1-2rx)^2}{(1-2rx+r^2)^2}\,. \tag{4.21c}$$

Note that we are focusing here on momentum instead of the usual velocity power spectrum, because the 1-loop velocity power spectrum in case of $\boldsymbol{\omega} = 0$ suffers from a UV divergence, see App. 4.B.3. This divergence is another hint that the system of fluid-like equations (4.15) is unphysical.

4.5 Conclusion

The double expansion in small scales (η) and the small potentials (ϵ) of the Einstein equations with a dust fluid contains the Newtonian fluid equations (4.8) in form of the master equations

[5] The expression for $P_{22,\delta\delta}$ is the same in the two cases. See App. 4.B.2.

(4.5), if one assumes that metric vector perturbations are present and of order $\boldsymbol{\omega} = \mathcal{O}(\epsilon^2/\eta)$. Additionally, this scheme also predicts the $\mathcal{O}(\epsilon)$ quantities $\Delta(\Psi - \Phi)$, and $\Delta\chi_{ij}$, corresponding to the slip and tensor perturbations. Although they are not relevant for the dynamics of the dust fluid itself, they extend Newtonian gravity to consistently include effects of light propagation, like nonlinear contributions to gravitational lensing or the Sachs-Wolfe effect, and gravitational waves. Closely related to this work is [BTW13], which is based on a post-Friedmann expansion of the small metric perturbations in powers of c^{-1} in Poisson gauge, which for the dust case considered here seems to be equivalent to the ϵ-η-expansion. In [BTW13] the vector $\boldsymbol{\omega}$ was measured in a Newtonian N-body simulation and the effect on the weak lensing convergence power spectrum was estimated. They were found to be negligible but still much larger than expected from perturbation theory. With the same methods also $\Delta(\Psi - \Phi)$ and $\Delta\chi_{ij}$ could be obtained and their effect on lensing estimated.

We showed that only inclusion of vector perturbations renders the master (4.5) and fluid systems (4.8) with standard initial conditions equivalent. Forcing $\boldsymbol{\omega} \equiv 0$, significantly truncates the allowed space of initial conditions. In particular inflationary initial conditions where the gravitational potential Ψ is a Gaussian random field are excluded. Ignoring this constraint in (4.13), as was effectively done in [BR11b], results in non-standard fluid-like equations (4.15) and deviations in perturbation theory that become manifest at second order for velocity and third order for the density perturbations. The 1-loop momentum power spectrum shows 50% deviations at 10 Mpc scales compared to SPT, while the 1-loop velocity power spectrum is not even converging, suggesting the unphysical nature of the master equation studied in [BR11b].

The coupled nonlinear equations of motion for metric perturbations $\boldsymbol{\omega}$ and Ψ, Eq. (4.5), should be used as a starting point for investigations following the route of [BR11b] where Eq. (4.13a) was used. We established that our result shares the remarkable feature found by [BR11b] that the matter source term, the curly brackets in (4.5c), are switched off once the density contrast δ becomes large. Therefore the master system (4.5) for Ψ and $\boldsymbol{\omega}$ will prove useful in understanding the quasistatic dynamics and decay of the Newtonian potential Ψ in nonlinear structure formation.

In the context of linear relativistic perturbation theory – linear in ϵ, non-perturbative in η – we found in Chapter 3 that the relativistic dynamics of dust can be mapped to Newtonian dynamics and that therefore all relativistic information is encoded and can be extracted from Newtonian simulations or other Newtonian techniques at the linear level.

In this chapter we considered the "opposite" regime where the density contrast can become nonlinear but scales are much smaller than the horizon. Fortunately these two regimes, the large and linear as well as small and nonlinear scales cover all situations relevant for cosmology and in both cases Newtonian gravity does accurately describe the dynamics of a dust fluid. This means that we can safely use Newtonian gravity to model linear and nonlinear structure formation while the strongest relativistic effects arise through light propagation when dark matter is observed (indirectly through galaxy surveys) with straightforward Newtonian interpretation as redshift space distortion and gravitational lensing.

In the next chapter we will consider the nonlinear (and small scale) regime in more detail and point out the shortcomings of the dust model and how a complex scalar field supersedes the dust fluid in modelling selfgravitating collisionless cold dark matter.

Appendix 4

4.A Explicit calculation of the equivalence

4.A.1 between (4.8) and (4.5)

The derivative of $\boldsymbol{j} = -2/(3\mathcal{H}^2)[\boldsymbol{\nabla}(\Psi' + \mathcal{H}\Psi) - \Delta\boldsymbol{\omega}/4]$ is given by

$$j^{i\prime} = \mathcal{H} j^i - \frac{2}{3\mathcal{H}^2}\left[(\Psi'' + \mathcal{H}\Psi' - \frac{1}{2}\mathcal{H}^2\Psi)_{,i} - \frac{1}{4}\Delta\omega_i'\right] \tag{4.22}$$

We now write the master equation in terms of $\boldsymbol{j}$ and $\delta = 2/(3\mathcal{H}^2)\,\Delta\Psi$ and take the gradient of the Ψ equation (4.5a)

$$(\Psi'' + 3\mathcal{H}\Psi' + \frac{1}{2}(\nabla\Psi)^2)_{,i} = \frac{\nabla_k\nabla_m}{\nabla^2}\nabla_i\left(\Psi_{,k}\Psi_{,m} + \frac{3\mathcal{H}^2}{2}\frac{j^m j^k}{1+\delta}\right) \tag{4.23a}$$

$$\frac{1}{4}\Delta\omega_i' + \frac{1}{2}\Delta\omega_i\mathcal{H} = \left(\frac{\nabla_i\nabla_m}{\Delta} - \delta_i^m\right)\nabla_k\left(\Psi_{,k}\Psi_{,m} + \frac{3\mathcal{H}^2}{2}\frac{j^k j^m}{1+\delta}\right) \tag{4.23b}$$

and subtract the second from the first equation

$$(\Psi'' + 3\mathcal{H}\Psi' + \frac{1}{2}(\nabla\Psi)^2)_{,i} - \frac{1}{4}\Delta\omega_i' - \frac{1}{2}\Delta\omega_i\mathcal{H} = \left(\Psi_{,k}\Psi_{,i} + \frac{3\mathcal{H}^2}{2}\frac{j^k j^i}{1+\delta}\right)_{,k} \tag{4.24}$$

We now have an expression for the square bracket in Eq. (4.22)

$$\begin{aligned}\left[(\Psi'' + \mathcal{H}\Psi' - \frac{1}{2}\mathcal{H}^2\Psi)_{,i} - \frac{1}{4}\Delta\omega_i'\right] &= -2\mathcal{H}\Psi_{,i}' - \frac{1}{2}\mathcal{H}^2\Psi_{,i} + \Delta\Psi\Psi_{,i} + \frac{1}{2}\mathcal{H}\Delta\omega_i + \frac{3\mathcal{H}^2}{2}\left(\frac{j^k j^i}{1+\delta}\right)_{,k} \\ &= \frac{3\mathcal{H}^2}{2}\left(2\mathcal{H} j^i + (1+\delta)\Psi_{,i} + \left(\frac{j^k j^i}{1+\delta}\right)_{,k}\right),\end{aligned} \tag{4.25}$$

where we used in the second line the Poisson equation and the definition of $\boldsymbol{j}$. Equation (4.22) then becomes

$$j^{i\prime} = -\mathcal{H} j^i - (1+\delta)\Psi_{,i} - \left(\frac{j^k j^i}{1+\delta}\right)_{,k}, \tag{4.26}$$

which is just the Euler equation (4.8b). Of course it is only the Euler equation (usually written in terms of $\boldsymbol{v} = \boldsymbol{j}/(1+\delta)$) if also the continuity equation $\delta' = -\boldsymbol{\nabla}\cdot\boldsymbol{j}$ holds. In order to show the other direction we can simply follow all the steps backwards. We start with (4.26) and insert the definition of $\boldsymbol{\omega}$, Eq. (4.10), which from the Newtonian point of view is just the curl part of $\boldsymbol{j}$, while the longitudinal part is fixed by the continuity and Poisson equations, see also Eq. (4.20). Therefore we can derive Eq. (4.25) with this definition of $\boldsymbol{\omega}$. After reversing the algebraic manipulations from (4.25) to (4.24), we only need to project onto the longitudinal and transverse parts to obtain the master system (4.23), which is equivalent to (4.5a) if we assume vanishing boundary conditions. Note that the equivalence only holds if we assume that a satisfies the same Friedmann equations in both systems, which corresponds to the assumption of vanishing backreaction.

4.A.2 between (4.15) and (4.13a)

The derivative of $\boldsymbol{j} = -2/(3\mathcal{H}^2)\boldsymbol{\nabla}(\Psi' + \mathcal{H}\Psi)$ is given by

$$j^{i\prime} = \mathcal{H} j^i - \frac{2}{3\mathcal{H}^2}\left[(\Psi'' + \mathcal{H}\Psi' - \frac{1}{2}\mathcal{H}^2\Psi)_{,i}\right] \tag{4.27}$$

We now write the master equation in terms of $\boldsymbol{j}$ and δ and take the gradient of the Ψ equation (4.13a)

$$(\Psi'' + 3\mathcal{H}\Psi' + \frac{1}{2}(\nabla\Psi)^2)_{,i} = \frac{\nabla_k\nabla_m}{\nabla^2}\nabla_i\left(\Psi_{,k}\Psi_{,m} + \frac{3\mathcal{H}^2}{2}\frac{j^k j^m}{1+\delta}\right), \tag{4.28}$$

which can be used to eliminate Ψ'' in Eq. (4.27). Using the definition of $\boldsymbol{j}$, we get

$$j^{i\prime} = -\mathcal{H} j^i - \Psi_{,i} - \frac{2}{3\mathcal{H}^2}\nabla_i\left(-\frac{1}{2}(\nabla\Psi)^2 + \frac{\nabla_k\nabla_m}{\Delta}\left(\Psi_{,k}\Psi_{,m} + \frac{3\mathcal{H}^2}{2}\frac{j^k j^m}{1+\delta}\right)\right). \tag{4.29}$$

Using again the definition of $\boldsymbol{j}$ and the Poisson equation this can be simplified to

$$j^{i\prime} = -\mathcal{H} j^i - \frac{\nabla_i\nabla_j}{\Delta}\left[(1+\delta)\Psi_{,j} + \left(\frac{j^k j^j}{1+\delta}\right)_{,k}\right], \tag{4.30}$$

which is equivalent to

$$\boldsymbol{\nabla}\cdot\left(\boldsymbol{j}' + \mathcal{H}\boldsymbol{j} + \boldsymbol{\nabla}\cdot\left(\frac{\boldsymbol{j}\boldsymbol{j}}{1+\delta}\right) + (1+\delta)\boldsymbol{\nabla}\Psi\right) = 0\,, \tag{4.31a}$$

$$\boldsymbol{\nabla}\times\boldsymbol{j} = 0\,. \tag{4.31b}$$

Since all steps can be reversed we have shown the equivalence between the master equation of [BR11b], our (4.13a) and the fluid like equation (4.15).

4.B Perturbation theory

We follow [BR11b] to expand the master system Eq. (4.5)

$$\Psi'' + 3\mathcal{H}\Psi' - 2\left(\mathcal{H}^2 - 2\frac{a''}{a}\right)\Psi \tag{4.32a}$$
$$= -\frac{1}{2}(\nabla\Psi)^2 + \frac{\nabla^i\nabla^j}{\Delta}\left(\Psi_{,i}\Psi_{,j} + \frac{2}{3\mathcal{H}^2}\left\{\frac{\left[(\Psi' + \mathcal{H}\Psi)_{,i} - \frac{1}{4}\Delta\omega_i\right]\left[(\Psi' + \mathcal{H}\Psi)_{,j} - \frac{1}{4}\Delta\omega_j\right]}{1 + \frac{2}{3\mathcal{H}^2}\Delta\Psi}\right\}\right),$$

$$\frac{1}{4}\Delta\omega_i' + \frac{1}{2}\Delta\omega_i\mathcal{H} \tag{4.32b}$$
$$= \left(\frac{\nabla^i\nabla^m}{\Delta} - \delta_i^m\right)\nabla^k\left(\Psi_{,k}\Psi_{,m} + \frac{2}{3\mathcal{H}^2}\left\{\frac{\left[(\Psi' + \mathcal{H}\Psi)_{,k} - \frac{1}{4}\Delta\omega_k\right]\left[(\Psi' + \mathcal{H}\Psi)_{,m} - \frac{1}{4}\Delta\omega_m\right]}{1 + \frac{2}{3\mathcal{H}^2}\Delta\Psi}\right\}\right)$$

perturbatively as in Eqs. (3.1)-(3.20) of [BR11b]. For convenience, this is done for the case of matter domination. We do this in order make it easier for the reader of [BR11b] to understand where and how perturbative solutions presented in [BR11b] are modified through the inclusion of ω. The underscored equation numbers below correspond to equations in [BR11b]. Since we have already proven the nonperturbative equivalence of the master system (4.32) and the standard Newtonian dust fluid system (4.8), it does not come as a surprise that a perturbative expansion of (4.32) agrees with standard perturbation theory (SPT), based on (4.8), see for instance [GGRW86]. The Friedmann equations and background quantities read

$$3\mathcal{H}^2 = a^2\bar{\varrho}, \quad \left(\mathcal{H}^2 - 2\frac{a''}{a}\right) = 0, \quad \bar{\varrho} = \varrho_0\frac{a_0^3}{a^3} \quad \Rightarrow \quad a = \tau^2, \quad \mathcal{H} = \frac{2}{\tau}. \tag{4.33}$$

Ψ and ω are expanded up to third order employing that ω is a second order quantity

$$\begin{aligned}\Psi &= \Psi_1 + \Psi_2 + \Psi_3 + \dots,\\ \omega_i &= \quad\ \omega_i^{(2)} + \omega_i^{(3)} + \dots.\end{aligned} \tag{4.34}$$

The standard perturbative expansion does not treat gradients in a special way. Therefore we have to remember that although we estimated in the non-perturbative case, for instance, that $\Delta\omega = \mathcal{O}(\epsilon^2/\eta^3) = \mathcal{O}(\epsilon/\eta)$ and $\Delta\Psi/\mathcal{H}^2 = \mathcal{O}(\epsilon/\eta^2) \simeq 1$, we have now $\Delta\omega = \mathcal{O}(\epsilon^2)$ and $\Delta\Psi/\mathcal{H}^2 = \mathcal{O}(\epsilon)$ to leading order in Eqs. (4.34), where order ϵ^n is denoted by the sub- and superscript of Ψ_n and $\omega_i^{(n)}$, respectively. Plugging expansion (4.34) into Eqs. (4.32) and demanding that the equations are fulfilled order by order, one can solve Eq. (4.32) iteratively. At order n only metric perturbations Ψ_m, $\omega_i^{(m)}$ with $m < n$ appear on the right hand side of Eq. (4.32). Therefore considering the system (4.32) at order n, all the Ψ_m and $\omega_i^{(m)}$ can be replaced by the lower order solutions obtained a step earlier. From the solution for Ψ and ω the density contrast δ and the velocity v^i are obtained by perturbatively expanding the 00 and $0i$ Einstein equation:

$$\delta = \frac{2}{3\mathcal{H}^2}\Delta\Psi, \qquad v = -\frac{2}{3\mathcal{H}^2}\frac{\nabla(\Psi' + \mathcal{H}\Psi) - \frac{1}{4}\Delta\omega}{1 + \delta}. \tag{4.35}$$

4.B.1 First order

We obtain neglecting the decaying mode

$$\Psi_1'' + 3\mathcal{H}\Psi_1' = 0 \quad \Rightarrow \quad \Psi_1(\boldsymbol{x},\tau) = \Psi_1(\boldsymbol{x},\tau_{\rm ini}) =: \Psi_L(\boldsymbol{x})\,. \tag{4.36}$$

There is no $\mathcal{O}(\epsilon)$ contribution to $\boldsymbol{\omega}$. The solutions for δ_1 and the peculiar velocity $\boldsymbol{v}_1$ are

$$\delta_1 = \frac{\tau^2}{6}\Delta\Psi_L =: \delta_L\,, \tag{4.37}$$

$$\boldsymbol{v}_1 = -\frac{2}{3\mathcal{H}^2}\boldsymbol{\nabla}(\Psi_1' + \mathcal{H}\Psi_1) = -\frac{\tau}{3}\boldsymbol{\nabla}\Psi_L\,, \tag{4.38}$$

which are the SPT results in first order.

4.B.2 Second order

To obtain the second order contribution we insert Ψ_1 into the right hand side of the Ψ-equation

$$\Psi_2'' + 3\mathcal{H}\Psi_2' = \frac{5}{3}\frac{\nabla_i\nabla_j}{\Delta}(\Psi_{L,i}\Psi_{L,j}) - \frac{1}{2}(\Psi_{L,i})^2\,, \tag{3.6}$$

in which there is again no $\boldsymbol{\omega}$, and separate the time dependence from the spatial one

$$\Delta\Psi_2 = \frac{\tau^2}{14}\left[\frac{5}{3}(\Delta\Psi_L)^2 + \frac{7}{3}\Delta\Psi_{L,i}\Psi_{L,i} + \frac{2}{3}(\Psi_{L,ij})^2\right]. \tag{3.11}$$

The density contrast is related to the Newtonian potential

$$\delta_2(\boldsymbol{p}_3,\tau) = -\frac{\tau^2}{6}p_3^2\Psi_2(\boldsymbol{p}_3,\tau) = \int\frac{d^3p_1d^3p_2}{(2\pi)^3}F_2(\boldsymbol{p}_1,\boldsymbol{p}_2)\delta_D(\boldsymbol{p}_3-\boldsymbol{p}_1-\boldsymbol{p}_2)\delta_L(\boldsymbol{p}_1,\tau)\delta_L(\boldsymbol{p}_2,\tau)\,,$$

$$F_2(\boldsymbol{p}_1,\boldsymbol{p}_2) = \frac{5}{7} + \frac{1}{2}(\boldsymbol{p}_1\cdot\boldsymbol{p}_2)\frac{p_1^2+p_2^2}{p_1^2p_2^2} + \frac{2}{7}\frac{(\boldsymbol{p}_1\cdot\boldsymbol{p}_2)^2}{p_1^2p_2^2}\,. \tag{3.12}$$

where we obtained F_2 by reading off the coefficients and gradient structure from (3.11), used $\delta = -\tau^2k^2\Psi/6$ and symmetrized the second term. The velocity is obtained from

$$v_2^i = -\frac{2}{3\mathcal{H}^2}(\Psi_2' + \Psi_2\mathcal{H})_{,i} + \frac{4}{9\mathcal{H}^4}(\Psi_1' + \Psi_1\mathcal{H})_{,i}\Delta\Psi_1 + \frac{1}{6\mathcal{H}^2}\Delta\omega_i^{(2)}\,, \tag{4.39}$$

with divergence $\theta = \boldsymbol{\nabla}\cdot\boldsymbol{v}$ given by

$$-\theta_2 = \delta_2' + \boldsymbol{\nabla}\cdot(\delta_1\boldsymbol{v}_1)\,, \tag{4.40}$$

in which the $\Delta\omega_i^{(2)}$ drops out. Using the linear solution and δ_2 we obtain its Fourier transform

$$\begin{aligned}-\frac{\theta_2(\boldsymbol{p}_3,\tau)}{\mathcal{H}} &= \mathcal{F}\left[2\delta_2 - \delta_L^2 - \boldsymbol{\nabla}\delta_L\cdot\frac{\boldsymbol{\nabla}\delta_L}{\Delta}\right](\boldsymbol{p}_3)\\ &= \int\frac{d^3p_1d^3p_2}{(2\pi)^3}G_2(\boldsymbol{p}_1,\boldsymbol{p}_2)\delta_D(\boldsymbol{p}_3-\boldsymbol{p}_1-\boldsymbol{p}_2)\delta_L(\boldsymbol{p}_1,\tau)\delta_L(\boldsymbol{p}_2,\tau)\,,\end{aligned} \tag{4.41}$$

$$G_2(\boldsymbol{p}_1,\boldsymbol{p}_2) = \frac{3}{7} + \frac{1}{2}(\boldsymbol{p}_1\cdot\boldsymbol{p}_2)\frac{p_1^2+p_2^2}{p_1^2p_2^2} + \frac{4}{7}\frac{(\boldsymbol{p}_1\cdot\boldsymbol{p}_2)^2}{p_1^2p_2^2}\,. \tag{3.15}$$

We see that in the derivation of δ_2 and θ_2 no $\boldsymbol{\omega}$ contributed, such that one obtains the SPT result for F_2 and G_2 even in the case where one sets to zero vector perturbations. This can be also understood from the fluid-like system (4.15), equivalent to the master equation (4.32a) with $\boldsymbol{\omega} = 0$ and neglecting (4.32b). The modified Euler equation (4.15b)

$$\nabla_i \left[(1+\delta)\mathrm{Euler}^i\right] = 0\,, \qquad \mathrm{Euler}^i := v^{i\prime} + \mathcal{H}v^i + v^i_{,j}v^j + \Psi_{,i}\,, \tag{4.42}$$

at first order $\nabla_i \left(\mathrm{Euler}^i_1\right) = 0$ is simply the Bernoulli equation and therefore equivalent to (4.8b) in case of vanishing curl of $\boldsymbol{v}$

$$\mathrm{Euler}^i = 0 \quad \overset{\boldsymbol{\nabla}\times\boldsymbol{v}=0}{\Leftrightarrow} \quad \nabla_i \mathrm{Euler}^i = 0\,. \tag{4.43}$$

At second order, the modified Euler equation (4.15b) takes the form

$$\nabla_i \left(\mathrm{Euler}^i_2\right) = \nabla_i \left(\delta_1 \mathrm{Euler}^i_1\right)\,, \tag{4.44}$$

which, upon using the 1st order solution, simplifies to

$$\nabla_i \left(\mathrm{Euler}^i_2\right) = 0\,. \tag{4.45}$$

Therefore θ_2 is not modified, even though v^i_2 with $\boldsymbol{\omega} = 0$ is not curl-free and does not solve $\mathrm{Euler}^i_2 = 0$; it solves only (4.45). The v^i_2 including $\boldsymbol{\omega}$, (4.39) does solve $\mathrm{Euler}^i_2 = 0$ and is curl-free.

To show this, let us calculate $\omega^{(2)}_i$ and the curl part of v^i_2. At second order in perturbation theory we can neglect ω_i on the right hand side of (4.32b) since they are always multiplied by Ψ and therefore contribute to higher orders only. Using a growing mode ansatz for the time dependence we find $\omega^{(n)}_i(\boldsymbol{x},\tau) = \tau^{(n-2)+1}\tilde{\omega}^{(n)}_i(\boldsymbol{x})$ for $n \geq 2$, such that we obtain at second order

$$\Delta\omega^{(2)}_i = \frac{8}{3\mathcal{H}}\left(\frac{\nabla^i\nabla^m}{\Delta} - \delta^m_i\right)\nabla^k(\Psi_{1,k}\Psi_{1,m})\,. \tag{4.46}$$

In Fourier space we can write down the kernel Ω^i_2 for

$$\begin{aligned} i\frac{\widetilde{\Delta\omega^{(2)}_i}(\boldsymbol{p}_3,\tau)}{6\mathcal{H}^3} &= i\mathcal{F}\left[\left(\frac{\nabla^i\nabla^m}{\Delta} - \delta^m_i\right)\nabla^k\left(\frac{\delta_{L,k}}{\Delta}\frac{\delta_{L,m}}{\Delta}\right)\right](\boldsymbol{p}_3) \\ &= \int \frac{d^3p_1 d^3p_2}{(2\pi)^3}\Omega^i_2(\boldsymbol{p}_1,\boldsymbol{p}_2)\delta_D(\boldsymbol{p}_3-\boldsymbol{p}_1-\boldsymbol{p}_2)\delta_L(\boldsymbol{p}_1,\tau)\delta_L(\boldsymbol{p}_2,\tau)\,, \end{aligned} \tag{4.47}$$

$$\Omega^i_2(\boldsymbol{p}_1,\boldsymbol{p}_2) = \left(\frac{(\boldsymbol{p}_1+\boldsymbol{p}_2)^i(\boldsymbol{p}_1+\boldsymbol{p}_2)^m}{(\boldsymbol{p}_1+\boldsymbol{p}_2)^2} - \delta^m_i\right)(\boldsymbol{p}_1+\boldsymbol{p}_2)\cdot\frac{\boldsymbol{p}_1}{p_1^2}\frac{p_2^m}{p_2^2}\,. \tag{4.48}$$

The solution for the velocity v^i_2 is now curl-free, $(\delta^j_i - \nabla^i\nabla^j/\Delta)v^j_2 = 0$. To show this, we expand the $0i$ equation

$$v^i = \frac{-2(\Psi' + \Psi\mathcal{H})_{,i} + \frac{1}{2}\Delta\omega_i}{3\mathcal{H}^2 + 2\Delta\Psi} \tag{4.49}$$

to calculate the vector part of

$$v_2^i = -\frac{2}{3\mathcal{H}^2}(\Psi_2' + \Psi_2\mathcal{H})_{,i} + \frac{4}{9\mathcal{H}^4}(\Psi_1' + \Psi_1\mathcal{H})_{,i}\Delta\Psi_1 + \frac{1}{6\mathcal{H}^2}\Delta\omega_i^{(2)} \tag{4.50}$$

using the transverse projector and the second order solution for $\omega_i^{(2)}$, Eq. (4.46). The simple calculation

$$\left(\delta_i^j - \frac{\nabla^i\nabla^j}{\Delta}\right)v_2^j = \frac{4}{9\mathcal{H}^3}\left(\frac{\nabla^i\nabla^m}{\Delta} - \delta_i^m\right)(\Psi_{1,k}\Psi_{1,mk}) \tag{4.51}$$

$$= \frac{4}{9\mathcal{H}^3}\left(\frac{\nabla^i\nabla^m}{\Delta} - \delta_i^m\right)\frac{1}{2}(\nabla\Psi)^2_{,m} = 0 \tag{4.52}$$

shows that $\nabla \times \boldsymbol{v}_2 = 0$ and therefore v_2^i, including $\boldsymbol{\omega}$, is a solution to $\text{Euler}_2^i = 0$.

4.B.3 Third order

At third order in perturbation theory, $\boldsymbol{\omega}$ will show up in F_3 and G_3. Therefore, contrary to claims in [BR11b], perturbation theory based on $\boldsymbol{\omega} = 0$ is not equivalent to SPT. We will only consider the Ψ-equation, because at order $n = 3$ only $\omega_i^{(2)}$ will be necessary to obtain F_3 and G_3. Taking into account that $\Psi_2' = \mathcal{H}\Psi_2$ we obtain

$$\Psi_3'' + 3\mathcal{H}\Psi_3' = -\Psi_{L,i}\Psi_{2,i} + \frac{14}{3}\frac{\nabla_i\nabla_j}{\Delta}(\Psi_{L,i}\Psi_{2,j}) - \frac{4}{9\mathcal{H}^2}\frac{\nabla_i\nabla_j}{\Delta}\left(\Psi_{L,i}\Psi_{L,j}\Delta\Psi_L\right) - \tag{3.16}$$
$$- \frac{1}{3\mathcal{H}}\frac{\nabla_i\nabla_j}{\Delta}\left(\Psi_{L,i}\Delta\omega_j^{(2)}\right),$$

where the second line is not present in Eq. 3.16 of [BR11b]. One can separate the time dependence from the spatial one and switch to Fourier space and use that a product in real space is a convolution in Fourier space. In addition we use that $\delta = -\tau^2 k^2\Psi/6$ and insert the expression for Ψ_2 and $\omega_i^{(2)}$ to obtain

$$\delta_3(\boldsymbol{p}_4, \tau) = -\frac{\tau^2}{6}p_4^2\Psi_3(\boldsymbol{p}_4, \tau) \tag{3.20}$$
$$= \int \frac{d^3p_1 d^3p_2 d^3p_3}{(2\pi)^6}F_3(\boldsymbol{p}_1, \boldsymbol{p}_2, \boldsymbol{p}_3)\delta_D(\boldsymbol{p}_4 - \boldsymbol{p}_1 - \boldsymbol{p}_2 - \boldsymbol{p}_3)\delta_L(\boldsymbol{p}_1)\delta_L(\boldsymbol{p}_2)\delta_L(\boldsymbol{p}_3)\,.$$

The $F_3 = F_3^{(1)} + F_3^{(2)} + F_3^{(3)} + F_3^{(4)}$ can be decomposed into 4 parts of Eq. (3.16), of which only the first 3 survive for $\omega = 0$. In the following expressions $\boldsymbol{p}_4 = \boldsymbol{p}_1 + \boldsymbol{p}_2 + \boldsymbol{p}_3$.

$$F_3^{(1)} = -\frac{1}{6}\frac{\boldsymbol{p}_1\cdot(\boldsymbol{p}_2+\boldsymbol{p}_3)\,p_4^2}{p_1^2|\boldsymbol{p}_2+\boldsymbol{p}_3|^2}F_2(\boldsymbol{p}_2,\boldsymbol{p}_3) \tag{3.20a}$$
$$= -\frac{1}{14}\frac{\boldsymbol{p}_1\cdot(\boldsymbol{p}_2+\boldsymbol{p}_3)\,p_4^2}{p_1^2p_2^2p_3^2}\left\{\frac{5}{3}\frac{(\boldsymbol{p}_2+\boldsymbol{p}_3)\cdot\boldsymbol{p}_2\;(\boldsymbol{p}_2+\boldsymbol{p}_3)\cdot\boldsymbol{p}_3}{|\boldsymbol{p}_2+\boldsymbol{p}_3|^2} - \frac{1}{2}(\boldsymbol{p}_2\cdot\boldsymbol{p}_3)\right\},$$

$$F_3^{(2)} = \frac{7}{9}\frac{(\boldsymbol{p}_4\cdot\boldsymbol{p}_1)[\boldsymbol{p}_4\cdot(\boldsymbol{p}_2+\boldsymbol{p}_3)]}{p_1^2|\boldsymbol{p}_2+\boldsymbol{p}_3|^2}F_2(\boldsymbol{p}_2,\boldsymbol{p}_3) \tag{3.20b}$$
$$= \frac{1}{3}\frac{(\boldsymbol{p}_4\cdot\boldsymbol{p}_1)[\boldsymbol{p}_4\cdot(\boldsymbol{p}_2+\boldsymbol{p}_3)]}{p_1^2p_2^2p_3^2}\left\{\frac{5}{3}\frac{(\boldsymbol{p}_2+\boldsymbol{p}_3)\cdot\boldsymbol{p}_2\;(\boldsymbol{p}_2+\boldsymbol{p}_3)\cdot\boldsymbol{p}_3}{|\boldsymbol{p}_2+\boldsymbol{p}_3|^2} - \frac{1}{2}(\boldsymbol{p}_2\cdot\boldsymbol{p}_3)\right\},$$

$$F_3^{(3)} = -\frac{1}{9}\frac{(\boldsymbol{p}_4\cdot\boldsymbol{p}_1)(\boldsymbol{p}_4\cdot\boldsymbol{p}_2)p_3^2}{p_1^2p_2^2p_3^2}, \tag{3.20c}$$

$$F_3^{(4)} = -\frac{2}{9}\frac{\boldsymbol{p}_4\cdot\boldsymbol{p}_1}{p_1^2p_2^2p_3^2}p_4^j\left(\frac{(\boldsymbol{p}_2+\boldsymbol{p}_3)^j(\boldsymbol{p}_2+\boldsymbol{p}_3)^m}{|\boldsymbol{p}_2+\boldsymbol{p}_3|^2} - \delta_j^m\right)p_3^m(\boldsymbol{p}_2+\boldsymbol{p}_3)\cdot\boldsymbol{p}_2\,. \tag{3.20d}$$

In the main text we denoted the power spectrum calculated from $F_3^{\omega=0} = F_3^{(1)} + F_3^{(2)} + F_3^{(3)}$ (the F_3 of [BR11b]) by $P^{\omega=0}$. The power spectrum calculated from $F_3 = F_3^{(1)} + F_3^{(2)} + F_3^{(3)} + F_3^{(4)}$ was denoted by P^{SPT}. Since the expression for δ_3 only depends on the symmetrized part of F_3, denoted by F_3^{sym}, one must use F_3^{sym} in the power spectrum. The F_3^{sym} then has to be compared to the symmetrized versions from the literature in order to verify that our F_3 really coincides with SPT. We did this in *Mathematica* and checked against the formulas provided in [GGRW86] and [JB94]. We also explicitly show in this file the difference between the symmetrized $F_3^{\omega=0}$ and F_3. The *Mathematica* notebook is enclosed in the arXiv source file for this document [KUH14].

In the following we won't need the vector part of $\boldsymbol{v}_3$, since we will only require $\boldsymbol{\theta}_3$ for the velocity power spectrum at 1-loop order. We start with the $0j$-Einstein equation

$$v^i(1+\delta) = -\frac{2}{3\mathcal{H}^2}\left((\Psi' + \Psi\mathcal{H})_{,i} - \tfrac{1}{4}\Delta\omega_i\right) \tag{4.53}$$

expand to third order and take the divergence

$$-\theta_3 = 3\mathcal{H}\delta_3 + \boldsymbol{\nabla}\cdot(\boldsymbol{v}_2\delta_1) + \boldsymbol{\nabla}\cdot(\boldsymbol{v}_1\delta_2) \tag{4.54}$$

If δ_3 and $\boldsymbol{v}_2$ take their SPT forms also θ_3 will coincide with SPT, see for instance Eq. (6b) of [GGRW86]. Therefore in the case of dynamical $\boldsymbol{\omega}$ we find $G_3 = G_3^{\mathrm{SPT}}$. In the case where we set $\boldsymbol{\omega} = 0$, the resulting expression differs due the differing $F_3^{\omega=0}$ and $\boldsymbol{v}_2$ developing a nonzero curl

$$\boldsymbol{v}_2^{\omega=0} = -2\mathcal{H}\frac{\boldsymbol{\nabla}\delta_2}{\Delta} - \delta_1\boldsymbol{v}_1\,. \tag{4.55}$$

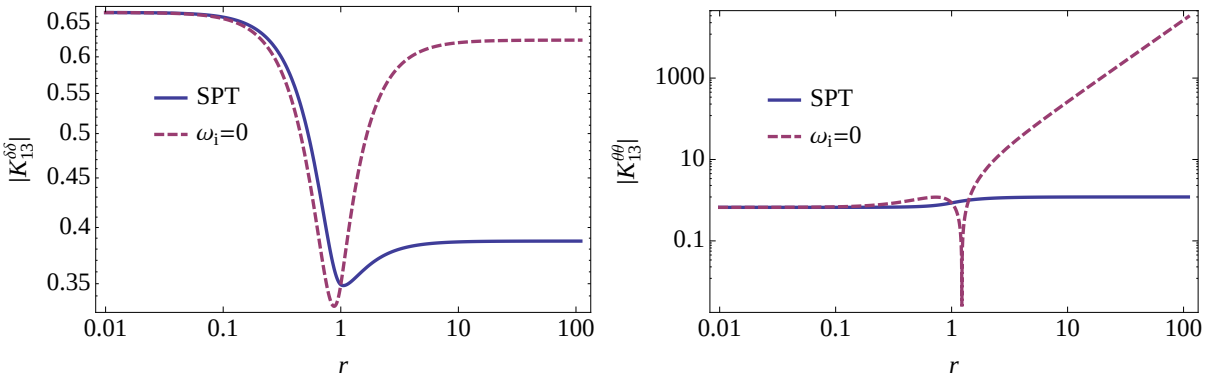

FIGURE 4.3: *Left*: Comparison between integration kernels $K_{13}^{\delta\delta}$ of the 1-loop matter power spectrum for $P_{13,\delta\delta}$. *Right*: Comparison between the integration kernels $K_{13}^{\theta\theta}$ of the 1-loop velocity power spectrum $P_{13,vv}$. For $\omega = 0$ the velocity kernel $K_{13}^{\theta\theta}$ goes like r^2 for $r \gg 1$ and leads to UV-divergent $P_{13,vv}^{\omega=0}$.

Therefore $G_3^{\omega=0}$ changes to

$$-\frac{\theta_3(\boldsymbol{p}_4,\tau)}{\mathcal{H}} = \int \frac{d^3p_1 d^3p_2 d^3p_3}{(2\pi)^6} G_3(\boldsymbol{p}_1,\boldsymbol{p}_2,\boldsymbol{p}_3)\delta_D(\boldsymbol{p}_4-\boldsymbol{p}_1-\boldsymbol{p}_2-\boldsymbol{p}_3)\delta_L(\boldsymbol{p}_1,\tau)\delta_L(\boldsymbol{p}_2,\tau)\delta_L(\boldsymbol{p}_3,\tau)$$

$$G_3^{\omega=0} = 3F_3^{\omega=0} - \boldsymbol{p}_4\cdot\left(\frac{\boldsymbol{p}_1+\boldsymbol{p}_2}{|\boldsymbol{p}_1+\boldsymbol{p}_2|^2}F_2(\boldsymbol{p}_1,\boldsymbol{p}_2)+\frac{\boldsymbol{p}_2}{p_2^2}\right) - \boldsymbol{p}_4\cdot\frac{\boldsymbol{p}_1}{p_1^2}F_2(\boldsymbol{p}_2,\boldsymbol{p}_3)\,. \tag{4.56}$$

The velocity power spectrum is defined via $\langle \boldsymbol{v}(\boldsymbol{k})\cdot\boldsymbol{v}(\boldsymbol{p})\rangle = (2\pi)^3\delta_{\rm D}(\boldsymbol{k}+\boldsymbol{p})P_{vv}(k)$. Because of the Dirac function the power spectrum splits into $P_{vv}(k) = P_{\theta\theta}(k) + P_{ww}(k)$. At 1-loop order using the symmetrized G_2, G_3 and Ω_2^i we find

$$P_{vv}^{\omega=0}(k) = \frac{1}{k^2}\left(\mathcal{H}^2P_1(k) + P_{22,\theta\theta}(k) + P_{13,\theta\theta}^{\omega=0}(k)\right) + P_{22,ww}^{\stackrel{!}{=}0}(k) \tag{4.57a}$$

$$P_{vv}^{\rm SPT}(k) = \frac{1}{k^2}\left(\mathcal{H}^2P_1(k) + P_{22,\theta\theta}(k) + P_{13,\theta\theta}^{\rm SPT}(k)\right)\,, \tag{4.57b}$$

with

$$P^{\omega=0}_{22,ww}(k) = \frac{\mathcal{H}^2 k}{2\cdot 4\pi^2}\int_0^\infty dr \int_{-1}^1 dx\; P_1(k\sqrt{1-2rx+r^2})P_1(kr)\frac{(1-x^2)(1-2rx)^2}{(1-2rx+r^2)^2} \tag{4.58a}$$

$$= P^{\rm SPT}_{22,\omega\omega}(k) \tag{4.58b}$$

$$P^{\omega=0}_{13,\theta\theta}(k) = \frac{\mathcal{H}^2 k^3}{42\cdot 4\pi^2}P_1(k)\int_0^\infty dr\; P_1(kr)\Bigg\{\frac{20}{r^2}-\frac{319}{3}+\frac{76}{3}r^2-25r^4+ \tag{4.58c}$$

$$+\frac{5}{2r^3}(r^2-1)^3(-5r^2+4)\ln\left|\frac{1+r}{1-r}\right|\Bigg\}$$

$$P^{\rm SPT}_{13,\theta\theta}(k) = \frac{\mathcal{H}^2 k^3}{42\cdot 4\pi^2}P_1(k)\int_0^\infty dr\; P_1(kr)\Bigg\{\frac{6}{r^2}-41+2r^2-3r^4+ \tag{4.58d}$$

$$+\frac{3}{2r^3}(r^2-1)^3(r^2+2)\ln\left|\frac{1+r}{1-r}\right|\Bigg\}.$$

Here $P_{22,\theta\theta}$ is the standard expression, since G_2 does not depend on ω, see (3.15). The $P_{13,\theta\theta}$ are quite different, though. While $P^{\rm SPT}_{13,\theta\theta}$ converges, $P^{\omega=0}_{13,\theta\theta}$ is UV-divergent for standard P_1, which go in the UV like $k^{0.96}(\ln k/k^2)^2$. We plot in Fig. 4.3 the integration kernels

$$K^{\delta\delta}_{13}(r) = 6r^2\int_{-1}^1 F_3^{\rm sym}(\boldsymbol{q},-\boldsymbol{q},\boldsymbol{k})dx\,, \qquad K^{\theta\theta}_{13}(r) = 6r^2\int_{-1}^1 G_3^{\rm sym}(\boldsymbol{q},-\boldsymbol{q},\boldsymbol{k})dx\,, \tag{4.59}$$

where $r = q/k$ and $x = \boldsymbol{q}\cdot\boldsymbol{k}/(qk)$. These kernels correspond to the curly brackets in (4.18a) and (4.18b) as well as (4.58c) and (4.58d), respectively. The divergence of $P^{\omega=0}_{13,\theta\theta}$ is not cancelled by $P^{\omega=0}_{22,ww}$ in Eq. (4.57a). The physical interpretation of this result remains unclear. Note that also for power-laws $P_1 \propto k^n$ UV-divergences can appear in SPT, whose physical meaning is not well understood, see for instance the discussion in [BCGS02a], Sec 4.2.2. The 1-loop power spectra for matter $P_{\delta\delta}$, (4.18), and momentum P_{jj}, (4.21), on the other hand are well behaved in the case of $\boldsymbol{\omega} = 0$, see also Fig. 4.2.

On the basis of these convergent expressions for $P_{\delta\delta}$ and P_{jj} we can already conclude that solutions obtained by setting $\boldsymbol{\omega} = 0$ and therefore solutions to (4.15) significantly deviate from solutions of the standard curl-free and pressureless fluid equations (4.8). Having in addition a divergent result for $P^{\omega=0}_{vv}$ might suggest the unphysical nature of (4.15).

4.C Master Equation for perfect fluid and cosmological constant

We generalize the master equation to the case of an imperfect fluid with pressure/bulk viscosity p and include a cosmological constant Λ. This serves as an example of how to generalize

the master equation to arbitrary energy momentum tensors that extend the simple perfect and pressureless dust fluid $T_{\mu\nu} = \varrho u_\mu u_\nu$. For instance, to model multi-streaming effects one might want to include an effective pressure and shear, see for instance [BNSZ12b]. If these additional tensors are functionals of G_{00} and G_{0i} only, they can be again eliminated from the Einstein equations. As an example we assume a perfect non-relativistic fluid with pressure $p = c_s^2\bar{\varrho}\delta$. We simplify the energy momentum tensor according to the double expansion scheme and assuming non-relativistic velocities $\boldsymbol{v}$.

$$\begin{aligned}
T_{\mu\nu} &= \varrho u_\mu u_\nu + p(u_\mu u_\nu + g_{\mu\nu}) - \Lambda g_{\mu\nu}\,,\\
T_{00} &\simeq \varrho u_0^2 + p(u_0^2 - a^2) - \Lambda g_{00} \simeq (\varrho + \Lambda)a^2\\
T_{0i} &\simeq (\varrho + p)u_0 u_i\\
T_{ij} &\simeq (\varrho + p)u_i u_j + (p - \Lambda)(1 + 2\Psi)a^2\delta_{ij}
\end{aligned}$$

We can rewrite the first term in T_{ij} using the Einstein equations

$$(\varrho + p)u_i u_j = \frac{T_{0i}T_{0j}}{(\varrho + p)u_0^2} = \frac{T_{0i}T_{0j}}{(\varrho + \Lambda + p - \Lambda)u_0^2} = \frac{G_{0i}G_{0j}}{G_{00} + (p - \Lambda)a^2}$$

The new source term therefore is

$$\tilde{S}_{ij} = \frac{1}{2}(1+2\Psi)a^2(p-\Lambda)\delta_{ij} + \Psi_{,i}\Psi_{,j} + \frac{2}{3\mathcal{H}^2}\left\{\frac{\left[(\Psi' + \mathcal{H}\Psi)_{,i} - \frac{1}{4}\Delta\omega_i\right]\left[(\Psi' + \mathcal{H}\Psi)_{,j} - \frac{1}{4}\Delta\omega_j\right]}{1 + \frac{1}{3\mathcal{H}^2}\left[2\Delta\Psi + a^2(p - \Lambda)\right]}\right\}$$

which should be used in (4.5) and (4.7), with the right hand side of (4.5a) replaced by

$$\Psi'' + 3\mathcal{H}\Psi' + \left(\mathcal{H}^2 - 2\frac{a''}{a}\right)\left(\frac{1}{2} - 2\Psi\right) + \frac{1}{2}(\nabla\Psi)^2\,.$$

If the pressure is negligible compared to the energy density $p \ll \varrho$, as it is the case for a fluid that models CDM, the only relevant new term is the first term in $\tilde{S}_{ij}$. In a similar fashion a shear viscosity η as well as a bulk viscosity ζ could be added to the dust model $T_{\mu\nu} = \varrho u_\mu u_\nu$,

$$\Sigma_{\mu\nu} = -\eta(u_\mu u^\alpha + \delta_\mu^\alpha)(u^\beta u_\nu + \delta_\nu^\beta)(u_{(\alpha;\beta)} - \frac{2}{3}g_{\alpha\beta}u^\varrho_{;\varrho}) - \zeta u^\varrho_{;\varrho}(u_\mu u_\nu + g_{\mu\nu})\,,$$

in which case the tensorial structure of the resulting $\bar{S}_{ij}$ would be more complicated. Assuming that in the small velocity limit, $\Sigma_{00} \ll T_{00}$ as well $\Sigma_{0i} \ll T_{0i}$ holds, the dominant parts of Σ_{ij} are given by $\Sigma_{ij} \simeq -\eta a(v_{(i,j)} - \frac{2}{3}\delta_{ij}\nabla\cdot\boldsymbol{v}) - \zeta\delta_{ij}\nabla\cdot\boldsymbol{v}$. In this case any tensor depending only on δ and $\boldsymbol{v}$, can be rewritten according to 00 and $0i$ component of the Einstein equation

$$v_i = \frac{(\Psi' + \mathcal{H}\Psi)_{,i} - \frac{1}{4}\Delta\omega_i}{1 + \frac{2}{3\mathcal{H}^2}\Delta\Psi}\,, \qquad \delta = \frac{2}{3\mathcal{H}^2}\Delta\Psi\,.$$

5

The Schrödinger Method

This chapter is published as an article [UKH14], and arose in collaboration with Cora Uhlemann and Thomas Haugg. We investigate large-scale structure formation of collisionless dark matter in the phase space description based on the Vlasov (or collisionless Boltzmann) equation whose nonlinearity is induced solely by gravitational interaction according to the Poisson equation. Determining the time-evolution of density and peculiar velocity demands solving the full Vlasov hierarchy for the moments of the phase space distribution function. In the presence of long-range interaction no consistent truncation of the hierarchy is known apart from the pressureless fluid (dust) model which is incapable of describing virialization due to the occurrence of shell-crossing singularities and the inability to generate vorticity and higher cumulants like velocity dispersion. Our goal is to find a simple ansatz for the phase space distribution function that approximates the full Vlasov distribution function without pathologies in a controlled way and therefore can serve as theoretical N-body double and as a replacement for the dust model. We argue that the coarse-grained Wigner probability distribution obtained from a wave function fulfilling the Schrödinger-Poisson equation (SPE) is the sought-after function. We show that its evolution equation approximates the Vlasov equation and therefore also the dust fluid equations before shell-crossing, but cures the shell-crossing singularities and is able to describe regions of multi-streaming and virialization. This feature was already employed in cosmological simulations of large-scale structure formation by Widrow and Kaiser [WK93]. The coarse-grained Wigner ansatz allows to calculate all higher moments from density and velocity analytically, thereby incorporating nonzero higher cumulants in a self-consistent manner. On this basis we are able to show that the Schrödinger method (ScM) automatically closes the corresponding hierarchy such that it suffices to solve the SPE in order to directly determine density and velocity and all higher cumulants.

5.1 Introduction

The standard model of large-scale structure (LSS) formation and halo formation is based on collisionless cold dark matter (CDM), a yet unknown particle species that for purposes of LSS and larger halos can be assumed to interact only gravitationally and to be cold or initially single-streaming. We are therefore interested in the dynamics of a large collection of identical point particles that via gravitational instability evolve from initially small density perturbations into eventually bound structures, like halos that are distributed along the loosely bound LSS composed of superclusters, sheets, and filaments [Pee80, SWJ+05, TSM+14]. All these structures depend on cosmological parameters, in particular the background energy density of CDM and the cosmological constant. We therefore require accurate modelling and theoretical understanding of CDM dynamics to extract those cosmological parameters from observations. While the shape of the LSS can be reasonably well described by modelling the CDM as a pressureless fluid (dust), it necessarily fails at small scales where multiple streams form. Multi-streaming is especially important for halo formation (virialization), but already affects LSS and its observation in redshift-space.

On sub-Hubble scales and for non-relativistic velocities the Newtonian limit of the Einstein equations is sufficient to describe the time evolution of structures within the universe [CZ11, GW12] and Chapters 3 and 4. Furthermore the large number of particles under consideration suppresses collisions such that the phase space dynamics is only affected by the smooth Newtonian potential [Gil68]. Therefore the time-evolution of the phase space distribution function $f(t, \boldsymbol{x}, \boldsymbol{p})$ is governed by the Vlasov (or collisionless Boltzmann) equation whose nonlinearity is induced by the gravitational force obtained from the Poisson equation sourced by $\int d^3p\, f(t, \boldsymbol{x}, \boldsymbol{p})$.

Even though this model seems to be quite simple from a conceptual point of view, no general solution is known and one usually has to resort to N-body simulations which tackle the problem of solving the dynamical equations numerically, see for instance [Tey02, SWJ+05, SFW06, BSW+09, KPGD09, KPR+11, AHK12, HAK13]. From the analytical point of view, different methods to describe LSS formation based on the dust model have been developed. The dust model describes CDM as a pressureless fluid using hydrodynamic equations [Pee80], and is studied especially in the context of perturbation theory. Among them the two most commonly used methods are the Eulerian framework describing the dynamics of density and velocity fields, see Chapters 4 and 6.3.1 or e.g. [BCGS02b], and the Lagrangian description following the field of trajectories of particles, see Chapter 6.3.2 or e.g. [BMW94a]. The dust model is an exact solution to the Vlasov equation which describes "absolutely" cold dark matter and works quite well in the linear and quasi-linear regime of LSS formation. But the dust model not only fails to catch the dynamics when multiple streams occur in the N-body dynamics, but actually runs into so called shell-crossing singularities or caustics forming at the smallest scales. One might therefore say that the dust model is UV-incomplete.

A possibility to circumvent the formation of singularities and to restore agreement with simulations in the weakly nonlinear regime is to introduce an artificial viscosity term in the pressureless fluid equations which is effective only in regions where the dust evolution would predict a singularity. This phenomenological model proposed in [GSS89] is known as adhesion ap-

proximation and was shown to be able to reproduce the skeleton of the cosmic web in [WG90]. However, such ad-hoc constructions remain quite unsatisfying from a conceptual point of view; for example the size of formed structures directly depends on the viscosity parameter rather then the initial conditions and it is unclear how well the Vlasov equation is approximated.

A more general reasoning was pursued in the direction of coarse-grained perturbation theory which led to models that were argued to incorporate adhesive features. When the dynamical evolution of a many-body system is described by means of a continuous phase space distribution one has to consider coarse-grained or macroscopic quantities, thereby neglecting detailed information about the microscopic degrees of freedom. Although at a first glance this might seem inconvenient, it is indeed an advantageous point of view, especially when comparing to data inferred from observations or simulations, that are fundamentally coarse-grained. Therefore the dynamical evolution of smoothed density and velocity fields relevant for cosmological structure formation has been under investigation, see for example [Dom00, BD05], where it was argued that coarse-graining may lead automatically to adhesive behavior. Furthermore it was shown in [PMSV12a] that for averaged fields the correspondence between the occurance of velocity dispersion and multi-streaming phenomena due to shell-crossing breaks down. This is due to the fact that the coarse-graining introduces a nonzero velocity dispersion between the particles within each coarse-graining cell which mimics microscopic velocity dispersion connected to genuine multi-streaming.

Solving the Vlasov equation is equivalent to solving the infinite coupled hierarchy of equations for the cumulants of the distribution function f with respect to momentum $\boldsymbol{p}$. This means that in order to determine the time evolution of the zeroth and first cumulants, related to density and velocity, all higher cumulants starting with velocity dispersion are relevant, see [PS09]. Only neglecting them entirely is consistent [PS09]; in this case one is lead to the popular dust model [Pee80]. Gravity is the dominant force on cosmological scales and in the early stages of gravitational instability matter is distributed very smoothly with nearly single-valued velocities. Therefore the dust model has proven quite successful in describing the evolution as long as the collective motion of particles is well-described by this coherent flow. However, as soon as the density contrast becomes non-linear, multiple streams form and become relevant in the Vlasov dynamics while caustics – called 'shell-crossing' singularities – are developed indicating that the underlying approximations are no longer justified and the model looses its predictability. The problem of developing singularities and failure of being a good description afterwards, also occurs in the first order Lagrangian solution, called Zel'dovich approximation [Zel70], which is the exact solution in the plane-parallel collapse studied in Sec. 5.4.

The Schrödinger method (ScM), originally proposed in [WK93, DW96] as numerical technique for following the evolution of CDM, models CDM as a complex scalar field obeying the coupled Schrödinger-Poisson equations (SPE) [CS03, SC06, Gue95] in which $\hbar$ merely is a free parameter that can be chosen at will and determines the phase space resolution. The ScM is comprised of two parts; (1) solving the SPE with desired initial conditions and (2) taking the Husimi transform [Hus40] to construct a phase space distribution from the wave function. The correspondence between distribution functions in classical mechanics and phase space representations of quantum mechanics has been investigated in detail by [Tak89], both analytically as

well as by means of numerical examples. It turned out that the Wigner function, obtained from a wave function fulfilling the SPE, corresponds poorly to classical dynamics. In contrast, the coarse-grained Wigner or Husimi distribution was shown to be indeed a good model for coarse-grained classical mechanics [Tak89, WK93].

The SPE can be seen as the non-relativistic limit of the Klein-Gordon-Einstein equations [Wid97, GG12]. From this perspective the physical interpretation (if $\hbar$ takes the value of the Planck constant) is that CDM is actually a non-interacting and non-relativistic Bose-Einstein condensate, in which case the SPE can be interpreted as a special Gross-Pitaevskii equation, see [Ram13] for a review. The axion could be such a Bose-Einstein condensate [DGL+14].

In plasma and solid state physics as well as mathematical physics the equation is known as Choquard equation [Lie77, AS01]. In the context of "gravitational state reduction" this equation, denoted by Schrödinger-Newton equation, was studied e.g. in [MPT98]. There have also been investigations on the connection between general fluid dynamics and wave mechanics [Mad27, Spi80].

The similarity between the SPE and the dust model has been also employed in the context of wave mechanics. There the so-called free-particle approximation (based on the free-particle Schrödinger equation, see [Tho11]) was shown to closely resemble the Zel'dovich approximation [CS03, SC06] while avoiding singularities. In some works a modified SPE system with an added quantum pressure term was considered, [JLH09, TvJ11] which then is equivalent to the usual fluid system. Clearly this approach is not advantageous since the fluid description is known to break down at shell-crossing. This had lead to the claim in [JLH09] that also the Schrödinger method breaks down. In [SK03] perturbation theory based on the SPE in the limit $\hbar \to 0$ was considered where it was emphasized that shell-crossing singularities are avoided. However their calculations assumed $\hbar = 0$ identically, which leads to results equivalent to standard perturbation theory (SPT) based on a dust fluid, without solving the shell-crossing problem.

That the ScM is a viable model for cosmological structure formation and in particular capable of describing multi-streaming was exemplarily demonstrated by means of numerical examples in [WK93, DW96, SBR+13]. However, the bulk of these investigations were aimed at replacing N-body simulations by a numerical solution to the SPE. Therefore the methods applied therein are unsuitable and inconvenient for the genuine analytical approach we want to establish. In [WK93, DW96] a superposition of N Gaussian wave packets was used as initial wave function, thereby closely resembling the N particles in a N-body simulation. In [SBR+13] CDM was modelled by N wave functions coupled via the Poisson equation. We will study the case of a single wave function on an expanding background with nearly cold initial conditions. The result suggests that indeed the ScM is a substantially better suited analytical tool to study CDM dynamics than the dust model: in the single-stream regime they stay arbitrarily close to each other, but while dust fails and stops when multi-streaming should occur, the Schrödinger wave function continues without any pathologies and behaves like multi-streaming CDM when interpreted in a coarse-grained sense. Although it was already observed in [CS03] that the wave function does not run into singularities, it was claimed that it still cannot describe multi-streaming or virialization. Indeed, our numerical example closely resembling that of [CS03], but generalised to an expanding background, proves the contrary. Fig 5.1 and the flip-book animation in the right

corner show the dynamics of the Husimi function f_{H} using the ScM: the density remains finite at shell-crossing, f_{H} forms multi-stream regions and ultimately virializes. None of these features necessary for a full description of LSS and halo formation are accessible with the dust model.

Goal The aim of this chapter is to present the Schrödinger method, already investigated in the context of cosmological simulations, as a theoretical N-body double for the phase space distribution function f. We show that phase space density f_{H} obtained from the ScM solves the Vlasov equation approximately but in a controlled manner. We demonstrate that f_{H} closes the hierarchy of moments automatically but yet allows for multi-streaming and virialization. We give explicit analytic expressions for higher order non-vanishing cumulants, like velocity dispersion, in terms of the wave function and in terms of the macroscopic physical density and velocity fields. This constitutes a new approach to tackle the closure problem of the Vlasov hierarchy apart from truncation or restricting oneself to the dust model and its limitations. We shed light on the physical interpretation by means of a numerical study of pancake formation. In summary this means that the ScM models CDM in a well-behaved manner with initial conditions and single-stream dynamics arbitrarily close to dust. Unlike dust, the ScM captures all relevant physics for describing CDM dynamics even in the deeply nonlinear regime and does not break down on the smallest scales, therefore providing a UV-completion of dust.

Structure This chapter is organized as follows: In Sec. 5.2 we review the phase space description of cold dark matter and explain how one is lead to the Vlasov equation on an expanding background. After introducing the dust model we re-derive the coarse-grained Vlasov equation. We then introduce the Wigner function as an ansatz for the phase space distribution and explain its connection to the dust model. We derive the corresponding Wigner-Vlasov equation as well as its coarse-grained version and discuss their relations to the Vlasov equation and the coarse-grained Vlasov equation, respectively. In Sec. 5.3 we determine the moments of the three different phase space distributions – the dust model, the Wigner function and the coarse-grained Wigner or Husimi distribution. In Sec. 5.4 we investigate the pancake collapse to illustrate that the dynamics of the complex scalar field is free from the pathologies of the dust fluid and serves therefore both as a theoretical N-body double and as a UV completion of dust. On this basis we explain how the closure of the hierarchy of moments can be achieved and finally discuss the implications. In Sec. 5.5 we make suggestions about possible future research based on ScM and conclude in Sec. 5.6.

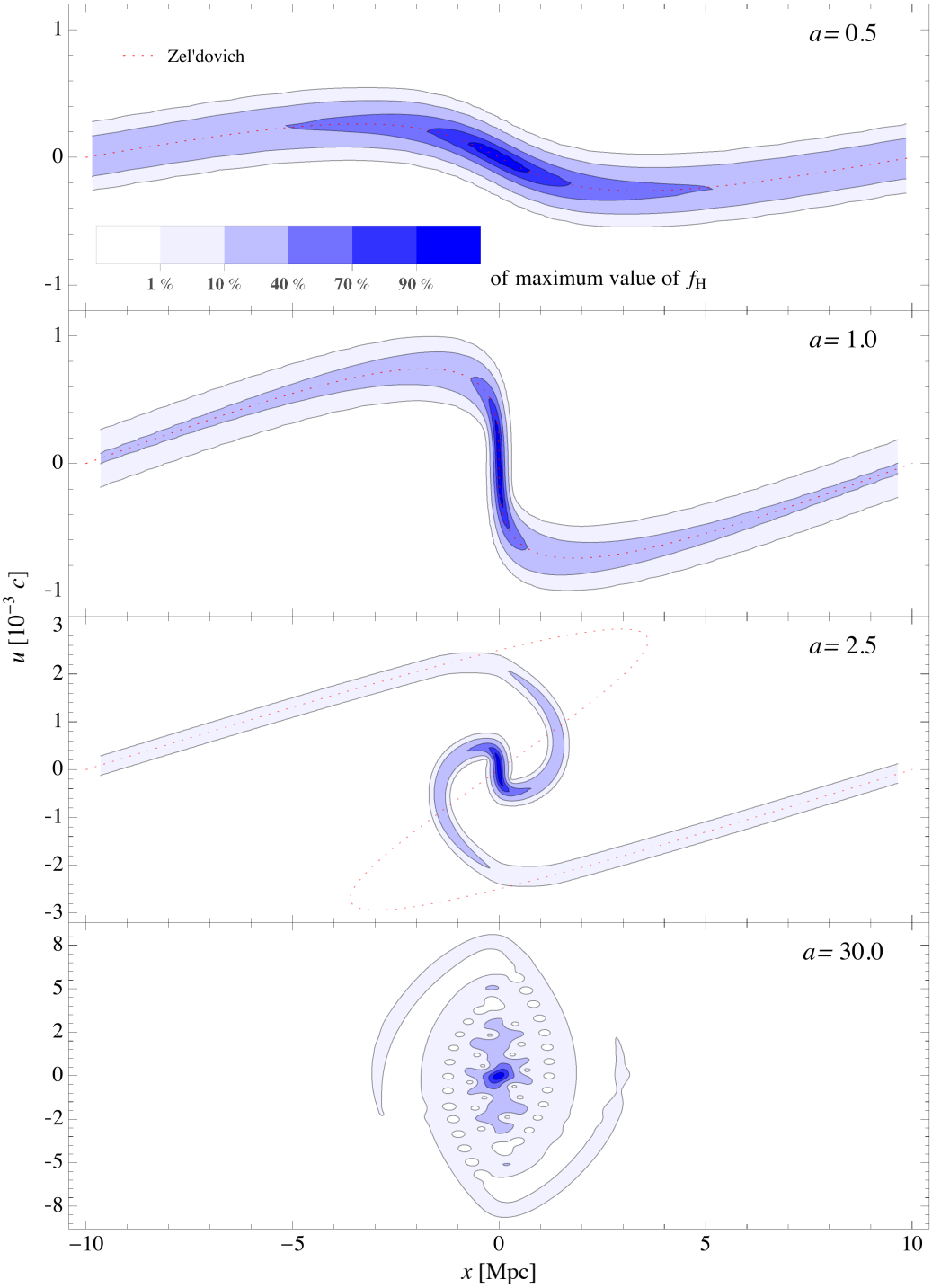

FIGURE 5.1: Collapse of a pancake (plane-parallel) density profile on a Einstein-de Sitter background as seen in phase space using the ScM. *blue* contours: Phase space density f_H calculated from Eqs. (5.13, 5.23) at four characteristic moments in time. *red dotted* line: the Zel'dovich solution of Eq. (5.60) is the exact dust solution, valid until $a = 1$. Only the first panel can be described by dust. Shell-crossing (2nd panel), multi-streaming (3rd panel) and viralisation (4th panel) are accessible with the ScM but not with dust. That the dynamics corresponds to CDM is proven in Sec. 5.2.4. How to obtain cumulants without constructing f_H is shown in Sec. 5.3.3.

5.2 Phase-space description of cold dark matter

5.2.1 From Klimontovich to Vlasov equation

The exact one-particle (Klimontovich) phase space density $f_{\rm K}$ of N identical particles following trajectories $\{\boldsymbol{x}_i(t), \boldsymbol{p}_i(t)\}$, $i \in 1, ..., N$, in phase space is given by a sum of δ-functions

$$f_{\rm K}(t, \boldsymbol{x}, \boldsymbol{p}) = \frac{1}{N} \sum_{i=1}^{N} \delta_{\rm D}\left(\boldsymbol{x} - \boldsymbol{x}_i(t)\right) \delta_{\rm D}\left(\boldsymbol{p} - \boldsymbol{p}_i(t)\right) . \tag{5.1}$$

We use comoving coordinates $\boldsymbol{x}$ with associated conjugate momentum $\boldsymbol{p} = a^2 m \, d\boldsymbol{x}/dt$, where a is the scale factor satisfying the Friedmann equation (3.3) of a ΛCDM or Einstein-de Sitter universe.[1] For convenience we will in general suppress the t-dependence of the distribution function in the following. This phase space density obeys the Klimontovich equation [Kli69] encoding phase space density conservation along phase space trajectories

$$\frac{D f_{\rm K}}{dt} = \frac{\partial f_{\rm K}}{\partial t} + \frac{d\boldsymbol{x}}{dt} \cdot \frac{\partial f_{\rm K}}{\partial \boldsymbol{x}} + \frac{d\boldsymbol{p}}{dt} \cdot \frac{\partial f_{\rm K}}{\partial \boldsymbol{p}} = 0 . \tag{5.2}$$

Upon using the equations of motion for non-relativistic particles with trajectories $\{\boldsymbol{x}_i(t), \boldsymbol{p}_i(t)\}$ one arrives at

$$\partial_t f_{\rm K} = -\frac{\boldsymbol{p}}{a^2 m} \cdot \nabla_x f_{\rm K} + m \nabla_x V \cdot \nabla_p f_{\rm K} . \tag{5.3a}$$

The nonlinearity in (5.3a) is induced by the fact that the Newtonian potential V describes gravitational interaction and therefore depends through the Poisson equation on the density field given by the integral of the distribution function over momentum

$$\Delta V = \frac{4\pi G \varrho_0}{a} \left(\int d^3p \, f_{\rm K} - 1 \right) , \tag{5.3b}$$

where ϱ_0 is the (constant) comoving matter background density such that $f_{\rm K}$ has a background value or spatial average value $\langle \int d^3p \, f_{\rm K} \rangle_{\rm vol} = 1$. When symbols like ∇ or $\Delta = \nabla \cdot \nabla$ are used without subscripts they refer to spatial derivatives ∇_x or Δ_x, respectively.

Retaining all details concerning the microstate of a system, the spiky Klimontovich density is not really of practical use. Rather one is interested in the statistical average taken over an ensemble of different realizations of the distribution of the N particles. This information is contained within the smooth one-particle phase space density f_1 given by

$$f_1(t, \boldsymbol{x}, \boldsymbol{p}) = \langle f_{\rm K}(t, \boldsymbol{x}, \boldsymbol{p}) \rangle , \tag{5.4}$$

where angle brackets denote the ensemble average of microstates $f_{\rm K}$ that lead to the same coarse-grained phase space density. If V was a specified external potential, f_1 would obey the same

[1] More generally, any expansion history is allowed as long as metric perturbations are only sourced by CDM.

equation as $f_{\rm K}$. However, since V is the gravitational potential computed self-consistently from the particles via (6.1b), the $\nabla_x V \cdot \nabla_p f_{\rm K}$ term in (5.3a) is quadratic in $f_{\rm K}$. Therefore when taking the ensemble average to derive an equation for the one-particle distribution function f_1 an additional correlation term emerges which involves the irreducible part f_{2c} of two-particle distribution function $f_2(\boldsymbol{x}, \boldsymbol{p}, \boldsymbol{x}', \boldsymbol{p}') = f_1(\boldsymbol{x}, \boldsymbol{p}) f_1(\boldsymbol{x}', \boldsymbol{p}') + f_{2c}(\boldsymbol{x}, \boldsymbol{p}, \boldsymbol{x}', \boldsymbol{p}')$, compare [Ber93]

$$\begin{aligned} \partial_t f_1 = &-\frac{\boldsymbol{p}}{a^2 m} \cdot \nabla_x f_1 + m \nabla_x V \cdot \nabla_p f_1 \\ &+ m \int d^3x' d^3p' \, \nabla_x V(\boldsymbol{x} - \boldsymbol{x}') \cdot \nabla_p f_{2c}(\boldsymbol{x}, \boldsymbol{p}, \boldsymbol{x}', \boldsymbol{p}') \, . \end{aligned} \tag{5.5}$$

This leads to a set of coupled kinetic equations where the n-particle distribution in turn depends on the $(n+1)$-particle distribution. This is the so-called BBGKY (Bogoliubov-Born-Green-Kirkwood-Yvon) hierarchy, describing the dynamics of an interacting N-particle system. The resulting equation (5.5) for f_1 differs from the Klimontovich equation (5.3) by a correlation term which vanishes in the absence of pair correlations. Fortunately, for the case of interest here - CDM particles - these collisional effects are completely negligible since they are suppressed by $1/N$ where N is the number of particles, see [Gil68].[2] The corresponding Vlasov-Poisson system for the one-particle phase space density f_1, which we will denote simply by f from now on, describes collisionless dark matter in the absence of two-body correlations

$$\partial_t f = -\frac{\boldsymbol{p}}{a^2 m} \cdot \nabla_x f + m \nabla_x V \cdot \nabla_p f \, , \tag{5.6a}$$

$$= \left[\frac{\boldsymbol{p}^2}{2a^2 m} + m V(\boldsymbol{x}) \right] \left(\overleftarrow{\nabla}_x \overrightarrow{\nabla}_p - \overleftarrow{\nabla}_p \overrightarrow{\nabla}_x \right) f \, , \tag{5.6b}$$

$$\Delta V = \frac{4\pi G \, \varrho_0}{a} \left(\int d^3p f - 1 \right) . \tag{5.6c}$$

5.2.2 Dust model

The dust model describes CDM as a pressureless fluid with density $n_{\rm d}(\boldsymbol{x})$ and fluid momentum given by an irrotational flow $\nabla \phi_{\rm d}(\boldsymbol{x})$ which remains single-valued at each point, and therefore absolutely cold, meaning that particle trajectories are not allowed to cross and velocity dispersion cannot arise. This regime is usually referred to as 'single-stream', meaning that the validity of this model breaks down as soon as 'shell-crossings' occur and multiple streams develop. The corresponding distribution function is given by

$$f_{\rm d}(\boldsymbol{x}, \boldsymbol{p}) = n_{\rm d}(\boldsymbol{x}) \delta_{\rm D}\Big(\boldsymbol{p} - \nabla \phi_{\rm d}(\boldsymbol{x}) \Big) \, . \tag{5.7}$$

[2] Those $1/N$ corrections make a virialized object like a globular cluster, composed of a few thousand stars, unstable through "evaporation" during which the system becomes even hotter because it contracts [LW68, BT08]. This evaporation happens on much larger time scales compared to virialization and can be completely neglected for dark matter halos. It is interesting that this effect might be physically related to Hawking evaporation of black holes, if black holes are systems of self-gravitating gravitons [DG12].

As we will see in section 5.3, the Vlasov equation (6.1a) for f_d implies the hydrodynamical equations for a perfect pressureless fluid with density n_d and velocity potential ϕ_d/m. The fluid equations consist of the continuity equation, the Bernoulli and Poisson equation

$$\partial_t n_\mathrm{d} = -\frac{1}{ma^2}\nabla\cdot(n_\mathrm{d}\nabla\phi_\mathrm{d})\,, \tag{5.8a}$$

$$\partial_t \phi_\mathrm{d} = -\frac{1}{2a^2 m}(\nabla\phi_\mathrm{d})^2 - mV_\mathrm{d}\,, \tag{5.8b}$$

$$\Delta V_\mathrm{d} = \frac{4\pi G\,\varrho_0}{a}\Big(n_\mathrm{d}-1\Big)\,. \tag{5.8c}$$

By defining an irrotational velocity according to $\boldsymbol{u}_\mathrm{d} = \nabla\phi_\mathrm{d}/m$ one can rewrite (5.8a) and (5.8b) in the following equivalent form

$$\partial_t n_\mathrm{d} = -\frac{1}{a^2}\nabla\cdot(n_\mathrm{d}\boldsymbol{u}_\mathrm{d})\,, \tag{5.9a}$$

$$\partial_t \boldsymbol{u}_\mathrm{d} = -\frac{1}{a^2}(\boldsymbol{u}_\mathrm{d}\cdot\nabla)\boldsymbol{u}_\mathrm{d} - \nabla V_\mathrm{d}\,, \tag{5.9b}$$

$$\nabla\times\boldsymbol{u}_\mathrm{d} = 0\,. \tag{5.9c}$$

5.2.3 Coarse-grained Vlasov equation

The coarse-grained distribution function $\bar{f}$ is obtained from f by convolution with a Gaussian of width σ_x and σ_p in $\boldsymbol{x}$ and $\boldsymbol{p}$ space, respectively. For convenience we will adopt the shorthand operator representation of the smoothing which can be easily obtained by switching to Fourier space

$$\bar{f}(\boldsymbol{x},\boldsymbol{p}) = \int \frac{d^3x'd^3p'}{(2\pi\sigma_x\sigma_p)^3}\exp\left[-\frac{(\boldsymbol{x}-\boldsymbol{x}')^2}{2{\sigma_x}^2}-\frac{(\boldsymbol{p}-\boldsymbol{p}')^2}{2{\sigma_p}^2}\right]f(\boldsymbol{x}',\boldsymbol{p}')\,,$$
$$\bar{f} = \exp\left(\frac{{\sigma_x}^2}{2}\Delta_x + \frac{{\sigma_p}^2}{2}\Delta_p\right)f\,. \tag{5.10}$$

The corresponding coarse-grained Vlasov equation as given in [MW03] is easily obtained from the usual Vlasov equation (6.1) by applying the smoothing operator. We employ the following identity for the smoothing operator

$$\exp(\Delta)(AB) = [\exp(\Delta)A]\exp\left(2\overleftarrow{\nabla}\overrightarrow{\nabla}\right)[\exp(\Delta)B]\,, \tag{5.11}$$

in order to express the coarse-graining of a product in terms of its coarse-grained factors. The result is the cosmological analogue to the evolution equation for coarse-grained classical distribution

$$\partial_t\bar{f} = -\frac{\boldsymbol{p}}{a^2 m}\nabla_x\bar{f} - \frac{{\sigma_p}^2}{a^2 m}\nabla_x\nabla_p\bar{f} + m\nabla_x\bar{V}\exp({\sigma_x}^2\overleftarrow{\nabla}_x\overrightarrow{\nabla}_x)\nabla_p\bar{f}\,, \tag{5.12a}$$

$$= \exp\left(\frac{{\sigma_x}^2}{2}\Delta_x + \frac{{\sigma_p}^2}{2}\Delta_p\right)\left[\frac{\boldsymbol{p}^2}{2a^2 m} + mV\right]\times \tag{5.12b}$$
$$\times\exp\left({\sigma_x}^2\overleftarrow{\nabla}_x\overrightarrow{\nabla}_x + {\sigma_p}^2\overleftarrow{\nabla}_p\overrightarrow{\nabla}_p\right)\left(\overleftarrow{\nabla}_x\overrightarrow{\nabla}_p - \overleftarrow{\nabla}_p\overrightarrow{\nabla}_x\right)\bar{f}\,,$$

which was given in [Tak89] for $a = 1$ and units where ${\sigma_x}^2 = {\sigma_p}^2 = \hbar/2$.

Note that this result holds on a FRW background with cosmic time t, comoving $\boldsymbol{x}$ and canonical conjugate 1-form $\boldsymbol{p}$, where $\bar{V}$ fulfills Eq. (6.1b) with f is replaced by $\bar{f}$. If derivative operators like ∇_x and ∇_p carry left or right arrows over them, they specify that they only act on quantities on their left or right hand side, respectively. The notation of Eq. (5.12) is the same as used in [Tak89].

At a first glance the coarse-graining introduced in (5.10) might seem like an unfavorable artifact which complicates calculations on the one hand and erases relevant information on the other hand. However, one has to bear in mind that when sampling the distribution function numerically using a finite number of particles, a coarse-graining is inevitable to provide a proper phase space description [BD05]. This is of particular importance since solving the Vlasov-Poisson equation analytically is a formidable task and one typically has to resort to numerical simulations, for example N-body codes [Tey02, SWJ+05, SFW06, BSW+09, AHK12, HAK13]. The coarse-grained phase space distribution function $\bar{f}$ can therefore be seen as a theoretical N-body double. Another important property of $\bar{f}$ is that it can be obtained from f_{K} directly by coarse-graining in phase space, $\bar{f} = \exp\left[\frac{1}{2}{\sigma_x}^2\Delta_x + \frac{1}{2}{\sigma_p}^2\Delta_p\right] f_{\mathrm{K}}$, without the need of obtaining first f and the Vlasov equation via ensemble averaging f_{K}.

5.2.4 Husimi-Vlasov equation

5.2.4.1 Schrödinger Poisson system

The Schrödinger-Poisson system in a ΛCDM universe with scale factor a is given by

$$i\hbar\partial_t\psi = -\frac{\hbar^2}{2a^2m}\Delta\psi + mV\psi\,, \tag{5.13a}$$

$$\Delta V = \frac{4\pi G\,\varrho_0}{a}\Big(|\psi|^2 - 1\Big)\,, \tag{5.13b}$$

see for instance [WK93]. Using the so-called Madelung representation for the wave function $\psi(\boldsymbol{x}) = \sqrt{n(\boldsymbol{x})}\exp\left(i\phi(\boldsymbol{x})/\hbar\right)$ one can obtain fluid-like equations of motion for the normalized density[3] n and the velocity potential ϕ directly from the Schrödinger equation [Mad27]. By separating real and imaginary parts one obtains the continuity equation (5.8a), and an equation for ϕ which is similar to the Bernoulli equation (5.8b) but contains an extra term proportional to $\hbar^2$, the so-called 'quantum pressure'

$$\partial_t n = -\frac{1}{ma^2}\nabla\cdot(n\nabla\phi)\,, \tag{5.14a}$$

$$\partial_t\phi = -\frac{1}{2a^2m}(\nabla\phi)^2 - mV + \frac{\hbar^2}{2a^2m}\frac{\Delta\sqrt{n}}{\sqrt{n}}\,, \tag{5.14b}$$

$$\Delta V = \frac{4\pi G\,\varrho_0}{a}\Big(n - 1\Big)\,. \tag{5.14c}$$

[3] The volume average is $\langle n\rangle_{\mathrm{vol}} = 1$, if vol approaches the homogeneity scale.

With the definition $\boldsymbol{u} = \nabla\phi/m$, the modified Bernoulli equation for ϕ is then equivalent to a modified Euler equation with the constraint $\nabla \times \boldsymbol{u} = 0$

$$\partial_t n = -\frac{1}{a^2}\nabla_x \cdot (n\boldsymbol{u})\,, \tag{5.15a}$$

$$\partial_t \boldsymbol{u} = -\frac{1}{a^2}(\boldsymbol{u}\cdot\nabla)\boldsymbol{u} - \nabla V + \frac{\hbar^2}{2a^2m^2}\nabla\left(\frac{\Delta\sqrt{n}}{\sqrt{n}}\right)\,. \tag{5.15b}$$

At this stage we want to emphasize again that the Schrödinger equation is considered here as a mere tool to model CDM dynamics. Therefore the value of $\hbar$ has to be treated as a parameter which is not necessarily connected to the value of $\hbar$ in the context of ordinary quantum mechanics, but rather must be adjusted to computational feasibility and the physical problem at hand [WK93]. Another important remark is in order. The Madelung respresentation Eqs. (5.14) is only equivalent to the Schrödinger system Eqs. (5.13) as long as $n \neq 0$. We will see later that during shell-crossings interference in the wave-function ψ will cause $n = 0$ at isolated points in space and time. Once this happens the Madelung representation breaks down because ϕ develops infinite spatial gradients and phase jumps, leading to infinite time derivatives. In App. (5.B) we investigate the Lagrangian formulation of the SPE, which suffers from the same problem. If one still prefers to stay in the fluid picture, one needs to solve instead for the momentum $\boldsymbol{j} \equiv n\boldsymbol{u}$, which is well behaved during these phase jumps and fulfills

$$\partial_t n = -\frac{1}{a^2}\nabla\cdot\boldsymbol{j}\,, \tag{5.15c}$$

$$\partial_t \boldsymbol{j} = -\frac{1}{a^2}\nabla_i\left(\frac{j_i\boldsymbol{j}}{n}\right) - n\nabla\left(V - \frac{\hbar^2}{2a^2m^2}\frac{\Delta\sqrt{n}}{\sqrt{n}}\right)\,. \tag{5.15d}$$

We will comment on the nature of phase jumps in Sec. 5.4.2. The dynamics of ψ in Eqs. (5.13) is free from pathologies.

5.2.4.2 Wigner quasi-probability distribution

Originally introduced to study quantum corrections to classical statistical mechanics, the Wigner quasi-probability distribution [Wig32] allows to link the Schrödinger wave function $\psi(\boldsymbol{x})$ to a function $f(\boldsymbol{x},\boldsymbol{p})$ in phase space

$$f_{\mathrm{W}}(\boldsymbol{x},\boldsymbol{p}) = \int \frac{d^3\tilde{x}}{(\pi\hbar)^3}\exp\left[2\frac{i}{\hbar}\boldsymbol{p}\cdot\tilde{\boldsymbol{x}}\right]\psi(\boldsymbol{x}-\tilde{\boldsymbol{x}})\psi^*(\boldsymbol{x}+\tilde{\boldsymbol{x}})\,, \tag{5.16}$$

where ψ^* denotes the complex conjugate of ψ. f_{W} is a quasi-probability distribution since it become negative in general. For the dust-like initial conditions studied later see Fig. 5.2, left.

Wigner Vlasov equation The time evolution equation for f_{W} is obtained by using the Schrödinger equation (5.13a) and performing an integration by parts twice which yields

$$\partial_t f_{\mathrm{W}} = -\frac{\boldsymbol{p}}{a^2m}\nabla_x f_{\mathrm{W}} + \frac{i}{\hbar}\int\frac{d^3\tilde{x}}{(\pi\hbar)^3}\exp\left[2\frac{i}{\hbar}\boldsymbol{p}\cdot\tilde{\boldsymbol{x}}\right]\times \tag{5.17}$$
$$\times\; m\left[V(\boldsymbol{x}+\tilde{\boldsymbol{x}}) - V(\boldsymbol{x}-\tilde{\boldsymbol{x}})\right]\psi(\boldsymbol{x}-\tilde{\boldsymbol{x}})\psi^*(\boldsymbol{x}+\tilde{\boldsymbol{x}})\,.$$

In order to obtain a factorization of the form $V(\boldsymbol{x}) \cdot f_{\mathrm{W}}$ one has to perform a Taylor expansion of $V(\boldsymbol{x}-\tilde{\boldsymbol{x}}) - V(\boldsymbol{x}+\tilde{\boldsymbol{x}})$ around $\boldsymbol{x}$ using $\alpha \in \mathbb{N}_0^3$ as a multi-index

$$V(\boldsymbol{x}+\tilde{\boldsymbol{x}}) - V(\boldsymbol{x}-\tilde{\boldsymbol{x}}) = \sum_{|\alpha|\geq 1} \frac{\partial_x^{(\alpha)} V(\boldsymbol{x})}{\alpha!} \left[\tilde{\boldsymbol{x}}^\alpha - (-\tilde{\boldsymbol{x}})^\alpha\right] . \tag{5.18}$$

Obviously the difference in parenthes vanishes if $|\alpha|$ is even and gives $2\tilde{\boldsymbol{x}}^\alpha$ if $|\alpha|$ is odd. Therefore this term can be rewritten as derivative $-i\hbar\partial_p^{(\alpha)} \exp\left[2i\,\boldsymbol{p}\cdot\tilde{\boldsymbol{x}}/\hbar\right]$. Upon resummation one obtains the evolution equation for the Wigner function

$$\partial_t f_{\mathrm{W}} = -\frac{\boldsymbol{p}}{a^2 m}\nabla_x f_{\mathrm{W}} + mV\frac{2}{\hbar}\sin\left(\frac{\hbar}{2}\overleftarrow{\nabla}_x\overrightarrow{\nabla}_p\right) f_{\mathrm{W}} , \tag{5.19a}$$

$$= \left[\frac{\boldsymbol{p}^2}{2a^2 m} + mV\right]\frac{2}{\hbar}\sin\left(\frac{\hbar}{2}(\overleftarrow{\nabla}_x\overrightarrow{\nabla}_p - \overleftarrow{\nabla}_p\overrightarrow{\nabla}_x)\right) f_{\mathrm{W}} , \tag{5.19b}$$

which coincides with the result given in [Tak89] for the special case where $a = 1$. Note that on an FRW space $a(t)$ is the scale factor with t cosmic time, $\boldsymbol{x}$ comoving, $\boldsymbol{p}$ is the conjugate momentum 1-form and V fulfills Eq. (5.14c).

Relation to f_{d} The similarity between the equations (5.14) obtained from a Schrödinger wave function when decomposing it into modulus and phase $\psi = \sqrt{n}\exp(i\phi/\hbar)$ and the fluid equations (5.8) can also be understood from the point of view of distribution functions. Transforming variables $\tilde{x} \to \hbar\tilde{x}$ and adopting the shorthand notation $g^\pm = g(\boldsymbol{x} \pm \hbar\tilde{\boldsymbol{x}})$ the Wigner function can be rewritten in the following form

$$f_{\mathrm{W}}(\boldsymbol{x},\boldsymbol{p}) = \int \frac{d^3\tilde{x}}{\pi^3}\sqrt{n^+ n^-}\exp\left[i\left(2\boldsymbol{p}\cdot\tilde{\boldsymbol{x}} + \frac{\phi^- - \phi^+}{\hbar}\right)\right] ,$$

which allows to examine the formal limit $\hbar \to 0$. Taylor-expanding $n^\pm$ and $\phi^\pm$ to leading non-vanishing order in $\hbar$ and evaluating the integral gives [WK93]

$$f_{\mathrm{W}}(\boldsymbol{x},\boldsymbol{p}) \overset{\hbar\to 0}{=} n(\boldsymbol{x})\delta_{\mathrm{D}}\Big(\boldsymbol{p} - \nabla\phi(\boldsymbol{x})\Big) = f_{\mathrm{d}}(\boldsymbol{x},\boldsymbol{p}) . \tag{5.20}$$

Correspondence to Vlasov equation At leading order, the Wigner Vlasov equation (5.19) differs from the Vlasov equation (6.1) only by a term proportional to $\hbar^2$

$$\partial_t\left(f_{\mathrm{W}} - f\right) \simeq \frac{\hbar^2}{24}\partial_{x_i}\partial_{x_j}\nabla_x V\,\partial_{p_i}\partial_{p_j}\nabla_p f_{\mathrm{W}} + \mathcal{O}(\hbar^4) .$$

Therefore one might hope that they are in good agreement. However, as was shown exemplarily in [Tak89], the correspondence between the time-evolution of the Wigner distribution f_{W} and Vlasov distribution function f is in general very poor by virtue of the violent oscillations of f_{W} on scales $\hbar$, related to the fact that f_{W} can become negative. In this context one has to bear in mind that the semiclassical limit $\hbar \to 0$ is not meaningful in the sense that it does not drive the solution towards a classical one in a continuous way.

5.2.4.3 Coarse-grained Wigner distribution function

The so-called Husimi-Q [Hus40] representation can be understood as a smoothing of the Wigner quasi-probability distribution (5.16) by a Gaussian filter of width σ_x and σ_p in $\boldsymbol{x}$ and $\boldsymbol{p}$ space, respectively

$$\bar{f}_{\mathrm{W}} = \exp\left(\frac{{\sigma_x}^2}{2}\Delta_x + \frac{{\sigma_p}^2}{2}\Delta_p\right) f_{\mathrm{W}}\,. \tag{5.21}$$

In contrast to the Wigner distribution itself the coarse-grained version is a positive-semidefinite function if the filter is of appropriate size $\sigma_x\sigma_p \geq \hbar/2$ for a semi-classical description, see [Car75]. Note that for the FRW case, the form of $\bar{f}_{\mathrm{W}}$ remains unchanged provided $\boldsymbol{x}$ is comoving and $\boldsymbol{p}$ is the conjugate momentum 1-form.

Husimi-Vlasov equation The corresponding Husimi-Vlasov equation for the coarse-grained f_{W} is then easily obtained by acting with the coarse-graining operators onto Eq. (5.19) employing again the product rule (5.11)

$$\begin{aligned}\partial_t \bar{f}_{\mathrm{W}} &= -\frac{\boldsymbol{p}}{a^2 m}\nabla_x \bar{f}_{\mathrm{W}} - \frac{{\sigma_p}^2}{a^2 m}\nabla_x\nabla_p \bar{f}_{\mathrm{W}} + m\bar{V}\exp({\sigma_x}^2\overleftarrow{\nabla}_x\overrightarrow{\nabla}_x)\frac{2}{\hbar}\sin\left(\frac{\hbar}{2}\overleftarrow{\nabla}_x\overrightarrow{\nabla}_p\right)\bar{f}_{\mathrm{W}}\,, \qquad (5.22a)\\ &= \exp\left(\frac{{\sigma_x}^2}{2}\Delta_x + \frac{{\sigma_p}^2}{2}\Delta_p\right)\left[\frac{\boldsymbol{p}^2}{2a^2 m} + mV(\boldsymbol{x})\right]\exp\left({\sigma_x}^2\overleftarrow{\nabla}_x\overrightarrow{\nabla}_x + {\sigma_p}^2\overleftarrow{\nabla}_p\overrightarrow{\nabla}_p\right)\times\\ &\qquad\times\frac{2}{\hbar}\sin\left(\frac{\hbar}{2}(\overleftarrow{\nabla}_x\overrightarrow{\nabla}_p - \overleftarrow{\nabla}_p\overrightarrow{\nabla}_x)\right)\bar{f}_{\mathrm{W}}\,.\end{aligned}$$

This equation is the generalization of the result given in [Tak89] allowing for cosmological backgrounds, arbitrary potentials and smoothing scales σ_x, σ_p. It is the resummation of the equation given up to second order in σ_x in [SRV89], which we obtained by explicit calculation performed analogously to the one presented for f_{W}.

In [WK93] the Husimi representation was used instead, in which the wave function is represented in a (over-complete) basis of Gaussian wave packets

$$\psi_{\mathrm{H}}(\boldsymbol{x},\boldsymbol{p}) = \int d^3y\; K_{\mathrm{H}}(\boldsymbol{x},\boldsymbol{y},\boldsymbol{p})\psi(\boldsymbol{y})\,, \tag{5.23a}$$

$$K_{\mathrm{H}}(\boldsymbol{x},\boldsymbol{y},\boldsymbol{p}) = \frac{\exp\left[-\frac{(x-y)^2}{4{\sigma_x}^2} - \frac{i}{\hbar}\boldsymbol{p}\cdot\left(\boldsymbol{y}-\frac{1}{2}\boldsymbol{x}\right)\right]}{(2\pi\hbar)^{3/2}\,(2\pi{\sigma_x}^2)^{3/4}}\,, \tag{5.23b}$$

such that when going from ψ to ψ_{H} no information is sacrificed. Defining the Husimi distribution function to be

$$f_{\mathrm{H}} = |\psi_{\mathrm{H}}|^2\,, \tag{5.23c}$$

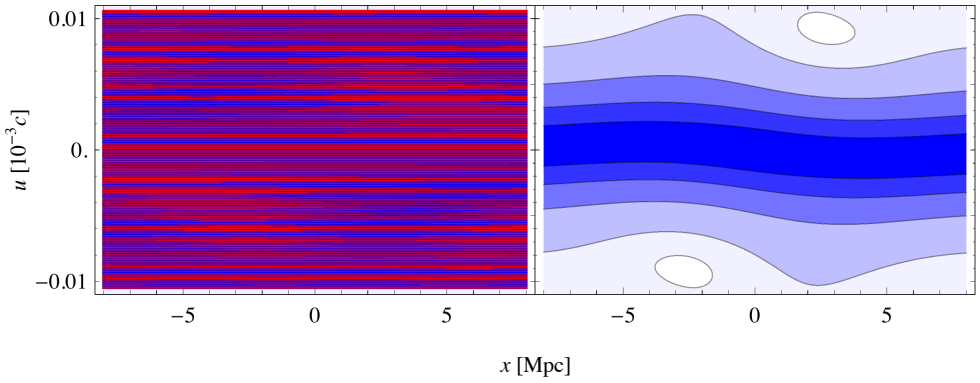

FIGURE 5.2: Comparison between $f_{\rm W}$ and $\bar{f}_{\rm W}$ at the initial time $a_{\rm ini} = 0.01$ using linear dust-like initial conditions $n = n_{\rm d}$ and $\phi = \phi_{\rm d}$. The left panel shows the strongly oscillating $f_{\rm W}$ (*red* is negative, *blue* is positive), the right panel is its smoothed version $\bar{f}_{\rm W}$ (with the same coloring as in Fig 5.1). We choose the minimal values of σ_x and σ_p such that $\bar{f}_{\rm W} \geq 0$, which turned out to be $\sigma_x\sigma_p = 0.03\hbar$.

it is easy to check that it is a special case of the coarse-grained Wigner function, namely

$$f_{\rm H} = \bar{f}_{\rm W} \quad \text{if} \quad \sigma_x\sigma_p = \hbar/2\,. \tag{5.23d}$$

This representation is very convenient numerically, because $f_{\rm H}$ is manifestly real and positive. Also the integration to get $f_{\rm H}$ from ψ is much simpler to evaluate than for $f_{\rm W}$. The main advantage is that one does not need to sample the quite heavily oscillating $f_{\rm W}$ to construct $\bar{f}_{\rm W}$. Fig .5.2 (*left*) provides an impression of $f_{\rm W}$ for cold initial conditions. We also know that $\sigma_x\sigma_p \geq \hbar/2$ ensures $\bar{f}_{\rm W} \geq 0$ [Car75]. Therefore the Husimi representation picks the smallest sufficient σ_p for a positive phase space distribution given a σ_x and $\hbar$. However we would like to point out that for cold dust-like initial conditions well within the linear regime we are free to choose even $\sigma_x\sigma_p < \hbar/2$ without encountering any trouble, compare Figs. 5.1 (1st panel) and 5.2 (*right*). It is also important to realize that the dynamics at early times well before shell-crossing is not affected by the seemingly poor phase space resolution, see Fig. 5.1 (1st panel). We can see this by inspecting the Madelung representation (5.14) of the Schrödinger equation from which it is clear that for smooth dust-like initial conditions the quantum potential with

$$Q = -\frac{\hbar^2}{2a^2m^2}\frac{\Delta\sqrt{n}}{\sqrt{n}}\,, \tag{5.24}$$

will be subdominant for sufficiently small $\hbar/m$.

Correspondence to coarse-grained Vlasov equation Comparing the coarse-grained Vlasov equation (5.12) and the Husimi-Vlasov equation (5.22) we find that they are equal at first order in σ_x^2 and σ_p^2

$$\partial_t\left(\bar{f}_{\rm W} - \bar{f}\right) \simeq \frac{\hbar^2}{24}\partial_{x_i}\partial_{x_j}\nabla_x\bar{V}\,\partial_{p_i}\partial_{p_j}\nabla_p\bar{f}_{\rm W} + \mathcal{O}(\hbar^4, \hbar^2{\sigma_x}^2)\,. \tag{5.25}$$

The Husimi-Vlasov equation (5.22) is in good correspondence to the coarse-grained Vlasov equation (5.12) if $\sigma_x\sigma_p \gtrsim \hbar/2$, which ensures the removal of the violent oscillations and therefore approximates the Vlasov equation well if $\sigma_x \ll x_{\rm typ}$ and $\sigma_p \ll p_{\rm typ}$. Hereby we compared the two distribution functions which are obtained with the same coarse-graining parameters σ_x and σ_p in phase space. As described in [Tak89], the coarse-grained Wigner function $\bar{f}_{\rm W}$ reveals a considerably better correspondence to the probability distribution function f in classical mechanics than the Wigner function $f_{\rm W}$ does.

5.2.4.4 Appropriate choice of the smoothing scales

If $x_{\rm typ}$ and $p_{\rm typ}$ are the (minimal) scales of interest we have to ensure that

$$\sigma_x \ll x_{\rm typ} \quad \text{and} \quad \sigma_p \ll p_{\rm typ}\,. \tag{5.26}$$

Furthermore in general the maximal achievable resolution in phase space is limited by the value of $\hbar$ such that σ_x and σ_p have to be chosen to fulfill

$$\hbar/2 \lesssim \sigma_x\sigma_p\,, \tag{5.27}$$

see however Fig. 5.2 for an exception well before shell-crossing. On a FRW background these bounds take the same form if distances are comoving and if $u_{\rm typ} = p_{\rm typ}/m$ is absolute value of the comoving (or canonical) momentum 1-form. For translating these bounds into requirements for numerical simulations, for example grid time resolution, we refer the reader to [WK93].

5.3 Hierarchy of Moments

In practice one is usually interested in following the evolution of the spatial distribution instead of describing the fully fledged phase space dynamics encoded in the Vlasov equation. For this purpose, the relevant information can be extracted by taking moments of the distribution function with respect to momentum.

Generating functional The moments $M^{(n)}$ of the phase space distribution function $f(\boldsymbol{x},\boldsymbol{p})$ can be obtained from the generating functional $G[\boldsymbol{J}]$ by taking functional derivatives. In a similar way the cumulants can be determined from the moments. They provide a good way to understand the prominent dust-model which is the only known consistent truncation of the Vlasov hierarchy. The generating functional, moments and cumulants are given by

$$G[\boldsymbol{J}] = \int d^3p\, \exp\left[i\,\boldsymbol{p}\cdot\boldsymbol{J}\right] f\,, \tag{5.28a}$$

$$M^{(n)}_{i_1\cdots i_n} := \int d^3p\, p_{i_1}\ldots p_{i_n} f = (-i)^n \left.\frac{\partial^n G[\boldsymbol{J}]}{\partial J_{i_1}\ldots\partial J_{i_n}}\right|_{\boldsymbol{J}=\boldsymbol{0}}\,, \tag{5.28b}$$

$$C^{(n)}_{i_1\cdots i_n} := (-i)^n \left.\frac{\partial^n \ln G[\boldsymbol{J}]}{\partial J_{i_1}\ldots\partial J_{i_n}}\right|_{\boldsymbol{J}=\boldsymbol{0}}\,. \tag{5.28c}$$

Vlasov hierarchy The evolution equations for the moments $M^{(n)}$ of the phase space distribution f can be determined from the Vlasov equation (6.1a) by multiplying it with $p_{i_1} \cdots p_{i_n}$ and performing an integration over momentum

$$\partial_t M^{(n)}_{i_1 \cdots i_n} = -\frac{1}{a^2 m} \nabla_j M^{(n+1)}_{i_1 \cdots i_n j} - m \nabla_{(i_1} V \cdot M^{(n-1)}_{i_2 \cdots i_n)} \,. \tag{5.29}$$

Indices enclosed in round brackets imply symmetrization according to $a_{(i} b_{j)} = a_i b_j + a_j b_i$. It turns out that a coupled Vlasov hierarchy for the moments emerges which means that in order to determine the time-evolution of the n-th moment the $(n+1)$-th moment is required. This closure problem for the hierarchy becomes more transparent when looking at the dynamical equation for the n-th cumulant $C^{(n)}$. The time evolution can be determined from the generating functional (5.28a) using the Vlasov equation (6.1a) and reads

$$\partial_t C^{(n)}_{i_1 \cdots i_n} = -\frac{1}{a^2 m} \left\{ \nabla_j C^{(n+1)}_{i_1 \cdots i_n j} + \sum_{S \in \mathcal{P}(\{i_1, \cdots, i_n\})} C^{(n+1-|S|)}_{l \notin S, j} \cdot \nabla_j C^{(|S|)}_{k \in S} \right\} - \delta_{n1} \cdot m \nabla_{i_1} V \,, \tag{5.30}$$

where S runs through the power set $\mathcal{P}$ of indices $\{i_1, \cdots, i_n\}$ and the Kronecker δ_{n1} in last term ensures that the potential contributes only to the equation for the first cumulant $C^{(1)}$ describing velocity. From this equation it becomes clear that one can set $C^{(n \geq 2)} \equiv 0$ in a consistent manner since each summand in the evolution equation of $C^{(2)}$ contains a factor of $C^{(n \geq 2)}$. In contrast, the time evolution of $C^{(3)}$ depends also on summands containing solely $C^{(2)}$ such that it cannot be trivially fulfilled when setting $C^{(n \geq 3)} \equiv 0$. A similar reasoning applies to all higher cumulants $C^{(n \geq 3)}$ and demonstrates that there is no consistent truncation of the hierarchy of cumulants apart from the one at second order. These arguments are seconded by numerical evidence indicating that as soon as velocity dispersion encoded in $C^{(2)}$ becomes relevant, even higher cumulants are sourced dynamically, see [PS09].

Strategies for closing the hierarchy Describing the physical system analytically in terms of a small number of degrees of freedom demands either (*i*) truncating the hierarchy (5.30) at some n by neglecting higher cumulants and setting them to zero, or (*ii*) to add an ansatz for the velocity dispersion to the Euler equation, or (*iii*) to resort to an ansatz $f[\Phi_a(\boldsymbol{x}, t), p]$ with some fields $\Phi_a(\boldsymbol{x}, t)$ for which the p-integrations can be performed analytically and for which the hierarchy is automatically fulfilled as soon the fields $\Phi_a(\boldsymbol{x}, t)$ fulfill their equations of motion.

The prominent dust model is an example which belongs to (*i*), (*ii*) and (*iii*); It provides the only known consistent truncation of Eq. (5.30), has the "ansatz" $\sigma_{ij} \equiv 0$ for the velocity dispersion and it is also of the type $f[\Phi_a(\boldsymbol{x}, t), p]$ with $\Phi_a = (n_\mathrm{d}(\boldsymbol{x}, t), \phi_\mathrm{d}(\boldsymbol{x}, t))$.

For instance, the approach of [McD11] is to assume $C^{(n>2)} = 0$ and corresponds to (*i*). Postulating an ansatz for the velocity dispersion – for example an imperfect fluid – or introducing an artificial adhesion-term in the evolution equation for the velocity, see [SZ89], corresponds to (*ii*). In both cases (*i*) and (*ii*) it is difficult to assess wether one is actually still modelling collisionless matter.

The ScM is an approach relying on (*iii*), namely it provides a special ansatz for the distribution function which allows to compute cumulants analytically, but it does not truncate the

cumulant hierarchy. The magic of the ScM is that if $\Phi_a(\boldsymbol{x},t) = \psi(\boldsymbol{x},t)$ fulfills the SPE, then the Vlasov hierarchy is automatically satisfied to arbitrary precision, if $\hbar, \sigma_x, \sigma_p$ are chosen appropriately.

In the following we will compare three different ansätze for the distribution function f: the dust model f_d, the Wigner function f_W as well as the Husimi distribution function $\bar{f}_\mathrm{W}$.

5.3.1 Hierarchy of moments of f_d

The generating functional for the dust model where f_d was inserted according to (5.7) is given by

$$G_\mathrm{d}[\boldsymbol{J}] = n_\mathrm{d} \exp\left[i\nabla\phi_\mathrm{d}\cdot\boldsymbol{J}\right] . \tag{5.31}$$

The moments $M_\mathrm{d}^{(n)}$ and cumulants $C_\mathrm{d}^{(n)}$ are then given by

$$M_\mathrm{d}^{(0)} = n_\mathrm{d} , \qquad M_{\mathrm{d}_i}^{(1)} = n_\mathrm{d}\phi_{\mathrm{d},i} , \qquad M_{\mathrm{d}_{i_1\cdots i_n}}^{(n\geq 2)} = n_\mathrm{d}\phi_{\mathrm{d},i_1}\cdots\phi_{\mathrm{d},i_n} , \tag{5.32a}$$

$$C_\mathrm{d}^{(0)} = \ln n_\mathrm{d} , \qquad C_{\mathrm{d}_i}^{(1)} = \phi_{\mathrm{d},i} , \qquad C_{\mathrm{d}_{i_1\cdots i_n}}^{(n\geq 2)} = 0 . \tag{5.32b}$$

Since the exponent of the generating functional is manifestly linear in $\boldsymbol{J}$, all cumulants of order higher than one vanish identically. This means that the dust model does not include effects like velocity dispersion, which is encoded in the second cumulant $C^{(2)}$, or vorticity since the velocity is determined from a potential ϕ. Therefore for the dust ansatz f_d, the Vlasov equation is equivalent to its first two equations of the hierarchy of moments, the pressureless fluid system (5.8) consisting of the continuity and Euler equation. The first two moments of the Vlasov hierarchy (5.29) are

$$\partial_t n_\mathrm{d} = -\frac{1}{a^2 m}\nabla_k\left(n_\mathrm{d}\phi_{\mathrm{d},k}\right) , \tag{5.33a}$$

$$\partial_t\left(n_\mathrm{d}\phi_{\mathrm{d},i}\right) = -\frac{1}{a^2 m}\nabla_j\left[n_\mathrm{d}\phi_{\mathrm{d},i}\phi_{\mathrm{d},j}\right] - m n_\mathrm{d}\nabla_i V_\mathrm{d} . \tag{5.33b}$$

If n_d and ϕ_d fulfill these equations then all evolution equations of the higher moments are automatically satisfied, for example Eqs. (5.33) imply that

$$\partial_t\left(n_\mathrm{d}\phi_{\mathrm{d},i}\phi_{\mathrm{d},j}\right) = -\frac{1}{a^2 m}\nabla_k\left(n_\mathrm{d}\phi_{\mathrm{d},i}\phi_{\mathrm{d},j}\phi_{\mathrm{d},k}\right) - m n_\mathrm{d}\nabla_{(i}V_\mathrm{d}\cdot\nabla_{j)}\phi_\mathrm{d} . \tag{5.34}$$

5.3.2 Hierarchy of moments of f_W

For simplicity we first consider the Wigner distribution function f_W as a model for a general distribution function f fulfilling the Vlasov equation. This case will serve as pedagogical demonstration how the closure of the hierarchy can be achieved by choosing a special ansatz for the distribution function. The generating functional can be computed by plugging the expression for

$f_{\rm W}$ in terms of $\psi = \sqrt{n}\exp(i\phi/\hbar)$ in (5.28a) and simplified by adopting again the shorthand notation $g^{\pm}(\boldsymbol{x}') := g\left(\boldsymbol{x}' \pm \frac{\hbar}{2}\boldsymbol{J}\right)$

$$G[\boldsymbol{J}] = \sqrt{n^+ n^-}\,\exp\left[\tfrac{i}{\hbar}(\phi^+ - \phi^-)\right] . \tag{5.35}$$

From this expression the calculation for the moments $M^{(n)}$ is straightforward and yields

$$M^{(0)} = n\,, \qquad M^{(1)}_i = n\phi_{,i}\,. \tag{5.36a}$$

As expected, even all higher moments $M^{(n\geq 2)}$ of $f_{\rm W}$ are given in terms of the two scalar degrees of freedom n and ϕ introduced as modulus and phase of the wave function ψ, respectively

$$M^{(2)}_{ij} = n\left[\phi_{,i}\phi_{,j} + \frac{\hbar^2}{4}\left(\frac{n_{,i}n_{,j}}{n^2} - \frac{n_{,ij}}{n}\right)\right], \tag{5.36b}$$

$$M^{(3)}_{ijk} = n\left[\phi_{,i}\phi_{,j}\phi_{,k} + \frac{\hbar^2}{4}\left(\overset{+\text{cyc. perm.}}{\left(\frac{n_{,i}n_{,j}}{n^2} - \frac{n_{,ij}}{n}\right)\phi_{,k}} - \phi_{,ijk}\right)\right], \tag{5.36c}$$

$$\sigma_{ij} := \frac{\hbar^2}{4}\left(\frac{n_{,i}n_{,j}}{n^2} - \frac{n_{,ij}}{n}\right) = C^{(2)}_{ij}\,, \quad C^{(3)}_{ijk} = -\frac{\hbar^2}{4}\phi_{,ijk}\,. \tag{5.36d}$$

To those terms which are marked by '+ cyc. perm.' cyclic permutations of the indices have to be added. As we will explain in the following, this special form of the higher moments and cumulants amounts to having closed the infinite Wigner-Vlasov hierarchy for the moments of $f_{\rm W}$ without truncating it. To demonstrate this we take moments of the Wigner-Vlasov equation (5.19) where we consider corrections to the Vlasov equation up to arbitrary order in $\hbar^2$. The $\hbar$-terms constitute correction terms to the Vlasov hierarchy (5.29) which become relevant for $M^{(n\geq 3)}$ but do not contribute to $M^{(n\leq 2)}$ since they have at least three derivatives with respect to momentum which cancel all lower moments than the third. Therefore the first three evolution equations are completely analogous to the ones obtained for the dust model. By plugging in the expression for $M^{(2)}$ we obtain a closed system of differential equations for n and $\phi_{,i}$.

$$\partial_t n = -\frac{1}{a^2 m}\nabla_k(n\phi_{,k})\,, \tag{5.37a}$$

$$\partial_t(n\phi_{,i}) = -\frac{1}{a^2 m}\nabla_j\left[n\phi_{,i}\phi_{,j} + \frac{\hbar^2}{4}\left(\frac{n_{,i}n_{,j}}{n} - n_{,ij}\right)\right] - nm\nabla_i V\,. \tag{5.37b}$$

We see that Eqs. (5.37) determining time evolution of the first two moments of $f_{\rm W}$ are identical to the fluid-like equations obtained directly from the Schrödinger equation (5.15). This can be verified easily by plugging (5.37a) into (5.37b) and using that the difference in the 'quantum velocity dispersion' term arising from (5.41c) and (5.14b) is only apparent since

$$\frac{\hbar^2}{4}\nabla_j\left(\frac{n_{,i}n_{,j}}{n} - n_{,ij}\right) = -\frac{\hbar^2}{2}n\nabla_i\left(\frac{\Delta\sqrt{n}}{\sqrt{n}}\right)\,. \tag{5.38}$$

Note that a proper pressure term in the Euler equation would have the form ∇p with some p and not the form $n\nabla Q$. Rather the left hand side of (5.37b) suggests that this term constitutes a 'quantum velocity dispersion', since it is of the form $\nabla_i(n\sigma_{ij})$. Equivalently, one can interpret the $\hbar$ term as a correction to the Newtonian potential $V \to V + Q$.

The evolution equation for the second moment $M^{(2)}$ involves the third moment $M^{(3)}$ and is given by

$$\partial_t M^{(2)}_{ij} = -\frac{1}{a^2 m}\nabla_k M^{(3)}_{ijk} - nm\nabla_{(i}V \cdot \nabla_{j)}\phi\,. \tag{5.39}$$

For the Wigner function f_W all moments $M^{(n)}$ can be expressed entirely in terms of the density n and conjugate velocity $\nabla\phi$. Hence, this ansatz closes the hierarchy since Eq. (5.39) is automatically fulfilled when $M^{(2)}$ and $M^{(3)}$, taken from (5.36b) and (5.36c) respectively, are expressed in terms of n and ϕ which fulfill the corresponding fluid equations (5.37). The same is true for all higher moments.

5.3.3 Hierarchy of moments of $\bar{f}_\mathrm{W}$

5.3.3.1 Moments up to third order

We want to resort to a special ansatz for the p-dependence of f which allows to compute moments up to arbitrary order analytically. The coarse-grained Wigner distribution function $\bar{f}_\mathrm{W}$ provides us with such an ansatz. Furthermore it is well-suited to model a general distribution function f fulfilling the Vlasov equation as was demonstrated in [WK93]. By plugging in the expression for $\bar{f}_\mathrm{W}$ in terms of $\psi = \sqrt{n}\exp(i\phi/\hbar)$ we can rewrite the generating functional to get

$$\bar{G}[\boldsymbol{J}] = \exp\left[\tfrac{{\sigma_x}^2}{2}\Delta - \tfrac{{\sigma_p}^2}{2}\boldsymbol{J}^2\right]\sqrt{n^+ n^-}\,\exp\left[\tfrac{i}{\hbar}(\phi^+ - \phi^-)\right]\,. \tag{5.40}$$

From this expression the calculation for the moments $\bar{M}^{(n)}$ is straightforward and yields

$$\bar{M}^{(0)} =: \bar{n} = \exp\left(\frac{{\sigma_x}^2}{2}\Delta\right)n\,, \tag{5.41a}$$

$$\bar{M}^{(1)}_i =: m\bar{n}\bar{u}_i = \exp\left(\frac{{\sigma_x}^2}{2}\Delta\right)(n\phi_{,i})\,. \tag{5.41b}$$

The corresponding velocity $\bar{\boldsymbol{u}}$ is mass-weighted which is obtained by smoothing the momentum field and then dividing by the smoothed density field. This is precisely the definition commonly used in the effective field theory of large-scale structure, compare [MP13, BNSZ12c]. From a physical point of view $\bar{\boldsymbol{u}}$ describes the center-of-mass velocity of the collection of particles inside a coarsening cell of diameter σ_x around $\boldsymbol{x}$.
As expected, even all higher moments $\bar{M}^{(n\geq 2)}$ of $\bar{f}_\mathrm{W}$ are given in terms of the two scalar degrees

of freedom n and ϕ introduced as modulus and phase of the wave function ψ, respectively

$$\bar{M}^{(2)}_{ij} = \exp\left(\frac{{\sigma_x}^2}{2}\Delta\right)\left\{n\left[\phi_{,i}\phi_{,j} + {\sigma_p}^2\delta_{ij} + \sigma_{ij}\right]\right\}, \tag{5.41c}$$

$$\bar{M}^{(3)}_{ijk} = \exp\left(\frac{{\sigma_x}^2}{2}\Delta\right)\left\{n\left[\phi_{,i}\phi_{,j}\phi_{,k} + \overset{+\text{cyc. perm.}}{\left({\sigma_p}^2\delta_{ij} + \sigma_{ij}\right)\phi_{,k}} - \frac{\hbar^2}{4}\phi_{,ijk}\right]\right\}. \tag{5.41d}$$

The corresponding cumulants can be calculate from the previous results using

$$\bar{C}^{(2)}_{ij} = \frac{\bar{M}^{(2)}_{ij}}{\bar{M}^{(0)}} - \frac{\bar{M}^{(1)}_i \bar{M}^{(1)}_j}{[\bar{M}^{(0)}]^2} \tag{5.41e}$$

$$= {\sigma_p}^2\delta_{ij} + \frac{\overline{n\sigma_{ij}}}{\bar{n}} + \frac{\overline{n\phi_{,i}\phi_{,j}}}{\bar{n}} - \frac{\overline{n\phi_{,i}}\;\overline{n\phi_{,j}}}{\bar{n}^2}, \tag{5.41f}$$

$$\bar{C}^{(3)}_{ijk} = \frac{\bar{M}^{(3)}_{ijk}}{\bar{M}^{(0)}} - \overset{+\text{cyc. perm.}}{\frac{\bar{M}^{(2)}_{ij}\bar{M}^{(1)}_k}{[\bar{M}^{(0)}]^2}} + 2\frac{\bar{M}^{(1)}_i\bar{M}^{(1)}_j\bar{M}^{(1)}_k}{[\bar{M}^{(0)}]^3} \tag{5.41g}$$

$$= \frac{\bar{M}^{(3)}_{ijk}}{\bar{M}^{(0)}} - \overset{+\text{cyc. perm.}}{\bar{C}^{(2)}_{ij}\bar{C}^{(1)}_k} - \bar{C}^{(1)}_i\bar{C}^{(1)}_j\bar{C}^{(1)}_k. \tag{5.41h}$$

As we will explain in the following, this allows to close the infinite hierarchy for the moments of $\bar{f}_{\mathrm{W}}$ arising from the Husimi-Vlasov Eq. (5.22) without setting any of the cumulants to zero. Instead, all higher moments are determined self-consistently from the lowest two, which are dynamical and represent the coarse-grained density $\bar{n}$ and velocity $\bar{\boldsymbol{u}}$, respectively. This distinguishes our formalism fundamentally from phenomenological models which attempt to close the hierarchy by postulating an ansatz for the second cumulant, called stress tensor $n\sigma_{ij}$, but simultaneously setting all higher cumulants to zero. For example, the ansatz for the velocity dispersion of a cosmological imperfect fluid is given by $n\sigma_{ij} = p\delta_{ij} + \eta(\nabla_i u_j \nabla_j u_i - \frac{2}{3}\delta_{ij}\nabla\cdot u) + \zeta\delta_{ij}\nabla\cdot u$ where p denotes the pressure and η and ζ are shear and bulk viscosity coefficients respectively. The underlying approximation $\sigma_{ij} \approx 0$ is valid during the first stages of gravitational instability when structures are well described by a single coherent flow (single-stream). However, as soon as multiple streams become relevant after shell-crossings, velocity dispersion and vorticity are generated dynamically and at once all higher moments become relevant too [PS09]. Thus, the hierarchy of cumulants of CDM dynamics cannot be truncated after shell-crossing has occurred.

In the subsequent calculation it will be necessary to reexpress all higher moments entirely in terms of $\bar{M}^{(0)} \propto \bar{n}$ and $\bar{M}^{(1)} \propto \bar{n}\bar{u}_i$. For this purpose we introduce the D-symbol which allows us to express the coarse-graining of any product or quotient entirely in terms of its coarse-grained constituents, for example

$$\exp\left[\tfrac{1}{2}\sigma^2\Delta\right]\left(n\phi_{,i}\phi_{,j}\right) = \exp\left[\tfrac{1}{2}\sigma^2(\Delta - D)\right]\left(\frac{(\bar{n}\bar{u}_i)(\bar{n}\bar{u}_j)}{\bar{n}}\right). \tag{5.42}$$

5.3.3.2 Properties of the D-symbol

D fulfills the Leibniz product rule of a first derivative operator when acting on compositions of

$$A, B, C \in \{\bar{n}, \bar{j}_i\}$$

or derivatives thereof, but when acting on a single function it is the Laplacian.

$$D(A) = \Delta A \ , \ D(g(A)) = \partial_A g(A) DA = \partial_A g(A) \Delta A \, , \tag{5.43a}$$

$$D(AB) = (DA)B + A(DB) = (\Delta A)B + A(\Delta B) \, . \tag{5.43b}$$

Applying the definition of the D-symbol one can derive the following expressions for the evaluation of D^n

$$D^n \left(\frac{AB}{C} \right) = \sum_{k=0}^{n} \binom{n}{k} \sum_{l=0}^{n-k} \binom{n-k}{l} \Delta^l A \cdot \Delta^{n-k-l} B \cdot D^k \left(\frac{1}{C} \right) , \tag{5.44a}$$

$$D^k \left(\frac{1}{C} \right) = \sum_{r=0}^{k} \frac{(-1)^r r!}{C^{r+1}} B_{k,r} \left(\Delta C, \Delta^2 C, ..., \Delta^{k-r+1} C \right) , \tag{5.44b}$$

where $B_{k,r}$ are the Bell polynomials. Furthermore we have that

$$\frac{1}{\exp\left({\sigma_x}^2 \Delta\right) C} = \exp\left({\sigma_x}^2 D\right) \left(\frac{1}{C} \right) . \tag{5.44c}$$

5.3.3.3 Evolution equations for the moments of $\bar{f}_{\mathrm{W}}$

We take moments of the Husimi-Vlasov equation where we consider corrections to the Vlasov equation up to arbitrary order in ${\sigma_x}^2$, ${\sigma_p}^2$ and $\hbar^2$. Eq. (5.22) can be employed to obtain evolution equations for the first two moments $\bar{n} = \bar{M}^{(0)}$ and $\bar{u}_i = \bar{M}_i^{(1)}/(m\bar{n})$ which correspond to density and mass-weighted velocity, respectively. The velocity $\bar{u}_i$ which follows from a coarse-grained distribution function $\bar{f}$ is automatically a mass-weighted one computed according to $m\bar{u}_i = \overline{n\phi_{,i}}/\bar{n}$ and does not coincide with the volume-weighted velocity $\bar{\phi}_{,i}$. In particular, the volume-weighted velocity is automatically curl-free whereas the mass-weighted velocity will have vorticity in general.
By plugging in the expression for $\bar{M}^{(2)}$ and rewriting it according to (5.42) we obtain a closed system of differential equations for $\bar{n}$ and $\bar{u}_i$

$$\partial_t \bar{n} = -\frac{1}{a^2} \boldsymbol{\nabla} \cdot (\bar{n} \bar{\boldsymbol{u}}) \, , \tag{5.45a}$$

$$\begin{aligned} \partial_t (\bar{n} \bar{u}_i) &= -\frac{1}{a^2 m^2} \nabla_j \bar{M}_{ij}^{(2)} - \nabla_i \bar{V} \exp\left({\sigma_x}^2 \overleftarrow{\nabla}_x \overrightarrow{\nabla}_x \right) \bar{n} + \frac{{\sigma_p}^2}{a^2 m^2} \nabla_i \bar{n} \\ &= \exp\left(\frac{{\sigma_x}^2}{2} (\Delta - D) \right) \left\{ -\frac{1}{a^2 m^2} \nabla_j \left[\frac{(\bar{n}\bar{u}_i)(\bar{n}\bar{u}_j)}{\bar{n}} + \frac{\hbar^2}{4} \left(\frac{\bar{n}_{,i} \bar{n}_{,j}}{\bar{n}} - \bar{n}_{,ij} \right) \right] - \bar{n} \, \nabla_i \bar{V} \right\} , \end{aligned} \tag{5.45b}$$

$$\Delta \bar{V} = \frac{4\pi G \, \varrho_0}{a} \left(\bar{n} - 1 \right) . \tag{5.45c}$$

These equations are supplemented by the constraint that there exists a scalar function $\bar{\phi}$ such that

$$m\,\bar{n}\,\bar{\boldsymbol{u}} = \bar{n}\exp\left(\sigma_x{}^2\overleftarrow{\nabla}_x\overrightarrow{\nabla}_x\right)\nabla\bar{\phi}\,. \tag{5.45d}$$

The last constraint equation is the analogue of the curl-free constraint Eq. (5.9c). It enforces a very particular non-zero vorticity for $\bar{\boldsymbol{u}}$. The evolution equation for the second moment $\bar{M}^{(2)}$ involves the third moment $\bar{M}^{(3)}$ and is given by

$$\partial_t\bar{M}^{(2)}_{ij} = -\frac{1}{a^2m}\nabla_k\bar{M}^{(3)}_{ijk} - m\nabla_{(i}\bar{V}\exp\left(\sigma_x{}^2\overleftarrow{\nabla}_x\overrightarrow{\nabla}_x\right)(\bar{n}\bar{u}_{j)}) + \frac{\sigma_p{}^2}{a^2}(\bar{n}\bar{u}_{(i)}{}_{,j)}\,. \tag{5.46}$$

For the coarse-grained Wigner distribution function $\bar{f}_{\mathrm{W}}$ all moments $\bar{M}^{(n)}$ can be expressed entirely in terms of the density $\bar{n}$ and velocity $\bar{\boldsymbol{u}}$. This ansatz closes the $\bar{f}_{\mathrm{W}}$ hierarchy since all higher moment equations are automatically fulfilled when $\bar{M}^{(n)}$ is calculated from (6.5), expressed in terms of $\bar{n}$ and $\bar{\boldsymbol{u}}$ which are to be determined from the coarse-grained fluid equations (5.45). In appendix 5.A we show by explicit computation that Eq. (5.34) is automatically satisfied when $\bar{M}^{(2)}$ and $\bar{M}^{(3)}$ are taken from (5.41c) and (5.41d) respectively.
Alternatively and for practical applications, instead of solving the coarse-grained fluid equations (5.45) for $\bar{n}$ and $\bar{\boldsymbol{u}}$ one can simply solve the SPE (5.13) for n and ϕ and construct the cumulants of interest according to (5.41). Both procedures automatically and self-consistently include multi-streaming effects. Note that Eqs. (5.45) are naturally written in terms of the macroscopic momentum $\bar{\boldsymbol{j}} \equiv \bar{n}\bar{\boldsymbol{u}}$, which is just the coarse-grained quantum momentum and therefore free from phase jump pathologies, see Sec. 5.2.4.1.

5.3.4 Comparison between the models

If we compare the fluid equations obtained via the Husimi approach Eqs. (5.45) with the one obtained directly from the Madelung representation Eqs. (5.14) of the underlying Schrödinger-Vlasov system we see that our special ansatz for the distribution function $f = \bar{f}_{\mathrm{W}}$ amounts to considering a spatially coarse-grained Schrödinger-Vlasov system. However, we have to bear in mind that this is not equivalent with a direct coarse-graining of n and $\phi_{,i}$ since the mass-weighted velocity is $m\bar{u}_i = \overline{n\phi_{,i}}/\bar{n}$ is not the same as the volume-weighted velocity $\bar{\phi}_{,i}$. It is nontrivial that although $\bar{f}_{\mathrm{W}}$ is coarse-grained with respect to space and momentum, the Schrödinger equation (5.14) and the first moment equations (5.45) of $\bar{f}_{\mathrm{W}}$ are related only by spatial coarse-graining. Note however that for instance the velocity dispersion $\bar{C}^{(2)}_{ij}$ does depend on σ_p as well as on σ_x and $\hbar$, see Eq. (5.41c).

One the one hand, by neglecting the $\hbar$-corrections which constitute a 'quantum velocity dispersion' term in the Euler-type equation in (5.45b) we obtain the same evolution equations for the coarse-grained fields $\bar{n}$ and $\bar{\boldsymbol{u}}$ as given in [Dom00, BD05]. Their approach started from a microscopic system of N particles, which was spatially coarse-grained to obtain a set of hydrodynamic equations for the macroscopic fluid variables $\bar{n}$ and $\bar{\boldsymbol{u}}$. This was done by expanding the smoothing operator $\exp\left[\frac{1}{2}\sigma_x{}^2\Delta\right]$ up to first order in the so-called large-scale expansion. Interestingly, these closed-form equations can be derived from our formalism based on the Schrödinger

equation when setting $\hbar \to 0$ in (5.45b)

$$\partial_t(\bar{n}\bar{u}_i) = \exp\left(\frac{{\sigma_x}^2}{2}(\Delta - D)\right)\left\{-\frac{1}{a^2m^2}\nabla_j\left[\frac{(\bar{n}\bar{u}_i)(\bar{n}\bar{u}_j)}{\bar{n}}\right] - \bar{n}\,\nabla_i\bar{V}\right\}. \tag{5.47}$$

In this sense we provide a formal resummation in the large-scale parameter of [Dom00]. Furthermore we can clearly see that one would have arrived exactly at same equation by spatially coarse-graining a dust fluid (5.33). However, this identification is only meaningful as long as no shell-crossing has occurred in the microscopic dust fluid as otherwise the filtering cannot be inverted. This explains the apparent contradiction between the fact that the dust model breaks down at shell-crossing although, according to [Dom00], the macroscopic system shows adhesive behavior. Obviously, the exact dust solution extended after shell-crossing, see red dashed line in Fig. 5.1, does not exhibit adhesive behavior and coarse-graining cannot change this. This exemplifies that it is no longer possible to obtain the macroscopic quantities as the coarse-grained solution to the microscopic dust equations (5.33).

On the other hand, numerical examples show that the $\hbar$-term in the ScM regularizes shell-crossing caustics already on the microscopic level, see [Tak89, CS03] and the next section. This allows to derive (5.45) from the SPE (5.13) and shows that in order to obtain a solution to the macroscopic system (5.45) one can simply coarse-grain the solution to the microscopic system. Therefore the Schrödinger method may be viewed as improved dust model with built-in infinity regularization (quantum potential proportional to $\hbar^2$ in (5.15d)) as well as built-in eraser of regularization artefacts (spatial coarse-graining with σ_x in (5.45)).

Nearly cold initial conditions can be implemented by choosing

$$\psi_{\mathrm{ini}}(x) = \sqrt{n_{\mathrm{d}}(a_{\mathrm{ini}}, x)}\exp\left[i\,\phi_{\mathrm{d}}(a_{\mathrm{ini}}, x)/\hbar\right], \tag{5.48}$$

at some early time where shell-crossings have not occurred yet, where n_{d} and ϕ_{d} denote solutions to the dust system (5.8). Although we have our focus on cold dark matter, let us remark that ScM also opens up the possibility to study warm initial conditions.

5.4 Numerical example

We study the standard toy example of sine wave collapse, whose exact solution up to shell-crossing is given by the (in this case exact) Zel'dovich approximation [Zel70] and therefore has a long tradition in testing techniques of LSS calculations [KS83]. Of particular relevance to our work is [CS03] were the collapse of a wave function fulfilling the Schrödinger Poisson equation and modifications to it were studied and compared to the exact Zel'dovich solution.

5.4.1 Initial conditions

As reviewed in App. 5.B, the Zel'dovich approximation in the 1D (or plane parallel or pancake) collapse is the exact solution to the hydrodynamic Eqs. (5.9). We choose as initial linear density contrast

$$\delta_{\mathrm{lin}}(a, q) = D(a)\cos\left(\frac{\pi q}{L}\right), \tag{5.49a}$$

which guarantees collapse at $a = 1$, because according to Eq. (5.61) the nonlinear density for dust is given by

$$n_{\rm d}(a,q) = [1-\delta_{\rm lin}(a,q)]^{-1} \tag{5.49b}$$

choosing $D(1) = 1$. The displacement field Ψ describes the trajectories $x(q) = q + \Psi(a,q)$ of fluid elements and is given by

$$\Psi_{\rm d}(a,q) = -D(a)\frac{L}{\pi}\,\sin\left(\frac{\pi q}{L}\right)\,, \tag{5.49c}$$

which can be used to express the velocity

$$\partial_x \phi_{\rm d} = u_{\rm d}(q) = a^3 H(a)\partial_a \Psi_{\rm d}(a,q) \tag{5.49d}$$

and density $n_{\rm d}$ in terms of x. We choose an Einstein-de Sitter universe, $H^2 = 8\pi G/3\,\varrho_0 a^{-3}$ with $H(a=1) = 70\,{\rm km\,s^{-1}Mpc^{-1}}$ and we pick $L = 10\,{\rm Mpc}$.

We start to solve the Schrödinger equation at $a_{\rm ini} = 0.01$ and choose as initial wave function Eq. (5.48) with periodic boundary conditions such that $-L < x < L$. We verified that during the linear stage of collapse, the phase ϕ and amplitude n of the wave function, agree with their dust analogues $\phi_{\rm d}$ and $n_{\rm d}$ if $\tilde{\hbar} \equiv \hbar/m \lesssim 10^{-4}\,{\rm Mpc}\,c$, where c is the speed of light. This agrees with findings of [CS03]. In the remaining section we will mostly show results for $\tilde{\hbar} = 2\times 10^{-5}\,{\rm Mpc}\,c$ and $\sigma_x = 0.1\,{\rm Mpc}$. Only for the study of relaxation ($a = 30.0$ in the following plots) as well as the Bohmian trajectories – the integral lines of $\partial_x\phi$ – in App. 5.B we choose the larger value $\tilde{\hbar} = 10^{-4}\,{\rm Mpc}$ and $\sigma_x = 0.2\,{\rm Mpc}$. Note that the mass m can be absorbed in ϕ and $\phi_{\rm d}$, whereby m disappears from the Schrödinger and fluid equations, respectively. The Wigner and coarse-grained Wigner functions are depicted in Fig. 5.2.

It turns out that in single-streaming regions one can choose $\sigma_x\sigma_p \ll \hbar$ while still ensuring $\bar{f}_{\rm W} \geq 0$, see Fig. 5.2. Comparing to the top panel of Fig. 5.1, it becomes clear that $\bar{f}_{\rm W}$ can achieve a much higher resolution than $f_{\rm H}$ in u-direction. It exemplifies that the initial conditions are well modeled by the SPE and that the large width of $f_{\rm H}$ in the initial conditions shown in Fig. 5.1 does not imply that the dynamics is poorly resolved. In contrast, it only means that if we want to use the more convenient $f_{\rm H}$ we sacrifice available information once we calculate moments and cumulants. Another possibility to circumvent the oscillatory behaviour of the Wigner function is to use a mixed state corresponding to N gravitating wave functions rather than a single one. This was the method of choice in [SBR+13]. It turns out that if N is large enough, the Wigner function becomes well behaved even without any smoothing. Since our goal is to develop analytical tools on the basis of the ScM, is seems to be more prospective to consider a single wave function and adopt the Husimi representation.

5.4.2 Time evolution of ψ, $f_{\rm H}$ and moments

We numerically evolve the initial wave function ψ Eqs. (5.48, 5.49) describing a nearly cold and linear CDM overdensity using the SPE (5.13). Within the linear regime the phase ϕ and amplitude n are basically indistinguishable from $\phi_{\rm d}$ and $n_{\rm d}$, however once shell-crossing is approached

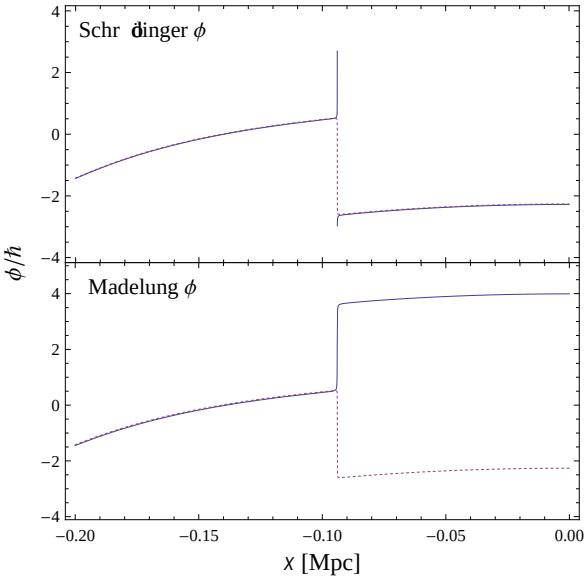

FIGURE 5.3: The first phase jump $\Delta\phi = 2\pi$ occurred around $a_\phi \simeq 1.07$.

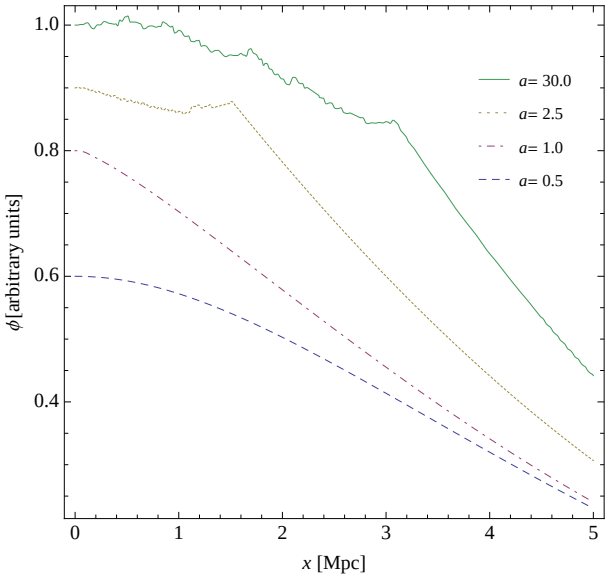

FIGURE 5.4: The phase ϕ of the wave function at different times. The wiggly behaviour is characteristic for multi-streaming regions.

they start to deviate. The occurrence of singularities in n_d and phase jumps ϕ are the most dramatic differences. In Fig. 5.3 we show the phase closely before and after the time of first phase jump a_ϕ, shortly after the time $a = 1$, where n_d diverges. Shortly before (*full*) and after (*dotted*) a_ϕ, ϕ develops very steep gradients (diverging at the the time of phase jump and changing sign). For the wave function ψ this causes no problem since the amplitude $\sqrt{n}$ vanishes when the step becomes infinitely sharp and allows the phase to "reconnect" (*upper panel*), while keeping ψ smooth. For the Madelung representation this causes another problem: at the moment of phase jump, not only $\nabla\phi$ but also $\dot{\phi}$ diverges on a whole spatial interval (*lower panel*). This second type of divergence is an artifact caused by neglecting the fact that ϕ is defined only modulo 2π.

At the time a_ϕ and point x_ϕ where the phase develops the sharp step we have $\sqrt{n} = 0$. Therefore it makes sense to determine the variance of position and momentum

$$\langle x^2\rangle = \frac{\int_{-x_\phi}^{x_\phi} |\psi|^2 x^2\, dx}{\int_{-x_\phi}^{x_\phi} |\psi|^2\, dx} \quad , \quad \langle p^2\rangle = -\hbar^2 \frac{\int_{-x_\phi}^{x_\phi} \psi^* \Delta\psi\, dx}{\int_{-x_\phi}^{x_\phi} |\psi|^2\, dx} \,. \tag{5.50}$$

Doing the numerical integrals it shows that $\langle x^2\rangle\langle p^2\rangle \simeq (\hbar/2)^2$, with $\hbar/(2m) = 10^{-5}\mathrm{Mpc}\,c$ specified for our simulation. The physical interpretation of this result is that the wave function collapsed to its densest possible state given the initial conditions: a minimum uncertainty wave packet forms within $[-x_\phi, x_\phi]$ at the time a_ϕ, which expands consequently. We therefore can say that the ScM contains "shell-crossing without shell-crossing". This bounce only looks like shell-crossing when coarse-grained over, see App. 5.B. The result also suggests optimal values for the coarse-graining parameters ${\sigma_p}^2 = \langle p^2\rangle$ and ${\sigma_x}^2 = \langle x^2\rangle$ of the 1D collapse. We therefore conclude that shell-crossing infinities appearing in n_d are now traded for infinities in $\nabla\phi$, which

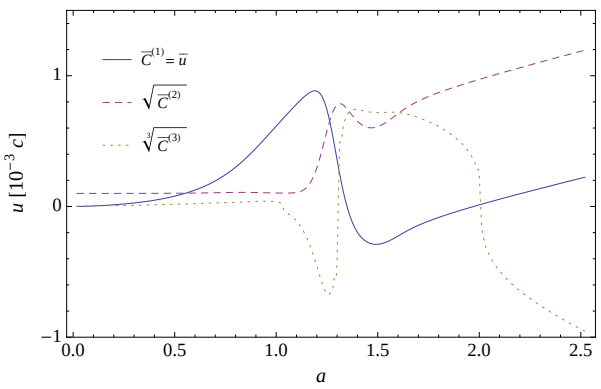

FIGURE 5.5: Comparison between the first three cumulants at the position $x = -0.5\,\mathrm{Mpc}$. They are all equally important after shell-crossing: the hierarchy cannot be truncated.

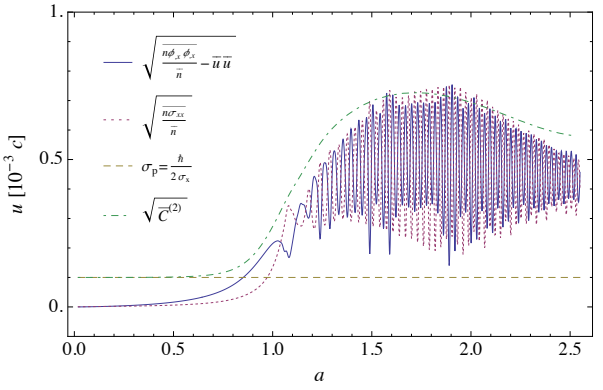

FIGURE 5.6: Comparison between the different parts of the second cumulant at $x = 0$.

fortunately do not cause infinities or other pathologies in ψ because n vanishes at those instances and ψ remains smooth.

The wiggly form of the phase, see Fig. 5.4, corresponds to large $\nabla\phi$, which are visible as the strongly oscillating green dotted lines in the right panel of Fig. 5.7. Because of many phase jumps the amplitude n shows strong spatial oscillations Fig. 5.7, left. These oscillations are invisible in the physical quantities of interest: the moments and cumulants of f_{H}. We show the density and the first 3 cumulants in Fig. 5.7 and Fig. 5.5. They are smooth and physically meaningful. Fig. 5.5 also shows that all higher cumulants are switched on at the same time such that the cumulant hierarchy cannot be truncated. In the ScM the two degrees of freedom of ψ store information about all cumulants.

It is also interesting to note that $\bar{C}^{(2)}$, Eq. (6.6e), can be decomposed into a purely spatial average induced velocity dispersion, a smoothed but microscopic velocity dispersion and a constant part. Most notably, the first two contributions are equally large and show oscillations over time but add up to a smooth sum, see Fig. 5.6. Finally let us consider the full phase space dynamics in Fig. 5.1. The Husimi distribution f_{H} contains like ψ the information about all cumulants, but unlike ψ, in a form directly related to physical quantities. The most interesting features are the regularity at shell-crossing, the formation of multi-stream regions and the possibility to follow the dynamics until virialization.

Notice that $\bar{C}^{(2)}$ within multi-stream regions remains always positive while $\bar{C}^{(1)}$ basically vanishes. We therefore checked that the (macroscopic) tensor virial theorem [BT08], following from the Euler-type equation (5.45b) and a steady state assumption (within the virialized object $\bar{u} = 0$),

$$\frac{1}{a^2}\int_{-x_{\mathrm{vir}}}^{x_{\mathrm{vir}}} \mathrm{d}x\,(\bar{M}^{(2)}_{xx} - {\sigma_p}^2\bar{n}) = \int_{-x_{\mathrm{vir}}}^{x_{\mathrm{vir}}} \mathrm{d}x\,x\,\exp[\tfrac{1}{2}{\sigma_x}^2\Delta]\,(n(x)\partial_x V(x)) \tag{5.51}$$

is approximately satisfied for $x_{\mathrm{vir}} \simeq 2.8\,\mathrm{Mpc}$ for $a = 30$. The σ_p-term as well as the boundary terms from integrating by parts are completely negligible. Looking at the right panel of Fig. 5.7 we see that below x_{vir} the macroscopic velocity $\bar{u}$ is basically zero for $a = 30.0$, looking at the

left panel we see that the macroscopic density peaks around $x_{\rm vir}$ and drops off afterwards. Note that relaxation is known to take much longer in 1D than 3D [TGK96].

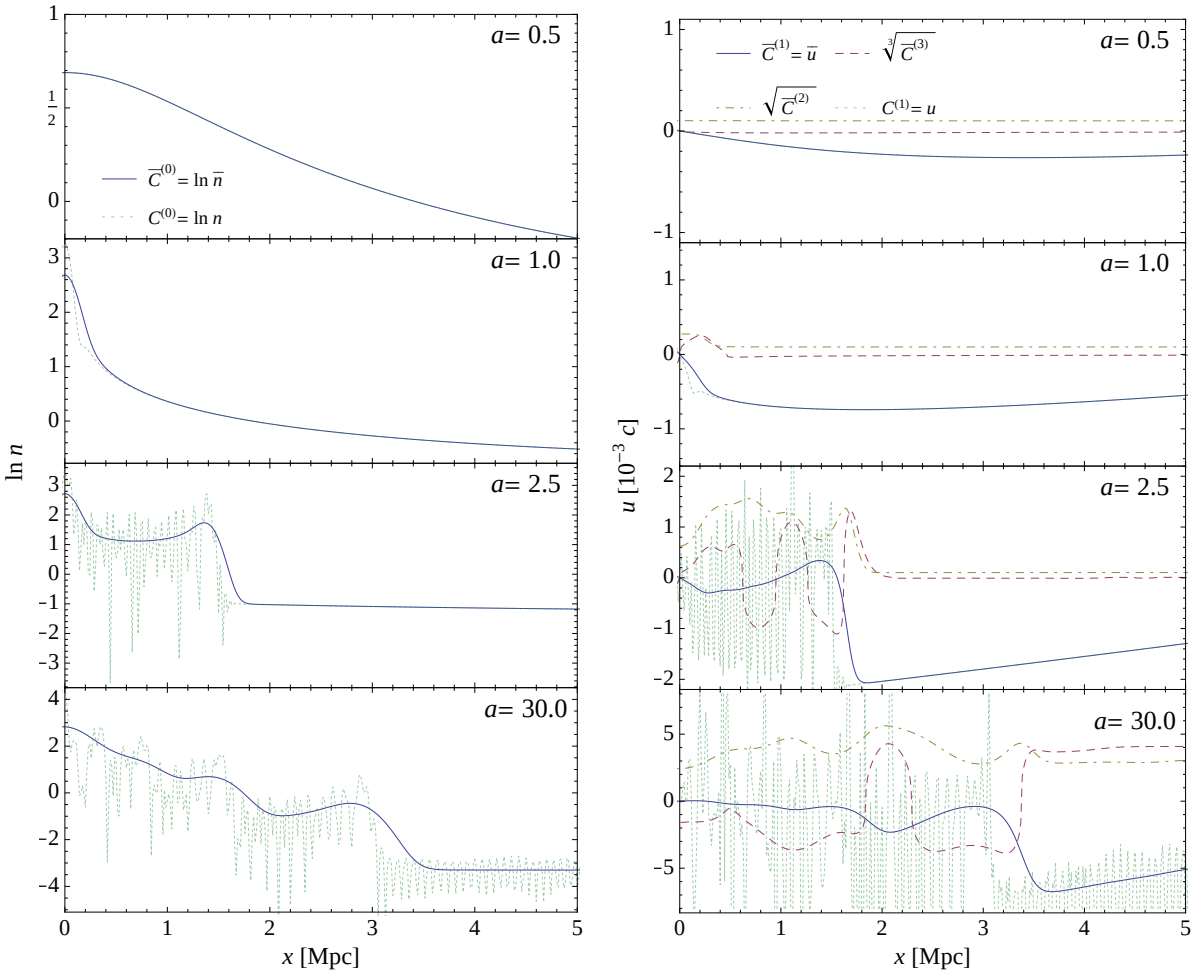

FIGURE 5.7: *left* Number density (*full*) and amplitude squared of wave function (*dotted*). *right* The first three cumulants and the gradient of phase of the wave function, $\nabla\phi$. All these quantities are shown at four characteristic times: the unset of the nonlinear regime around $a = 0.5$, shell-crossing of the dust model at $a = 1$, formation of multi-stream regions around the second shell-crossing at $a = 2.5$, and virialization $a = 30$. These four times are also shown in Fig. 5.1.

5.5 Prospects

For analysing, understanding as well as estimating statistical errors of observations of LSS, one is interested in n-point correlation functions of the phase space density. Within ScM these correlation functions are simply related to the $2n$-point correlation functions of the scalar ψ

$$\langle f(t,\boldsymbol{r}_1,\boldsymbol{p}_1)...f(t,\boldsymbol{r}_n,\boldsymbol{p}_n)\rangle = \left(\prod_{i=1}^{n}\int d^3x_i d^3y_i\; K_{\rm H}(\boldsymbol{r}_i,\boldsymbol{x}_i,\boldsymbol{p}_i)K^*_{\rm H}(\boldsymbol{r}_i,\boldsymbol{y}_i,\boldsymbol{p}_i)\right)\times \\ \times\langle\psi(t,\boldsymbol{x}_1)\psi^*(t,\boldsymbol{y}_1)...\psi(t,\boldsymbol{x}_n)\psi^*(t,\boldsymbol{y}_n)\rangle\,,$$

where $K_{\rm H}$ is the Husimi kernel Eq. (5.23) and the angle brackets denote ensemble average over all initial conditions, usually assumed to be Gaussian distributed. This allows the construction of n-point redshift space matter and halo correlation functions through a simple projection

$$\langle\bar{n}(t,\boldsymbol{s}_1)...\bar{n}(t,\boldsymbol{s}_n)\rangle = \left(\prod_{i=1}^{n}\int d^3p_i d^3r_i\;\delta_{\rm D}\left(\boldsymbol{s}_i-\boldsymbol{r}_i-\frac{\boldsymbol{p}_i\cdot\hat{\boldsymbol{z}}}{a^2mH}\hat{\boldsymbol{z}}\right)\right)\langle f(t,\boldsymbol{r}_1,\boldsymbol{p}_1)...f(t,\boldsymbol{r}_n,\boldsymbol{p}_n)\rangle\,,$$

where $\hat{\boldsymbol{z}}$ points along the line of sight and $\boldsymbol{s}_i$ are the observed positions in redshift space. As a first step one can study the redshift space 2-point correlation in the case where $\hbar = 0$, keeping only σ_x and σ_p. This will be the topic of Chapter 6. This approach is motivated by the observation that keeping only σ_x results in a resummation in the large-scale parameter of the macroscopic model suggested in [Dom00, BD05], namely Eq. (5.47).

Ultimately we would like to keep $\hbar$, since from our numerical study it is clear that the quantum pressure plays a crucial rule not only in shell-crossing regularization but also within the cumulants, see Fig. 5.6. Therefore we need a method to calculate the time evolution of $\langle\psi(t,\boldsymbol{x}_1)...\psi^*(t,\boldsymbol{y}_n)\rangle$ including $\hbar$ and most desirably in a non-perturbative fashion.

There is a simple Lagrangian and action for ψ from which the SPE follow from the variational principle [AS01]. Therefore one might take the route of [Tas11] and integrate the nonperturbative renormalization group flow with time as flow parameter [GKP10]. Another possibility would be to explore the fact that $\hbar$ corresponds to the phase space resolution and thus might be used as a flow parameter with interpretation of Kadanoff's block spin transformation [Kad66].

It might also be possible to interpret the formation of wiggly phases via phase jumps, see Figs. 5.3 and 5.4, as something akin to a phase transition. Halo formation under time evolution would then correspond to magnetic domain formation in a ferromagnet under adiabatic cooling.

The ScM could also be connected to effective field theory formulations of LSS formation [BNSZ12c, PSZ13, CLP13]. Since the ScM is a "UV complete" theory it might be possible to derive an effective field theory including its parameters.

Another research route could be to look for stationary complex solutions of the SPE[4] with the aim of understanding the universality of density profiles of virialized objects by varying the entropy functional $S[\psi] = -\int d^3x d^3p\; f_{\rm H}\ln f_{\rm H}$. Since ScM allows for virialization it could prove useful in further analytical understanding of violent relaxation [Lyn67, SH92] that leads to universal phase space and density profiles [NFW97, HK11, He12, DM14].

The original aim of the Schrödinger method was to provide a numerical alternative to N-body simulations in order to follow the phase space dynamics of collisionless and only gravitationally

[4] To our knowledge, so far only real solutions have been studied [AS01, MPT98]. Fig. 5.4 however suggests that stationary solutions that result from gravitational collapse are complex.

interacting matter [WK93]. Note that although [WK93] showed that nothing is gained in terms of speed and resources, both methods have different strengths. Let us mention here some advantages of the ScM. A N-body simulation samples phase much more detailed in regions of high density, because there are simply more particles, while the ScM has fixed phase space resolution. For instance, in order to understand the phase space structure of voids, which are sparsely sampled in N-body simulations, the ScM should be better suited. Another advantage of the ScM is that after a slight modification – using a complex Klein-Gordon equation instead of the Schrödinger equation [Wid97] – it can model relativistic collisionless matter. This would allow to follow the phase space dynamics of relativistic neutrinos, that depending on mass can become non-relativistic once the frozen-in but decreasing temperature falls below their rest mass. For every species – be it warm, cold, relativistic or non-relativistic collisionless matter – a complex Klein-Gordon or Schrödinger field has to be introduced and the corresponding equations have to be solved. The set of these equations then needs to be supplemented by the Poisson equation sourced by all the fields.[5] For numerical simulations [WK93, Wid97] explain how to create the desired initial conditions, which need not to be cold and in case of initially relativistic neutrinos, should be sampled from a Fermi-Dirac distribution.[6] Therefore the ScM opens up the possibility to self-consistently study the combined dynamics of CDM and neutrinos and thus provides a way to constrain neutrino masses and their mass hierarchy through the study of large-scale structure formation [MCV+11], which together with CMB observations, might even lead to first measurement of neutrino masses.

5.6 Conclusion

We started with the coupled nonlinear Vlasov-Poisson system (6.1) for the phase space distribution function f which is relevant for LSS formation of CDM particles which interact only by means of the gravitational potential. Inspired by the Schrödinger method (ScM) proposed in [WK93] for numerical simulations we aimed at employing its ability to describe effects of multi-streaming while extending recent studies regarding coarse-grained descriptions of CDM and their implications investigated in [PMSV12b, Dom00].

Following closely [WK93], we introduced a complex field ψ whose time-evolution is governed by the Schrödinger-Poisson equation (SPE) (5.13) and constructed the coarse-grained Wigner probability distribution $\bar{f}_{\mathrm{W}}$ according to (5.21) from this wave function. We derived that the time-evolution of $\bar{f}_{\mathrm{W}}$ is determined by Eq. (5.22) which is in good correspondence to the one governed by the coarse-grained Vlasov equation (5.12). Using a numerical toy example we showed how the ScM is able to regularize shell-crossing singularities and allows to follow the dynamics into the fully nonlinear regime. Furthermore we showed how higher order cumulants (5.41) like velocity dispersion can be calculated directly from the wave function and that a vorticity is generated by the coarse-graining procedure.

[5] A priori one should rather use the Einstein equation sourced by the energy momentum tensors of all the fields and check that Newtonian gravity is justified, as we did in the case for pure CDM in Chapters 3 and 4.

[6] Note that one cannot describe fermions using a scalar field on a fundamental level, but one can still model the phase distribution of fermions with a scalar field if the fermions behave collisionless.

This means that it suffices to solve the SPE (5.13) with dust-like initial conditions (5.48), express the result obtained for ψ in Madelung form $\sqrt{n}\exp(i\phi/\hbar)$, and then simply coarse-grain n and $n\nabla\phi$ to obtain the physical density $\bar{n}$ and momentum $m\bar{n}\bar{\boldsymbol{u}}$, respectively. In a similar fashion all higher cumulants (5.28c) following from (6.5) can be obtained from a solution to SPE (5.13).

We derived the corresponding closed-form fluid-like equations (5.45) for the smooth density field $\bar{n}$ and the mass-weighted velocity $\bar{\boldsymbol{u}}$. This is only possible because the 'quantum pressure' term proportional to $\hbar^2$ resolves shell-crossing singularities already on the microscopic level. We showed that solving the macroscopic equations (5.45) means closing the hierarchy for the moments of $\bar{f}_{\mathrm{W}}$, without truncating the cumulant hierarchy, thereby proposing a different approach to the closure problem than truncation in terms of cumulants. Indeed, all higher cumulants can be written in terms of of $\bar{n}$ and $\bar{\boldsymbol{u}}$.

We are now equipped with a model containing only two degrees of freedom that is able to fully describe structure formation.

Appendix 5

5.A Explicit calculation for closure of the hierarchy

As mentioned in 6.2.1 it can be shown that the evolution equation for the second moment (5.46) is automatically fulfilled when the coarse-grained fluid equations (5.45) for density $\bar{n}$ and mass-weighted velocity $\bar{\boldsymbol{u}}$ are satisfied. In order to prove that we perform the following steps:

1. Start with the time evolution equation for the second moment (5.46) which involves the third one.

$$\partial_t \bar{M}^{(2)}_{ij} \stackrel{?}{=} -\frac{1}{a^2 m}\nabla_k \bar{M}^{(3)}_{ijk} - m\nabla_{(i}\bar{V}\exp\left({\sigma_x}^2 \overleftarrow{\nabla}_x \overrightarrow{\nabla}_x\right)(\bar{n}\bar{u}_{j)}) + \frac{{\sigma_p}^2}{a^2}(\bar{n}\bar{u}_{(i)})_{,j)} \tag{5.52}$$

2. Insert the explicit expressions for $\bar{M}^{(2)}$ and $\bar{M}^{(3)}$ given by (5.41c) and (5.41d).

$$\begin{aligned}
&\partial_t \exp\left(\frac{{\sigma_x}^2}{2}\Delta\right)\left[n\phi_{,i}\phi_{,j} + {\sigma_p}^2 n\delta_{ij} + \frac{\hbar^2}{4}\left(\frac{n_{,i}n_{,j}}{n} - n_{,ij}\right)\right] \qquad (5.53)\\
&\stackrel{?}{=} -\exp\left(\frac{{\sigma_x}^2}{2}\Delta\right)\nabla_k\left\{n\phi_{,i}\phi_{,j}\phi_{,k} + \overset{+\text{cyc. perm.}}{{\sigma_p}^2\delta_{ij}n\phi_{,k}} + \frac{\hbar^2}{4}\left[\left(\frac{n_{,i}n_{,j}}{n} - n_{,ij}\right)\overset{+\text{cyc. perm.}}{\phi_{,k}} - n\phi_{,ijk}\right]\right\}\\
&\quad - \nabla_{(i}\bar{V}\exp({\sigma_x}^2\overleftarrow{\nabla}_x\overrightarrow{\nabla}_x)(\bar{n}\bar{u}_{j)}) + {\sigma_p}^2(\bar{n}\bar{u}_{(i)})_{,j)}
\end{aligned}$$

3. Express everything in terms of $\bar{n}$ and $\bar{j}_i = \bar{n}\bar{u}_i = \overline{(n\phi_{,i})}$ using the rule for the D-symbol (5.42).

$$\begin{aligned}
&\partial_t\left\{\exp\left[\frac{{\sigma_x}^2}{2}(\Delta - D)\right]\left[\frac{\bar{j}_i\bar{j}_j}{\bar{n}} + \frac{\hbar^2}{4}\left(\frac{\bar{n}_{,i}\bar{n}_{,j}}{\bar{n}} - \bar{n}_{,ij}\right)\right] + {\sigma_p}^2\bar{n}\delta_{ij}\right\} \qquad (5.54)\\
&\stackrel{?}{=} -\exp\left[\frac{{\sigma_x}^2}{2}(\Delta - D)\right]\nabla_k\left[\frac{\bar{j}_i\bar{j}_j\bar{j}_k}{\bar{n}^2} + \frac{\hbar^2}{4}\left[\left(\frac{\bar{n}_{,i}\bar{n}_{,j}}{\bar{n}} - \bar{n}_{,ij}\right)\overset{+\text{cyc. perm.}}{\frac{\bar{j}_k}{\bar{n}}} - \frac{1}{3}\bar{n}\left(\frac{\bar{j}_i}{\bar{n}}\right)_{,jk}\right]\right]\\
&\quad - {\sigma_p}^2\nabla_k\overset{+\text{cyc. perm.}}{\left(\delta_{ij}\bar{j}_k\right)} - \nabla_{(i}\bar{V}\exp({\sigma_x}^2\overleftarrow{\nabla}_x\overrightarrow{\nabla}_x)\bar{j}_{j)} + {\sigma_p}^2\bar{j}_{(i,j)}
\end{aligned}$$

4. Pull the time-derivative through the smoothing operator and apply the product rule to re-express the terms.

$$\exp\left[\frac{{\sigma_x}^2}{2}(\Delta - D)\right]\left\{\frac{\partial_t \bar{j}_{(i}\bar{j}_{j)}}{\bar{n}} - \frac{\bar{j}_i\bar{j}_j\partial_t\bar{n}}{\bar{n}^2} + \frac{\hbar^2}{4}\left(\frac{\partial_t\bar{n}_{,(i}\bar{n}_{,j)}}{\bar{n}} - \frac{\partial_t\bar{n}\,\bar{n}_{,i}\bar{n}_{,j}}{\bar{n}^2} - \partial_t\bar{n}_{,ij}\right)\right\} \tag{5.55}$$
$$+ {\sigma_p}^2\partial_t\bar{n}\delta_{ij}$$
$$\stackrel{?}{=} \exp\left[\frac{{\sigma_x}^2}{2}(\Delta - D)\right]\left\{-\nabla_k\left(\frac{\bar{j}_i\bar{j}_k}{\bar{n}}\right)\frac{\bar{j}_j}{\bar{n}} - \frac{\bar{j}_i\bar{j}_k}{\bar{n}}\nabla_k\left(\frac{\bar{j}_j}{\bar{n}}\right) - \nabla_{(i}\bar{V}\bar{j}_{j)}\right.$$
$$\left. - \frac{\hbar^2}{4}\nabla_k\left[\left(\frac{\bar{n}_{,i}\bar{n}_{,j}}{\bar{n}} - \bar{n}_{,ij}\right)\frac{\bar{j}_k}{\bar{n}} - \frac{1}{3}\bar{n}\left(\frac{\bar{j}_i}{\bar{n}}\right)_{,jk}\right]\right\}^{+\text{cyc. perm.}} - {\sigma_p}^2\nabla_k\bar{j}_k\delta_{ij}$$

5. Employ the fluid equations (5.45) to carry out the time derivatives $\partial_t(\bar{n})$ and $\partial_t\bar{j}_i$.

$$\exp\left[\frac{{\sigma_x}^2}{2}(\Delta - D)\right]\left\{-\exp\left[\frac{{\sigma_x}^2}{2}(\Delta - D)\right]\left[\nabla_k\left(\frac{\bar{j}_k\bar{j}_{(i}}{\bar{n}}\right) + \nabla_{(i}\bar{V}\bar{n} + \frac{\hbar^2}{4}\nabla_k\left(\frac{\bar{n}_{,k}\bar{n}_{,(i}}{\bar{n}} - \bar{n}_{,k(i}\right)\right]\frac{\bar{j}_{j)}}{\bar{n}}\right. \tag{5.56}$$
$$\left. + \frac{\bar{j}_i\bar{j}_j\bar{j}_{k,k}}{\bar{n}^2} - \frac{\hbar^2}{4}\left(\frac{\bar{j}_{k,k(i}\bar{n}_{,j)}}{\bar{n}} - \frac{\bar{j}_{k,k}\bar{n}_{,i}\bar{n}_{,j}}{\bar{n}^2} - \bar{j}_{k,ijk}\right)\right\}$$
$$\stackrel{?}{=} \exp\left[\frac{{\sigma_x}^2}{2}(\Delta - D)\right]\left\{-\nabla_k\left(\frac{\bar{j}_i\bar{j}_k}{\bar{n}}\right)\frac{\bar{j}_j}{\bar{n}} - \frac{\bar{j}_i\bar{j}_k}{\bar{n}}\nabla_k\left(\frac{\bar{j}_j}{\bar{n}}\right) - \nabla_{(i}\bar{V}\bar{j}_{j)} - \right.$$
$$\left. \frac{\hbar^2}{4}\nabla_k\left[\left(\frac{\bar{n}_{,i}\bar{n}_{,j}}{\bar{n}} - \bar{n}_{,ij}\right)\frac{\bar{j}_k}{\bar{n}} - \frac{1}{3}\bar{n}\left(\frac{\bar{j}_i}{\bar{n}}\right)_{,jk}\right]\right\}^{+\text{cyc. perm.}}$$

6. Combine the different D-symbols acting successively on the terms to yield an overall D-symbol according to

$$\exp\left[\tfrac{1}{2}{\sigma_x}^2(\Delta - D_{ABC})\right]\left(\bar{A}\bar{B}\bar{C}\right) = \exp\left[\tfrac{1}{2}{\sigma_x}^2(\Delta - D_{A(BC)})\right]\left[\bar{A}\exp\left[\tfrac{1}{2}{\sigma_x}^2(\Delta - D_{BC})\right](\bar{B}\bar{C})\right].$$

This is possible since the action of the D-symbol depends on the product structure it is acting on.

$$\exp\left[\frac{{\sigma_x}^2}{2}(\Delta - D)\right]\left\{\frac{\hbar^2}{4}\left[\nabla_k\left(\frac{\bar{n}_{,k}\bar{n}_{,(i}}{\bar{n}} - \bar{n}_{,k(i}\right)\frac{\bar{j}_{j)}}{\bar{n}} + \frac{\bar{j}_{k,k(i}\bar{n}_{,j)}}{\bar{n}} - \frac{\bar{j}_{k,k}\bar{n}_{,i}\bar{n}_{,j}}{\bar{n}^2} - \bar{j}_{k,ijk}\right]\right\} \tag{5.57}$$
$$\stackrel{\checkmark}{=} \exp\left[\frac{{\sigma_x}^2}{2}(\Delta - D)\right]\left\{\frac{\hbar^2}{4}\nabla_k\left[\left(\frac{\bar{n}_{,i}\bar{n}_{,j}}{\bar{n}} - \bar{n}_{,ij}\right)\frac{\bar{j}_k}{\bar{n}} - \frac{1}{3}\bar{n}\left(\frac{\bar{j}_i}{\bar{n}}\right)_{,jk}\right]\right\}^{+\text{cyc. perm.}}$$

One has to note that equality is only established once we make use of the constraint Eq. (6.7c).

5.B Lagrangian formulation

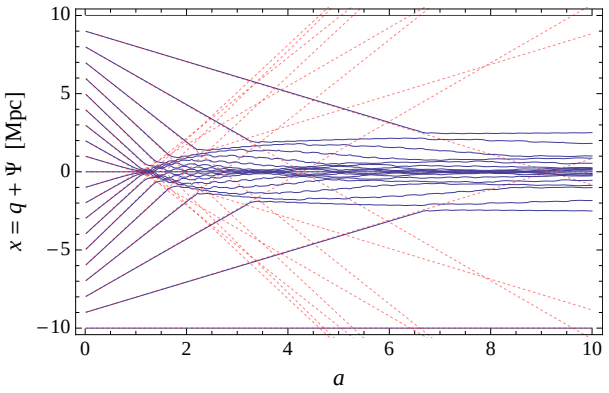

FIGURE 5.8: *red dotted* Zel'dovich trajectories Eq. (5.60), *blue* Bohmian trajectories Eq. (5.59).

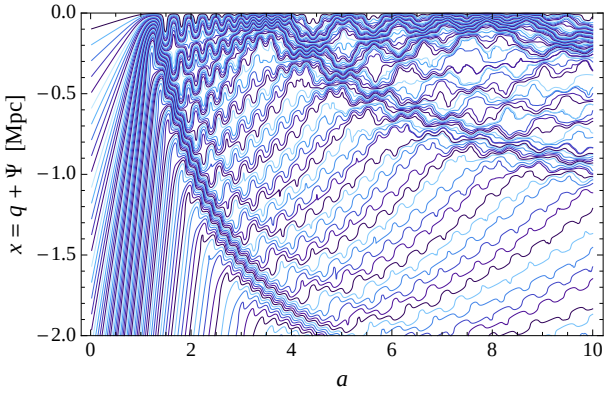

FIGURE 5.9: Detailed view of the Bohmian trajectories, Eq. (5.59).

We follow [RB12] to rewrite the fluid-like system Eqs. (5.15) formulated in terms n and $\nabla\phi$ evaluated at the Eulerian position $\boldsymbol{x}$, into a Lagrangian system in which the sole dynamical variable is the displacement field $\boldsymbol{\Psi}$, that maps between $\boldsymbol{x}$ and the Lagrangian (or initial coordinate of a fluid element) $\boldsymbol{q}$. Since the continuity and Euler equation Eqs. (5.9) are unchanged apart from the added quantum potential Q in Eq. (5.15b) the analogue of Eq. 2.31 in [RB12] is

$$\left[(1+\Psi_{l,l})\delta_{ij} - \Psi_{i,j} + \Psi^c_{i,j})\right]\Psi''_{i,j} = \alpha(\eta)(J^F - 1) + J^F \frac{\hbar^2}{4m^2}\Delta_x\left(\frac{\Delta_x[(J^F)^{-1/2}]}{(J^F)^{-1/2}}\right), \quad (5.58)$$

which can be obtained by solving the continuity equation with $1+\delta = 1/J^F$, where $J^F = \det(F_{ij}) = \det(\delta_{i,j} + \Psi_{i,j})$ and $F_{ij} = \partial x^i/\partial q^j$ is the Jacobian relating $\boldsymbol{x}$ and $\boldsymbol{q}$ and with $\nabla_x\phi/m = \boldsymbol{\Psi}'$, where a prime denotes a derivative wrt to superconformal time η related to cosmic time t via $dt = a^2 d\eta$. In eq. (5.58) the Laplacians are with respect to $\boldsymbol{x}$, rather than $\boldsymbol{q}$ and have therefore to be rewritten in terms of $\boldsymbol{q}$ using the Jacobian F_{ij}. The equation is supplemented by a constraint equation $F_{i,n}\epsilon_{njk}F_{l,j}F'_{l,k} = 0$ that follows from $\nabla_x \times \boldsymbol{u} = 0$. If the density and velocity distribution depend only on $\boldsymbol{x} = (x,0,0)$, (and therefore $\boldsymbol{q} = (q,0,0)$), the above system can be written, using $\epsilon_{qqq} = 0$ and $\Psi_i =: \Psi\delta_{iq}$ and $J^F = 1 + \Psi_{,q}$ as

$$\Psi'' = \alpha(\eta)\Psi + \frac{\hbar^2}{2m^2}\left(\frac{10(\Psi_{,qq})^3}{(1+\Psi_{,q})^6} - 8\frac{\Psi_{,qq}\Psi_{,qqq}}{(1+\Psi_{,q})^5} + \frac{\Psi_{,qqqq}}{(1+\Psi_{,q})^4}\right), \quad (5.59)$$

where $\alpha(\eta) = 4\pi G a \varrho_0$. Note that compared to the 3D case (5.58), we were able to integrate already once over q in order to obtain (5.59).

In the case of $\hbar = 0$, we recover the case of dust

$$\Psi''_{\rm d} = \alpha(\eta)\Psi_{\rm d}\,, \quad (5.60)$$

whose exact solution is the Zel'dovich approximation $\Psi_{,q}(\boldsymbol{q},a) = -D(a)\delta_{\rm lin}(\boldsymbol{x} = \boldsymbol{q})$, where $\delta_{\rm lin}(\boldsymbol{x})$ is the initial condition Eulerian density field (which is assumed to vanish at $a = 0$)

linearly extrapolated to $a = 1$ using the linear growth $D(a)$. The red dashed lines in Fig. 5.1 are points $(q + \Psi, \Psi')$, parametrized by q and can be extended after shell-crossing. Unfortunately, this continuation does not behave as CDM and the trajectories continue on their straight lines indefinitely, see red lines in Fig. 5.8. Including the $\hbar$-terms, a separation ansatz does not work anymore and we do not expect to find an exact solution of (5.59), see Figs. 5.8 and 5.9 for the complicated dynamics of Ψ for the case of initial conditions studied in Sec. 5.4. Under a coarse-grained view the Bohmian and collisionless CDM trajectories would turn into network that is indistinguishable. On a microscopic level though, they are very different, see Fig. 5.9. Although the phase space density $f_{\rm H}$ behaves as if shell-crossings and multi-stream regions form, the phase ϕ of the wave function ψ is single-valued and therefore the trajectories $\boldsymbol{q} + \boldsymbol{\Psi}$ never intersect. The intricate behaviour of $\boldsymbol{\Psi}$ *emulates* multi-streaming. Given the Bohmian trajectories $\boldsymbol{\Psi}(\boldsymbol{q}, a)$ one can recover $n(\boldsymbol{x}, a)$ and $\phi(\boldsymbol{x}, a)$ via

$$n(x, a) = \frac{1}{1 + \Psi_{,q}(q,\, a)}\Big|_{q=q(x,a)} \tag{5.61}$$

$$\partial_x \phi(x, a)/m = \Psi'(q,\, a)\Big|_{q=q(x,a)}\,, \tag{5.62}$$

where the q-dependent expressions are converted into x-depend ones via inversion of $x = q + \Psi(q, a)$. The Lagrangian formulation Eq. (5.58) of the Madelung representation, Eq. (5.14) suffers from the same singularities as the Euler-type equation Eq. (5.15b); at the isolated space-time points where the phase ϕ jumps about 2π, the velocity $\nabla\phi$ and therefore $\ddot{\boldsymbol{\Psi}}$ diverge and change sign. Figs. 5.8 and 5.9 were constructed from the solution of the Schrödinger-Poisson equation (5.13) and not from Eq. (5.59).

6

Gaussian multi-streaming model for redshift space distortions

This chapter arose in collaboration with Cora Uhlemann and Thomas Haugg. We study the effect of coarse-graining the dynamics of a pressureless selfgravitating fluid (coarse grained dust) in the context of nonlinear cosmological perturbation theory, both in the Eulerian und Lagrangian framework, as well as in real and redshift space. We calculate from first principles the large scale vorticity power spectrum. We extend the Gaussian streaming model (GSM) together with convolution Lagrangian perturbation theory (CLPT) to the case of general phase space distribution functions and explicitly evaluate it for case of "coarse grained dust", which is the limit $\hbar \to 0$ of the Schrödinger method discussed in the last chapter. This extendeded CLPT we denote by cg-CLPT. Large scale vorticity and velocity dispersion are automatically included and we compare results for halo correlation functions in real and redshift space to our measurements within the publicly available Horizon Run 2 halo catalog. We find that the real space correlation functions of halos and the mean pairwise velocity are optimised if the coarse graining scale is chosen to be $1\,\mathrm{Mpc}/h$, while the second pairwise velocity moment entering the GSM is optimised if the smoothing scale is chosen to be the Lagrangian size of the halo. CLPT is basically the same as the (Post-)Zel'dovich approximation, for which it is well known that a smoothing of the initial conditions can improve the agreement with N-body simulations. We therefore compare our cgCLPT to the case where one only coarse-grains the initial conditions but uses standard dust dynamics and CLPT.

6.1 Introduction

Among analytical methods developed to describe the formation of large-scale structure (LSS), perturbative schemes based on the popular dust model [Pee80] play an important part. The dust model describes self-gravitating collisionless cold dark matter (CDM) as a pressureless fluid which fulfills a coupled system of differential equations consisting of continuity, Euler and Poisson equation. These equations can be solved perturbatively – either in the Eulerian frame [BCGS02b] where everything is expanded in terms of density and velocity or in the Lagrangian framework [BMW94b] where fluid-trajectories or displacements are considered. Those perturbative techniques provide satisfactory results within the linear regime of structure formation and resumming some classes of perturbative corrections [SC06, MP07, Mat08] can enhance their range of applicability towards mildly nonlinear scales. However, they are condemned to break down eventually in the deeply nonlinear regime due to their fundamental limitation to describe the ensemble of self-gravitating dark matter particles as a pressureless fluid characterized solely by density and velocity. Indeed, the dust model is a truncation of the infinite hierarchy for the cumulants of the phase-space distribution of particles which fulfills the Vlasov (or collisionless Boltzmann) equation. Truncating the hierarchy is only consistent as long as the particle trajectories are well described by a single coherent flow, called single-stream approximation, since as soon as multiple streams become relevant all higher cumulants are sourced dynamically, see [PS09].

To tackle this shortcoming several semi-analytical methods based on Effective Field Theory (EFT) both in the Eulerian [PMSV12b, CHS12, CFGS13, MP13] and Lagrangian framework [PSZ13, SZ14] as well as in a path integral approach [CLP13] have been developed. They describe the large scale physics in terms of an effective fluid that is treated perturbatively and characterized by several parameters arising from small scale physics. These parameters are not calculable within the EFT framework itself but have to be inferred from observations or N-body simulations, at least as long as no full theory describing the small scale physics is at hand. The strategy of EFT is to integrate out (or formally solve) the dynamics of the short-wavelength part in order to obtain closed-form equations of motion for the long-wavelength quantities. All formulations of EFT of LSS have an underlying coarse-graining approach in common but differ in the precise implementation of the cut-off, while some rely on sharp-k filtering, others employ smooth filters like spherical top-hat or Gaussian window functions. The coarse-graining procedure allows to separate long from short scale modes and handle the former perturbatively while regarding the latter as source terms for higher phase space cumulants like velocity dispersion.

In [Dom00] a spatially coarse-grained description of a many-body gravitating system for the evolution of LSS has been studied and shown to lead to a fluid-like description which recovers the usual dust model when scales substantially larger than the coarse-graining scale are considered. It was noted that the corresponding hierarchy for the moments can in principle be closed by expressing the microscopic degrees of freedom through the macroscopic density and velocity. This requires the filtering to be invertible which excludes sharp-k and top-hat filter but favors the Gaussian window which was considered. In contrast to the Schrödinger method, the Gaussian filter was Taylor-expanded in the filter length σ_x up to leading order, called large-scale expansion. In this expansion the lowest order term was shown to automatically yield the dust model whereas

the first order involves a correction proportional to the coarse-graining scale squared ${\sigma_x}^2$. It was demonstrated that this term gives rise to a velocity dispersion which enters into the Euler equation and it was argued that it leads to adhesive behavior, see also [BD05]. This method was conjectured to allow for successive improvements over the aforementioned dust and adhesion models.

Our approach is based on the Schrödinger method (ScM) as described in Chapter 5, which is able to catch the fully-fledged N-body dynamics and incorporate higher cumulants like velocity dispersion which are relevant for multi-streaming. In the limit $\hbar \to 0$, which will be considered in the following, the ScM constitutes a full resummation in the filter length σ_x of the coarse grained hydrodynamics described in [Dom00]. In this limit the ScM method reduces to the coarse grained dust model which will – in analogy to the dust model – be studied perturbatively.

One shortcoming of the dust model, namely the absence of vorticity and inability to generate it dynamically, becomes evident if one compares velocity power spectra obtained from perturbation theory directly to cosmological N-body simulations, see for example [PS09, HAA14]. While it has been supposed in [PS09] that considering a mass-weighted velocity may account for large scale vorticity, we provide the first consistent implementation of this idea and perform a comprehensive analysis based on a coarse-graining approach.

We are mainly interested in studying the coarse-grained dust model in terms of the displacement field within Lagrangian perturbation theory (LPT). In first order LPT it is possible to exactly compute the density correlation function from the first order displacement field in a nonperturbative fashion which is called Zel'dovich approximation (ZA), see [Zel70]. In the ZA particles are displaced along straight trajectories, parametrized by the linear growth function, with an initial velocity determined by the Newtonian potential at their initial position. The ZA is capable of accurately describing gravitational dynamics over a surprisingly wide range of scales. In [CMS93] the so-called truncated Zel'dovich approximation (TZA) was proposed as phenomenological method to improve agreement with N-body data by artificially smoothing the initial power spectrum at the nonlinear scale of the final time of the simulation. The effect of the smoothing is to reduce velocity in high density regions thereby preventing shell-crossings and subsequent erasure of overdensities. Therefore, counterintuitively, smoothing the initial power spectrum, thereby reducing the initial power on small scales, in turn increases the final power on these scales. A detailed study and comparison between different filters in [MPS94] revealed that a Gaussian leads to best agreement with N-body data and considerable improvement over sharp k-truncation as originally suggested in [CMS93] and top-hat in coordinate space as studied in [PMSV12b]. This is an empirical indication, entirely independent from the theoretical one described before, why the invertability of Gaussian smoothing should prove useful in describing CDM dynamics. Furthermore, it also provides a prescription how to appropriately choose the filter size σ_x, namely in correspondence to the nonlinear scale k_{TZA} by requiring $\sigma_x k_{\mathrm{TZA}} \simeq 1$. Note that, similarly, assuming $\hbar = 0$ in the ScM requires σ_x to be large enough to prevent shell-crossing singularities, see Sec. 5.3.4. Focusing on statistical properties of the nonlinearly evolved density field like the power spectrum, the TZA amounts to smoothing the linear initial power spectrum without affecting the dynamics itself.

It is known that the Post-Zel'dovich approximation (PZA), where the displacement fields are calculated from second rather than first order perturbation theory, improves over the ZA. Ac-

cordingly, the truncated Post-Zel'dovich approximation (TPZA), in which again only the initial power spectrum is smoothed, performs even better than TZA, compare [BMW94b, WGB96]. Our coarse-graining dust model recovers the TZA at lowest order. At second and higher order though – unlike TPZA – it is not only a smoothing of the initial conditions that occurs but also the underlying dynamics is changed. In particular, we apply the framework of Convolution Lagrangian perturbation theory (CLPT) developed in [CRW13] for the dust model to our coarse-grained dust model. CLPT can be understood as a partial resummation of the formalism presented in [Mat08] which provides a partial resummation of LPT while incorporating nonlinear halo bias. A big advantage of ZA/PZA/CLPT is the clearer physical picture it offers for the study of halo correlation functions, which are a key ingredient of the halo model [CS02] that is widely used in the analysis of galaxy, cluster and lensing surveys. In order to understand halo correlations one needs to understand halo bias. But halo bias is best understood using the spherical collapse model and excursion set theory, both of which operate in the initial conditions and therefore in Lagrangian space, where they locally assign mass and collapse time to clouds or proto-halos within the initial density field. Therefore once the clustered or biased field of proto-halos is known it can be propagated to Eulerian space using a Lagrangian method.

Another advantage concerns convergence properties and accuracy of the correlation function on scales of interest, like the BAO scale or the mildly nonlinear scales. It is known that ZA performs much better on those scales, see the first Figure of [Tas14]; a higher precision is achieved with a smaller order in perturbation theory. This is in part due to better convergence properties of the LPT displacement field and in part due to fact that ZA takes place in real space rather than Fourier space such that potentially wrong small k parts of the power spectrum $P(k)$ cannot get mixed into large r parts of the correlation function $\xi(r)$. Although independent, but making use of the same advantage is the observation that small r in the correlation function can be strongly affected by baryonic physics, while large r, most importantly the BAO peak, are not affected, see [AWSH13].

In order to infer the correlation function in redshift space, relevant to observations made in galaxy surveys, one has to take peculiar velocities into account which affect the observed redshift due to the Doppler shift. In [Fis95] the correlation function in redshift space was derived by considering the joint probability distribution of density and velocity. Assuming that the density is a Gaussian random field and the velocity is related to density as in linear perturbation theory, one obtains that the redshift space correlation function is given by a convolution of the real space distribution function and an approximately Gaussian kernel whose mean and variance are given by the the scale dependent mean and variance of the pairwise velocity. This so-called Gaussian streaming model (GSM) can be understood as generalization of the streaming model originally introduced in [Pee80] to a scale-dependent rather than constant velocity dispersion which correctly reproduces the linear theory result derived in [Kai87]. To compute correlation functions and in particular halo correlation functions in redshift space the GSM has also been applied in the context of second order perturbation theory (CLPT) for the dust model in [RW11, WRW14, Whi14].

Structure This chapter is organized as follows: In Sec. 6.2 we review the dust model, introduce the coarse-grained dust model and determine the moments of the different phase space distribution of coarse grained dust. In Sec. 6.3 we provide a review of the two standard schemes of perturbation theory, Eulerian as well as Lagrangian Perturbation Theory and explain their connection. Sec. 6.4 is devoted to the derivation of the corresponding Eulerian perturbation kernels to determine the power and cross spectra for the coarse-grained dust model. Then we describe how these kernels can be mapped to Lagrangian space. In Sec. 6.5 we recapitulate the Gaussian Streaming model for the single-stream case and generalize it to include multiple streams. Finally we apply this result to compute the functions entering the Gaussian streaming model for the coarse-grained dust model. In Sec. 6.6 we present the results for the halo correlation functions in real and redshift space as well as halo velocity statistics and compare them to measurements of the same quantities within the publicly available Horizon Run 2 (HR2) halo catalog [KPGD09, KPR+11]. We propose a new "hybrid" approach which introduces two smoothing scales, one to optimise the real space correlation function and mean pairwise velocity and one to optimise the second pairwise velocity moment. We conclude in Sec. 6.7.

6.2 Coarse-grained dust model

6.2.1 Vlasov equation and cumulant hierarchy

We recapitulate from Chapter 5 that the dynamics of cold dark matter (CDM) can be conveniently described using a phase space distribution function $f(t, \boldsymbol{x}, \boldsymbol{p})$ which contains all relevant information about the system. Imposing phase-space conservation one directly obtains the Vlasov (or collisionless Boltzmann) equation which governs the time evolution of the distribution function. This equation is supplemented by the Poisson equation which encodes gravitational interaction and causes the Vlasov equation

$$\partial_t f = -\frac{\boldsymbol{p}}{a^2 m} \cdot \nabla_x f + m \nabla_x V \cdot \nabla_p f \,, \tag{6.1a}$$

$$\Delta V = \frac{4\pi G \varrho_0}{a} \left(\int d^3 p f - 1 \right) \tag{6.1b}$$

to be nonlocal and nonlinear in the phase space distribution f. We use comoving coordinates $\boldsymbol{x}$ with associated conjugate momentum $\boldsymbol{p} = a^2 m \, d\boldsymbol{x}/dt$, where a is the scale factor satisfying the Friedmann equation of a ΛCDM or Einstein-de Sitter universe. ϱ_0 is the (constant) comoving matter background density such that f has a background value or spatial average value $\langle \int d^3 p f \rangle_{\text{vol}} = 1$ for volumes larger than the homogeneity scale. For convenience we will in general suppress the t-dependence of the distribution function.

The phase space distribution function f encodes all information about the dynamics of the system. However, as it depends on seven variables in total – three each for position and momentum and one for time – it is more manageable to consider purely spatial distributions which characterize the system. This can be done by taking cumulants of the phase space distribution function with respect to momentum. We explained in Sec. 5.3 that the amount of complexity is

conserved in going from the single Vlasov equation for $f(\boldsymbol{x},\boldsymbol{p},t)$ to the hierarchy of local cumulants $C^{(n)}(\boldsymbol{x},t)$ equations since it is an infinite hierarchy of coupled partial differential for the $C^{(n)}(\boldsymbol{x},t)$ if we want to describe multi-streaming collisionless matter. Only for single streaming collisionless matter – dust – the truncation at second order is possible.

In Chapter 5 we described an approach relying on a special ansatz for the distribution function $\bar{f}_{\rm W}[\psi(\boldsymbol{x},t),\boldsymbol{p}]$ that allows to obtain cumulants analytically due the simple $\boldsymbol{p}$-dependence, while at the same time the cumulant hierarchy is kept intact and solved automatically if $\psi(\boldsymbol{x},t)$ satisfies the Schrödinger poisson equation. In Sec. 5.3 we compared three different ansätze for the distribution function f: the dust model $f_{\rm d}$, the Wigner function $f_{\rm W}$ constructed out of a wave function fulfilling the Schrödinger equation as well as the coarse grained Wigner distribution function $\bar{f}_{\rm W}$. In the following we will consider the coarse-grained dust model $\bar{f}_{\rm d}$ which can also be obtained from the coarse-grained Wigner ansatz $\bar{f}_{\rm W}$ when sending $\hbar \to 0$.

The distribution function for the coarse-grained dust model is simply the coarse grained dust phase space distribution (5.7) by a Gaussian filter of width σ_x and σ_p in $\boldsymbol{x}$ and $\boldsymbol{p}$ space, respectively. For convenience we will adopt the shorthand operator representation of the smoothing which can be easily obtained by switching to Fourier space

$$\begin{aligned}\bar{f}_{\rm d} &= \int \frac{d^3x'd^3p'}{(2\pi\sigma_x\sigma_p)^3}\exp\left[-\frac{(\boldsymbol{x}-\boldsymbol{x}')^2}{2{\sigma_x}^2}-\frac{(\boldsymbol{p}-\boldsymbol{p}')^2}{2{\sigma_p}^2}\right]f_{\rm d}(\boldsymbol{x}',\boldsymbol{p}')\,,\\ \bar{f}_{\rm d} &= \exp\left(\tfrac{1}{2}{\sigma_x}^2\Delta_x+\tfrac{1}{2}{\sigma_p}^2\Delta_p\right)f_{\rm d}\,,\end{aligned} \tag{6.2}$$

which can be obtained from the coarse grained Wigner function $\bar{f}_{\rm W}$ in the limit $\hbar \to 0$

$$\bar{f}_{\rm W}(\boldsymbol{x},\boldsymbol{p}) \overset{\hbar\to 0}{=} \bar{f}_{\rm d}(\boldsymbol{x},\boldsymbol{p})\,. \tag{6.3}$$

If $x_{\rm typ}$ and $p_{\rm typ}$ are the (minimal) scales of interest we have to ensure that

$$\sigma_x \ll x_{\rm typ} \quad \text{and} \quad \sigma_p \ll p_{\rm typ}\,. \tag{6.4}$$

Moments and cumulants The generating functional for the coarse-grained dust model is given by

$$\bar{G}_{\rm d}[\boldsymbol{J}] = \exp\left(\tfrac{1}{2}{\sigma_x}^2\Delta-\tfrac{1}{2}{\sigma_p}^2\boldsymbol{J}^2\right)G_{\rm d}[\boldsymbol{J}]\,. \tag{6.5}$$

From this expression the calculation for the moments $\bar{M}^{(n)}$ is straightforward and shows that the first two moments are given by a spatial coarse-graining of the dust moments (5.32a)

$$\bar{M}^{(0)} = \exp\left(\tfrac{1}{2}{\sigma_x}^2\Delta\right)M^{(0)} =: \bar{n} \quad , \quad \bar{C}^{(0)} = \ln\bar{n} \tag{6.6a}$$

$$\bar{M}^{(1)}_i = \exp\left(\tfrac{1}{2}{\sigma_x}^2\Delta\right)M^{(1)}_i =: m\bar{n}\bar{u}_i \;,\; \bar{C}^{(1)}_i = m\bar{u}_i\,. \tag{6.6b}$$

Note that we drop the label d on $n, \bar{n}$ and $\boldsymbol{u}, \bar{\boldsymbol{u}}$ from now on and it is understood that microscopic quantities $n, \boldsymbol{u}$ now refer to dust, and barred quantities $\bar{n}, \bar{\boldsymbol{u}}$ to coarse-grained dust. The coarse-grained velocity $\bar{\boldsymbol{u}}$ is a mass-weighted one which is obtained by smoothing the momentum field

$M_i^{(1)}$ and then dividing by the smoothed density field. This is precisely the definition commonly used in the EFT of LSS, compare [MP13, BNSZ12c]. From a physical point of view $\bar{\boldsymbol{u}}$ describes the center-of-mass velocity of the collection of particles inside a coarsening cell of diameter σ_x around $\boldsymbol{x}$.
Note that higher moments $\bar{M}^{(n\geq 2)}$ are not simply given by the coarse-graining of $M^{(n\geq 2)}$ but receive an extra ${\sigma_p}^2$-term

$$\bar{M}_{ij}^{(2)} = \exp\left(\tfrac{1}{2}{\sigma_x}^2\Delta\right)\left\{M_{ij}^{(2)} + {\sigma_p}^2 M^{(0)}\delta_{ij}\right\}, \tag{6.6c}$$

$$\bar{M}_{ijk}^{(3)} = \exp\left(\tfrac{1}{2}{\sigma_x}^2\Delta\right)\left\{M_{ijk}^{(3)} + {\sigma_p}^2 M_i^{(1)}\delta_{jk}\right\}^{+\text{cyc. perm.}}. \tag{6.6d}$$

Similarly the corresponding cumulants are not just given by a coarse graining of the dust cumulants (5.32b), which would vanish for $n > 1$, rather we find nonzero expressions for all n. For instance

$$\bar{C}_{ij}^{(2)} = {\sigma_p}^2\delta_{ij} + \frac{\overline{n\phi_{,i}\phi_{,j}}}{\bar{n}} - \frac{\overline{n\phi_{,i}}\;\overline{n\phi_{,j}}}{\bar{n}^2}, \tag{6.6e}$$

$$\bar{C}_{ijk}^{(3)} = \frac{\bar{M}_{ijk}^{(3)}}{\bar{M}^{(0)}} - \bar{C}_{ij}^{(2)}\bar{C}_k^{(1)}{}^{+\text{cyc. perm.}} - \bar{C}_i^{(1)}\bar{C}_j^{(1)}\bar{C}_k^{(1)}, \tag{6.6f}$$

with the shorthand notation $\overline{n\phi_{,i}\phi_{,j}} := \exp\left(\tfrac{1}{2}{\sigma_x}^2\Delta\right)\left\{n\phi_{,i}\phi_{,j}\right\}$ and $\overline{n\phi_{,i}} := \exp\left(\tfrac{1}{2}{\sigma_x}^2\Delta\right)\{n\phi_{,i}\}$. We can observe that all higher moments are determined self-consistently from the lowest two, which are dynamical and represent the coarse-grained density $\bar{n}$ and mass-weighted velocity $\bar{\boldsymbol{u}}$, respectively.

Evolution equations The dust equations (5.8) can be employed to obtain evolution equations for the first two moments $\bar{n} = \bar{M}^{(0)}$ and $\bar{u}_i = \bar{M}_i^{(1)}/(m\bar{n})$ corresponding to coarse-grained density and mass-weighted velocity, respectively

$$\partial_t\bar{n} = -\frac{1}{a^2}\nabla\cdot(\bar{n}\bar{\boldsymbol{u}}), \tag{6.7a}$$

$$\partial_t(\bar{n}\bar{u}_i) = -\exp\left(\tfrac{1}{2}{\sigma_x}^2\Delta\right)\left\{\frac{1}{a^2m^2}\nabla_j\left[n\phi_{,i}\phi_{,j}\right] + n\,\nabla_i V\right\}. \tag{6.7b}$$

Note that one would obtain exactly the same expressions and evolution equations when considering the coarse-grained Vlasov equation and sending $\hbar \to 0$ in the final equations (5.41) and (5.45). A specific feature of the Gaussian filter we employed in Chapter 5 was that it can be inverted for sufficiently smooth functions such that there exists a closed-form analogue of Eq. (6.7b) for the macroscopic quantities $\bar{n}$ and $\bar{\boldsymbol{u}}$, namely Eq. (5.47).

The velocity $\bar{u}_i$ which follows from a coarse-grained distribution function $\bar{f}$ is automatically a mass-weighted one computed according to $m\bar{u}_i = \overline{n\phi_{,i}}/\bar{n}$ and does not coincide with the volume-weighted velocity $\bar{\phi}_{,i}$. Therefore these equations are supplemented by the constraint

$$m\,\bar{n}\,\bar{\boldsymbol{u}} = \exp\left(\tfrac{1}{2}{\sigma_x}^2\Delta\right)(n\nabla\phi). \tag{6.7c}$$

which is the analogue of the curl-free constraint $\boldsymbol{u} = \nabla\phi/m$ Eq. (5.9c) and enforces a very particular non-zero vorticity for $\bar{\boldsymbol{u}}$. For practical applications, instead of solving the coarse-grained fluid equations (6.7) for $\bar{n}$ and $\bar{\boldsymbol{u}}$ one can simply solve (5.8) for n and ϕ and construct the cumulants of interest according to (6.6) . Note that Eqs. (6.7) are naturally written in terms of the macroscopic momentum $\bar{\boldsymbol{j}} \equiv \bar{n}\bar{\boldsymbol{u}}$.

6.3 Perturbation Theory for dust

In this section we will shortly review the standard of perturbation theory for the dust model both in the Eulerian (SPT) and Lagrangian framework (LPT).

6.3.1 Eulerian perturbation theory

In Eulerian perturbation theory the quantities under consideration are the density contrast $\delta(\tau, \boldsymbol{x})$, which is defined via the normalised number density field $n(\tau, \boldsymbol{x}) = 1 + \delta(\tau, \boldsymbol{x})$ and the peculiar velocity field $\boldsymbol{v}(\tau, \boldsymbol{x}) = \boldsymbol{u}(\tau, \boldsymbol{x})/a(\tau)$ with conformal time τ given by $dt = a(\tau)d\tau$. Then the dust equations (5.9) can be recast in the following form

$$\partial_\tau \delta + \nabla \cdot [(1+\delta)\boldsymbol{v}] = 0\,, \tag{6.8a}$$

$$\partial_\tau \boldsymbol{v} + \mathcal{H}\boldsymbol{v} + (\boldsymbol{v}\cdot\nabla)\boldsymbol{v} = -\nabla V\,. \tag{6.8b}$$

The two coupled evolution equations for a fluid modeling CDM are supplemented by the Poisson equation

$$\Delta V = \frac{4\pi G \varrho_0}{a}\delta\,. \tag{6.8c}$$

The velocity field $\boldsymbol{v}$ can be decomposed into velocity divergence $\theta = \nabla\cdot\boldsymbol{v}$ and vorticity $\boldsymbol{w} = \nabla\times\boldsymbol{v}$. The corresponding equations on an Einstein-de Sitter background can be obtained easily from (6.8b) when using the Poisson equation (6.8c)

$$\partial_\tau \theta + \mathcal{H}\theta + \nabla[(\boldsymbol{v}\cdot\nabla)\boldsymbol{v}] = -\frac{3}{2}\mathcal{H}^2\delta\,, \tag{6.9a}$$

$$\partial_\tau \boldsymbol{w} + \mathcal{H}\boldsymbol{w} + \nabla\times(\boldsymbol{v}\times\boldsymbol{w}) = 0\,. \tag{6.9b}$$

We see that if there is no initial vorticity then it cannot be generated, which we discussed already in Chapter 4. Since furthermore in linear perturbation theory any initial vorticity decays due to the expansion of the universe, it seems to be a good assumption that velocity is a gradient field given by $\boldsymbol{v} = \nabla\theta/\Delta$.

Perturbative expansion The density contrast δ and the divergence of velocity $\theta = \nabla\cdot\boldsymbol{v} = \Delta\phi/am$ can be written in Fourier space and expanded in terms of the scale factor $a(\tau)$ for the

fastest growing mode

$$\delta(\tau, \boldsymbol{k}) = \sum_{n=1}^{\infty} a^n(\tau)\, \delta_n(\boldsymbol{k})\,, \tag{6.10a}$$

$$\theta(\tau, \boldsymbol{k}) = \mathcal{H}(\tau) \sum_{n=1}^{\infty} a^n(\tau)\, \theta_n(\boldsymbol{k})\,. \tag{6.10b}$$

Although we restricted ourselves here to the Einstein-de Sitter (EdS) case, one can easily translate the result to a general ΛCDM universe, as described in [BCGS02b], by replacing $a \to D$ and $H \to fH$, where $D(\tau)$ is the linear growth function and $f(\tau) = d\ln D(\tau)/d\ln a(\tau)$ the linear growth rate.

We define the integral kernels F_n and G_n of δ and θ with respect to the linear density contrast δ_1 as

$$\delta_n(\boldsymbol{k}) = \int \frac{\mathrm{d}^3\boldsymbol{p}_1 \ldots \mathrm{d}^3\boldsymbol{p}_n}{(2\pi)^{3(n-1)}}\, \delta_{\mathrm{D}}(\boldsymbol{k} - \boldsymbol{p}_{1\ldots n})\, F_n(\boldsymbol{p}_1, \ldots, \boldsymbol{p}_n)\delta_1(\boldsymbol{p}_1)\ldots\delta_1(\boldsymbol{p}_n)\,, \tag{6.10c}$$

$$\theta_n(\boldsymbol{k}) = -\int \frac{\mathrm{d}^3\boldsymbol{p}_1 \ldots \mathrm{d}^3\boldsymbol{p}_n}{(2\pi)^{3(n-1)}}\, \delta_{\mathrm{D}}(\boldsymbol{k} - \boldsymbol{p}_{1\ldots n})\, G_n(\boldsymbol{p}_1, \ldots, \boldsymbol{p}_n)\delta_1(\boldsymbol{p}_1)\ldots\delta_1(\boldsymbol{p}_n)\,, \tag{6.10d}$$

where $\boldsymbol{p}_{1\ldots n} = \boldsymbol{p}_1 + \cdots + \boldsymbol{p}_n$. Substituting the ansatzes (6.10) into the fluid equations (6.8a) and (6.9a) rewritten in Fourier space allows to separate the time dependence and obtain for $n > 1$

$$n\delta_n(\boldsymbol{k}) + \theta_n(\boldsymbol{k}) = -\sum_{m=1}^{n-1} \frac{\boldsymbol{k}_1 \cdot \boldsymbol{k}_2}{k_1^2} \delta_{n-m}(\boldsymbol{k}_2)\theta_m(\boldsymbol{k}_1)\ ,$$

$$3\delta_n(\boldsymbol{k}) + (1+2n)\theta_n(\boldsymbol{k}) = -\sum_{m=1}^{n-1} \frac{k^2(\boldsymbol{k}_1 \cdot \boldsymbol{k}_2)}{2k_1^2 k_2^2} \theta_{n-m}(\boldsymbol{k}_2)\theta_m(\boldsymbol{k}_1)\,,$$

where $\boldsymbol{k} = \boldsymbol{k}_1 + \boldsymbol{k}_2$. Solving this system for δ_n and θ_n, respectively we obtain recursion relations for F_n and G_n with starting values $F_1 = G_1 = 1$, compare [JB94]

$$F_n(\boldsymbol{p}_1, \ldots, \boldsymbol{p}_n) = \sum_{m=1}^{n-1} \frac{G_m(\boldsymbol{p}_1, \ldots, \boldsymbol{p}_m)}{(2n+3)(n-1)} \Bigg[(2n+1)\frac{\boldsymbol{k}\cdot\boldsymbol{k}_1}{k_1^2} F_{n-m}(\boldsymbol{p}_{m+1}, \ldots, \boldsymbol{p}_n) + \frac{k^2(\boldsymbol{k}_1\cdot\boldsymbol{k}_2)}{k_1^2 k_2^2} G_{n-m}(\boldsymbol{p}_{m+1}, \ldots, \boldsymbol{p}_n) \Bigg]\,, \tag{6.12a}$$

$$G_n(\boldsymbol{p}_1, \ldots, \boldsymbol{p}_n) = \sum_{m=1}^{n-1} \frac{G_m(\boldsymbol{p}_1, \ldots, \boldsymbol{p}_m)}{(2n+3)(n-1)} \Bigg[3\frac{\boldsymbol{k}\cdot\boldsymbol{k}_1}{k_1^2} F_{n-m}(\boldsymbol{p}_{m+1}, \ldots, \boldsymbol{p}_n) + n\frac{k^2(\boldsymbol{k}_1\cdot\boldsymbol{k}_2)}{k_1^2 k_2^2} G_{n-m}(\boldsymbol{p}_{m+1}, \ldots, \boldsymbol{p}_n) \Bigg]\,, \tag{6.12b}$$

where $\boldsymbol{k}_1 = \boldsymbol{p}_1 + \ldots + \boldsymbol{p}_m$, $\boldsymbol{k}_2 = \boldsymbol{p}_{m+1} + \ldots + \boldsymbol{p}_n$ and $\boldsymbol{k} = \boldsymbol{k}_1 + \boldsymbol{k}_2$.

6.3.2 Lagrangian Perturbation Theory

In the Lagrangian scheme the quantity under consideration is the displacement field $\boldsymbol{\Psi}(\tau, \boldsymbol{q})$ which maps initial particle or fluid element positions $\boldsymbol{q}$ into their final Eulerian position $\boldsymbol{x}(\tau)$

$$\boldsymbol{x}(\tau) = \boldsymbol{q} + \boldsymbol{\Psi}(\tau, \boldsymbol{q}) \,. \tag{6.13}$$

The Jacobian F_{ij} of the transformation from Eulerian to Lagrangian coordinates is given by

$$F_{ij} = \frac{\partial x_i}{\partial q_j} = \delta_{ij} + \Psi_{i,j} \,, \tag{6.14a}$$

and has the following properties

$$J_F = \det\left[\delta_{ij} + \Psi_{i,j}\right] \;,\; F^{-1}_{ij} = \tfrac{1}{2} J_F^{-1} \varepsilon_{ilm} \varepsilon_{jpq} F_{pl} F_{qm} \,, \tag{6.14b}$$

where ε_{ijk} refers to the totally antisymmetric Levi-Civita symbol. Mass conservation implies the following relation between the Jacobian determinant $J_F(\boldsymbol{q})$ and the density contrast $\delta(\boldsymbol{x})$

$$\bar{\varrho}[1 + \delta(\boldsymbol{x})] \, \mathrm{d}^3 x = \bar{\varrho} \, \mathrm{d}^3 q \quad \Leftrightarrow \quad 1 + \delta = J_F^{-1} \,. \tag{6.14c}$$

The equation of motion for the Eulerian position $\boldsymbol{x}$ is

$$\frac{d^2 \boldsymbol{x}}{d\tau^2} + \mathcal{H}(\tau) \frac{d\boldsymbol{x}}{d\tau} = -\nabla_x V \,. \tag{6.15a}$$

By taking the divergence of (6.15a) and using the Poisson equation (6.8c) as well as mass conservation (6.14c) one obtains an equation for the displacement field $\boldsymbol{\Psi}$

$$J_F(\tau, \boldsymbol{q}) \, \nabla_x \cdot \left[\frac{d^2 \boldsymbol{\Psi}}{d\tau^2} + \mathcal{H}(\tau) \frac{d\boldsymbol{\Psi}}{d\tau} \right] = \bar{\varrho} \left[J_F(\tau, \boldsymbol{q}) - 1 \right] \,, \tag{6.15b}$$

supplemented by the constraint $\nabla \times \boldsymbol{v} = 0$

$$\varepsilon_{ijk} (F_{mj})^{-1} F'_{km} = 0 \,. \tag{6.15c}$$

The exact displacement field $\boldsymbol{\Psi}(\tau, \boldsymbol{q})$ can be expanded in a series with spatial parts $\boldsymbol{\Psi}^{(n)}(\boldsymbol{q})$ and temporal coefficients using the scale factor $a(\tau)$, concentrating on the fastest growing mode within an EdS universe

$$\boldsymbol{\Psi}(\tau, \boldsymbol{q}) = \sum_{n=1}^{\infty} a^n(\tau) \boldsymbol{\Psi}^{(n)}(\boldsymbol{q}) \,. \tag{6.16}$$

Then we express the different orders $\boldsymbol{\Psi}^{(n)}$ in Fourier space with the help of perturbative kernels $\boldsymbol{L}^{(n)}$ in terms of powers of the linear density field δ_1

$$\boldsymbol{\Psi}^{(n)}(\boldsymbol{k}) = i \int \frac{d^3 p_1 \, \ldots \, d^3 p_n}{(2\pi)^{3(n-1)}} \delta_{\mathrm{D}}(\boldsymbol{k} - \boldsymbol{p}_{1\cdots n}) \boldsymbol{L}^{(n)}(\boldsymbol{p}_1, \ldots, \boldsymbol{p}_n) \delta_1(\boldsymbol{p}_1) \cdots \delta_1(\boldsymbol{p}_n) \,. \tag{6.17}$$

Note that we employ here a different notation for $\boldsymbol{L}^{(n)}$ compared to Eq. (A2) in [Mat08] such that when translating the results an additional prefactor $n!$ has to be taken into account. The vector valued kernels $\boldsymbol{L}^{(n)}$ can be split into a longitudinal component $\boldsymbol{S}^{(n)}$ and a transverse part $\boldsymbol{T}^{(n)}$ according to

$$\boldsymbol{L}^{(n)} = \boldsymbol{S}^{(n)} + \boldsymbol{T}^{(n)}\,, \tag{6.18a}$$

$$\boldsymbol{k} \times \boldsymbol{S}^{(n)}(\boldsymbol{p}_1, \ldots, \boldsymbol{p}_n) = 0\,, \tag{6.18b}$$

$$\boldsymbol{k} \cdot \boldsymbol{T}^{(n)}(\boldsymbol{p}_1, \ldots, \boldsymbol{p}_n) = 0\,, \tag{6.18c}$$

where $\boldsymbol{k} = \boldsymbol{p}_1 + \ldots + \boldsymbol{p}_n$.

6.3.3 Mapping between Eulerian and Lagrangian picture

Note that LPT correctly recovers SPT when the exact relation between the density and displacement field, encoded in the continuity equation (6.14c) with (6.14b), is expanded in the same manner. In lowest order LPT it is possible to keep this nonperturbative relation between Ψ and the δ, which is done in the Zel'dovich approximation (ZA) [Zel70]. This allows to partially resum perturbation theory in a physically motivated way by combining *i*) an approximate law for the movement of particles from first order LPT (1LPT) with (*ii*) a proper determination of the density within a small volume as the sum of all particles divided by this volume. Performing this proper counting is the resummation, giving it up leeds to SPT. The generalization of the ZA to second order LPT (2LPT) is referred to as Post-Zel'dovich approximation (PZA), for which an exact translation from displacement to density field Eq. (6.14c) would demand solving a non-Gaussian integral when computing correlation functions. Since this is analytically not tractable some approximation methods to the PZA, like integrated perturbation theory (iPT) [**?**] or Convolution Lagrangian perturbation theory (CLPT) [CRW13] have been proposed that leave the relation, which is solved exactly in the ZA, at least partially resummed. It is because of those and many other advantages of the Lagrangian approach [Tas14] that we also derive LPT for the coarse grained dust model. In particular, for ZA it is known that a smoothing of the initial linear power spectrum improves ZA even further. This coarse graining procedure is known as "truncated" ZA [BMW94b], but compared to our coarse grained dust, only the initial conditions are smoothed while the dynamics is that of dust. We will explore CLPT, "truncated" CLPT both based on dust to a modified CLPT based on coarse grained dust (cgCLPT) in Sec. 6.5.

In the following we will shortly describe the relation between the Eulerian framework that is based on the density contrast δ and the velocity divergence θ and the Lagrangian description which relies on the displacement field $\boldsymbol{\Psi}$. For a more detailed study of the connection between the series in Lagrangian and Eulerian perturbation theory we refer to [RB12]. Rewriting the density contrast in Fourier space and employing (6.14c) gives

$$\delta(\boldsymbol{k}) = \int d^3x\, e^{-i\,\boldsymbol{k}\cdot\boldsymbol{x}} \delta(\boldsymbol{x})\,, \tag{6.19a}$$

$$= \int d^3q\, e^{-i\,\boldsymbol{k}\cdot\boldsymbol{q}} \left(e^{-i\,\boldsymbol{k}\cdot\boldsymbol{\Psi}(\boldsymbol{q})} - 1 \right)\,. \tag{6.19b}$$

Similarly, the divergence of the velocity $\theta = \nabla_x \cdot \boldsymbol{v}$ can be transformed to Lagrangian space by using $\boldsymbol{v} = d\boldsymbol{x}/d\tau = \boldsymbol{\Psi}'(\boldsymbol{q})$ with (6.16) and transforming ∇_x to ∇_q which leads to

$$\frac{\theta(\boldsymbol{x}(\boldsymbol{q}))}{\mathcal{H}} = F_{ij}^{-1}\left(a\Psi_{j,i}^{(1)} + 2a^2\Psi_{j,i}^{(2)} + 3a^3\Psi_{j,i}^{(3)}\right)(\boldsymbol{q})\,. \tag{6.19c}$$

Using the explicit formula for F_{ij}^{-1} (6.14b) we can obtain the Fourier transform of $\theta(\boldsymbol{q})$

$$\frac{\theta(\boldsymbol{k})}{\mathcal{H}} = \int d^3q\, e^{-i\boldsymbol{k}\cdot\boldsymbol{q}-i\boldsymbol{k}\cdot\boldsymbol{\Psi}(\boldsymbol{q})}\, J_F\, \frac{\theta(\boldsymbol{x}(\boldsymbol{q}))}{\mathcal{H}}\,. \tag{6.19d}$$

Note that, within the mapping from Eulerian to Lagrangian frame the absence of vorticity $\boldsymbol{w} = 0$ implies a constraint (6.15c) for the transverse parts of $\boldsymbol{\Psi}$, see [RB12].

6.4 Perturbation theory for coarse grained dust

In order to obtain a solution to Eq. (6.7) for the coarse grained quantities $\bar{\delta}$ and $\bar{\boldsymbol{v}}$, we can solve the microscopic system (5.8) for $\delta = n - 1$ and $\boldsymbol{v} = \nabla\theta/\Delta$ where $\theta = \Delta\phi/am$ and then simply coarse grain the result according to

$$\bar{\delta} = \exp\left(\tfrac{1}{2}{\sigma_x}^2\Delta\right)\delta\,, \tag{6.20a}$$

$$(1+\bar{\delta})\bar{\boldsymbol{v}} = \exp\left(\tfrac{1}{2}{\sigma_x}^2\Delta\right)[(1+\delta)\boldsymbol{v}]\,. \tag{6.20b}$$

As mentioned before, this procedure is possible as long as the solution space of the "microscopic" functions δ, θ allows to invert the gaussian smoothing operation; this it what justified the use of Eq. (6.7b) instead of Eq. (5.47). However, at shell-crossing caustics, where δ diverges at point-, line- or sheetlike structures a deconvolution is impossible. Therefore considering the coarse-grained dust case does not allow us to genuinely go beyond shell crossing. However, microscopic vorticity and velocity dispersion contribute to the true macroscopic vorticity $\bar{\boldsymbol{w}}$ and velocity dispersion $\bar{\sigma}_{ij}$. Those microscopic contributions simply add to the corresponding quantities of the coarse grained dust model that arise without any microscopic origin [PMSV12a]. Therefore one might hope that coarse grained dust captures some aspects of the true macroscopic $\bar{\boldsymbol{w}}$ and $\bar{\sigma}_{ij}$. Indeed, we will see in the following that it improves the modelling of a collisionless fluid compared to the standard dust model.

6.4.1 Eulerian kernels for density and velocity

We write the solution of the coarse-grained dust model (6.20) again as a perturbative series by separating time and momentum dependence,

$$\bar{\delta}(\tau,\boldsymbol{k}) = \sum_{n=1}^{\infty} a^n(\tau)\bar{\delta}_n(\boldsymbol{k}) \tag{6.21a}$$

$$\bar{\boldsymbol{v}}(\tau,\boldsymbol{k}) = \mathcal{H}(\tau)\sum_{n=1}^{\infty} a^n(\tau)\bar{\boldsymbol{v}}_n(\boldsymbol{k})\,. \tag{6.21b}$$

To obtain formal solutions we proceed in the same manner as in standard perturbation theory, see 6.3.1. The general solution may be written in terms of Fourier kernels

$$\bar{\delta}_n(\boldsymbol{k}) = \int \frac{\mathrm{d}^3 p_1 \dots \mathrm{d}^3 p_n}{(2\pi)^{3(n-1)}} \delta_{\mathrm{D}}(\boldsymbol{k} - \boldsymbol{p}_{1\dots n}) \bar{F}_n(\boldsymbol{p}_1, \dots, \boldsymbol{p}_n) \delta_1(\boldsymbol{p}_1) \cdots \delta_1(\boldsymbol{p}_n) \,, \tag{6.22a}$$

$$\bar{\boldsymbol{v}}_n(\boldsymbol{k}) = i \int \frac{d^3 p_1 \cdots d^3 p_n}{(2\pi)^{3(n-1)}} \delta_{\mathrm{D}}(\boldsymbol{k} - \boldsymbol{p}_{1\dots n}) \bar{\boldsymbol{V}}_n(\boldsymbol{p}_1, \dots, \boldsymbol{p}_n) \delta_1(\boldsymbol{p}_1) \cdots \delta_1(\boldsymbol{p}_n) \,. \tag{6.22b}$$

It is convenient to decompose the velocity $\bar{\boldsymbol{v}}$ into velocity divergence $\bar{\theta} := \boldsymbol{\nabla} \cdot \bar{\boldsymbol{v}}$ and vorticity $\bar{\boldsymbol{w}} := \boldsymbol{\nabla} \times \bar{\boldsymbol{v}}$ for which we also define Fourier kernels according to

$$\bar{\theta}_n(\boldsymbol{k}) = - \int \frac{d^3 p_1 \cdots d^3 p_n}{(2\pi)^{3(n-1)}} \delta_{\mathrm{D}}(\boldsymbol{k} - \boldsymbol{p}_{1\dots n}) \bar{G}_n(\boldsymbol{p}_1, \dots, \boldsymbol{p}_n) \delta_1(\boldsymbol{p}_1) \cdots \delta_1(\boldsymbol{p}_n) \,, \tag{6.22c}$$

$$\bar{\boldsymbol{w}}_n(\boldsymbol{k}) = - \int \frac{d^3 p_1 \cdots d^3 p_n}{(2\pi)^{3(n-1)}} \delta_{\mathrm{D}}(\boldsymbol{k} - \boldsymbol{p}_{1\dots n}) \bar{\boldsymbol{W}}_n(\boldsymbol{p}_1, \dots, \boldsymbol{p}_n) \delta_1(\boldsymbol{p}_1) \cdots \delta_1(\boldsymbol{p}_n) \,. \tag{6.22d}$$

The corresponding kernels are related to those of velocity $\bar{\boldsymbol{V}}_n$ via $\bar{G}_n = \boldsymbol{k} \cdot \bar{\boldsymbol{V}}_n$ and $\bar{\boldsymbol{W}}_n = \boldsymbol{k} \times \bar{\boldsymbol{V}}_n$. Since the macroscopic density contrast $\bar{\delta}$ is trivially related to the microscopic δ, see Eq. (6.20a) we have that

$$\bar{F}_n = \exp\left(-\tfrac{1}{2}{\sigma_x}^2 k^2\right) F_n \,. \tag{6.23a}$$

where F_n are the SPT kernels from (6.12). Therefore, in Eulerian perturbation theory, the matter power spectrum for the coarse-grained dust model at any order is simply given by the coarse-graining of the dust power spectrum, see Eq. (6.26a).

In order to determine the coarse-grained velocity field we have to expand Eq. (6.20b) perturbatively in terms of the micro- and macroscopic fields we have solved for before which gives

$$\bar{\boldsymbol{v}}_n = \exp\left(\tfrac{1}{2}{\sigma_x}^2 \Delta\right) \boldsymbol{v}_n + \sum_{m=1}^{n-1} \left\{ \exp\left(\tfrac{1}{2}{\sigma_x}^2 \Delta\right) (\delta_m \boldsymbol{v}_{n-m}) - \bar{\delta}_m \bar{\boldsymbol{v}}_{n-m} \right\} \,, \tag{6.23b}$$

where $\boldsymbol{v}_n = \boldsymbol{\nabla}\theta_n / \Delta$. Note that the curly bracket in (6.23b) basically calculates the difference between the average of a product and the product of averages (this statement is exact at 2nd order). It is precisely this deviation that sources the vorticity $\bar{\boldsymbol{w}}_n = \boldsymbol{\nabla} \times \bar{\boldsymbol{v}}_n$ which becomes relevant at 2nd order. In the limit $\sigma_x \to 0$, this contribution vanishes identically at all orders such that the velocity remains a gradient field thereby recovering the standard SPT kernels from (6.12) for $\sigma_x \to 0$. The kernels $\bar{\boldsymbol{V}}_n$ for the velocity $\bar{\boldsymbol{v}}$ can be read off from (6.23b) and give

$$\begin{aligned} \bar{\boldsymbol{V}}_n(\boldsymbol{p}_1, \dots, \boldsymbol{p}_n) = & \frac{\boldsymbol{k}}{k^2} \exp\left(-\tfrac{1}{2}{\sigma_x}^2 k^2\right) G_n \\ & + \sum_{m=1}^{n-1} \left\{ \exp\left(-\tfrac{1}{2}{\sigma_x}^2 k^2\right) F_m \frac{\boldsymbol{k}_2}{k_2^2} G_{n-m} - \bar{F}_m \bar{\boldsymbol{V}}_{n-m} \right\} \end{aligned} \tag{6.23c}$$

Note that the kernel $\bar{G}_n$ of $\bar{\theta} = \boldsymbol{\nabla} \cdot \bar{\boldsymbol{v}}$ is not simply given by the coarse-graining of the kernel G_n of $\theta = \Delta\phi / am$ since the velocity is mass-weighted according to (6.20b) . However, at first order we recover a curl-free velocity $\bar{\boldsymbol{v}}_1 = \exp\left(\tfrac{1}{2}{\sigma_x}^2 \Delta\right) \boldsymbol{\nabla}\theta_1 / \Delta$ and $\bar{\theta}_1(\boldsymbol{k}) = -\bar{\delta}_1(\boldsymbol{k})$.

6.4.2 Eulerian power and cross spectra

In order to check whether our new kernels give sound results in perturbation theory, we calculate here some power and cross spectra up to one-loop order and therefore up to third order in perturbation theory. It turns out that expressions, displayed in App. 6.A are convergent and reduce to the correct results in the limit where $\sigma_x \to 0$. The most interesting result of these checks will be the power spectrum for the vorticity $\boldsymbol{w}$, because it vanishes identically in the standard dust model.

The power spectra $P(k)$ corresponding to density δ, velocity divergence θ and vorticity $\boldsymbol{w}$ are defined via the two-point correlation in Fourier-space

$$\langle \delta(\boldsymbol{k})\delta(\boldsymbol{k}')\rangle = (2\pi)^3\delta_D(\boldsymbol{k}+\boldsymbol{k}')P_{\delta\delta}(k)\,, \tag{6.24a}$$

$$\langle \theta(\boldsymbol{k})\theta(\boldsymbol{k}')\rangle = (2\pi)^3\delta_D(\boldsymbol{k}+\boldsymbol{k}')P_{\theta\theta}(k)\,, \tag{6.24b}$$

$$\langle \boldsymbol{w}(\boldsymbol{k})\cdot\boldsymbol{w}(\boldsymbol{k}')\rangle = (2\pi)^3\delta_D(\boldsymbol{k}+\boldsymbol{k}')P_{ww}(k)\,. \tag{6.24c}$$

Furthermore we have the cross spectrum between density δ and velocity divergence θ

$$\langle \delta(\boldsymbol{k})\theta(\boldsymbol{k}')\rangle = (2\pi)^3\delta_D(\boldsymbol{k}+\boldsymbol{k}')P_{\delta\theta}(k)\,. \tag{6.24d}$$

The velocity power spectrum is defined accordingly

$$\langle \boldsymbol{v}(\boldsymbol{k})\cdot\boldsymbol{v}(\boldsymbol{k}')\rangle = (2\pi)^3\delta_D(\boldsymbol{k}+\boldsymbol{k}')P_{vv}(k)\,. \tag{6.25a}$$

Since $\boldsymbol{v} = (\boldsymbol{\nabla}\theta - \boldsymbol{\nabla}\times\boldsymbol{w})/\Delta$ it can be easily obtained from the divergence $\theta = \boldsymbol{\nabla}\cdot\boldsymbol{v}$ and vorticity $\boldsymbol{w} = \boldsymbol{\nabla}\times\boldsymbol{v}$ power spectra

$$k^2 P_{vv}(k) = P_{\theta\theta}(k) + P_{ww}(k)\,. \tag{6.25b}$$

In the following we will derive the power and cross spectra up to one-loop order for the coarse-grained dust model (cgSPT), and compare it to both standard SPT as well as standard SPT with a different coarse-graining procedure (SPTcg) where only the linear input power spectrum P_L is smoothed. This is done merely to illustrate the effect of the coarse graining on the perturbation kernels rather than to suggest an improvement of SPT. SPT is known to fail to converge as a perturbative series, see [BGK13] and is less accurate in predicting the nonlinear density field than Lagrangian methods [Tas14], which will be our main focus in the following sections.

Density power spectrum For the density power spectrum the effect of the coarse grained fluid equations (6.7) is simply to coarse grain the power spectrum obtained from SPT according to

$$P_{\bar\delta\bar\delta}(k) = \bar P_{\delta\delta}(k) = \exp\left(-{\sigma_x}^2k^2\right)P_{\delta\delta}(k)\,. \tag{6.26a}$$

This result holds at any order in SPT and shows that, as expected, the smoothing becomes effective only at small scales $k \gtrsim 1/\sigma_x$. Note that, since the power spectrum is quadratic in δ it gets smoothed with $\sqrt{2}\sigma_x$ when δ is coarse-grained on scale σ_x. Therefore we will write in the following $\bar P(k) := \exp\left(-{\sigma_x}^2k^2\right)P(k)$ even though $\bar\delta(\boldsymbol{k}) := \exp\left(-\frac{1}{2}{\sigma_x}^2k^2\right)\delta(\boldsymbol{k})$. The resulting power spectrum depicted in Fig. 6.1 shows that power on small spatial scales corresponding to large k is suppressed due to the coarse-graining.

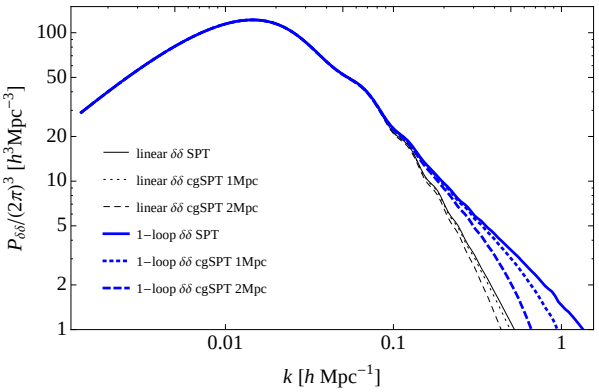

FIGURE 6.1: Comparison between density powerspectrum for SPT and cgSPT in 1st (lin) and 2nd (one-loop) order perturbation theory.

Velocity power spectrum At linear level the velocity kernel $\bar{\boldsymbol{V}}_1$ obtained from Eq. (6.23c) has only one contribution corresponding to a coarse-graining of the microscopic velocity divergence. Because of this, the linear power spectrum of macroscopic velocity divergence $\bar{\theta}$ is just given by the coarse-grained SPT result and the vorticity vanishes identically

$$P_{\bar{\theta}\bar{\theta},L}(k) = \bar{P}_{\theta\theta,L}(k)\,, \tag{6.27a}$$
$$P_{\bar{\boldsymbol{w}}\bar{\boldsymbol{w}},L}(k) = P_{\boldsymbol{ww},L}(k) = 0\,. \tag{6.27b}$$

Note that since $\bar{\theta}_1(\boldsymbol{k}) = -\bar{\delta}_1(\boldsymbol{k})$ the linear velocity power spectrum is identical to the linear density power spectrum. At one-loop level the different contributions to the total velocity kernel $\bar{\boldsymbol{V}}_n$ according to Eq. (6.23c) have been evaluated explicitly in Appendix 6.A.

As can be seen in the Fig. 6.3, the effect of the dynamical coarse graining (cgSPT) for the velocity $\boldsymbol{v}$ power spectrum differs from coarse graining the initial conditions in SPT (SPTcg). Most notably, our coarse-graining procedure determining the mass-weighted velocity $\bar{\boldsymbol{v}}$ introduces a nonzero vorticity $\bar{\boldsymbol{w}} = \boldsymbol{\nabla} \times \bar{\boldsymbol{v}}$ which manifests itself from second order on. This vorticity slightly affects the velocity power spectrum at one-loop order via its contribution $P_{\bar{\boldsymbol{w}}\bar{\boldsymbol{w}},22}$. This term is a fundamental difference to SPT where vorticity vanishes by definition. The corresponding expression can be computed from the recursion relations for the kernels of velocity given in (6.23c) and reads

$$\begin{aligned} P_{\bar{\boldsymbol{w}}\bar{\boldsymbol{w}},22}(k) &= 2\int \frac{d^3p}{(2\pi)^3} \left|\bar{\boldsymbol{W}}_2^{(s)}(\boldsymbol{p}, \boldsymbol{k}-\boldsymbol{p})\right|^2 P_L(p)\, P_L(|\boldsymbol{k}-\boldsymbol{p}|) \\ &= \frac{k^3}{2\pi^2}\int_0^\infty dr \int_{-1}^1 dx\; \bar{P}_L(kr)\, \bar{P}_L\left(k\sqrt{1-2rx+r^2}\right) \\ &\quad \times \frac{\left(1-x^2\right)\left(1-2rx\right)^2\left(e^{\sigma_x{}^2 k^2 (r^2-rx)}-1\right)^2}{4\left(r^2-2rx+1\right)^2}\,. \end{aligned} \tag{6.28}$$

Note that we wrote in the second line the result in terms of the smooth $\bar{P}_L$. The bracket containing the exponential in the third line partially undos the smoothing, see App. 6.A for details.

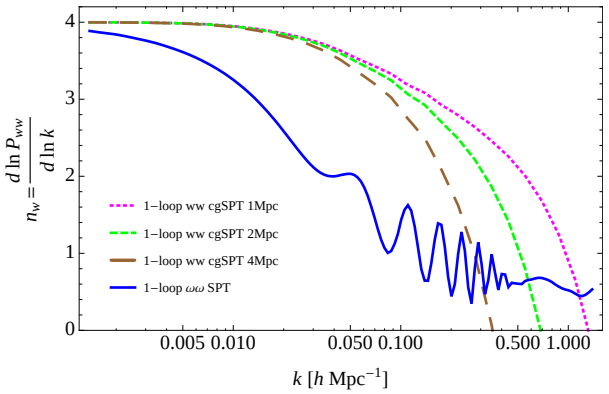

FIGURE 6.2: Spectral index n_w of the vorticity power spectrum $P_{ww} \simeq k^{n_w(k)}$ as function of wavenumber k

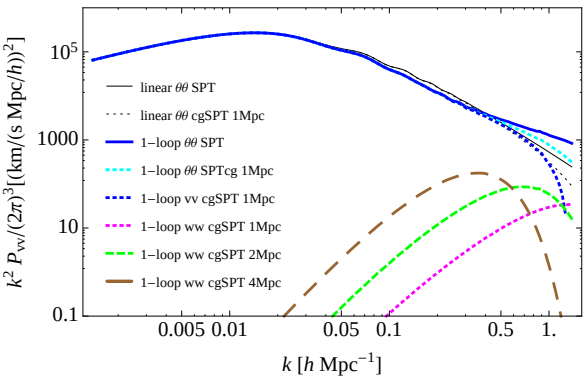

FIGURE 6.3: Comparison between velocity powerspectrum for SPT and cgSPT in 1st (lin) and 2nd (one-loop) order perturbation theory.

Very interestingly, the only effect of increasing the coarse-graining scale is to cause vorticity to become relevant at larger length scales. However, the shape of the vorticity power spectrum remains unchanged and the slope seems to be a universal feature.

In [Sco00, PS09] it has been suggested that the basic features of the vorticity power spectrum can be understood if one assumes that the vorticity is induced by mass-weighting the single-stream velocities in each coarsening cell. However, they used as estimate $\boldsymbol{w} \propto \boldsymbol{\nabla} \times [(1+\delta)\boldsymbol{v}]/(1+\delta)$ where, in contrast, no real mass-weighting has been performed. Instead, they considered the vorticity of the momentum $\boldsymbol{j} = (1+\delta)\boldsymbol{v}$ and afterwards divided by $(1+\delta)$. In contrast, our approach based on coarse-graining automatically implements this idea correctly and yields a vorticity according to $\bar{\boldsymbol{w}} = \boldsymbol{\nabla} \times \bar{\boldsymbol{v}} = \boldsymbol{\nabla} \times \left[\overline{(1+\delta)\boldsymbol{v}}/(1+\bar{\delta})\right]$. Since in [PS09] there was no prediction for the amplitude of the vorticity power spectrum we can only compare the spectral index $n_w := d \ln P_{ww}/d \ln k$ which is depicted in Fig 6.2.

Interestingly, our results qualitatively agree with predictions made in the context of EFT of LSS, see [CFGS13], which gives

$$n_w = \begin{cases} 4 & \text{for} \quad k\ [h\text{Mpc}^{-1}] \lesssim 0.1 \\ 3.6 & \text{for} \quad 0.1 \lesssim k\ [h\text{Mpc}^{-1}] \lesssim 0.3 \\ 2.8 & \text{for} \quad 0.3 \lesssim k\ [h\text{Mpc}^{-1}] \lesssim 0.6\,. \end{cases} \tag{6.29}$$

Both the large scale limit as well as the slow decrease of the spectral index can be observed for the top curves in Fig 6.2.

The blue (bottom) curve in Fig 6.2 falls off much faster and it corresponds to the estimate $\boldsymbol{w} \propto \boldsymbol{\nabla} \times [(1+\delta)v]/(1+\delta)$ made in [Sco00, PS09]. Note that their expression is actually proportional to the metric vector perturbation in Poisson gauge $\boldsymbol{\omega}$ and related to vorticity via Eq. (4.12). We therefore denoted the spectral index of the corresponding power spectrum in Fig. 6.2 by $\omega\omega$ since we calculated it from Eq. (4.21c).

We can compare the vorticity power spectrum also to cosmological numerical simulations, as given in [PS09] and [HAA14]. Note that within both works a different Fourier convention has

been employed. Therefore we show our power spectra divided by $(2\pi)^3$ in order to allow for comparison which reveals good qualitative agreement. Note also that our $\theta(k)$ is dimensionless because we factored out $a^n\mathcal{H}$ in (6.10b), while [HAA14] measure θ in km/(s Mpc/h). Taking this into account and comparing to Fig.12 in [HAA14] and Fig.3 in [PS09] we see that the vorticity power spectra are in good qualitative agreement. In [PS09] it was noted that the vorticity power spectrum shows significant sensitivity on the mass resolution which was confirmed by [HAA14]. Similarly, a strong dependence on the smoothing scale shows up in the vorticity power spectrum for cgSPT. The main effect of an increased coarse-graining scale is to shift the wavenumber at which vorticity becomes relevant to smaller values corresponding to larger length scales. However, the spectral index n_w is a rather universal feature of the vorticity power spectrum and was determined in [HAA14] as a function of k. Its asymptotic values were found to agree with $P_{ww} \propto k^{5/2}$ on large scales, consistent with [CFGS13], and $P_{ww} \propto k^{-3/2}$ on small scales.

6.4.3 Lagrangian displacement kernels

Well before the onset of strong non-linearity the dynamics of a perfect pressureless fluid qualitatively resembles coarse-grained hydrodynamics. Therefore the Zel'dovich approximation based on the dust fluid, which in the mildly nonlinear regime has proven quite successful, should retain its applicability even in the coarse grained dust model. We will thus consider the effect of the coarse-graining on LPT and employ in following section the CLPT resummation scheme to derive a Post-Zel'dovich approximation.

In order to compute the correlators in Lagrangian space we closely follow the notation and procedure described in [Mat08]. First, we expand the displacement field $\bar{\boldsymbol{\Psi}}(\tau, \boldsymbol{k})$ perturbatively according to (6.16). Then we express the different orders $\bar{\boldsymbol{\Psi}}^{(n)}$ with the help of the perturbative kernels $\bar{\boldsymbol{L}}^{(n)}$, see (6.17), and their longitudinal $\bar{\boldsymbol{S}}^{(n)}$ and transverse parts $\bar{\boldsymbol{T}}^{(n)}$ according to (6.18). The expressions given for microscopic density δ and velocity divergence θ in terms of displacements $\boldsymbol{\Psi}$, see (6.19), can be directly translated to those for the macroscopic quantities $\bar{\delta}$ and $\bar{\theta}$. In addition we need a corresponding expression for the vorticity $\bar{\boldsymbol{w}}$ which is present in the coarse-grained dust model but absent in the dust model. We perform a transformation to Lagrangian coordinates $\boldsymbol{q}$ in which the particle postions are given by the old Eulerian coordinates $\boldsymbol{x} = \boldsymbol{q} + \bar{\boldsymbol{\Psi}}$, where $\bar{\boldsymbol{\Psi}}(\boldsymbol{q}, \tau)$ are the integral lines of $\bar{\boldsymbol{v}}(\boldsymbol{q}, \tau) = \partial_\tau|_q \bar{\boldsymbol{\Psi}}(\boldsymbol{q}, \tau)$ with initial positions at $\boldsymbol{q}$ which now encode all the dynamical information. Using the Jacobian $\bar{F}_{ij} = \partial x_i / \partial q_j$, we can write the vorticity as

$$\bar{w}_i = (\nabla_x \times \bar{\boldsymbol{v}})_i = \varepsilon_{ijk}\partial_{x_j}\bar{v}_k = \varepsilon_{ijk}(\bar{F}_{mj})^{-1}\bar{F}'_{km} \tag{6.30a}$$

By multiplying with $J_{\bar{F}} = \det \bar{F}_{ij}$, the solution to the continuity equation (6.14c), inserting F_{ij} according to (6.14a) and using Eqs. (3d) and (6f) from [EB97] to simplify the expression we obtain

$$\begin{aligned} J_{\bar{F}}\bar{w}_i &= \bar{F}_{in}\varepsilon_{njk}\bar{F}_{lj}\bar{F}'_{lk} \\ &= -\varepsilon_{ijk}\left(\bar{\Psi}'_{k,j} - \bar{\Psi}_{l,j}\bar{\Psi}'_{l,k}\right) - \bar{\Psi}_{i,n}\varepsilon_{njk}\left(\bar{\Psi}'_{k,j} - \bar{\Psi}_{l,j}\bar{\Psi}'_{l,k}\right) . \end{aligned} \tag{6.30b}$$

This allows to express the vorticity $\bar{\boldsymbol{w}}$ in Fourier space entirely in terms of $\bar{\boldsymbol{\Psi}}$ according to

$$\bar{w}_i(\boldsymbol{k}) = \int d^3q\, e^{-i\,\boldsymbol{k}\cdot\boldsymbol{q}-i\,\boldsymbol{k}\cdot\bar{\boldsymbol{\Psi}}}\, J_{\bar{F}}\,\bar{w}_i(\boldsymbol{q})\,. \tag{6.30c}$$

Inserting the above expression for $J_{\bar{F}}\bar{w}_i$ and the perturbative ansatz for $\bar{\boldsymbol{\Psi}}$, see (6.16), we can match the Eulerian and Lagrangian expressions at each order

$$-\bar{\boldsymbol{W}}_{\rm s}^{(2)}(\boldsymbol{p}_1,\boldsymbol{p}_2) = 2\,\boldsymbol{k}\times\bar{\boldsymbol{T}}^{(2)}(\boldsymbol{p}_1,\boldsymbol{p}_2)\,, \tag{6.31a}$$

$$\begin{aligned}-\bar{\boldsymbol{W}}_{\rm s}^{(3)}(\boldsymbol{p}_1,\boldsymbol{p}_2,\boldsymbol{p}_3) = 3\,\boldsymbol{k}\times\bar{\boldsymbol{T}}^{(3)} + \frac{1}{3}\Big[\Big(\boldsymbol{k}_1\times\boldsymbol{k}_2\,\bar{\boldsymbol{S}}^{(1)}\cdot\Big[\bar{\boldsymbol{S}}^{(2)}+\bar{\boldsymbol{T}}^{(2)}\Big] + 2\,\boldsymbol{k}_2\times\bar{\boldsymbol{T}}^{(2)}\,\boldsymbol{k}\cdot\bar{\boldsymbol{S}}^{(1)} - \\ - 2\,\bar{\boldsymbol{S}}^{(1)}\,\boldsymbol{k}_1\cdot\Big(\boldsymbol{k}_2\times\bar{\boldsymbol{T}}^{(2)}\Big)\Big) \;+\; \text{cyclic permutations of } (\boldsymbol{p}_1,\boldsymbol{p}_2,\boldsymbol{p}_3)\Big]\,.\end{aligned} \tag{6.31b}$$

For the sake of brevity we suppress the functional dependencies on the right hand side. They can be easily restored by attaching each $\bar{\boldsymbol{S}}^{(n)}$ or $\bar{\boldsymbol{T}}^{(n)}$ a dependence on $(\boldsymbol{p}_i,\ldots,\boldsymbol{p}_{i+n-1})$ in ascending order beginning with $i=1$ from the left, for example $\bar{\boldsymbol{S}}^{(1)}\cdot\bar{\boldsymbol{T}}^{(2)} := \bar{\boldsymbol{S}}^{(1)}(\boldsymbol{p}_1)\cdot\bar{\boldsymbol{T}}^{(2)}(\boldsymbol{p}_2,\boldsymbol{p}_3)$. Note that $\bar{\boldsymbol{W}}_{\rm s}^{(n)}(\boldsymbol{p}_1,..,\boldsymbol{p}_n) = \frac{1}{n!}\sum_{\sigma\in S_n}\bar{\boldsymbol{W}}^{(n)}(\boldsymbol{p}_{\sigma(1)},..,\boldsymbol{p}_{\sigma(n)})$, where the sum goes over all $n!$ permutations σ of n indices. Similar equations can be derived from the energy conservation relating $\bar{F}_n$ and $\boldsymbol{S}^{(n)}$, see Eqs. (6.9) and (B1)-(B3) in [RB12]

$$\bar{F}_1^{\rm s}(\boldsymbol{p}_1) = \boldsymbol{k}\cdot\bar{\boldsymbol{S}}^{(1)}\,, \tag{6.32a}$$

$$\bar{F}_2^{\rm s}(\boldsymbol{p}_1,\boldsymbol{p}_2) = \boldsymbol{k}\cdot\bar{\boldsymbol{S}}^{(2)} + \frac{1}{2}\Big(\boldsymbol{k}\cdot\bar{\boldsymbol{S}}^{(1)}\Big)\Big(\boldsymbol{k}\cdot\bar{\boldsymbol{S}}^{(1)}\Big)\,, \tag{6.32b}$$

$$\bar{F}_3^{\rm s}(\boldsymbol{p}_1,\boldsymbol{p}_2,\boldsymbol{p}_3) = \boldsymbol{k}\cdot\bar{\boldsymbol{S}}^{(3)} + \frac{1}{6}\Big(\boldsymbol{k}\cdot\bar{\boldsymbol{S}}^{(1)}\Big)\Big(\boldsymbol{k}\cdot\bar{\boldsymbol{S}}^{(1)}\Big)\Big(\boldsymbol{k}\cdot\bar{\boldsymbol{S}}^{(1)}\Big) + \overbrace{\frac{1}{3}\Big(\boldsymbol{k}\cdot\bar{\boldsymbol{S}}^{(1)}\Big)\Big(\boldsymbol{k}\cdot\Big[\bar{\boldsymbol{S}}^{(2)}+\bar{\boldsymbol{T}}^{(2)}\Big]\Big)}^{+\text{cyclic permutation of } (\boldsymbol{p}_1,\boldsymbol{p}_2,\boldsymbol{p}_3)}\,. \tag{6.32c}$$

Since $\boldsymbol{k}\cdot\bar{\boldsymbol{T}} = 0$ we have $\boldsymbol{k}\times(\boldsymbol{k}\times\bar{\boldsymbol{T}}) = -k^2\bar{\boldsymbol{T}}$ which allows to invert (6.31) for $\bar{\boldsymbol{T}}$. Therefore we can determine the longitudinal $\bar{\boldsymbol{S}}^{(n)}$ and transverse $\bar{\boldsymbol{T}}^{(n)}$ kernels of the displacement field from

the Eulerian kernels for density $\bar{F}_n$ and vorticity $\bar{\boldsymbol{W}}_n$.

$$\begin{aligned}
\bar{\boldsymbol{S}}^{(1)}(\boldsymbol{p}_1) &= \exp\left(-\tfrac{1}{2}{\sigma_x}^2 p_1^2\right)\frac{\boldsymbol{p}_1}{p_1^2}\,, \\
\bar{\boldsymbol{T}}^{(1)}(\boldsymbol{p}_1) &= 0\,, \qquad (6.33a)\\
\bar{\boldsymbol{S}}^{(2)}(\boldsymbol{p}_1,\boldsymbol{p}_2) &= \frac{\boldsymbol{p}_{12}}{p_{12}^2}\left(\bar{F}_2^{\rm s} - \frac{1}{2}\left(\boldsymbol{p}_{12}\cdot\bar{\boldsymbol{S}}^{(1)}\right)\left(\boldsymbol{p}_{12}\cdot\bar{\boldsymbol{S}}^{(1)}\right)\right)\,, \\
\bar{\boldsymbol{T}}^{(2)}(\boldsymbol{p}_1,\boldsymbol{p}_2) &= \frac{1}{2}\frac{1}{p_{12}^2}\boldsymbol{p}_{12}\times\bar{\boldsymbol{W}}_{\rm s}^{(2)}(\boldsymbol{p}_1,\boldsymbol{p}_2)\,, \qquad (6.33b)\\
\bar{\boldsymbol{S}}^{(3)}(\boldsymbol{p}_1,\boldsymbol{p}_2,\boldsymbol{p}_3) &= \frac{\boldsymbol{p}_{123}}{p_{123}^2}\Bigg\{\bar{F}_3^{\rm s} - \frac{1}{6}\left(\boldsymbol{p}_{123}\cdot\bar{\boldsymbol{S}}^{(1)}\right)\left(\boldsymbol{p}_{123}\cdot\bar{\boldsymbol{S}}^{(1)}\right)\left(\boldsymbol{p}_{123}\cdot\bar{\boldsymbol{S}}^{(1)}\right) - \\
&\qquad - \frac{1}{3}\left(\boldsymbol{p}_{123}\cdot\bar{\boldsymbol{S}}^{(1)}\right)\left(\boldsymbol{p}_{123}\cdot\left[\bar{\boldsymbol{S}}^{(2)}+\bar{\boldsymbol{T}}^{(2)}\right]\right)\Bigg\}^{+\text{cyclic permutation of }(\boldsymbol{p}_1,\boldsymbol{p}_2,\boldsymbol{p}_3)}\,, \qquad (6.33c)\\
\bar{\boldsymbol{T}}^{(3)}(\boldsymbol{p}_1,\boldsymbol{p}_2,\boldsymbol{p}_3) &= \frac{1}{3}\frac{\boldsymbol{p}_{123}}{p_{123}^2}\times\Bigg\{\bar{\boldsymbol{W}}_{\rm s}^{(3)} + \frac{1}{3}\Big[\boldsymbol{p}_1\times\boldsymbol{p}_{23}\left(\bar{\boldsymbol{S}}^{(1)}\cdot\left[\bar{\boldsymbol{S}}^{(2)}+\bar{\boldsymbol{T}}^{(2)}\right]\right) + \\
&\qquad + 2\,\boldsymbol{p}_{23}\times\bar{\boldsymbol{T}}^{(2)}\left(\boldsymbol{p}_{123}\cdot\bar{\boldsymbol{S}}^{(1)}\right) - 2\,\bar{\boldsymbol{S}}^{(1)}\left(\boldsymbol{p}_1\cdot\left[\boldsymbol{p}_{23}\times\bar{\boldsymbol{T}}^{(2)}\right]\right) + \\
&\qquad + \text{cyclic permutation of }(\boldsymbol{p}_1,\boldsymbol{p}_2,\boldsymbol{p}_3)\Big]\Bigg\}\,.
\end{aligned}$$

Note that our expressions for $\bar{\boldsymbol{S}}^{(n)}$ and $\bar{\boldsymbol{T}}^{(n)}$ reduces to the corresponding expressions in App. A of [RB12] in the limit $\sigma_x \to 0$. The next sections are devoted to apply the Lagrangian kernels.

6.5 Generalized Gaussian Streaming model

In order to infer predictions for the correlation function in redshift space we use the Gaussian streaming model, originally derived in [Fis95] and combine it with Convolution Lagrangian perturbation theory (CLPT), introduced in [CRW13]. Since we will modify CLPT into cgCLPT using the new coarse grained dust kernels from the last section, we present a self-contained yet concise derivation of the Gaussian streaming model, suggested in [RW11] for the dust case and consistently generalize it to multiple streams relevant for the coarse-grained dust model.

6.5.1 Single-stream case

We will assume in the following that for biased tracers[1] X the following relations hold

$$(1+\delta_X(\boldsymbol{s},t))\,\mathrm{d}^3 s = (1+\delta_X(\boldsymbol{r},t))\,\mathrm{d}^3 r = F[\delta_R(\boldsymbol{q}),t]\,\mathrm{d}^3 q\,. \qquad (6.34)$$

[1] X can stand for galaxies, clusters, or halos. Given the simplicity of the bias model F used later on, we will think of X as halos of a given mass.

The first equality states the trivial fact that objects in a real space volume d^3r observed in a redshift space volume d^3s cannot disappear (assuming that all objects remain observable). The second equality states that proto-halos identified in the linear initial conditions, depending only on the smoothed initial linear density field $\delta_R(\boldsymbol{q})$ are conserved until they form a proper halo at time t. The proto-halo initial density field is assumed to be a local function $F[\delta_R(\boldsymbol{q}), t]$ of the initial linear density field $\delta_1(\boldsymbol{q})$ smoothed over some scale related to the Lagrangian size R of the proto-halo

$$\delta_R(\boldsymbol{q}) = \int \frac{d^3k}{(2\pi)^3} W(kR) e^{i\boldsymbol{k}\cdot\boldsymbol{q}} \delta_1(\boldsymbol{k}) \tag{6.35}$$

and each proto-halo moves along trajectories, determined by fluid trajectories $\boldsymbol{x}(\boldsymbol{q}, t)$ with initial conditions $\delta_R(\boldsymbol{q})$. This means we assume local Lagrangian bias for the halo density field and zero velocity bias. In Sec. 6.6.1 we will say more about the choice of R. In the distant observer approximation, the line of sight is assumed to be a fixed direction $\hat{\boldsymbol{z}}$, without loss of generality chosen as the direction of the $z-$axis, such that the observed comoving distance

$$\boldsymbol{s} = \boldsymbol{r} + \mathcal{H}^{-1}(\boldsymbol{v}\cdot\hat{\boldsymbol{z}})\,\hat{\boldsymbol{z}}\,, \tag{6.36}$$

is affected by the peculiar velocity $\boldsymbol{v}\cdot\hat{\boldsymbol{z}} = v_z$ of the tracer along the line of sight. The tracer's observed position perpendicular to the line of sight $\boldsymbol{s}_\perp$ remains unaffected if we neglect gravitational lensing, whereas its coordinate $s_\parallel$ parallel to the line of sight $\hat{\boldsymbol{z}}$ depends on v_z

$$\boldsymbol{s}_\perp = \boldsymbol{r}_\perp \quad , \quad s_\parallel = \boldsymbol{s}\cdot\hat{\boldsymbol{z}} = r_\parallel + \mathcal{H}^{-1}v_z\,. \tag{6.37}$$

Although $\mathcal{H}^{-1}v_z \ll r_\parallel$, the clustering is affected considerably since the change of volume measure, the Jacobian between d^3s and d^3r, involves the gradient of v_z, which we know from Chapters 3 and 4 is as large as density fluctuation.

We can rewrite the relation (6.34) between the densities in redshift, real and Lagrangian space in the following ways

$$1+\delta_X(\boldsymbol{s},t) = \int d^3r\,(1+\delta_X(\boldsymbol{r},t))\,\delta_{\rm D}\left(\boldsymbol{s}-\boldsymbol{r}-\frac{v_z(\boldsymbol{r},t)}{\mathcal{H}}\hat{\boldsymbol{z}}\right)\,, \tag{6.38}$$

$$1+\delta_X(\boldsymbol{r},t) = \int d^3q\,F[\delta_R(\boldsymbol{q}),t]\,\delta_{\rm D}\left(\boldsymbol{r}-\boldsymbol{q}-\boldsymbol{\Psi}(\boldsymbol{q},t)\right)\,, \tag{6.39}$$

or in a single step

$$1+\delta_X(\boldsymbol{s},t) = \int d^3q\,F[\delta_R(\boldsymbol{q}),t]\delta_{\rm D}\left(\boldsymbol{s}-\boldsymbol{q}-\boldsymbol{\Psi}(\boldsymbol{q},t)-\frac{\boldsymbol{v}(\boldsymbol{q},t)\cdot\hat{\boldsymbol{z}}}{\mathcal{H}}\hat{\boldsymbol{z}}\right)\,. \tag{6.40}$$

Within LPT we can replace $\boldsymbol{v} = a\dot{\boldsymbol{\Psi}}$ which follows from the fact that the integral lines of the single-streaming velocity $\boldsymbol{v}$ are given by the displacement field $\boldsymbol{\Psi}$. In the next subsection 6.5.2, we will generalize this to multiple streams.

Previous studies Originally, in [CRW13] Eq. (6.40) was used to obtain a Post-Zel'dovich approximation for biased tracers (CLPT) and to derive an expression for the two-point correlation function

$$1 + \xi_X(\boldsymbol{s}, t) = \Big\langle (1 + \delta_X(\boldsymbol{s}_1))(1 + \delta_X(\boldsymbol{s}_2)) \Big\rangle , \tag{6.41}$$

where $\boldsymbol{s} = \boldsymbol{s}_2 - \boldsymbol{s}_1$. Later on, in [WRW14], Eq. (6.39) together with the Gaussian streaming model [Fis95, Sco04] was employed instead to take care of the redshift space distortions and obtain the redshift-space correlation function. The following formula (6.42) was suggested in [RW11] to calculate Gaussian streaming redshift space distortions (GSRSD) as an approximation to the full Gaussian streaming model [Fis95] and as its extension to the nonlinear case. It is given by

$$1 + \xi_X(s_\parallel, s_\perp, t) = \int_{-\infty}^{\infty} \frac{dr_\parallel}{\sqrt{2\pi}\tilde{\sigma}_{12}(r, r_\parallel, t)} (1 + \xi_X(r, t)) \exp\left[-\frac{\big(s_\parallel - r_\parallel - v_{12}(r, t) r_\parallel / r\big)^2}{2\tilde{\sigma}_{12}^2(r, r_\parallel, t)} \right] , \tag{6.42}$$

where within this integral $r^2 = r_\parallel^2 + s_\perp^2$. The mean pairwise velocity is computed according to

$$v_{12}(r) \frac{r_\parallel}{r} := \frac{\langle (1 + \delta_X(\boldsymbol{r}_1))(1 + \delta_X(\boldsymbol{r}_2)) \left[(\boldsymbol{v}(\boldsymbol{r}_2) - \boldsymbol{v}(\boldsymbol{r}_1)) \cdot \hat{\boldsymbol{z}} \right] \rangle}{1 + \xi_X(r, t)} , \tag{6.43a}$$

with $\boldsymbol{r} = \boldsymbol{r}_2 - \boldsymbol{r}_1$ and the 2nd pairwise velocity moment is

$$\tilde{\sigma}_{12}^2(r, r_\parallel) := \frac{\langle (1 + \delta_X(\boldsymbol{r}_1))(1 + \delta_X(\boldsymbol{r}_2)) \left[(\boldsymbol{v}(\boldsymbol{r}_2) - \boldsymbol{v}(\boldsymbol{r}_1)) \cdot \hat{\boldsymbol{z}} \right]^2 \rangle}{1 + \xi_X(r, t)} . \tag{6.43b}$$

The quantities v_{12} and $\tilde{\sigma}_{12}$ entering the model can be calculated using standard perturbation theory [RW11] or CLPT [WRW14].

Derivation We show here that, with a slight modification, one can directly obtain formula (6.42), proposed in [RW11] and applied in [WRW14], from Eq. (6.40). We start combining Eqs. (6.38, 6.39) into

$$1 + \delta_X(\boldsymbol{s}, t) = \int d^3r \int d^3q \, F[\delta_R(\boldsymbol{q}), t] \delta_{\rm D} \left(\boldsymbol{s} - \boldsymbol{r} - \frac{\dot{\boldsymbol{\Psi}}(\boldsymbol{q}, t) \cdot \hat{\boldsymbol{z}}}{H} \hat{\boldsymbol{z}} \right) \delta_{\rm D} \left(\boldsymbol{r} - \boldsymbol{q} - \boldsymbol{\Psi}(\boldsymbol{q}, t) \right) . \tag{6.44}$$

From this we obtain the redshift space two-point correlation function $1 + \xi_X(\boldsymbol{s}, t) = \langle (1 + \delta_X(\boldsymbol{s}_2, t))(1 + \delta_X(\boldsymbol{s}_1, t)) \rangle$, with $\boldsymbol{s} = \boldsymbol{s}_2 - \boldsymbol{s}_1$. In the course of the calculation we will choose cylindrical coordinates

$$\boldsymbol{s} = s_\perp [\cos(\phi) \hat{\boldsymbol{x}} + \sin(\phi) \hat{\boldsymbol{y}}] + s_\parallel \hat{\boldsymbol{z}}$$

since $\xi_X(\boldsymbol{s}, t)$ does not depend on ϕ. After expressing $\delta_{\rm D}$ in Fourier space and integrating over $\boldsymbol{Q} = \boldsymbol{q}_1 + \boldsymbol{q}_2$ and $\boldsymbol{X} = \boldsymbol{x}_1 + \boldsymbol{x}_2$ as well as over two Fourier space momentum integrals, we obtain

$$1+\xi_X(\boldsymbol{s},t) = \int d^3r \int \frac{d^3p}{(2\pi)^3} e^{i\boldsymbol{p}\cdot(\boldsymbol{r}-\boldsymbol{s})} Z\Big(\boldsymbol{r}, \boldsymbol{J}=(\boldsymbol{p}\cdot\hat{\boldsymbol{z}})\,\hat{\boldsymbol{z}}, t\Big)\,, \tag{6.45a}$$

$$Z(\boldsymbol{r},\boldsymbol{J},t) = \int d^3q \int \frac{d^3k}{(2\pi)^3} e^{i\boldsymbol{k}\cdot(\boldsymbol{q}-\boldsymbol{r})} \int \frac{d\lambda_1 d\lambda_2}{(2\pi)^2} \tilde{F}(\lambda_1)\tilde{F}(\lambda_2)\langle e^{iX}\rangle\,, \tag{6.45b}$$

with

$$X = \lambda_1\delta_R(\boldsymbol{q}_1) + \lambda_2\delta_R(\boldsymbol{q}_2) + \boldsymbol{k}\cdot\boldsymbol{\Delta} + \boldsymbol{J}\cdot\frac{\dot{\boldsymbol{\Delta}}}{H}\,, \tag{6.45c}$$

where $\boldsymbol{q} = \boldsymbol{q}_2 - \boldsymbol{q}_1$ and $\boldsymbol{\Delta} = \boldsymbol{\Psi}(\boldsymbol{q}_2,t) - \boldsymbol{\Psi}(\boldsymbol{q}_1,t)$. Note that the $\boldsymbol{p}$ and $\boldsymbol{r}$ integrals in (6.45) can be trivially done, and one ends up with the original CLPT expression [CRW13]

$$1+\xi_X(\boldsymbol{s},t) = \int d^3q \int \frac{d^3k}{(2\pi)^3} e^{i\boldsymbol{k}\cdot(\boldsymbol{q}-\boldsymbol{s})} \int \frac{d\lambda_1 d\lambda_2}{(2\pi)^2} \tilde{F}(\lambda_1)\tilde{F}(\lambda_2)\langle e^{iX(J=(\boldsymbol{k}\cdot\hat{\boldsymbol{z}})\,\hat{\boldsymbol{z}})}\rangle\,. \tag{6.46}$$

We will however not do that, since (6.46) involves a 3D integral and we want to derive the computationally simpler Gaussian streaming model. To this end we Taylor expand $W(\boldsymbol{J}) := \ln Z$ around $\boldsymbol{J}=0$

$$W(\boldsymbol{J}) = \sum_{n=0}^{\infty} \frac{1}{n!} \frac{\partial^n W}{(\partial i\boldsymbol{J})^n}\bigg|_{J=0} (i\boldsymbol{J})^n\,. \tag{6.47}$$

Keeping only the terms up to second order $n=2$ we obtain

$$W(\boldsymbol{J}) \simeq \ln(1+\xi_X(r,t)) + i\boldsymbol{v}_{12}\cdot\boldsymbol{J} - \frac{1}{2}\boldsymbol{J}^T\boldsymbol{\sigma}^2_{12}\boldsymbol{J}\,, \tag{6.48a}$$

with

$$\boldsymbol{v}_{12}(\boldsymbol{r},t) = \frac{\partial W}{(i\,\partial\boldsymbol{J})}\bigg|_{J=0} = \frac{\frac{\partial Z}{(\partial i\boldsymbol{J})}\big|_{J=0}}{(1+\xi_X(r,t))}\,, \tag{6.48b}$$

$$\begin{aligned}\boldsymbol{\sigma}^2_{12}(\boldsymbol{r},t) &= \frac{\partial^2 W}{(i\,\partial\boldsymbol{J})^2}\bigg|_{J=0} = \frac{\frac{\partial^2 Z}{(i\partial\boldsymbol{J})^2}\big|_{J=0}}{(1+\xi_X(r,t))} - \frac{\frac{\partial Z}{(i\partial\boldsymbol{J})}\frac{\partial Z}{(i\partial\boldsymbol{J})}\big|_{J=0}}{(1+\xi_X(r,t))^2} \\ &= \tilde{\boldsymbol{\sigma}}^2_{12}(\boldsymbol{r},t) - \boldsymbol{v}_{12}(\boldsymbol{r},t)\boldsymbol{v}_{12}(\boldsymbol{r},t)\,.\end{aligned} \tag{6.48c}$$

The justification for the Taylor expansion up to second order is the observation that the final result (6.49) looks very much like the Gaussian streaming model (6.42) of [RW11, WRW14] which requires only 2D integrals and is known to provide a good fit to N-body simulations. The expansion of W up to 2nd order in $\boldsymbol{J}$ in (6.47) means that all redshift space distortion induced clustering is encoded in the scale dependent mean $v_{12}r_\parallel/r$ and width σ_{12} of the Gaussian. Performing five of the six integrals in Eq. (6.45a) we obtain what we will call in the following the

Gaussian streaming model (GSM)

$$1+\xi_X(s_\parallel,s_\perp,t)=\int_{-\infty}^{\infty}\frac{dr_\parallel}{\sqrt{2\pi}\sigma_{12}(r,r_\parallel,t)}(1+\xi_X(r,t))\exp\left[-\frac{\left(s_\parallel-r_\parallel-v_{12}(r,t)r_\parallel/r\right)^2}{2\sigma_{12}^2(r,r_\parallel,t)}\right]. \tag{6.49}$$

More precisely, the p_z integral in (6.45) introduces the Gaussian, while the trivial p_x, p_y integrals enforce $\boldsymbol{r}_\perp=\boldsymbol{s}_\perp$.[2] The $\boldsymbol{r}_\perp$ integral ensures $r^2=r_\parallel^2+s_\perp^2$, while the ϕ-integral gives a factor 2π. We defined

$$v_{12}(r,t)\frac{r_\parallel}{r}:=\boldsymbol{v}_{12}(\boldsymbol{r},t)\cdot\hat{\boldsymbol{z}}\,,\qquad \sigma_{12}^2(r,r_\parallel,t):=\hat{\boldsymbol{z}}^T\boldsymbol{\sigma}_{12}^2(\boldsymbol{r},t)\hat{\boldsymbol{z}} \tag{6.50}$$

which deviates from the notation of [WRW14] where the 2nd pairwise velocity moment $\tilde{\sigma}_{12}^2$ is denoted by σ_{12}^2 related to the actual pairwise velocity dispersion σ_{12}^2 via Eq. (6.48c). Also their $r_\parallel$ is our $s_\parallel$, while their y is our $r_\parallel$. If Z is evaluated within CLPT we recover the Gaussian streaming model (6.49) that differs from (6.42) by a different expression for the variance of the Gaussian. If we had expanded $Z=Z_0(1+Z_1/Z_0+Z_2/Z_0+...)$ instead of $Z=\exp(W_0+W_1+W_2+...)$, we would have obtained (6.42) after writing $Z\simeq Z_0\exp(Z_1/Z_0+Z_2/Z_0+...)$. It is however more natural to follow an expansion in W, since for an exactly Gaussian pairwise velocity distribution, characterized by $W_{n>2}=0$, the Taylor expansion up to second order in $\boldsymbol{J}$ becomes exact. Note also that after linearizing both expressions, (6.49) and (6.42) agree because v_{12}^2 is 2nd order.

In order to evaluate and compare $\xi_X(s_\parallel,s_\perp)$ to N-body simulations it will be useful to expand $\xi_X(s_\parallel,s_\perp)$ into Legendre polynomials $L_n(\mu)$ using $s^2=s_\parallel^2+s_\perp^2$ and $\mu=s_\parallel/s$

$$\xi_X(s,\mu,t)=\sum_{n=0}^{\infty}L_n(\mu)\xi_{X,n}(s,t), \tag{6.51}$$

where $\xi_{X,n}=(1+2n)/2\int_{-1}^{1}\xi_X(s,\mu,t)L_n(\mu)d\mu$ vanishes for all odd n. In linear perturbation theory, the only non-zero moments are the monopole ξ_0, quadrupole ξ_2 and hexadecapole ξ_4. We will see in Sec. 6.6 that the magnitude of ξ_n rapidly decreases with n.

6.5.2 Generalization to multiple streams

If at a position $\boldsymbol{r}$ the tracer velocity is not single valued but has multiple streams, the observed value $\boldsymbol{s}$ will depend in general on the full line of sight. The previously one-to-one relation $\boldsymbol{s}=\boldsymbol{r}+\mathcal{H}^{-1}\boldsymbol{v}\cdot\hat{\boldsymbol{z}}$ which we started with, does not hold anymore and the multi-valued relation between $\boldsymbol{s}$ and $\boldsymbol{r}$ is determined by f_X and the redshift space density is given by

$$1+\delta_X(\boldsymbol{s},t)=\int d^3r\int d^3u\; f_X(\boldsymbol{r},\boldsymbol{u},t)\delta_{\rm D}\left(\boldsymbol{s}-\boldsymbol{r}-\frac{\boldsymbol{u}\cdot\hat{\boldsymbol{z}}}{a^2H}\hat{\boldsymbol{z}}\right), \tag{6.52}$$

[2] This conditions breaks down if we would also take into account gravitational lensing; while redshift space distortions distort the apparent position along the line of sight, gravitational lensing distorts the apparent position perpendicular to it, see Eq. (3.9). The neglected lensing becomes only important for large redshifts [CL11, BD11].

see [SM11]. In the case of single-streaming tracers, $f_{\rm d} = (1+\delta_X(\boldsymbol{r},t))\delta_{\rm D}(\boldsymbol{u}-a\boldsymbol{v}(\boldsymbol{r},t))$, we recover (6.38). As before we can re-introduce the Lagrangian formulation and obtain

$$1+\xi_X(\boldsymbol{s},t) = \int d^3r \int \frac{d^3p}{(2\pi)^3} e^{i\boldsymbol{p}\cdot(\boldsymbol{r}-\boldsymbol{s})} Z(\boldsymbol{r}, \boldsymbol{J}=(\boldsymbol{p}\cdot\hat{\boldsymbol{z}})\,\hat{\boldsymbol{z}}, t)\,, \tag{6.53a}$$

$$Z(\boldsymbol{r},\boldsymbol{J},t) = \int d^3q \int \frac{d^3k}{(2\pi)^3} e^{i\boldsymbol{k}\cdot(\boldsymbol{q}-\boldsymbol{r})} \int \frac{d\lambda_1 d\lambda_2}{(2\pi)^2} \tilde{F}(\lambda_1)\tilde{F}(\lambda_2) \Big\langle \int d^3u_1 \int d^3u_2\, \tilde{f}_1 \tilde{f}_2\, e^{iX} \Big\rangle\,,$$

with

$$X = \lambda_1 \delta_R(\boldsymbol{q}_1) + \lambda_2 \delta_R(\boldsymbol{q}_2) + \boldsymbol{k}\cdot\boldsymbol{\Delta} + \boldsymbol{J}\cdot\frac{\boldsymbol{u}_2-\boldsymbol{u}_1}{a^2H}\,. \tag{6.53b}$$

In the following we will make the assumption for $\tilde{f}$

$$\tilde{f}(\boldsymbol{u},\boldsymbol{r},t) := \frac{f_X(\boldsymbol{u},\boldsymbol{r},t)}{1+\delta_X(\boldsymbol{r},t)} \simeq \frac{f(\boldsymbol{u},\boldsymbol{r},t)}{1+\delta(\boldsymbol{r},t)}\,, \tag{6.54}$$

which means – in analogy to the single-streaming case – that we assume that tracers and dark matter are unbiased with respect to velocity.

Comparing the general expression for multiple streams (6.53) to the single-streaming one (6.45) suggests to define a $\widetilde{X}$ via

$$\Big\langle \int d^3u_1 \int d^3u_2\, \tilde{f}_1 \tilde{f}_2\, e^{iX} \Big\rangle \equiv \Big\langle e^{i\widetilde{X}} \Big\rangle$$

such that the formula (6.53) can be recast in a structurally analogous form (6.45). This can be achieved by using the moment generating functional $G[\boldsymbol{J}]$ which allows to relate the expression for $\widetilde{X}$ via the cumulant expansion theorem to the cumulants $C^{(n)}$ of the phase-space distribution function f, computed according to Eq. (5.28c)

$$\begin{aligned}
&\int d^3u_1 \int d^3u_2\, \tilde{f}_1 \tilde{f}_2 \exp\left[i\boldsymbol{J}\cdot(\boldsymbol{u}_2-\boldsymbol{u}_1)\right] \\
&\qquad = \left(\int d^3u_2\, \tilde{f}_2 \exp\left[i\boldsymbol{J}\cdot\boldsymbol{u}_2\right]\right)\left(\int d^3u_1\, \tilde{f}_1 \exp\left[-i\boldsymbol{J}\cdot\boldsymbol{u}_1\right]\right) \\
&\qquad = \frac{G[\boldsymbol{J}]}{G[\boldsymbol{J}=0]}(\boldsymbol{x}_2)\frac{G[-\boldsymbol{J}]}{G[\boldsymbol{J}=0]}(\boldsymbol{x}_1) \\
&\qquad = \exp\left[\sum_{N=1}^{\infty}\frac{i^N}{N!}J_{i_1}\ldots J_{i_N}\left(C^{(N)}_{i_1\ldots i_N}(\boldsymbol{x}_2)+(-1)^N C^{(N)}_{i_1\ldots i_N}(\boldsymbol{x}_1)\right)\right].
\end{aligned}$$

Hence we can rewrite the Gaussian streaming model for multiple streams in analogy to the one for single-streaming (6.45)

$$1+\xi_X(\boldsymbol{s},t) = \int d^3r \int \frac{d^3p}{(2\pi)^3} e^{i\boldsymbol{p}\cdot(\boldsymbol{r}-\boldsymbol{s})} Z\Big(\boldsymbol{r}, \boldsymbol{J}=(\boldsymbol{p}\cdot\hat{\boldsymbol{z}})\,\hat{\boldsymbol{z}}, t\Big)\,, \tag{6.55a}$$

$$Z(\boldsymbol{r},\boldsymbol{J},t) = \int d^3q \int \frac{d^3k}{(2\pi)^3} e^{i\boldsymbol{k}\cdot(\boldsymbol{q}-\boldsymbol{r})} \int \frac{d\lambda_1 d\lambda_2}{(2\pi)^2} \tilde{F}(\lambda_1)\tilde{F}(\lambda_2)\langle e^{i\widetilde{X}}\rangle\,, \tag{6.55b}$$

with

$$\widetilde{X} = \lambda_1 \delta_R(\boldsymbol{q}_1) + \lambda_2 \delta_R(\boldsymbol{q}_2) + \boldsymbol{k}\cdot\boldsymbol{\Delta} + \\ + \sum_{N=1}^{\infty} \frac{i^{N-1}}{N!} J_{i_1}\ldots J_{i_N} \left[C^{(N)}_{i_1\ldots i_N}(\boldsymbol{x}_2(\boldsymbol{q}_2) + (-1)^N C^{(N)}_{i_1\ldots i_N}(\boldsymbol{x}_1(\boldsymbol{q}_1)) \right] . \tag{6.55c}$$

The first cumulants $C^{(1)}$ corresponding to the term $\dot{\boldsymbol{\Delta}}/H$ in Eq. (6.45c) are also present in the single-streaming Gaussian streaming model and contribute both to the mean and variance of the Gaussian. In contrast, the second cumulant $C^{(2)}$ is conceptually knew and contributes only to the variance whereas all higher cumulants $C^{(n\geq 3)}$ are irrelevant for the Gaussian streaming model. It would be interesting to compare this approach to [VSOD13], which is also based on the phase space distribution function.

In analogy to [CRW13, WRW14] we define

$$K_{p,i_1,\ldots,i_p}(\boldsymbol{k},\boldsymbol{q},\lambda_1,\lambda_2) = \left\langle \left(\frac{\partial}{i\,\partial \boldsymbol{J}_{i_k}}\right)^p e^{i\widetilde{X}} \right\rangle \Bigg|_{\boldsymbol{J}=0} , \tag{6.56a}$$

which allows to compute

$$\frac{\partial^p Z}{(i\,\partial \boldsymbol{J}_{i_k})^p} = \int d^3q \int \frac{d^3k}{(2\pi)^3} e^{i\,\boldsymbol{k}\cdot(\boldsymbol{q}-\boldsymbol{r})} \int \frac{d\lambda_1 d\lambda_2}{(2\pi)^2} \tilde{F}(\lambda_1)\tilde{F}(\lambda_2) K_{p,i_1,\ldots,i_p}(\boldsymbol{k},\boldsymbol{q},\lambda_1,\lambda_2) . \tag{6.56b}$$

By integrating over λ we obtain the bias parameters, which are expectation values of derivatives of the Lagrangian halo density field $F[\delta_R(\boldsymbol{q})]$, according to [Mat08]

$$\int \frac{\mathrm{d}\lambda}{2\pi} \tilde{F}(\lambda)(i\,\lambda)^n \exp\left(-\tfrac{1}{2}\lambda^2\sigma_R^2\right) = \langle F^{(n)} \rangle . \tag{6.56c}$$

6.5.3 Application to the coarse-grained dust model

In the following we will concentrate on the coarse-grained dust model, such that $f = \bar{f}_{\mathrm{d}}$. We again Taylor expand $W = \ln Z$ up to second order in $\boldsymbol{J}$. But this time we also need to do the $\boldsymbol{u}$-integrals. Note that $Z|_{J=0}$ and $\partial Z/\partial J_i|_{J=0}$ have the same form as the single-stream expressions when all displacements $\boldsymbol{\Psi}$ and velocities $\boldsymbol{v}$ are replaced by their corresponding averages $\bar{\boldsymbol{\Psi}}$ and $\bar{\boldsymbol{v}}$, respectively. This is because

$$\int d^3u\, \tilde{f}(\boldsymbol{u},\boldsymbol{r},t) = \frac{\bar{M}^{(0)}}{(1+\bar{\delta})}(\boldsymbol{r},t) = 1 , \tag{6.57a}$$

$$\int d^3u u_i\, \tilde{f}(\boldsymbol{u},\boldsymbol{r},t) = \frac{\bar{M}^{(1)}_i}{(1+\bar{\delta})}(\boldsymbol{r},t) = a\bar{v}_i(\boldsymbol{r},t) . \tag{6.57b}$$

In contrast, the second order term $\partial^2 Z/(\partial J_i \partial J_j)|_{J=0}$ introduces extra structure, because it is given by the second moment $\bar{M}^{(2)}$, see (6.6c) which cannot be written in terms of $\bar{M}^{(1)}\bar{M}^{(1)}/\bar{M}^{(0)}$

$$\int d^3u u_i u_j\, \tilde{f}(\boldsymbol{u},\boldsymbol{r},t) = \frac{\bar{M}^{(2)}_{ij}}{(1+\bar{\delta})}(\boldsymbol{r},t) \;\neq\; a^2\bar{v}_i\bar{v}_j(\boldsymbol{r},t) . \tag{6.57c}$$

If Z is evaluated within CLPT using the dust model we recover the Gaussian streaming model (6.49) with a different expression for the variance of the Gaussian (see the discussion above). Apart from this, the CLPT evaluation is affected by the coarse-graining via (*i*) modified expressions for the kernels involving average displacements $\bar{\boldsymbol{\Psi}}$ and velocities $\bar{\boldsymbol{v}} = a\dot{\bar{\boldsymbol{\Psi}}}$ (including vorticity) instead of microscopic ones and (*ii*) the ocurrance of velocity dispersion $\bar{C}^{(2)}$ related to multi-streaming.

Evaluation of $1+\xi_X$ and v_{12} The expressions for the real-space two-point correlation function $1 + \xi_X(\boldsymbol{r}, t)$ and the mean pairwise velocity $\boldsymbol{v}_{12}(\boldsymbol{r}, t)$ are

$$1 + \xi_X(\boldsymbol{r}, t) = \int d^3q \int \frac{d^3k}{(2\pi)^3} e^{i\boldsymbol{k}\cdot(\boldsymbol{q}-\boldsymbol{r})} \int \frac{d\lambda_1 d\lambda_2}{(2\pi)^2} \tilde{F}(\lambda_1)\tilde{F}(\lambda_2) K_0(\boldsymbol{k}, \boldsymbol{q}, \lambda_1, \lambda_2)\,, \tag{6.58a}$$

$$[(1 + \xi_X)v_{12,i}](\boldsymbol{r}, t) = \int d^3q \int \frac{d^3k}{(2\pi)^3} e^{i\boldsymbol{k}\cdot(\boldsymbol{q}-\boldsymbol{r})} \int \frac{d\lambda_1 d\lambda_2}{(2\pi)^2} \tilde{F}(\lambda_1)\tilde{F}(\lambda_2) K_{1,i}(\boldsymbol{k}, \boldsymbol{q}, \lambda_1, \lambda_2)\,. \tag{6.58b}$$

where K_0 and K_1 have to be evaluated according to Eq. (6.56a). Since for those quantities only effect (i) is relevant, they can be computed in full analogy to [WRW14] but with coarse-grained instead of microscopic correlators, see appendices 6.C.1 and 6.109.

Evaluation of $\tilde{\sigma}_{12}$ In order to evaluate $\boldsymbol{\sigma}_{12}$ given by

$$[(1 + \xi_X)\tilde{\sigma}^2_{12,ij}](\boldsymbol{r}, t) = \int d^3q \int \frac{d^3k}{(2\pi)^3} e^{i\boldsymbol{k}\cdot(\boldsymbol{q}-\boldsymbol{r})} \int \frac{d\lambda_1 d\lambda_2}{(2\pi)^2} \tilde{F}(\lambda_1)\tilde{F}(\lambda_2) K_{2,ij}(\boldsymbol{k}, \boldsymbol{q}, \lambda_1, \lambda_2)\,, \tag{6.58c}$$

we need to determine K_2 which can be computed using

$$\begin{aligned}\widetilde{X} = \lambda_1\bar{\delta}_L(\boldsymbol{q}_1) + \lambda_2\bar{\delta}_L(\boldsymbol{q}_2) + \boldsymbol{k}\cdot\bar{\boldsymbol{\Delta}}(\boldsymbol{q}) + \\ + \sum_{N=1}^{\infty} \frac{i^{N-1}}{N!} J_{i_1}\ldots J_{i_N} \left[\bar{C}^{(N)}_{i_1\ldots i_N}(\boldsymbol{x}_2(\boldsymbol{q}_2) + (-1)^N \bar{C}^{(N)}_{i_1\ldots i_N}(\boldsymbol{x}_1(\boldsymbol{q}_1))\right].\end{aligned} \tag{6.59}$$

The cumulants $\bar{C}$ for the coarse-grained dust model can be simply taken from Eqs. (6.6). We recall that the second cumulant $\bar{C}^{(2)}$ contributes only to the variance of the Gaussian and all higher cumulants $\bar{C}^{(n\geq 3)}$ are irrelevant for the Gaussian streaming model. It is therefore interesting to study how the pairwise velocity dispersion $\sigma^2_{12,ij}\hat{z}^i\hat{z}^j$ depends on σ_x and σ_p as well as keeping or dropping the second cumulant which only contributes to the pairwise velocity dispersion. This will be investigated in the next section.

It is useful to split $\tilde{\sigma}^2_{12,ij}(\boldsymbol{r})$ into the components

$$\tilde{\sigma}^2_{12,ij}(\boldsymbol{r}) = \tilde{\sigma}^2_{\parallel}\hat{r}^i\hat{r}^j + \tilde{\sigma}^2_{\perp}(\delta^{ij} - \hat{r}^i\hat{r}^j) \tag{6.60a}$$

parallel and perpendicular to the pair separation vector $\boldsymbol{r}$ with

$$\tilde{\sigma}_{\parallel}^2 = \tilde{\sigma}_{12,ij}^2 \hat{r}^i \hat{r}^j, \quad \tilde{\sigma}_{\perp}^2 = (\tilde{\sigma}_{12,ij}^2 \delta^{ij} - \sigma_{\parallel}^2)/2 \tag{6.60b}$$

and similarly $\sigma_{12,ij}^2(\boldsymbol{r})$, such that $\sigma_{\parallel}^2 = \tilde{\sigma}_{\parallel}^2 - v_{12}^2$ and $\sigma_{\perp}^2 = \tilde{\sigma}_{\perp}^2$.

The explicit expression which has to be evaluated up to second order to obtain $\sigma_{12,ij}^2$ within cgCLPT is

$$\begin{aligned} K_{2,ij} = \exp\left[\sum_{N=1}^{\infty} \frac{i^N}{N!} \langle \widetilde{X}_{\boldsymbol{J}=0}^N \rangle_c\right] \Bigg(& \sum_{N=0}^{\infty} \frac{i^N}{N!} \left\langle \dot{\Delta}_i \dot{\Delta}_j \widetilde{X}_{\boldsymbol{J}=0}^N \right\rangle_c + \\ & + \sum_{N=0}^{\infty} \frac{i^N}{N!} \left\langle \dot{\Delta}_i \widetilde{X}_{\boldsymbol{J}=0}^N \right\rangle_c \sum_{M=0}^{\infty} \frac{i^M}{M!} \left\langle \dot{\Delta}_j \widetilde{X}_{\boldsymbol{J}=0}^M \right\rangle_c \\ & + \sum_{N=0}^{\infty} \frac{i^N}{N!} \left\langle \left\{ 2\sigma_p^2 \delta_{ij} + \left[\overline{\frac{(1+\delta) v_i v_j}{1+\bar{\delta}}} - \bar{v}_i \bar{v}_j \right] (\boldsymbol{x}_1(\boldsymbol{q}_1)) + \right.\right. \\ & \left.\left. + \left[\overline{\frac{(1+\delta) v_i v_j}{1+\bar{\delta}}} - \bar{v}_i \bar{v}_j \right] (\boldsymbol{x}_2(\boldsymbol{q}_2)) \right\} \widetilde{X}_{\boldsymbol{J}=0}^N \right\rangle_c \Bigg), \end{aligned} \tag{6.61}$$

where

$$\begin{aligned} \overline{(1+\delta) v_i v_j} &= \exp\left(\tfrac{1}{2} {\sigma_x}^2 \Delta\right) \left\{ (1+\delta) v_i v_j \right\} \\ (1+\bar{\delta}) \bar{v}_i &= \exp\left(\tfrac{1}{2} {\sigma_x}^2 \Delta\right) \left\{ (1+\delta) v_i \right\}. \end{aligned}$$

Within the large round brackets of (6.61), only the first two terms survive the limit $\sigma_x \to 0$, $\sigma_p \to 0$ and then agree with standard CLPT for the dust model Eq. (34) in [WRW14]. The explicit and tedious calculations for the modified first two terms and for the conceptually new third term in (6.61) can be found in appendix 6.C.3, where we assume Gaussian statistics for the linear initial conditions.

6.6 Results: Improved two-point statistics

In order to understand the effects of the various modifications introduced by the coarse-grained evolution, we will compare our model called cgCLPT to original CLPT and to CLPT in which we use a smoothed input power spectrum motivated by [Mat12]. We will compare predictions for halo correlation functions as well as pairwise velocity statistics to measurements within the publicly available Horizon Run 2 (HR2) simulation halo catalog [KPGD09, KPR+11]. As this is work in progress we restrict our attention the case where $\sigma_p = 0$ and consider only $z = 0$.

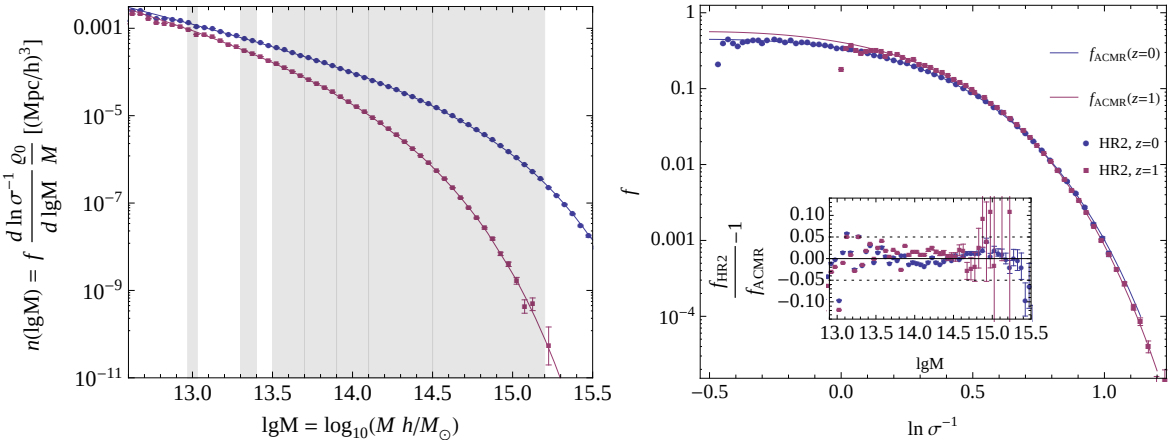

FIGURE 6.4: *left* mass function measured from HR2 at $z = 0$ and $z = 1$ (dots) and the best fitting mass function obtained from Eqs. (6.63) and (6.64). *right* Here we converted the mass function into the multiplicity function f. The Inset shows the relative difference between model and HR2.

6.6.1 Horizon Run halo catalog and mass function

The HR2 has an enormous size of 7200 Mpc/h and consists of 6000^3 particles of mass lgM $=$ 11.097, where we introduced the notation lgM $\equiv \log_{10}(Mh/M_\odot)$. We measured halo correlation functions and velocity statistics from large galaxy-sized halos lgM $= 13.0$ to cluster-sized halos lgM $= 15.2$ at the redshifts $z = 0$ and $z = 1$. In Fig. 6.4 (left) we show the measured halo mass function (dots) and the mass bins used in grey. The relevant cosmological parameters are

$$\begin{aligned} \Omega_m &= 0.26\,, \\ \Omega_b &= 0.044 \\ h &= 0.72 \\ \sigma_8 &= 1/1.26 \simeq 0.794\,. \end{aligned}$$

The halo mass function is of interest because it directly determines the bias parameters trough the conditional mass function. We will use the formalism developed in [Mat08, Mat12], that relate $\langle F'\rangle$ and $\langle F''\rangle$ to the Lagrangian bias parameters following from a excursion set mass function. Dark matter halos result from the non-linear collapse of initial density perturbations. The abundance and clustering of these virialized structures depends on both the properties of the initial matter density field and the nonlinear dynamics encapsulated in the collapse threshold δ_c. Following the seminal work of [PS74], the excursion set approach [BCEK91] computes the abundance of dark matter halos as a function of their mass. The method involves the at scale R smoothed initial density field $\delta_R(\boldsymbol{q})$ and the idea that once $\delta_R(\boldsymbol{q})$ is above a threshold $\delta_c(z)$ for the largest possible smoothing scale $R(M)$, that the region will collapse at z and correspond to a halo of mass M

$$M = \frac{4\pi}{3}\varrho_0 R(M)^3\,. \tag{6.62}$$

The excursion set mass function $n(M)$ is obtained by equating the fraction of collapsed comoving volume to the comoving density of halos $n(M)$ per mass range $[M, M + dM]$

$$n(M) = f(\sigma)\frac{\varrho_0}{M}\frac{d\ln\sigma^{-1}}{dM}\,, \tag{6.63}$$

where ϱ_0 is the comoving background matter density and $f(\sigma)$ is related to the fraction of collapsed volume per mass and is called multiplicity function. For the multiplicity function f we use Eq. (2.52) based on [MR10a, MR10b, CA11b, CA11a] which we will denote in this chapter

$$f_{\mathrm{ACMR}}(\sigma) = f_0(\sigma) + f_{1,\beta=0}^{m-m}(\sigma) + f_{1,\beta^{(1)}}^{m-m}(\sigma) + f_{1,\beta^{(2)}}^{m-m}(\sigma)\,, \tag{6.64}$$

where f_0 is the Markovian part, while the other terms are non-Markovian corrections that arise when taking into account correlations between different scales introduced by a top-hat smoothing. In [ARSC12] it was shown that the first order approximation in κ is sufficient to reproduce the exact solution to $\sim 5\%$ accuracy, using parameter values $\beta = 0.12$, $D_B = 0.4$. In order to fit the HR2 halo mass function we find different values, namely $\beta = -0.07$, $D_B = 0.34$ for $z = 0$, and $\beta = -0.245$, $D_B = 0.29$ for $z = 1$. With these values f_{ACMR} fits the HR2 mass function again within 5% accuracy, see Fig. 6.4. The fact that a negative β is required in both cases might signal a problem within HR2. A positive β corresponds to the physically well understood picture that small masses require a larger density amplitude to collapse due to the more likely ellipticity of low variance peaks [SMT01]. In the following we will fix $\beta = -0.07$, $D_B = 0.34$ because we will restrict our attention to $z = 0$. We will see that these parameters will lead to reasonable predictions for the bias parameters $\langle F'\rangle$ and $\langle F''\rangle$, which we will derive in the next section from $f_0(\sigma, \beta = -0.07, D_B = 0.34)$.

6.6.2 Correlation functions and pairwise velocity

We estimate the correlation functions using a simple estimator [MW96], which is sufficient for our purposes because of the large number of about 4×10^8 of halos in the periodic box. By resampling the whole box with 27 jackknife samples [EG83], we estimate the covariance matrix of the various correlation functions for model parameter fits and error bars in the plots. Each of these 27 subsamples consists of the whole box, with 1 out of 27 sub-boxes of size 2400 Mpc/h removed.

6.6.2.1 Real space correlation function

In real space the simplest estimator for the full box is given by [MW96]

$$1 + \hat{\xi}(r) = \frac{\Delta P(r)}{n_{\mathrm{tot}} 4\pi r^2 \Delta r}\,, \tag{6.65}$$

where $\Delta P(r)$ is the mean number of neighbour halos in a shell at distance r with width Δr around a halo at $r = 0$, and n_{tot} is the mean number density of halos in the simulation at a given time, such that $n_{\mathrm{tot}} 4\pi r^2 \Delta r$ gives the mean number of neighbour halos if the halos were evenly

distributed. Therefore $\hat{\xi}(r)$ estimates the excess probability to find a halo within an interval $I_r := [r - \Delta r/2, r + \Delta r/2]$ away from another halo. We determine $\Delta P(r)$ as $DD(r)/N_{\rm tot}$, where $N_{\rm tot}$ is the total number of halos in the box and $DD(r)$ is the number of all halo pairings with distance $r \pm \Delta r/2$. In practice we calculate

$$DD(r) = \sum_{k,i,k\neq i}^{N_{\rm tot}} \delta_{r_{ik},r}\delta_{r_{ki},r}\,, \tag{6.66}$$

where $r_{ik} = |\boldsymbol{r}_i - \boldsymbol{r}_k|$ is the distance between a halo at $\boldsymbol{r}_i$ and another halo at $\boldsymbol{r}_k$ and $\delta_{r_{ik},r}$ is 1 if $r_{ik} \in I_r$ and 0 otherwise. In order to estimate the error bars and the covariance matrix of $\hat{\xi}(r)$, we instead calculate

$$1 + \hat{\xi}^{(j)}(r) = \frac{\Delta P^{(j)}(r)}{n_{\rm tot} 4\pi r^2 \Delta r}\,, \tag{6.67}$$

where $\Delta P^{(j)}(r)$ is the mean number of neighbour halos in a shell at distance $r \pm \Delta r/2$ around a halo in the subsample j, which is obtained be removing the subbox j. Therefore $\hat{\xi}^{(j)}(r)$ is the excess probability to find a halo at distance $r \pm \Delta r/2$ away from another halo within the subsample j. We determine $\Delta P^{(j)}(r)$ as $DD^{(j)}(r)/N_{\rm tot}^{(j)}$, where $N_{\rm tot}^{(j)}$ is the total number of halos in the subsample j and $DD^{(j)}(r)$ is the number of all halo pairings with distance $r \pm \Delta r/2$, with at least one partner lying in j

$$DD^{(j)}(r) = \sum_{k,i,k\neq i}^{N_{\rm tot}} \delta_{r_{ik},r}\delta^{(j)}_{r_{ki},r}\,, \tag{6.68}$$

where $\delta^{(j)}_{r_{ik},r}$ is 1 if $r_{ik} \in I_r$ and $\boldsymbol{r}_k$ lies the subsample j and 0 otherwise. The correlation function is then given by

$$\hat{\bar{\xi}}(r) = \frac{1}{27}\sum_{j=1}^{27} \hat{\xi}^{(j)}(r)\,, \tag{6.69}$$

with covariance matrix

$$C_{\hat{\xi}}(r,r') = \frac{26}{27}\sum_{i=1}^{27}\left[\hat{\xi}^{(j)}(r) - \hat{\bar{\xi}}(r)\right]\left[\hat{\xi}^{(j)}(r') - \hat{\bar{\xi}}(r')\right]\,, \tag{6.70}$$

which will be used for fitting the bias model. The error bar

$$\sigma_{\hat{\xi}}(r) = \sqrt{\frac{26}{27}\sum_{i=1}^{27}\left[\hat{\xi}^{(j)}(r) - \hat{\bar{\xi}}(r)\right]^2} \tag{6.71}$$

is only used in plots. We choose $\Delta r = 2\,{\rm Mpc}/h$ and cover 100 r-bins. Fig. 6.5 shows the halo correlation for 7 mass bins at $z = 0$. We indicate with the dotted line at $\xi = 1$ the nonlinear regime. For the largest mass bin corresponding to large galaxy clusters, a drop in the correlation function for r smaller than twice the virial radius is due to halo exclusion arising in a friend-of-friend halo finder that was used in HR2.

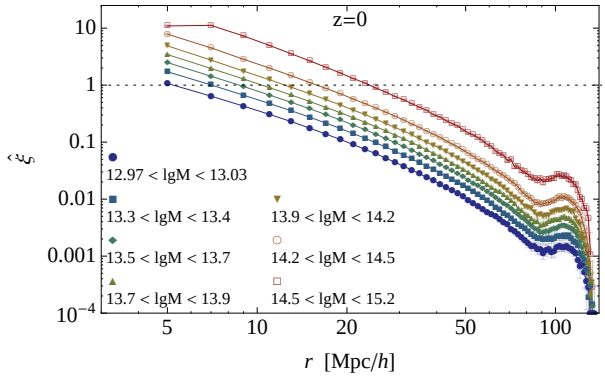

FIGURE 6.5: The measured halo auto-correlation function at $z = 0$ for masses specified in the legend.

The bias model We will later fit for the optimal mass $M_{\rm opt}$ using a bias model (6.75a) to determine the two parameters

$$\langle F' \rangle \equiv b_1(M_{\rm opt}) \quad \text{and} \quad \langle F'' \rangle \equiv b_2(M_{\rm opt}) \tag{6.72}$$

entering the cgCLPT as well as the CLPT model. For a given mass bin of the measured function $\hat{\hat{\xi}}$ the bias parameter b_1 and b_2 could also be predicted, but it makes sense to "help" the bias model by fitting for M similar to what was done in [CRW13, WRW14]. We derive the bias parameters b_n from f_0, Eq. (2.52b) because the full $f_{\rm ACMR}$, Eq. (6.64) which includes non-Markovian corrections κ cannot be interpreted as a conditional mass function [Ach12]. In contrast, the Markovian mass function f_0 is the limit $S_0 \to 0, \delta_{R_0} \to 0$ of the conditional mass function [Ach12] for a drifting and diffusing barrier

$$f_0(S|\delta_0, S_0) = \frac{\sqrt{\frac{2}{\pi}}(\delta_c - \delta_{R_0})\frac{S}{a_B}}{\left(\frac{S}{a_B} - S_0\right)^{3/2}} \exp\left[-\frac{(\delta_c + \beta S - \delta_0)^2}{2\left(\frac{S}{a_B} - S_0\right)}\right], \tag{6.73}$$

and therefore $f_0(S)$ can be used to obtain the bias parameters (6.75a). According to the peak-background split [BCEK91], where R (or S or M) is the peak scale, while R_0 (or S_0 or M_0) is the background scale, the conditional mass function describes the local mass function in a region of size R_0 that has an overall over/underdensity δ_{R_0}. The physical picture of (6.73) is that a long-wavelength mode $\delta_{R_0} > 0\,(< 0)$ reduces (increases) the local threshold for collapse. Another way to understand halo bias is in terms of the peak model [BBKS86], which takes into account that proto-halos are density peaks with high (low) δ_R/σ, which are naturally (anti-) clustered in a Gaussian random field. The subsequent gravitational dynamics described by the displacement field $\boldsymbol{\Psi}$ then leads to additional clustering which is a physically distinct effect and leads to a nonlocal Eulerian bias. The Lagrangian halo fluctuation field F introduced in Eq. (6.34) for

halos of mass $M(S)$ therefore is

$$F[\delta_{R_0}(\boldsymbol{q})] = \frac{f_0(S|\delta_{R_0}(\boldsymbol{q}), S_0)}{f_0(S)} \tag{6.74a}$$

$$= 1 + \sum_{n=1}^{\infty} \frac{b_n(S, S_0)}{n!} \delta_{R_0}(\boldsymbol{q})^n \,. \tag{6.74b}$$

It encodes the initial clustering of proto-halos. In the large scale limit $S \gg S_0$, the bias coefficients become independent of S_0 and can be calculated from f_0

$$b_n(M, z) = (-1)^n \frac{\partial^n_{\delta_c} f_0}{f_0} \tag{6.75a}$$

$$b_1(M, z) = a_B\beta - \delta_c^{-1} + \sigma^2 m a_B \delta_c \tag{6.75b}$$

$$b_2(M, z) = (a_B\beta)^2 - 2a_B\beta\delta_c^{-1} + \left(2a_B^2\beta\delta_c - 3a_B\right)\sigma^2 + a_B^2\delta_c^2\sigma^4 \,, \tag{6.75c}$$

where we used that $\partial_{\delta_{R_0}} f_0(S|\delta_{R_0}(\boldsymbol{q}), S_0)|_{S_0\to 0} = -\partial_{\delta_c} f_0(S)$. In principle, the numerical values of the bias parameters can also be calculated without the need to fit for $M_{\rm opt}$. The average bias parameters using the mass function (6.63) are given by

$$\bar{b}_n = \frac{\int_{\rm lgM_{min}}^{\rm lgM_{max}} d\,{\rm lgM}\, n({\rm lgM}) b_n({\rm lgM})}{\int_{\rm lgM_{min}}^{\rm lgM_{max}} d\,{\rm lgM}\, n({\rm lgM})} \,, \tag{6.76}$$

where $\rm lgM_{min}$ and $\rm lgM_{max}$ are lower and upper value of the mass bin. But as mentioned before we will assist the bias model by instead fitting for lgM. The bias parameters are then kept fixed for the prediction of v_{12}, $\sigma^2_\perp$ and $\sigma^2_\parallel$, Eqs. (6.58) and therefore also for the evaluation of the redshift space correlation functions $\xi_n(s)$ Eq. (6.55).

Choosing the smoothing scale It is important to note that once a smoothing scale is introduced in the initial conditions for the proto-halo density field F, the assumption of zero velocity bias, or $\boldsymbol{v}_X = \boldsymbol{v}$, requires the smoothing of the initial density field $\delta_1(\boldsymbol{q})$ entering all parts of the perturbation theory formalism, in particular within (cg)CLPT the initial conditions for $\boldsymbol{\Psi}$. This smoothing scale is a priori completely independent from σ_x which is an additional parameter in the coarse grained dust model. It is clear that F derived from the peak-background split depends on the smooth δ_{R_0} see Eq. (6.74a).

The reason for why we expect to smooth also the initial conditions for the displacement $\boldsymbol{\Psi}$ is that the initial proto-halo velocity field $\boldsymbol{v}_X$ should be smoothed at the same scale as the initial proto-halo density field F since the protohalo velocity corresponds to the mean velocity of CDM particles comprising the proto-halo. The velocity $\boldsymbol{v}$ of the (nonlinearly evolving) dark matter field δ and the conservation of the number of proto-halos up to virialization z_c can be written as

$$\frac{d\,\delta_X(\boldsymbol{x}, z)}{d\,\tau} = (1 + \delta_X(\boldsymbol{x}, z))\nabla_x \cdot \boldsymbol{v}_X(\boldsymbol{x}, z) \tag{6.77}$$

$$\frac{d\,\delta(\boldsymbol{x}, z)}{d\,\tau} = (1 + \delta(\boldsymbol{x}, z))\nabla_x \cdot \boldsymbol{v}(\boldsymbol{x}, z) \,. \tag{6.78}$$

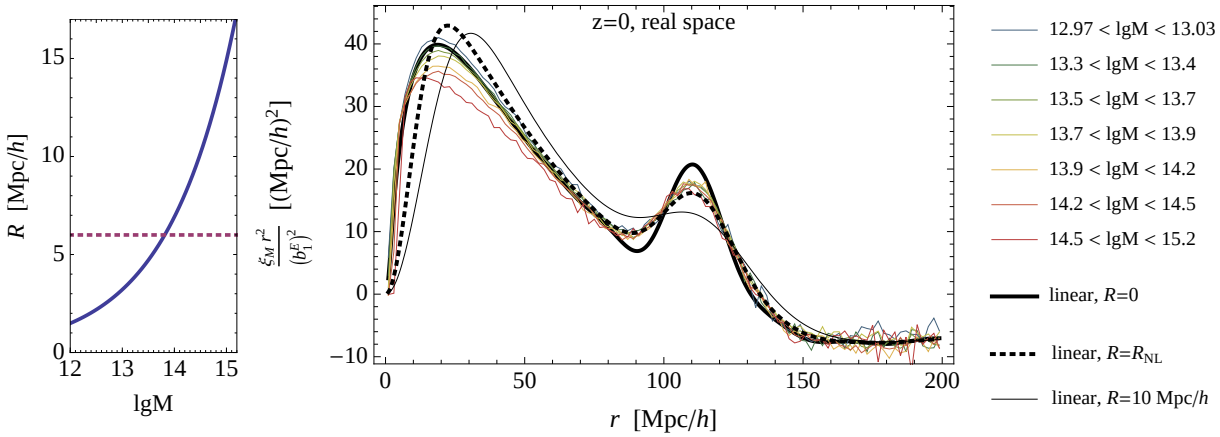

FIGURE 6.6: *left*: Comparison of $R_{\rm NL} \simeq 6\,{\rm Mpc}/h$ (*dashed*) to the Lagrange radius (*full*) as a function of lgM. *right* Comparison between real space halo correlation function times r^2 for 7 mass bins measured in HR2 (*thin lines*). All curves a rescaled by the best fitting $b_1(M_{\rm opt})$ for the nonlinear theory shown in Fig. 6.8. Also shown are the linear correlation function (*black, thick*), the linear correlation function convolved with $W(k\,6\,{\rm Mpc}/h)^2$ (*dotted*) and $W(k\,10\,{\rm Mpc}/h)^2$ (*thin, black*).

Where τ is conformal time, $d/d\tau = \partial_\tau + \boldsymbol{v}\cdot\boldsymbol{\nabla}_{\boldsymbol{x}}$ is the convective derivative and $\delta_X(\boldsymbol{x},z) = \delta_X(\boldsymbol{x},z|z_c,M)$ is short hand notation for the nonlinearly evolving proto-halo density field that will virialize at time z_c with mass M. For $\boldsymbol{v}_X = \boldsymbol{v}$, these equations can be integrated exactly

$$1+\delta_X(\boldsymbol{x},z|M) = \big(1+\delta_X(\boldsymbol{q},z|M)\big)\big(1+\delta(\boldsymbol{x},z)\big)\,, \tag{6.79}$$

with initial conditions $\delta(\boldsymbol{x},z\to\infty)) = 0$ and $\boldsymbol{x}(\boldsymbol{q},z\to\infty)) = \boldsymbol{q}$ and $\delta_X(\boldsymbol{x},z\to\infty|z_c,M) = \delta_X(\boldsymbol{q}|z_c,M)$. Writing

$$F = 1+\delta_X(\boldsymbol{q}|z,M)\,,$$

we see that Eq. (6.79) coincides with (6.34) if $\boldsymbol{v}_X = \boldsymbol{v}$. Therefore the smoothing scale entering the initial conditions for the proto-halo density field, should also be used in the initial conditions for the displacement field $\boldsymbol{\Psi}$ in order to ensure that there is no velocity bias [CLMP98]. If R_0 is kept consistently within the whole perturbation theory calculation, the shape of ξ_M would appear smeared out on scales below R_0. But $\xi_M(r)$ is affected even for $r \gg R_0$, in particular the BAO peak, see the thin black line in Fig. 6.6 for the rather small $R_0 = 10\,{\rm Mpc}/h$. To see how this arises we consider linear SPT and obtain from Eq. (6.34) or (6.79)

$$1+\delta_{1,M}(\boldsymbol{x}) = (1+\delta_{R_0}(\boldsymbol{x}))\,F[\delta_{R_0}(\boldsymbol{q}=\boldsymbol{x})] \tag{6.80a}$$

$$\delta_{1,M}(\boldsymbol{x}) = [1+b_1(S(M),S_0)]\delta_{R_0}(\boldsymbol{x}) \tag{6.80b}$$

and in Fourier space

$$\delta_{1,M}(\boldsymbol{k}) = [1+b_1(S(M),S_0)]W(kR_0)\delta_{\rm L}(\boldsymbol{k}), \tag{6.81}$$

such that the linear halo power spectrum and the correlation function become

$$P_{11,M}(k) = [1+b_1(S(M),S_0)]^2 W(kR_0)^2 P_{\rm L}(k)\,, \tag{6.82a}$$

$$\xi_{11,M}(r) = \frac{1}{2\pi^2}\int_0^\infty dk P_{11,M}(k)k^2\frac{\sin(kr)}{kr}\,. \tag{6.82b}$$

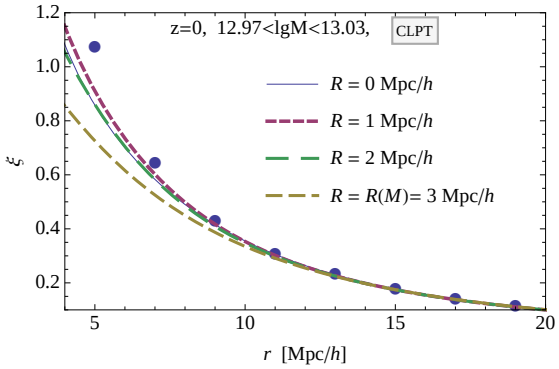

FIGURE 6.7: The halo correlation for lgM = 13 at small scales. It is clearly visible that that a smoothing of the initial conditions with $R = 1\,\mathrm{Mpc}/h$ increases the power on small scales and improves the agreement to HR2 (data points) compared to the cases $R = 0, 2\,\mathrm{Mpc}/h$ and $R = R(\mathrm{lgM}=13) \simeq 3\,\mathrm{Mpc}/h$.

Physically it is clear that the arbitrary scale R_0 should not enter the final result, because it was introduced as a tool to estimate how the local number density of halos depends on the initial density field. A formal way to avoid the introduction of R_0 right from the start is to consider a different conditional mass function, where the condition is not that there exists a large scale density field of a fixed value δ_{R_0} when the first up-crossing occurs at R, but rather that there exists another first up-crossing at the same scale R but at a different point in space [PMLC98]. In a Monte-Carlo realization of this idea one would consider a correlated pair of random walks at a fixed distance. It is clear from Fig. 2.8 that the positions of the first up-crossings (blue dots) are highly correlated. Another idea is to get rid of R_0 through renormalization by simply absorbing the background smoothing scale R_0 into renormalized albeit nonlocal bias coefficients [SJD13] such that the halo fluctuation field $F[\delta_{R(M)}(\boldsymbol{q})]$ only depends on the physical peak scale $R(M)$ and not on the arbitrary background scale R_0. After "renormalization", the expression for F might receive a nonlocal term proportional to the Laplacian of the density field and other correction terms which we neglect. The point we want to emphasise is that the smoothing scale R_0 in the window function gets replaced by the peak scale $R(M)$ leading to an expression free of R_0

$$F[\delta_R(\boldsymbol{q})] = 1 + \sum_{n=1}^{\infty} \frac{1}{n!}(b_n(S)\delta_R(\boldsymbol{q})^n + ...)\,. \tag{6.83}$$

Although smoothing at the peak scale $R(M)$ is physically meaningfull [BM96], the CLPT correlation function $\xi_M(r)$ and also the linear correlation function $\xi_{11,M}(r)$ again show significant deformations even if the Lagrangian smoothing scale $R(M)$ is used in the window function, see Figs. 6.6 and 6.7. For masses lgM $>$ 13.8, the smoothing scale $R(M)$ will be as large as the nonlinear scale

$$R_{\mathrm{NL}}(z) \equiv \sqrt{\langle \boldsymbol{\Psi}^2 \rangle / 3}\,, \tag{6.84}$$

which is also the average displacement of a particle. The problem becomes manifest in an approximation to CLPT, called iPT [Mat08], where it turns out that a Gaussian window function

with width $R_{\rm NL}$ multiplies the whole expression for the nonlinear halo correlation function:

$$P_{{\rm iPT},M} = W(kR_{\rm NL})^2 \left\{(1+b_1(M))^2 W(kR)^2 P_L(k) + ...\right\} , \tag{6.85}$$

where we omitted other nonlinear terms and restored the window function in front of P_L [Mat08]. At $z = 0$ the average displacement $R_{\rm NL} \simeq 6\,{\rm Mpc}/h$ is responsible for the nonlinear smoothing of the BAO peak in the Zel'dovich approximation. No extra mass-dependent smoothing is observed in the simulation; all mass bins show a similarly smoothed-out BAO peak after rescaling with the best fitting $b_1^{\rm E} = 1 + b_1(M_{\rm opt})$, see Fig. 6.6. Note that $M_{\rm opt}$ was obtained by fitting our cgCLPT model to the data, see the next paragraph, and not with the aim to overlap all BAO peaks for the different mass bins. As one can see in Eq. (6.85) any mass related smoothing $R(M)$ adds to the already existing $R_{\rm NL}$-smoothing leading to an effective smoothing $\sqrt{R_{\rm NL}^2 + R(M)^2}$. The shape of the thin black line around the BAO peak in Fig. 6.6 does look very similar[3] in iPT (6.85) and CLPT if one smoothes the initial conditions at $R = R({\rm lgM}=14.2) \simeq 8\ {\rm Mpc}/h$.

A pragmatic way to avoid this problem is the widespread negligence of the window function $W(kR(M))$ depending on the peak scale. For instance, in [Mat08] the problem is mentioned but it is argued that the window function can be set to 1 (or $R = 0$), at the end of the calculation if one is interested only in scales much larger than R.

Although this sounds reasonable, in reality, as we have just seen, the result for ξ_M is changed dramatically if the window function is kept, even on scales seemingly large compared to R; the BAO peak is smeared out much stronger than observed in simulations. The best correspondence between the nonlinear ξ_M and simulations, see Fig. 6.8, is obtained by choosing $\sigma_x, R \simeq 1\,{\rm Mpc}/h$ where σ_x is the coarse-graining scale within cgCLPT and R is the smoothing scale applied to the initial linear density field. Apart from the fact that this procedure seems to be ad hoc, it also does not lead to accurate predictions of the pairwise velocity dispersion $\tilde{\boldsymbol{\sigma}}_{12}$. As we will see soon, the agreement between theory and simulation actually improves significantly for $\tilde{\boldsymbol{\sigma}}_{12}$ if a smoothing around the Lagrangian scale $R(M)$ is performed!

All this combined seems paradoxical for several reasons

- We describe the dynamics of "particles", in our case (proto-)halos, in terms of a fluid. Why should we obtain the best result if we resolve the fluid on scales much smaller than inter-particle distance and even smaller than intrinsic size of the particles?

- In the Lagrangian point of view, the displacement field, generates both density field and the velocity field. Why is the velocity dispersion better described when we smooth at a "particle" size $R(M)$, while halo density correlation and pairwise velocity is better described if we smooth on a scale around $R = 1\,{\rm Mpc}/h$?

A possible explanation for this discrepancy is that the halo correlation function and pairwise velocity depend very sensitively on the relative displacements of the halos, because $\delta \simeq -\boldsymbol{\nabla}\cdot\boldsymbol{\Psi}$. In linear perturbation theory $\tilde{\sigma}_\parallel(r), \tilde{\sigma}_\perp(r)$ are independent of δ, while $\xi(r)$ and $v_{12}(r)$ do depend on δ. Since proto-halos move on average a distance $\langle|\boldsymbol{\Psi}|\rangle \simeq R_{\rm NL}$, it is clear that the typical

[3] The reason why it does not look exactly the same is that $R_{\rm NL}$ itself depends on the scale R with which the initial linear density field is smoothed.

scales $R_{\rm NL}/\delta$ over which $\boldsymbol{\Psi}$ varies can become much smaller than $R_{\rm NL}$. Therefore smoothing on scales $R_{\rm NL}$ will introduce a large error in the halo density field. The size of large proto-halos is about $R(M) \simeq R_{\rm NL}$, see Fig. 6.6. Thus if we smooth at the Lagrangian scale $R(M)$ we cannot analytically resolve the relative positions of formed halos which have sizes $R_{\rm vir} \simeq 0.14R(M)$, and whose centers of mass can be determined to even higher precision in the N-body simulation.

On the other hand the velocity of a proto-halo arises as the average velocity of all particles constituting the proto-halo. Since the proto-halo has a size $R(M)$, it is natural that one should average or smooth at the scale $R(M)$ to get $\dot{\boldsymbol{\Psi}}$.

While experimenting with the smoothing scale, we observed that the agreement with the N-body velocity statistics becomes worse for both $R \ll R(M)$ and $R \gg R(M)$. Similarly the halo correlation is optimized by a nonzero $R \simeq 1\,\mathrm{Mpc}/h$. The latter fact is also employed in the truncated Zel'dovich approximation (TZA) to improve ZA type simulations [MPS94, BCM94], as well as in analytical methods based on the ZA [MHP93, Por97]. In the case lgM $= 13$, where the smearing of the BAO peak is not strongly affected by changing $R = 0, 1, 2, 3\,\mathrm{Mpc}/h$, the increase and improvement on the small scale power is clearly visible in Fig. 6.7. In Sec. 6.6.3 we will consider the TZA in redshift space.

Within cgCLPT we have to deal with the additional smoothing scale σ_x which coarse grains the dynamics, while R coarse grains the initial conditions. If we would stick to first order displacements, then cgCLPT does exactly correspond the TZA, because $\boldsymbol{\Psi}_{\rm TZA}$ depends on R and σ_x exactly the same way. Taking into account nonlinear contributions to $\boldsymbol{\Psi}$, this degeneracy breakes down and we need to find a reasonable prescription to choose R and σ_x. In the following we will compare the cases

- $R = 1\,\mathrm{Mpc}/h$, $\sigma_x = 0$ and $R = R(M)$, $\sigma_x = 0$ will be labeled with CLPT in plots, because it corresponds to CLPT [CRW13] in which the input power spectrum is smoothed.

- $R = 0.1\,\mathrm{Mpc}/h$, $\sigma_x = 1\,\mathrm{Mpc}/h$ and $R = R(M)/\sqrt{2}$, $\sigma_x = R(M)/\sqrt{2}$ will be labeled with cgCLPT in plots, for which we use our new kernels and expressions (6.58) with $\sigma_p = 0$ to derive the ingredients of the GSM.

Fitting the bias model In this paragraph we fit $\langle F' \rangle = b_1(M)$, $\langle F'' \rangle = b_2(M)$ for the 7 mass bins trough a least square fit for M. We fix the cgCLPT model parameters to $R = 0.1\,\mathrm{Mpc}/h$, $\sigma_x = 1\,\mathrm{Mpc}/h$, $\sigma_p = 0$, and do not discuss $R = 1\,\mathrm{Mpc}/h$, $\sigma_x = 0$ because within the r-range of our fit they are undistinguishable. We will not consider the Lagrangian smoothing scales either, since as discussed in the last section it leads to unreasonable results for the halo correlation function. We will consider the Lagrangian smoothing for velocity statistics in the next subsection.

For the χ^2-fit we did not use all 100 r-values per mass bin of the measured correlation function $\hat{\xi}$, because we only want to force our model to match scales larger than $40\,\mathrm{Mpc}/h$. From the 80 remaining data points per mass bin we only used 26 linear combinations. The reason for this is that we measured the covariance matrix $C_{\hat{\xi}}(r_i, r_j)$, where i, j label r-bins, only trough 27 samples and therefore the 80 eigenvalues $\mathrm{Eval}_m(C)$, decreasing with increasing m, are sharply

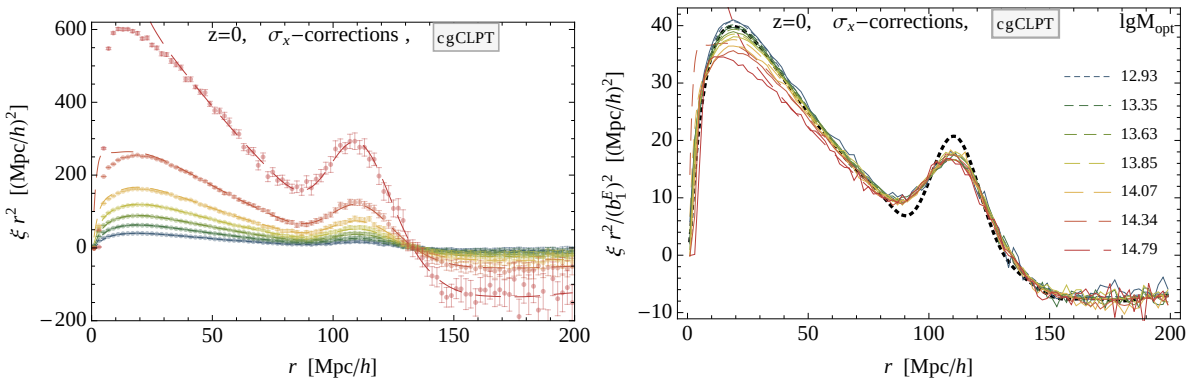

FIGURE 6.8: *left*. Comparison between halo correlation functions times r^2 obtained by cgCLPT ($\sigma_x = 1, R = 0.1$) (*thin* lines) and as measured in HR2 (data points). For each curve, $M_{\rm opt}$ was fitted by minimising the χ^2 (6.86). *right*. The same information is shown, but rescaled by the square of $b_1^{\rm E} = 1 + b_1(M_{\rm opt})$. The *thin* lines show HR2, the *dashed* lines cgCLPT and the *dotted black* line the linear correlation function.

$\overline{\rm lgM}$	13.00	13.35	13.59	13.79	13.99	14.25	14.67
lgM$_{\rm opt}$	12.93	13.35	13.63	13.85	14.07	14.39	14.79
χ^2	27.4	9.5	19.5	24.7	14.0	19.9	23.2
b_1(lgM$_{\rm opt}$)	-0.01	0.26	0.51	0.77	1.11	1.68	3.17
$\bar{b}_1$	0.02	0.25	0.47	0.69	0.98	1.49	2.71
b_2(lgM$_{\rm opt}$)	-0.74	-0.83	-0.79	-0.61	-0.18	1.06	7.41
$\bar{b}_2$	-0.76	-0.83	-0.80	-0.68	-0.36	0.64	5.37

TABLE 6.1: Best fit values for the mass lgM$_{\rm opt}$ of the given mass bin for $z = 0$, denoted here by the average mass $\overline{\rm lgM}$ (6.87). Also given are the bias parameters (6.75a) evaluated at lgM$_{\rm opt}$ as well as the average bias (6.76). There is good agreement between $\overline{\rm lgM}$ and lgM$_{\rm opt}$ as well as the resulting best fitting $b_{1,2}$(lgM$_{\rm opt}$) and model predictions $\bar{b}_{1,2}$, which becomes worse for the largest masses.

dropping to zero after $m = 26$. We therefore minimize

$$\chi^2 = \sum_{m=1}^{26} \left[\sum_{j=21}^{100} \frac{\mathrm{Evec}_{mj}(C)}{\mathrm{Eval}_m(C)} \left(\xi(r_j, M) - \hat{\bar{\xi}}(r_j) \right) \right]^2 . \tag{6.86}$$

$\mathrm{Evec}_{mj}(C)$ is the eigenvector matrix of $C_{\hat{\xi}}(r_i, r_j)$, that projects the data onto de-correlated linear combinations. Those linear combinations with the largest eigenvalues (smallest m) are called principal components and have the strongest impact on $M_{\rm opt}$.

The measured HR2 correlation functions times r^2 as well as the model with best fitting $M = M_{\rm opt}$ are shown in Fig. 6.8. The left plots show the halo correlation function measured for all mass bins (see the legend on the right) estimated using (6.69) with error bars (6.71). The full lines show the model predictions with $M_{\rm opt}$. In order to get an impression about the non-locality of the halo bias and its mass dependence, we divide all correlation functions by the linear local Eulerian bias $b_1^{\rm E} = 1 + b_1(M_{\rm opt})$. We plot in Fig. 6.8 on the right the HR2 correlation function as continuous lines and the model with dashed lines, whereby it becomes clear that the BAO peak can be aligned for all masses after rescaling with $(b_1^{\rm E})^2$ both theory and data. Therefore (*i*) the

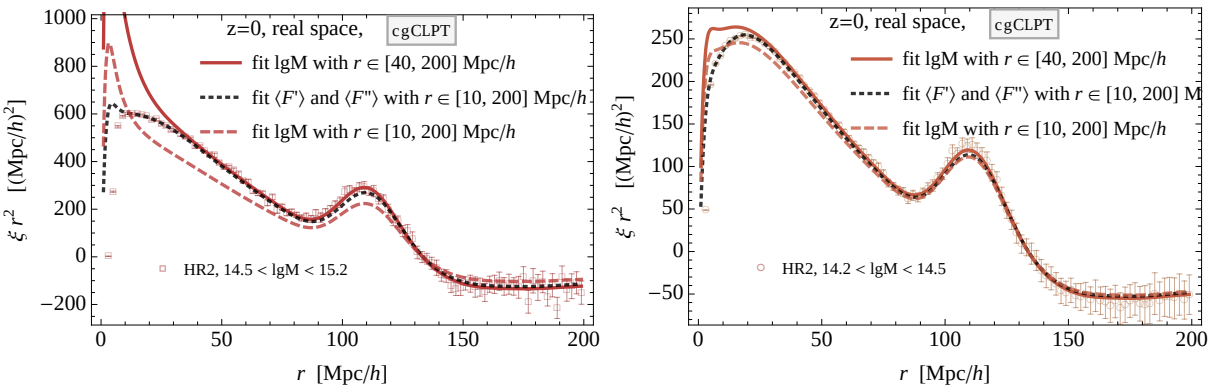

FIGURE 6.9: Real space correlation function times r^2 for the largest mass bins; the mass function fit for $\mathrm{lgM}_{\mathrm{opt}}$ does not work anymore. Finding $\mathrm{lgM}_{\mathrm{opt}}$ including correlation function data down to $10\,\mathrm{Mpc}/h$ causes the fit not to recover the linear scales for the biggest mass (left). Fitting for both $\langle F'\rangle$ and $\langle F''\rangle$ leads to a good χ^2 (*black dashed* line).

BAO peak height and shape are not affected by non-local biasing neither in the N-body simulation nor the theory and (*ii*) the nonlinear theory matches the shape of the BAO peak for all masses. We can also observe at scales $30\,\mathrm{Mpc}/h < r < 90\,\mathrm{Mpc}/h$ that the Eulerian non-locality induced by the nonlinearly evolved local Lagrangian bias spreads out the different correlation functions, with highest masses having the smallest slope and the biggest deviation with respect to linear theory (the black dashed line in Fig. 6.8).

It is also obvious from Fig. 6.8 that the nonlinear model has problems on small scales $r < 30\,\mathrm{Mpc}/h$ for the largest mass bins shown in red, corresponding to galaxy clusters. This problem persists regardless of the chosen filter scales σ_x and R (including CLPT as $\sigma_p = \sigma_x = 0$) and regardless of the chosen mass function; we tested also the Sheth-Tormen [ST99] mass function that gives similar results for b_1 and b_2 but is problematic because $\mathrm{lgM}_{\mathrm{opt}}$ can be far away from

$$\overline{\mathrm{lgM}} = \int_{\mathrm{lgM}_{\mathrm{min}}}^{\mathrm{lgM}_{\mathrm{max}}} n(\mathrm{lgM})\,\mathrm{lgM}\,d\,\mathrm{lgM}\,. \tag{6.87}$$

This shows that if the mass function is calibrated, as we have done for f_0 by fitting for D_B and β, then also the bias parameters become more consistent.

We also fitted for $\langle F'\rangle$ and $\langle F''\rangle$ independently to see whether they can be adjusted such that the problem for cluster-sized halos disappears. If only r-values larger than $40\,\mathrm{Mpc}/h$ are used, the independent fit for $\langle F'\rangle$ and $\langle F''\rangle$ gives values very close to $b_1(M_{\mathrm{opt}})$ and $b_2(M_{\mathrm{opt}})$ and thus the same problem occurs. For the largest halos $14.5 < \mathrm{lgM} < 15.2$ we find when taking into account a larger r-range, $r \in [10, 200]\,\mathrm{Mpc}/h$ for the fit, one obtains $\mathrm{lgM}_{\mathrm{opt}} = 14.66$ leading to $b_1(M_{\mathrm{opt}}) = 2.66$ destroying the agreement on large scales, see Fig. 6.9. We exclude scales smaller than $10\,\mathrm{Mpc}/h$ because we expect there halo exclusion: two objects identified in HR2 through a friend-of-friend algorithm cannot come arbitrary close to each other. The two-parameter fit ($\langle F'\rangle$, $\langle F''\rangle$) also shows some artefacts below $r = 10\,\mathrm{Mpc}/h$ for the largest mass bin but gives a good fit on larger scales for ($\langle F'\rangle_{\mathrm{opt}} = 3.01$, $\langle F''\rangle_{\mathrm{opt}} = 1.97$), compare the last row in Table 6.1. Therefore it is possible to fit cluster correlation functions with the local Lagrangian

bias model based on the Taylor expansion of a general function $F(\delta_R)$ around $\delta_R = 0$. It is however unclear whether this is physically meaningful due to the failure of the conditional mass function f_0 (6.73) that fills F with physics. In order to understand the reason of this failure we plan to look into the initial conditions of a N-body simulation in order to identify the proto-halos and measure the initial clustering and therefore properties of F directly.

6.6.2.2 Real space velocity statistics

An important ingredient of the Gaussian streaming model (6.49) is the statistics of the pairwise infall velocity of which the first two mass weighted moments are given by $v_{12,i}(\boldsymbol{r})$ and $\tilde{\sigma}^2_{12,ij}(\boldsymbol{r})$ and which can be split according to (6.60), into parts parallel and perpendicular to $\hat{\boldsymbol{r}}$. In the HR2 halo catalog, for fixed $r \in I_r$ and mass bin, we simply average over all velocity differences $(\boldsymbol{v}_i - \boldsymbol{v}_k)\cdot\hat{\boldsymbol{r}}_{ik}$ projected onto the pair separation vector $\boldsymbol{r}_{ik}$ and divide the result by the measured real space correlation function $\hat{\xi}$ to obtain a mass-weighted average of $\hat{v}_{12}(r)$

$$\hat{v}_{12}(r) = \sum_{k,i,k\neq i}^{N_{\rm tot}} \delta_{r_{ik},r}\delta_{r_{ki},r}\frac{(\boldsymbol{v}_i - \boldsymbol{v}_k)\cdot\boldsymbol{r}_{ik}}{r_{ik}DD(r)}\,. \tag{6.88}$$

We proceed similarly for $\tilde{\sigma}^2_\perp$ and $\tilde{\sigma}^2_\parallel$ according to (6.60).

The linearised expressions for all quantities can be found in [RW11] and are given by

$$\begin{aligned}
v_{12}^{\rm lin} &= -aH\frac{fb_1^{\rm E}}{\pi^2}\int_0^\infty dkP(k)j_1(kr)\\
\tilde{\sigma}_\parallel^{2\,\rm lin} &= 2(aH)^2f^2\left(R_{\rm NL}^2 - \frac{1}{2\pi^2}\int_0^\infty dkP(k)\left(j_0(kr) - \frac{2j_1(kr)}{kr}\right)\right)\\
\tilde{\sigma}_\perp^{2\,\rm lin} &= 2(aH)^2f^2\left(R_{\rm NL}^2 - \frac{1}{2\pi^2}\int_0^\infty dkP(k)\frac{j_1(kr)}{kr}\right)\,,
\end{aligned}$$

with $R^2_{\rm NL} = 1/(6\pi^2)\int_0^\infty dkP(k)$ evaluated in linear perturbation theory, see Eq. (6.84) . The linear expressions will be used as a reference when we compare theory to simulation in the following plots. Compared to the real space correlation, where the difference between cgCLPT and CLPT is nearly invisible, it will be significant for the velocity statistic. In particular we also show now the case where we smooth at the Lagrangian scale $R(M)$.

In Fig. 6.10 we show the HR2 data as dots. The CLPT results are overplotted in the left panels and the cgCLPT results are overplotted in the right panels. In both cases the thin lines correspond to a smoothing of $1\,\mathrm{Mpc}/h$ which optimizes the halo correlation function. The thick lines correspond to a smoothing on the Lagrangian size $R(M)$ of the halo, which clearly improves the agreement between HR2 and theory for the velocity statistics $\hat{v}_{12}(r)$, $\tilde{\sigma}^2_\perp$ and $\tilde{\sigma}^2_\parallel$.

Focusing only on v_{12} in the upper panels in Fig. 6.10, it becomes clear that cgCLPT slightly improves over CLPT for the case of $1\,\mathrm{Mpc}/h$ smoothing. We want to emphasize again that there is no further fit involved; we simply took the best fitting bias parameters obtained in the last section and use them to calculate the velocity statistics. Looking at the lower panels for σ^2_{12} it is obvious that the Lagrangian smoothing $R(M)$ moves the very large and strongly mass

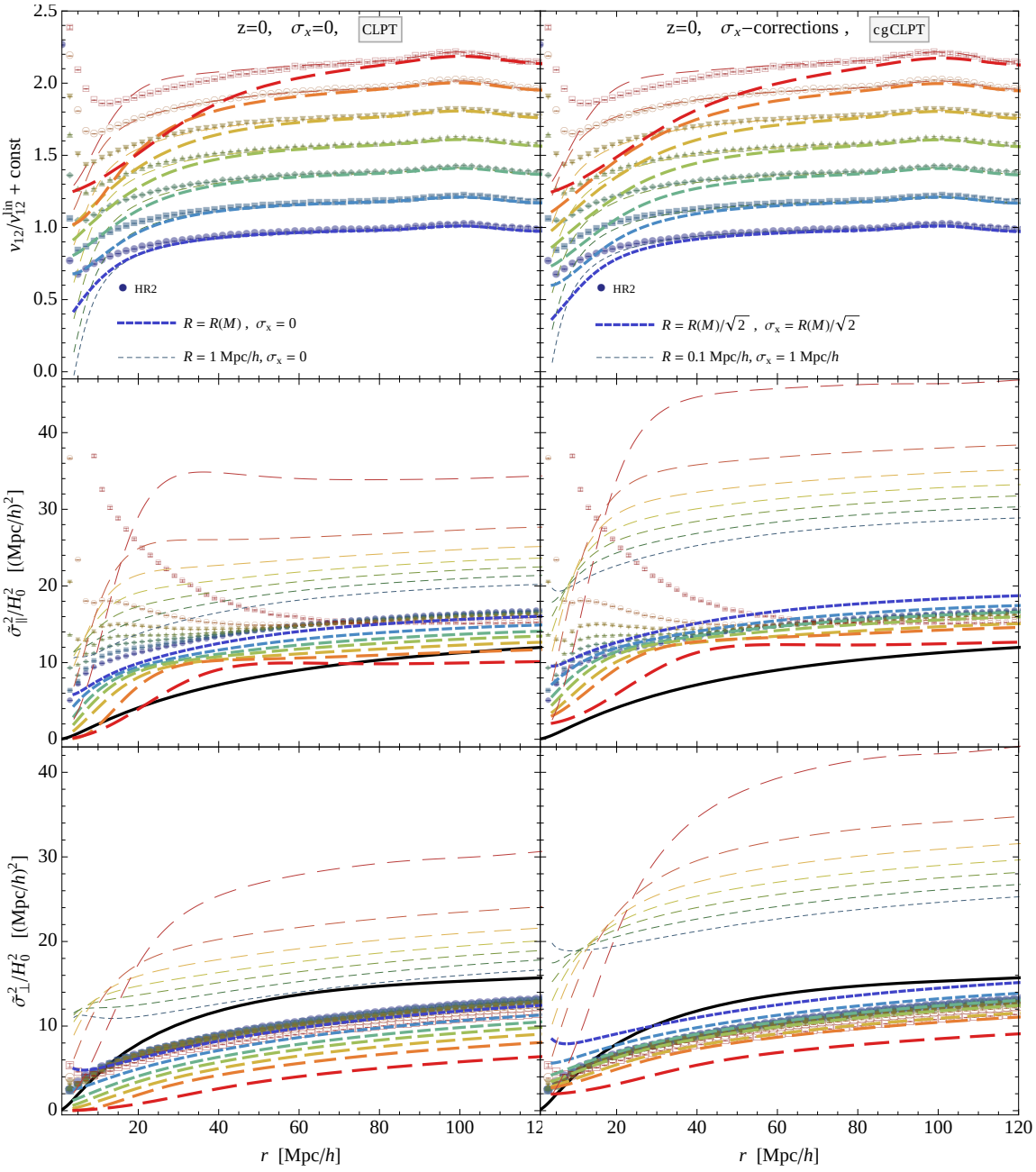

FIGURE 6.10: *top* Mean pairwise velocity v_{12} divided by the linear theory for the 7 mass bins (with largest mass on top). We shifted all values by a constant $(i-1)0.2$ according to the i-th mass bin for better visibility, with $i = 1$ for smallest mass. The data points are measurements from HR2 which we compare on left to CLPT and on the right cgCLPT. The thin lines correspond to smoothing $R = 1\,\mathrm{Mpc}/h, \sigma_x = 0$ in CLPT, or $R = 0.1\,\mathrm{Mpc}/h, \sigma_x = 1$ in cgCLPT. The thick lines use a smoothing $R = R(M), \sigma_x = 0$ for CLPT and $R = R(M)/\sqrt{2}, \sigma_x = R(M)/\sqrt{2}$ for cgCLPT. Smoothing at $R = 1\,\mathrm{Mpc}/h$ leads to a general improvement between theory and data, which becomes more significant for large masses (upper curves). It is also clearly visible that cgCLPT improves over CLPT on small scales.
middle and bottom 2nd pairwise velocity moment $\tilde{\sigma}^2_{ij}$ split into $\tilde{\sigma}^2_{\parallel}$ and $\tilde{\sigma}^2_{\perp}$. We observe a significant improvement if we smooth on the Lagrangian scale $R(M)$ rather than $1\,\mathrm{Mpc}/h$. The black lines show the linear theory which is independent of bias and since we did not include any smoothing, independent of mass.

depend predictions for $1\,\mathrm{Mpc}/h$ towards the data points which show comparatively small mass dependence.

It was noticed in [RW11] that within linear theory $\sigma_{12}^2(r,\mu) = \sigma_\parallel^2(r)\mu^2 + \sigma_\perp^2(r)(1-\mu^2)$ only contributes to redshift space correlations through its second derivative along the line of sight $\mathrm{d}^2/dr_\parallel^2\sigma_{12}^2(r, r_\parallel/r)$ and thus any isotropic constant added to σ_{12}^2 does not contribute. It is therefore interesting to compare the shape of $\sigma_\perp^2$ and $\sigma_\parallel^2$ by shifting them in such a way that the model agrees with the data on large scales and to check that the required shifts for $\sigma_\perp^2$ are identical to $\sigma_\parallel^2$. The result of the shift is shown in Fig. 6.11. For better visibility we added to the already shifted curves and the data points a constant for each mass bin. We find that within all models and mass bins considered the shift to make theory and data overlap at $r = 200\,\mathrm{Mpc}/h$ is basically identical for $\sigma_\perp^2$ to $\sigma_\parallel^2$.

Unfortunately, the shapes of the theory predictions for v_{12} and $\sigma_\parallel^2$ do not agree very well, see Fig. 6.11, at least compared to $\sigma_\perp^2$, see the bottom panels of Fig. 6.10. At the time of writing, we are still investigating this problem.

It is known that nonlocal Lagrangian bias derived from peaks theory is increasing the sharpness of the proto-halo correlation function despite the use of the physical Lagrangian scale [BDS14]. We therefore hope that once we use a peak bias and also the resulting velocity bias instead of the excursion set bias, it will turn out that the Lagrangian smoothing scale is the optimal choice for all statistical quantities. It is also possible that the inclusion of the σ_p-terms will improve the agreement.

6.6.2.3 Redshift space

From the HR2 halo catalog we generate the redshift space by simply changing the z-coordinate r_z of each halo to $s_z = r_z + v_z/(aH)$, where v_z is the z-component of the halo peculiar velocity $\boldsymbol{v}$. This, of course, does not correspond to the real observed light cone, but it directly corresponds to the distant observer approximation used in the theory Eq. (6.36). We choose again bins $I_s := [s - \Delta s/2, s + \Delta s/2]$ with width $\Delta s = 2\,\mathrm{Mpc}/h$, and s the pair separation in redshift space. In addition to s, we need to consider bins with respect to $\mu = \hat{\boldsymbol{s}} \cdot \hat{\boldsymbol{z}}$, the cosine of the angle between the line of sight and and the halo separation in redshift space. An analog of the simple estimator (6.65) in redshift space is

$$1 + \hat{\xi}(s,\mu) = \frac{\Delta P(s\,,\mu)}{n_{\mathrm{tot}} 2\pi s^2 \Delta s \Delta\mu}\,. \tag{6.89}$$

For convenience we display here only expressions for the full box while the Jackknife versions and covariance matrices can be obtained analogously to the real space $\hat{\xi}$ in Sec. 6.6.2.1. We are mostly interested in the Legendre moments of $\xi(s,\mu)$, because the size of the moments quickly decays as a function of n. In the linear theory the moments with $n > 4$ vanish identically. So instead of sampling in s and μ, we integrate directly over $\frac{1}{2}(1+2n)L_n(\mu)d\mu$ and obtain the

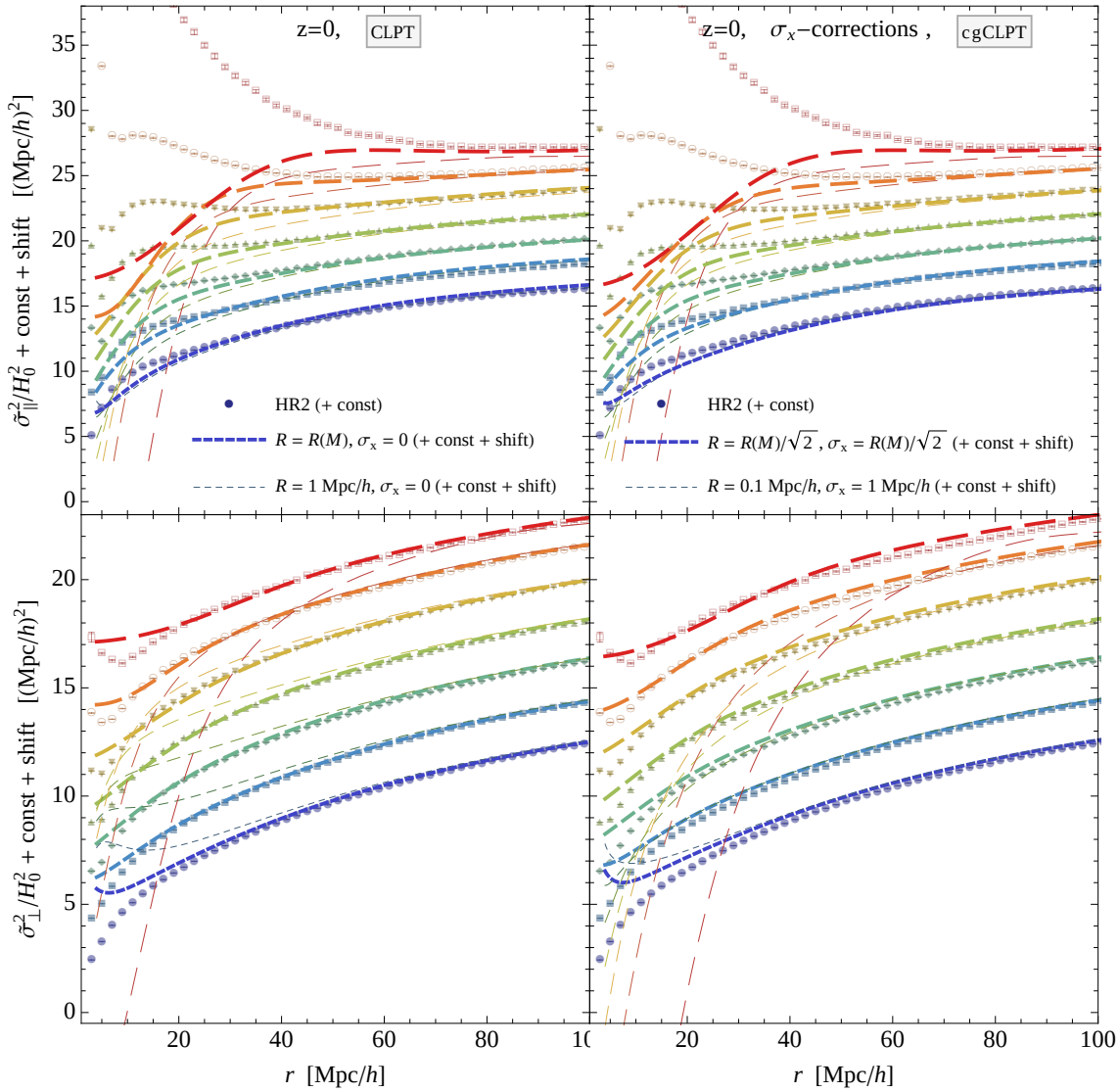

FIGURE 6.11: Another perspective on $\tilde{\sigma}_{ij}$ as shown in the middle and bottom panel of Fig. 6.10; here we shifted again all values by a constant $2(i-1)(\mathrm{Mpc}/h)^2$ according to the mass bin i, for better visibility. The smallest mass lgM = 13 is unshifted. But in addition to this constant shift the theory lines for 2nd velocity moments $\tilde{\sigma}_\parallel$ and $\tilde{\sigma}_\perp$ are shifted such that they agree with HR2 at 200 Mpc/h. Smoothing at $R(M)$ does not considerably improve the shape over $R = 1\,\mathrm{Mpc}/h$ apart from the largest masses. However the large scale "temperature" does improve, see Fig. 6.10

moments

$$1 + \hat{\xi}_0(s) = \sum_{k,i,k\neq i}^{N_{\rm tot}} \delta_{s_{ik},s}\delta_{s_{ki},s}\frac{1}{2}L_0(\mu_{ik})\frac{N_{\rm tot}^{-1}}{n_{\rm tot}2\pi s^2\Delta s} = \frac{\Delta P(s)}{n_{\rm tot}4\pi s^2\Delta s} \tag{6.90a}$$

$$\hat{\xi}_n(s) = \sum_{k,i,k\neq i}^{N_{\rm tot}} \delta_{s_{ik},s}\delta_{s_{ki},s}\frac{1+2n}{2}L_n(\mu_{ik})\frac{N_{\rm tot}^{-1}}{n_{\rm tot}2\pi s^2\Delta s}\,, \tag{6.90b}$$

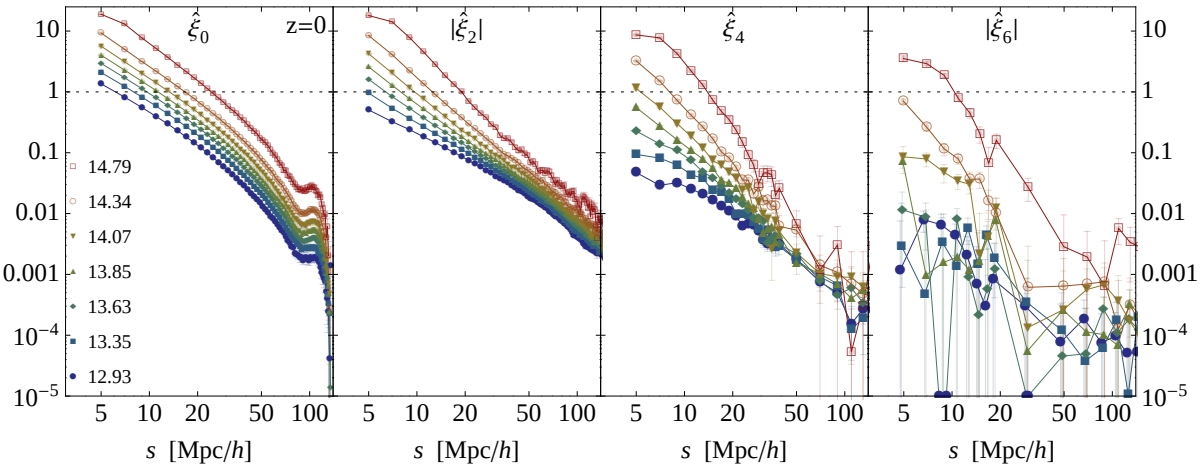

FIGURE 6.12: The first 4 multipoles of the redshift space correlation function $\xi(s,\mu)$ measured in the HR2 halo catalog. We indicate with the dotted line at $\xi = 1$ the nonlinear regime.

where $s_{ik} = |\boldsymbol{s}_i - \boldsymbol{s}_k|$ is the halo separation. Eq. (6.90b) holds only for $n > 0$ and vanishes for all odd n, because then L_n is odd in μ_{ik}, where μ_{ik} is the cosine of the angle between the halo separation vector $\boldsymbol{s}_i - \boldsymbol{s}_k$ and the line of sight $\hat{z}$, that will appear twice for each pair but with different sign. We calculated the first 4 moments using the Legendre polynomials

$$L_0 = 1\,, \quad L_2 = \frac{1}{2}(3\mu^2 - 1)\,, \quad L_4 = \frac{1}{8}(35\mu^4 - 30\mu^2 + 3)\,,$$
$$L_6 = \frac{1}{16}(231\mu^6 - 315\mu^4 + 105\mu^2 - 5)\,.$$

The hexacontatetrapole ξ_6, or for short the 64-pole, is a purely nonlinear effect since it vanishes in the linear, or Kaiser limit [Kai87] and therefore contains purely nonlinear information, similar to the three-point correlation in absence of primordial non-Gaussianity. In Fig. 6.12 we display the measured $\hat{\xi}_0, \hat{\xi}_2, \hat{\xi}_4, \hat{\xi}_6$. It is interesting to observe that for the smallest mass bin with lgM $\simeq$ 13 (the bottom curves), the clustering on small scales quickly decreases about two orders of magnitude with increasing n, while for largest halos with lgM $\simeq$ 14.7 (the top curves) the clustering decreases quite slowly, less than one order of magnitude, such that observed galaxy cluster correlation functions are strongly affected by redshift space distortions. Indeed, for the cluster-sized halos at the smallest scales the correlation strength is unchanged going from $n = 0$ to $n = 2$ and remains fully nonlinear even for the 64-pole. In the following figures we use the linear predictions, see e.g. [RW11], as a reference

$$\begin{aligned}
\xi_0^{\rm lin}(s) &= \frac{1}{2\pi}\left((b_1^E)^2 + \frac{2}{3}b_1^E f + \frac{1}{5}f^2\right)\int_0^\infty dk\, k^2 P_L(k) j_0(ks)\,,\\
\xi_2^{\rm lin}(s) &= -\frac{1}{2\pi}\left(\frac{4}{3}b_1^E f + \frac{4}{7}f^2\right)\int_0^\infty dk\, k^2 P_L(k) j_2(ks)\,,\\
\xi_4^{\rm lin}(s) &= \frac{1}{2\pi}\frac{8}{35}f^2\int_0^\infty dk\, k^2 P_L(k) j_4(ks)\,,
\end{aligned} \tag{6.91}$$

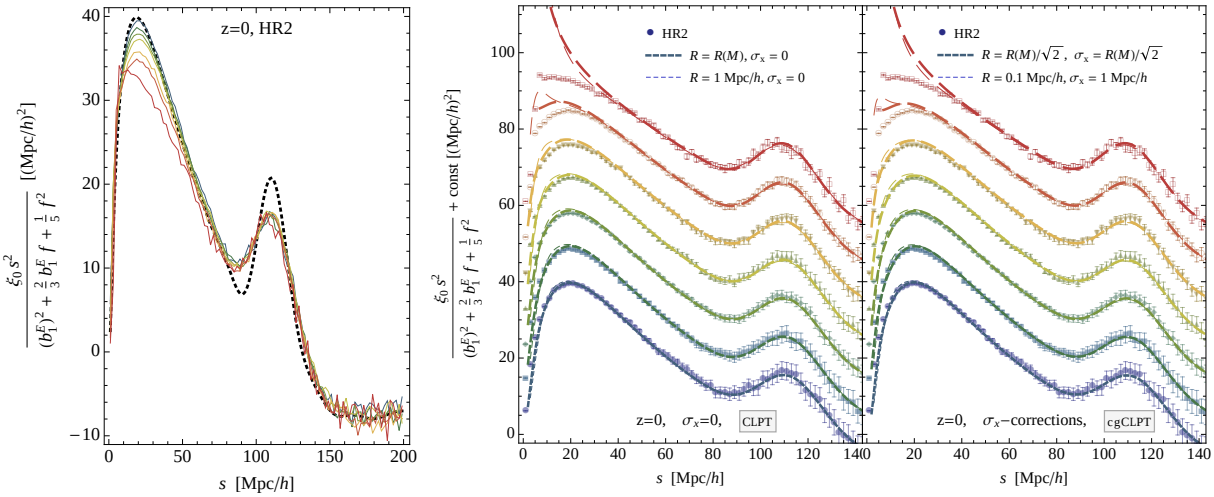

FIGURE 6.13: The monopole times r^2 for all masses. *left* We show the HR2 correlations as thin lines rescaled by the linear redshift bias (6.91), that is constructed from the best fitting real space bias. Note that BAO peaks all overlap similar to real space, see Fig. 6.6. The dashed line is the linear correlation function. *right* We again rescaled the HR2 points and the theory by the linear bias and shifted all lines according the $(i-1)10(\,\mathrm{Mpc}/h)^2$ for better visibility.

where the j_n are spherical Bessel functions.

Regarding the theory, we will use a hybrid approach; to construct the GSM correlation $\xi_n(s)$, Eq. (6.49) we will use the real space correlation $\xi(r)$ that was calculated by smoothing at $1\,\mathrm{Mpc}/h$, while for σ^2_{12} and v_{12} we use results from the last section that were either smoothed at $1\,\mathrm{Mpc}/h$ or $R(M)$. Note that when we use in the GSM the Lagrangian scale $R(M)$ for $\tilde{\sigma}^2_\perp$ and $\tilde{\sigma}^2_\parallel$ we will also use it for v_{12}. This ensures that σ^2_{12} is positive. In the Figs. 6.13, 6.14, 6.15, 6.16 the CLPT lines denoted by $R = R(M), \sigma_x = 0$, actually use $1\,\mathrm{Mpc}/h$ for the $1+\xi(r)$, but $R(M)$ for σ^2_{12} and v_{12} and analogously for the cgCLPT lines. In Fig. 6.13 we show the monopole ξ_0 times r^2 for all masses. We rescaled the HR2 points and the theory by a combination of linear bias and linear growth rate that multiplies the linear matter correlation to give the linear halo monopole (6.91). Similarly to the real space correlation Fig. 6.8, the rescaling reveals that apart from this Eulerian local bias factor, all BAO peaks lie on top of each with no mass dependence. And again, the mass dependence shows up for $r < 90\,\mathrm{Mpc}/h$ similar to Fig. 6.8. Let us emphasize that the theory lines are predictions based on the fitting of $\mathrm{lgM}_{\mathrm{opt}}$ in real space, no further fit was performed. They are in excellent agreement with the data, apart from the two largest mass bins, which were already problematic in real space. Note that the hybrid-GSM model (the thick lines) does fit the data better than the GSM model where we smoothed all quantities around $1\,\mathrm{Mpc}/h$. There is no significant difference between CLPT and cgCLPT.

For the quadrupole ξ_2, Fig. 6.14, there is a large difference between CLPT and cgCLPT, with CLPT performing better! This is hard to understand since we already established that the ingredients of the GSM are modelled equally well for $\xi(r)$ and that cgCLPT performs even better for v_{12}, σ^2_{12}. This paradox is currently under investigation; the plan is to test GSM in a model-independent way by inserting into GSM $\hat{\xi}(r)$, $\hat{v}_{12}$ and $\hat{\sigma}^2_{12}$ measured in the simulation, and see whether the resulting $\xi_n(s)$ agrees with $\hat{\xi}_n(s)$ measured directly. We will also calculate non-

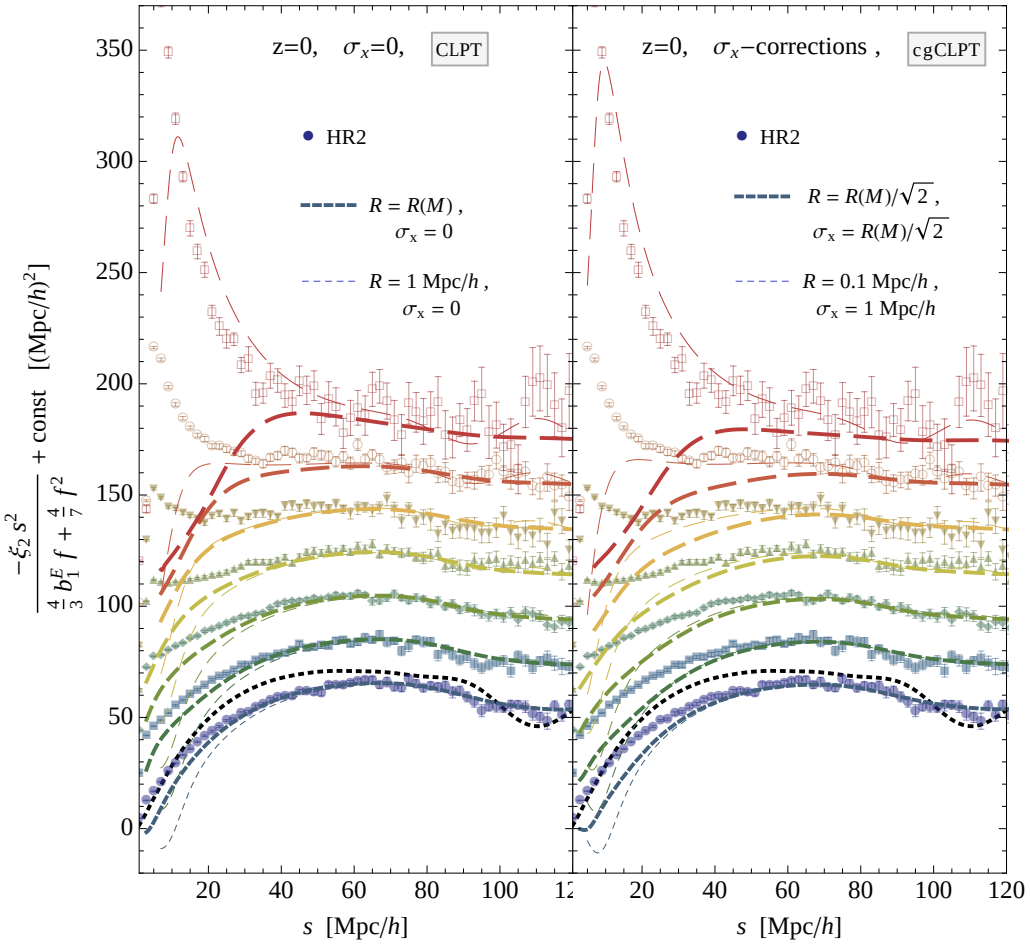

FIGURE 6.14: The quadrupole times r^2 for all masses. We rescaled the HR2 points and the theory by the linear bias. After this all lines overlap at large scales, therefore we shifted all lines and points according to $(i-1)20(\,\mathrm{Mpc}/h)^2$ for better visibility, where i labels the mass bin.

Gaussian corrections to the pairwise velocity distribution function and test different bias models. In particular the peak bias which successfully test in [BDS14].

Fig. 6.14 for the quadrupole and Fig. 6.15 for hexadecapole tell us that the hybrid-GSM is significantly better than smoothing only at $R = 1\,\mathrm{Mpc}/h$ (and, of course, it is better than $R = 0$ which is the wide-spread standard). This is clearly visible if the thick and thin lines are compared to the data points, especially for the lower mass range. The fact that for the largest mass bins the thin lines perform better is very likely an accident considering the nonsensical behavior of $\xi(r)$ for the largest mass bin for $r < 40\,\mathrm{Mpc}/h$ in Figs. 6.8 and 6.13.

The hybrid GSM model therefore significantly improves our abilities to model observations and the precision to extract cosmological parameters from them.

The 64-pole basically vanishes both in HR2 data as well as in CLPT+GSM as can be seen in Fig. 6.16 for the lower mass range. For the upper mass range the measured ξ_6 is clearly non-zero

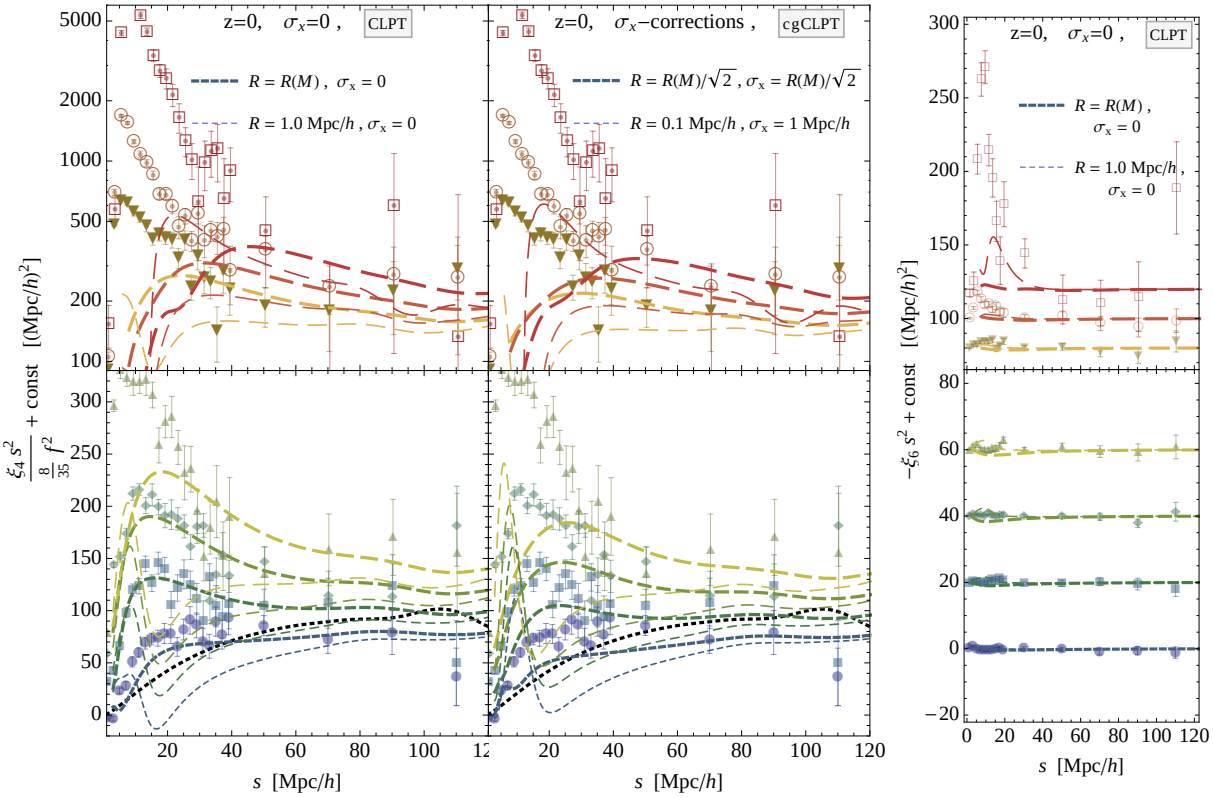

FIGURE 6.15: The hexadekapole times r^2 for all masses. We rescaled the HR2 points where i labels the mass bin. The hybrid method performs significantly better than smoothing only at $R = 1\,\mathrm{Mpc}/h$

FIGURE 6.16: The 64-pole and the theory by the linear bias. After this all lines overlap at large scales, therefore times r^2 for all masses, with we shifted all lines and points according to $(i-1)20(\,\mathrm{Mpc}/h)^2$ for better visibility, same shift as in Fig. 6.15.

on small scales, where it it also strongly scale dependent. The result for cgCLPT does not change qualitatively.

6.6.3 Status of the truncated (Post-)Zel'dovich approximation

It was recently claimed [Whi14] that a smoothing of the initial power spectrum P_L does not improve or change the resulting redshift space quadrupole ξ_2 within CLPT+GSM. However CLPT is basically the (Post-)Zel'dovich approximation and in the so called "truncated" Zel'dovich approximation (TZA) the linear power spectrum is smoothed with a Gaussian filter on an optimal scale depending on redshift and cosmology (we find $1\,\mathrm{Mpc}/h$) in order to significantly improve the ZA [MPS94]. The reason for the improvement is that within Lagrangian perturbation theory the displacements never stop and therefore, after the ocurrance of shell crossings, structures which should be held in place by gravity disperse instead indefinitely, see Fig. 5.8. We saw this improvement already in Fig. 6.7, where the power on small scales increased for a smoothing scale of $R = 1\,\mathrm{Mpc}/h$ compared to $R = 0$ or $R = 2$. Therefore contrary to what was claimed in

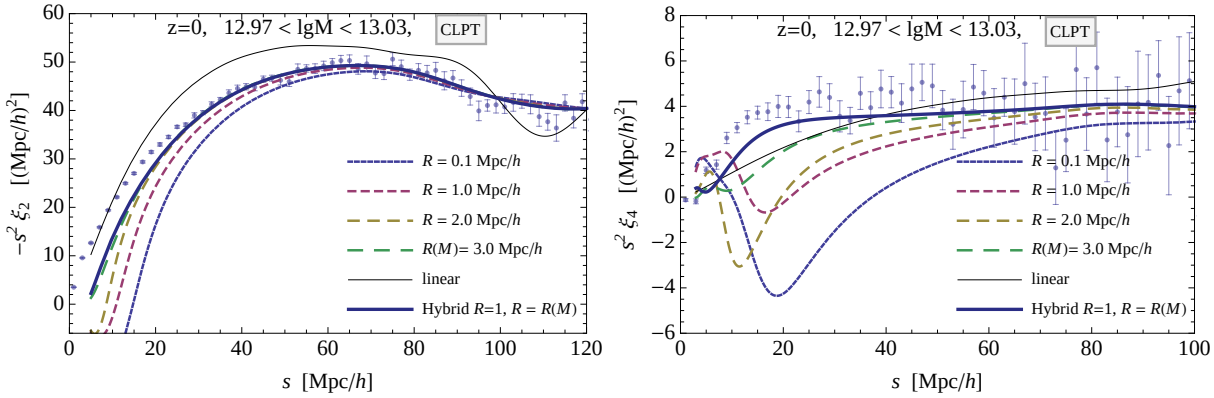

FIGURE 6.17: Comparison between different smoothing procedures within CLPT+GSM

[Whi14], the TZA does improve analytical computations. Although we are not the first to observe the better performance of TZA in analytical calculations for the real space [MHP93, Por97], we want to advocate the TZA and show that a much more significant improvement happens for the quadrupole and hexadecapole if the linear input power spectrum P_L is smoothed $P_L W(kR)^2$ and fed into the CLPT+GSM model, see Fig. 6.17. The dashed lines show the case where R is the same for calculating $\xi(r)$, v_{12}, $\sigma_\perp^2$ and $\sigma_\parallel^2$ with CLPT. The black thin line shows the linear theory. While the thick blue line shows the hybrid approach in which we smooth within CLPT at $1\,\mathrm{Mpc}/h$ to obtain $\xi(r)$, but at $R(M)$ to obtain v_{12}, $\sigma_\perp^2$ and $\sigma_\parallel^2$ and combine them to ξ_2 and ξ_4 using GSM. In particular note the improvement between the cases $R = 0.1\,\mathrm{Mpc}/h$ and $R = 1\,\mathrm{Mpc}/h$ which corresponds to ZA and TZA. In addition note that $R = 1\,\mathrm{Mpc}/h$ and therefore TZA, is outperformed by the hybrid-smoothing, which might be considered as the most practical result of this chapter.

6.7 Conclusion and Outlook

We considered a coarse grained dust fluid to model collisionless selfgravitating matter, which to a good approximation captures the basic properties of cold dark matter, baryons and even whole halos on large scales. We derived Eulerian perturbation kernels up to third order. From first principles we derived the vorticity power spectrum, which is in qualitative good agreement with complentary work where it was derived using effective field theory techniques [CFGS13] or measured in simulations [HAA14]. We translated the new Eulerian kernels to Lagrangian space in order to leave SPT behind and consider the Zel'dovich approximation (ZA) in its CLPT incarnation [CRW13] which performs much better in the nonlinear regime. We rederived the Gaussian streaming model for redshift space distortions from CLPT and generalized it to the case of arbitrary phase space distributions and applied it to the coarse grained dust model.

We extended CLPT to include our new kernels, which we denoted by cgCLPT. We find that the prediction of the mean pairwise velocity is significantly improved for all masses compared to CLPT, in particular compared to the standard procedure in which the linear power spectrum is not smoothed.

The introduction of the smoothing scale σ_x forced us to rethink the meaning of smoothing in perturbation theory and we found that for the halo correlation function in redshift space a hybrid approach delivers the best results, where the calculation is performed partially with $\sigma_x \simeq 1\,\mathrm{Mpc}/h$ to obtain the real space halo correlation, and partially with $\sigma_x = R(M)$, where $R(M)$ is the Lagrangian radius of halos with mass M, to obtain the pairwise velocity statistics of halos. This procedure also significantly improves the model if the standard Lagrangian kernels are used and the smoothing is only performed on the linear input power spectrum.

The improvement achieved by the smoothing of the linear power spectrum is well known in the context of the ZA as truncated ZA (TZA). We showed that our hybrid approach involving two different smoothing scales outperforms TZA.

Clearly, more work is necessary to fully understand all the ingredients of the model. Apart from this, we want to apply (cg)CLPT to higher order correlation functions in order test their accuracy against N-body simulations. This is because large angular surveys will contain enough statistics to measure these higher order correlation functions. In addition when two probes of LSS like cluster counts $n(M)$ and the cluster correlation function $\xi(r)$ are combined to infer cosmological parameters, as done for instance in [MGW+13], it is desirable to have analytic predictions not only for the observables but also for covariance matrices like $C_\xi(r, r')$ (6.70) and cross covariances between $n(M)$ and $\xi(r)$, including correlations for different mass bins. These covariance matrices are required to correctly estimate error bars on the inferred cosmological parameters. Analytic estimates of those covariance matrices require the knowledge of the connected three $\zeta(r_1, r_2, r_3)$ and four-point $\eta(r_1, r_2, ..., r_6)$ halo correlation functions, where the r_i are the edge lengths of the observed triangle or tetrahedron, respectively [SM14]. It would be interesting to check whether (cg)CLPT evaluation of these quantities is feasible and whether a Gaussian streaming model can be developed to convert the real space results into the redshift space quantities. The results for halo correlation function could then be implemented into the halo model [MF00, CS02] to additionally obtain correlation functions for the dark matter field which is required for predicting statistics involving weak gravitational lensing [TB07].

Appendix 6

6.A Power spectra

6.A.1 Vorticity and velocity divergence

$$
\begin{aligned}
P_{\bar{w}\bar{w},22}(k) &= [(2\pi)^3\delta_{\rm D}(0)]^{-1}\langle \bar{\boldsymbol{w}}_2(\boldsymbol{k})\cdot\bar{\boldsymbol{w}}_2(-\boldsymbol{k})\rangle \qquad (6.92a)\\
&= \int \frac{d^3p_1d^3p_2d^3\tilde{p}_1d^3\tilde{p}_2}{(2\pi)^9}\,\frac{\delta_{\rm D}(\boldsymbol{p}_1+\boldsymbol{p}_2-\boldsymbol{k})\delta_{\rm D}(\tilde{\boldsymbol{p}}_1+\tilde{\boldsymbol{p}}_2+\boldsymbol{k})}{\delta_{\rm D}(0)}\times\\
&\qquad\qquad \times \bar{\boldsymbol{W}}_2(\boldsymbol{p}_1,\boldsymbol{p}_2)\cdot\bar{\boldsymbol{W}}_2(\tilde{\boldsymbol{p}}_1,\tilde{\boldsymbol{p}}_2)\langle\delta_1(\boldsymbol{p}_1)\delta_1(\boldsymbol{p}_2)\delta_1(\tilde{\boldsymbol{p}}_1)\delta_1(\boldsymbol{p}_2)\rangle\\
&= 2\int\frac{d^3p}{(2\pi)^3}\left|\bar{\boldsymbol{W}}_2^{(s)}(\boldsymbol{p},\boldsymbol{k}-\boldsymbol{p})\right|^2 P_L(p)P_L(|\boldsymbol{k}-\boldsymbol{p}|)\\
&= \frac{k^3}{2\pi^2}\int_0^\infty dr\int_{-1}^1 dx\,\frac{\left(1-x^2\right)(1-2rx)^2e^{-{\sigma_x}^2k^2\left(2r^2+1\right)}\left(e^{{\sigma_x}^2k^2r^2}-e^{{\sigma_x}^2k^2rx}\right)^2}{4\left(r^2-2rx+1\right)^2}\times\\
&\qquad\qquad \times P_L(kr)P_L\left(k\sqrt{1-2rx+r^2}\right)\\
&= \frac{k^3}{2\pi^2}\int_0^\infty dr\int_{-1}^1 dx\,\frac{\left(1-x^2\right)(1-2rx)^2\left(e^{{\sigma_x}^2k^2(r^2-rx)}-1\right)^2}{4\left(r^2-2rx+1\right)^2}\times\\
&\qquad\qquad \times \bar{P}_L(kr)\bar{P}_L\left(k\sqrt{1-2rx+r^2}\right)
\end{aligned}
$$

$$
P_{ww,22}(k) = 0 \qquad (6.92b)
$$

$$
\begin{aligned}
P_{\bar{\theta}\bar{\theta},22}(k) &= [(2\pi)^3\delta_{\rm D}(0)]^{-1}\langle\bar{\theta}_2(\boldsymbol{k})\bar{\theta}_2(-\boldsymbol{k})\rangle \qquad (6.92c)\\
&= \int\frac{d^3p_1d^3p_2d^3\tilde{p}_1d^3\tilde{p}_2}{(2\pi)^9}\,\frac{\delta_{\rm D}(\boldsymbol{p}_1+\boldsymbol{p}_2-\boldsymbol{k})\delta_{\rm D}(\tilde{\boldsymbol{p}}_1+\tilde{\boldsymbol{p}}_2+\boldsymbol{k})}{\delta_{\rm D}(0)}\times\\
&\qquad\qquad \times \bar{G}_2^{(s)}(\boldsymbol{p}_1,\boldsymbol{p}_2)\bar{G}_2^{(s)}(\tilde{\boldsymbol{p}}_1,\tilde{\boldsymbol{p}}_2)\langle\delta_1(\boldsymbol{p}_1)\delta_1(\boldsymbol{p}_2)\delta_1(\tilde{\boldsymbol{p}}_1)\delta_1(\tilde{\boldsymbol{p}}_2)\rangle\\
&= 2\int\frac{d^3p}{(2\pi)^3}\left[\bar{G}_2^{(s)}(\boldsymbol{p},\boldsymbol{k}-\boldsymbol{p})\right]^2 P_L(p)P_L(|\boldsymbol{k}-\boldsymbol{p}|) \qquad (6.92d)\\
&= \frac{k^3}{2\pi^2}\int_0^\infty dr\int_{-1}^1 dx\,\frac{\left[2\left(10rx^2-3r-7x\right)e^{{\sigma_x}^2k^2(r^2-rx)}+7\left(-2rx^2+r+x\right)\right]^2}{196\left(r^2-2rx+1\right)^2}\\
&\qquad\qquad \times \bar{P}_L(kr)\bar{P}_L\left(k\sqrt{1-2rx+r^2}\right)
\end{aligned}
$$

$$
P_{\theta\theta,22}(k) = \frac{k^3}{196}\cdot\frac{1}{2\pi^2}\int_0^\infty dr\int_{-1}^1 dx\,\frac{\left(6rx^2+r-7x\right)^2}{\left(r^2-2rx+1\right)^2}P_L(kr)P_L\left(k\sqrt{1-2rx+r^2}\right) \qquad (6.92e)
$$

$$
\begin{aligned}
P_{\bar{\theta}\bar{\theta},13}(k) &= 2\cdot[(2\pi)^3\delta_{\rm D}(0)]^{-1}\langle\bar{\theta}_1(\boldsymbol{k})\bar{\theta}_3(-\boldsymbol{k})\rangle \qquad (6.92f)\\
&= 2\int\frac{d^3p_1d^3p_2d^3p_3d^3\tilde{p}_1}{(2\pi)^9}\,\frac{\delta_{\rm D}(\boldsymbol{p}_1+\boldsymbol{p}_2+\boldsymbol{p}_3-\boldsymbol{k})\delta_{\rm D}(\tilde{\boldsymbol{p}}_1+\boldsymbol{k})}{\delta_{\rm D}(0)}\times\\
&\qquad\times\bar{G}_3^{(s)}(\boldsymbol{p}_1,\boldsymbol{p}_2,\boldsymbol{p}_3)\bar{G}_1(\tilde{\boldsymbol{p}}_1)\langle\delta_1(\boldsymbol{p}_1)\delta_1(\boldsymbol{p}_2)\delta_1(\boldsymbol{p}_3)\delta_1(\tilde{\boldsymbol{p}}_1)\rangle\\
&= 6P_L(k)\int\frac{d^3p}{(2\pi)^3}\,\bar{G}_3^{(s)}(\boldsymbol{p},-\boldsymbol{p},\boldsymbol{k})\bar{G}_1(-\boldsymbol{k})P_L(p)\\
&= \frac{k^3}{2\pi^2}\bar{P}_L(k)\int_0^\infty dr\;\bar{P}_L(kr)\frac{e^{-{\sigma_x}^2k^2r}}{168r^3}\times\Big\{3\left(r^2-1\right)^3\times\\
&\quad\times\Big[3r^2e^{\frac{1}{2}{\sigma_x}^2k^2(r+1)^2}\left(\mathrm{Ei}\left[-\tfrac{1}{2}{\sigma_x}^2k^2(r-1)^2\right]-\mathrm{Ei}\left[-\tfrac{1}{2}{\sigma_x}^2k^2(r+1)^2\right]\right) \qquad (6.92g)\\
&\qquad-\left(7r^2+2\right)\log\left|\frac{r-1}{r+1}\right|e^{{\sigma_x}^2k^2r(r+1)}\Big]\\
&\quad+336r^5e^{{\sigma_x}^2k^2r}-2r\left(21r^6-50r^4+79r^2-6\right)e^{{\sigma_x}^2k^2r(r+1)}\\
&\quad+\frac{6r^2(r^2-1)}{(\sigma_xk)^2}\left[e^{2{\sigma_x}^2k^2r}(3r^2+6r-25)-(3r^2-6r-25)\right]\\
&\quad+\frac{12r}{(\sigma_xk)^4}\left[(3r^3-12r^2-19r-28)-e^{2{\sigma_x}^2k^2r}(3r^3+12r^2-19r+28)\right]\\
&\quad+\frac{48}{(\sigma_xk)^6}\left[e^{2{\sigma_x}^2k^2r}(3r^2-12r+7)-(3r^2+12r+7)\right]\\
&\qquad+\frac{576}{(\sigma_xk)^8}\left(e^{2{\sigma_x}^2k^2r}-1\right)\Big\}
\end{aligned}
$$

$$
\begin{aligned}
P_{\theta\theta,13}(k) = \frac{k^3}{168}\cdot\frac{1}{2\pi^2}P_L(k)\int_0^\infty dr\;P_L(kr)\Big\{&\frac{12}{r^2}-82+4r^2-6r^4-\qquad (6.92h)\\
&-\frac{3}{r^3}\left(r^2-1\right)^3\left(r^2+2\right)\log\left|\frac{r-1}{r+1}\right|\Big\}
\end{aligned}
$$

$\mathrm{Ei}(x)$ denotes the exponential integral defined as $\mathrm{Ei}(x) = -\int_{-x}^{\infty}t^{-1}e^{-t}\,dt$. In the limit $\sigma_x \to 0$ we recover the standard SPT kernel 6.92e and 6.92h as given in Eq. 5 in [SS91].

6.A.2 Cross spectrum between density and velocity divergence

$$
\begin{aligned}
P_{\bar{\delta}\bar{\theta},22}(k) &= [(2\pi)^3\delta_{\rm D}(0)]^{-1}\langle\bar{\delta}_2(\boldsymbol{k})\bar{\theta}_2(-\boldsymbol{k})\rangle \qquad (6.93a)\\
&= -\int\frac{d^3p_1d^3p_2d^3\tilde{p}_1d^3\tilde{p}_2}{(2\pi)^9}\,\frac{\delta_{\rm D}(\boldsymbol{p}_1+\boldsymbol{p}_2-\boldsymbol{k})\delta_{\rm D}(\tilde{\boldsymbol{p}}_1+\tilde{\boldsymbol{p}}_2+\boldsymbol{k})}{\delta_{\rm D}(0)}\times\\
&\qquad\times\bar{F}_2^{(s)}(\boldsymbol{p}_1,\boldsymbol{p}_2)\bar{G}_2^{(s)}(\tilde{\boldsymbol{p}}_1,\tilde{\boldsymbol{p}}_2)\langle\delta_1(\boldsymbol{p}_1)\delta_1(\boldsymbol{p}_2)\delta_1(\tilde{\boldsymbol{p}}_1)\delta_1(\tilde{\boldsymbol{p}}_2)\rangle\\
&= -\frac{k^3}{2\pi^2}\int_0^\infty dr\,\int_{-1}^1 dx\,\frac{\left(10rx^2-3r-7x\right)e^{{\sigma_x}^2k^2\left(r^2-rx\right)}}{196\left(r^2-2rx+1\right)^2}\\
&\qquad\times\left[2\left(10rx^2-3r-7x\right)e^{{\sigma_x}^2k^2\left(r^2-rx\right)}+7\left(-2rx^2+r+x\right)\right]\times\\
&\qquad\times\bar{P}_L(kr)\bar{P}_L\left(k\sqrt{1-2rx+r^2}\right)
\end{aligned}
$$

$$
P_{\delta\theta,22}(k) = -\frac{k^3}{2\pi^2}\int_0^\infty dr\,\int_{-1}^1 dx\,\frac{\left(10rx^2-3r-7x\right)\left(6rx^2+r-7x\right)}{196\left(r^2-2rx+1\right)^2}\times \qquad (6.93b)
$$
$$
\times P_L(kr)P_L\left(k\sqrt{1-2rx+r^2}\right)
$$

$$
\begin{aligned}
P_{\bar{\delta}\bar{\theta},13}(k) &= [(2\pi)^3\delta_{\rm D}(0)]^{-1}\left(\langle\bar{\delta}_1(\boldsymbol{k})\bar{\theta}_3(-\boldsymbol{k})\rangle+\langle\bar{\delta}_3(\boldsymbol{k})\bar{\theta}_1(-\boldsymbol{k})\rangle\right) \qquad (6.93c)\\
&= -\int\frac{d^3p_1d^3p_2d^3p_3d^3\tilde{p}_1}{(2\pi)^9}\,\frac{\delta_{\rm D}(\boldsymbol{p}_1+\boldsymbol{p}_2+\boldsymbol{p}_3-\boldsymbol{k})\delta_{\rm D}(\tilde{\boldsymbol{p}}_1+\boldsymbol{k})}{\delta_{\rm D}(0)}\times\\
&\qquad\times\left[\bar{G}_3^{(s)}(\boldsymbol{p}_1,\boldsymbol{p}_2,\boldsymbol{p}_3)\bar{F}_1(\tilde{\boldsymbol{p}}_1)+\bar{F}_3^{(s)}(\boldsymbol{p}_1,\boldsymbol{p}_2,\boldsymbol{p}_3)\bar{G}_1(\tilde{\boldsymbol{p}}_1)\right]\times\\
&\qquad\times\langle\delta_1(\boldsymbol{p}_1)\delta_1(\boldsymbol{p}_2)\delta_1(\boldsymbol{p}_3)\delta_1(\tilde{\boldsymbol{p}}_1)\rangle\\
&= -3P_L(k)\int\frac{d^3p}{(2\pi)^3}\left[\bar{F}_1(\boldsymbol{k})\bar{G}_3^{(s)}(\boldsymbol{p},-\boldsymbol{p},-\boldsymbol{k})+\bar{F}_3^{(s)}(\boldsymbol{p},-\boldsymbol{p},\boldsymbol{k})\bar{G}_1(-\boldsymbol{k})\right]P_L(p)
\end{aligned}
$$

$$
\begin{aligned}
P_{\bar{\delta}\bar{\theta},13}(k) = -\frac{k^3}{4\pi^2}\bar{P}_L(k)\int_0^\infty dr\ \bar{P}_L(kr)\frac{e^{-{\sigma_x}^2k^2r}}{504r^3}\times\Bigg\{3\left(r^2-1\right)^3\Bigg[9r^2e^{\frac{1}{2}{\sigma_x}^2k^2(r+1)^2}\times \\
\times\left(\mathrm{Ei}\left[-\tfrac{1}{2}{\sigma_x}^2k^2(r-1)^2\right]-\mathrm{Ei}\left[-\tfrac{1}{2}{\sigma_x}^2k^2(r+1)^2\right]\right)- \\
-2\left(7r^2+2\right)2\log\left|\frac{r-1}{r+1}\right|e^{{\sigma_x}^2k^2r(r+1)}\Bigg] \\
+108r^5e^{k^2r{\sigma_x}^2}-8r\left(21r^6-50r^4+79r^2-6\right)e^{{\sigma_x}^2k^2r(r+1)} \\
+\frac{18r^2(r^2-1)}{(\sigma_xk)^2}\left[e^{2{\sigma_x}^2k^2r}(3r^2+6r-25)-(3r^2-6r-25)\right] \\
+\frac{36r}{(\sigma_xk)^4}\left[(3r^3-12r^2-19r-28)-e^{2{\sigma_x}^2k^2r}(3r^3+12r^2-19r+28)\right] \\
+\frac{144}{(\sigma_xk)^6}\left[e^{2{\sigma_x}^2k^2r}(3r^2-12r+7)-(3r^2+12r+7)\right] \\
+\frac{1728}{(\sigma_xk)^8}\left(e^{2{\sigma_x}^2k^2r}-1\right)\Bigg\}
\end{aligned}
$$

$$
\begin{aligned}
P_{\delta\theta,13}(k) = -\frac{k^3}{504}\cdot\frac{1}{2\pi^2}P_L(k)\int_0^\infty dr\ P_L(kr)\Bigg\{\frac{24}{r^2}-202+56r^2- \\
-30r^4-\frac{3}{r^3}\left(r^2-1\right)^3\left(5r^2+4\right)\log\left|\frac{r-1}{r+1}\right|\Bigg\}
\end{aligned}
\tag{6.93d}
$$

In the limit $\sigma_x \to 0$ the kernels reduce to the standard SPT results 6.93b and 6.93d given in Eqs. (A25)-(A26) in [CWP09], note however that our convention for θ_n is different compared to [CWP09] such that the cross spectra have flipped signs.

6.B Lagrangian correlators

In addition to the definitions made in 6.3.2 it is useful to define the following mixed polyspectra of the linear density field and the displacement field in the same way as done in [Mat08]

$$
\begin{aligned}
&\left\langle\delta_L(\boldsymbol{k}_1)\cdots\delta_L(\boldsymbol{k}_l)\Psi_{i_1}^{(n_1)}(\boldsymbol{p}_1)\cdots\Psi_{i_m}^{(n_m)}(\boldsymbol{p}_m)\right\rangle_c = \\
&\quad(2\pi)^3\delta_{\mathrm{D}}(\boldsymbol{k}_1+\ldots+\boldsymbol{k}_l+\boldsymbol{p}_1+\ldots+\boldsymbol{p}_m)(-i)^m C_{i_1\cdots i_m}^{(n_1\cdots n_m)}(\boldsymbol{k}_1,\ldots,\boldsymbol{k}_l;\boldsymbol{p}_1,\ldots,\boldsymbol{p}_m)\,,
\end{aligned}
\tag{6.94}
$$

where an angle bracket with index c denote cumulants (connected correlators). For computations up to one-loop level we only have to consider terms up to $\mathcal{O}(P_L^2)$ which implies $l+n_1+n_2+n_3 \leq 4$ since due the properties of the cumulants only terms with $l+m \leq 3$ are relevant. Furthermore only even $l+n_1+n_2+n_3 \in 2\mathbb{N}$ contribute because the initial density field is assumed to be a

random Gaussian field. For $l + m = 2$ we adopt the simplified notation

$$C(\boldsymbol{k}) := C(\boldsymbol{k}, -\boldsymbol{k}) \quad , \quad C_i(\boldsymbol{k}) := C_i(\boldsymbol{k}; -\boldsymbol{k}) \quad , \quad C_{ij}(\boldsymbol{k}) := C_{ij}(\boldsymbol{k}, -\boldsymbol{k}) \,. \tag{6.95}$$

The C as defined in (6.94) should not be confused with cumulants of the phase space distribution function. We will also encounter mixed polyspectra with some $\boldsymbol{\Psi}$ replaced by $\bar{\boldsymbol{\Psi}}$ or by time derivatives. For the correlators involving time derivatives of $\boldsymbol{\Psi}$ we simply use that $\dot{\boldsymbol{\Psi}}^{(n)} = nf\mathcal{H}\boldsymbol{\Psi}^{(n)}$ and similarly for $\bar{\boldsymbol{\Psi}}$. The specific index structure enforced by translation symmetry allows to describe Lagrangian correlators in real space entirely in terms of scalar functions of $q = |\boldsymbol{q}| = |\boldsymbol{q}_2 - \boldsymbol{q}_1|$, since any tensor can be decomposed in terms of δ_{ij} and $\hat{q}_i$. For example, any rank-1 tensor can be written as $T_i(\boldsymbol{q}) = T(q)\hat{q}_i$ and similarly any rank-2 tensor can be decomposed according to $T_{ij}(\boldsymbol{q}) = T_{\delta q}(q)\delta_{ij} + T_{qq}(q)\hat{q}_i\hat{q}_j$. The q-dependence of the functions can be expressed using spherical Bessel functions, namely

$$\int_{-1}^{1} d\mu \, \cos(x\mu) = 2j_0(x) \,, \qquad \int_{-1}^{1} d\mu \, \mu^2 \cos(x\mu) = 2\left(j_0(x) - 2\frac{j_1(x)}{x}\right) . \tag{6.96}$$

We maintain the notation used in [Mat08] and [CRW13], in which the R and Q-functions, defined as

$$Q_n(k) = \frac{k^3}{4\pi^2}\int_0^\infty dr P_L(kr) \int_{-1}^{1} dx \; P_L(k\sqrt{1-2rx+r^2}) \; \tilde{Q}_n(k,r,x) \,, \tag{6.97}$$

$$R_n(k) = \frac{k^3}{4\pi^2} P_L(k) \int_0^\infty dr P_L(kr) \; \tilde{R}_n(k,r) \,, \tag{6.98}$$

have been computed for the standard fluid case. We state the corresponding results obtained via our cgCLPT approach.

Note that for the CLPT computation, see Eqs. (B20-30) and (B41-46) in [CRW13] only $Q_{1,2,5,8}$ are relevant such that they are the only ones which will be listed here. In addition to the usual $\tilde{\tilde{R}}_{n=1,2}$ we had to define another kernel $\tilde{\tilde{R}}_0$ which takes account of the fact, that in our case the quantities $C_i^{(3)}$ and $C_{ij}^{(13)}$ cannot be expressed in terms of $\tilde{\tilde{R}}_1$. This is due to the different smoothing structure of $C_i^{(3)}$ and $C_{ij}^{(13)}$, which both contain two quantities, compared to $C_i^{(2)}$ and $C_{ij}^{(12)}$, which both contain three parts. As explained in [Mat08] any transverse part of $C_{i_1\cdots i_m}^{(n_1\cdots n_m)}$ is irrelevant such that we only obtain longitudinal parts for $C_{i_1\cdots i_m}^{(n_1\cdots n_m)}$ for which, however, the transverse kernels $\boldsymbol{T}^{(n)}$ have to be taken into account.

$$\bar{C}_i^{(3)}(\boldsymbol{k}) = \frac{5}{21}\frac{k_i}{k^2}\bar{R}_0(k) \,, \qquad \bar{C}_{ij}^{(13)}(\boldsymbol{k}) = \bar{C}_{ij}^{(31)}(\boldsymbol{k}) = -\frac{5}{21}\frac{k_i k_j}{k^4}\bar{R}_0(k) \,. \tag{6.99}$$

This manifests itself in the following kernels which are instead of Eqs. (B26,43,46) in [CRW13]

then given by

$$\bar{U}^{(3)}(q) = \frac{1}{2\pi^2}\int_0^\infty dk\, k \left(-\frac{5}{21}\right) \bar{R}_0(k)\, j_1(kq) \tag{6.100}$$

$$\bar{X}^{(13)}(q) = \frac{1}{2\pi^2}\int_0^\infty dk\, \frac{5}{21}\bar{R}_0(k) \left[\frac{2}{3} - 2\frac{j_1(kq)}{kq}\right] \tag{6.101}$$

$$\bar{Y}^{(13)}(q) = \frac{1}{2\pi^2}\int_0^\infty dk\, \frac{5}{21}\bar{R}_0(k) \left[-2j_0(kq) + 6\frac{j_1(kq)}{kq}\right]. \tag{6.102}$$

Furthermore all quantities which contain the linear power spectrum, more precisely Eqs. (B20,25,41,44) in [CRW13], have to be computed with the smoothed linear power spectrum, such that $P_L(k) \to \bar{P}_L(k) = \exp\left(-{\sigma_x}^2 k^2\right) P_L(k)$.

$$\begin{aligned}
\tilde{\bar{R}}_0(k,r) = \frac{e^{-{\sigma_x}^2k^2(r^2+1)}}{480r^3}\Bigg\{ & 3\left(r^2-1\right)^3\Bigg[51\left(r^2+1\right)e^{\frac{1}{2}{\sigma_x}^2k^2(r^2+1)}\times \\
& \times\left(\mathrm{Ei}\left[-\tfrac{1}{2}{\sigma_x}^2k^2(r-1)^2\right] - \mathrm{Ei}\left[-\tfrac{1}{2}{\sigma_x}^2k^2(r+1)^2\right]\right) \\
& - 4\log\left|\frac{r-1}{r+1}\right|\left(\left(7r^2+2\right)e^{{\sigma_x}^2k^2r^2} + 21\left(r^2+1\right)\right)\Bigg] \\
& - 168r\left(3r^6 - 5r^4 + 9r^2 - 3\right) - 8r\left(21r^6 - 50r^4 + 79r^2 - 6\right)e^{{\sigma_x}^2k^2r^2} \\
& - 18e^{-{\sigma_x}^2k^2r}\left(\frac{1}{(\sigma_x k)^2}(r+1)(-17+51r+44r^2+68r^3-51r^4+17r^5)\right. \\
& \quad + \frac{2}{(\sigma_x k)^4}(17+44r+88r^2+68r^3-17r^4) \\
& \quad \left. + \frac{8}{(\sigma_x k)^6}(17r^2+24r+11) + \frac{192}{(\sigma_x k)^8}\right) \\
& + 18e^{{\sigma_x}^2k^2r}\left(\frac{1}{(\sigma_x k)^2}(r-1)(17+51r-44r^2+68r^3+51r^4+17r^5)\right. \\
& \quad - \frac{2}{(\sigma_x k)^4}(-17+44r-88r^2+68r^3+17r^4) \\
& \quad \left. + \frac{8}{(\sigma_x k)^6}(17r^2-24r+11) + \frac{192}{(\sigma_x k)^8}\right)\Bigg\}
\end{aligned} \tag{6.103a}$$

$$\tilde{\tilde{R}}_1(k,r) = \frac{e^{-{\sigma_x}^2k^2\left(r^2+1\right)}}{288r^3}\Bigg\{3\left(r^2-1\right)^4\left[28\log\left|\frac{r-1}{r+1}\right| - 17e^{\frac{1}{2}{\sigma_x}^2k^2(r^2+1)}\times\right. \tag{6.103b}$$
$$\times\left(\mathrm{Ei}\left[-\tfrac{1}{2}{\sigma_x}^2k^2(r-1)^2\right] - \mathrm{Ei}\left[-\tfrac{1}{2}{\sigma_x}^2k^2(r+1)^2\right]\right)\Big]$$
$$- 56r\left(-3r^6+11r^4+11r^2-3\right)$$
$$- 12\left[\frac{2r}{(\sigma_x k)^2}\left(17r^4+22r^2+17\right)+\frac{32r}{(\sigma_x k)^4}\left(r^2+1\right)\right]\cosh\left({\sigma_x}^2k^2r\right)$$
$$- 12\Big[\frac{1}{(\sigma_x k)^2}\left(r^2+1\right)\left(17r^4-90r^2+17\right) -$$
$$\left.- \frac{2}{(\sigma_x k)^4}\left(17r^4+22r^2+17\right) - \frac{32}{(\sigma_x k)^6}\left(r^2+1\right)\Big]\sinh\left({\sigma_x}^2k^2r\right)\right\}$$

$$\tilde{R}_1(k,r) = \lim_{\sigma_x\to 0}\tilde{\tilde{R}}_1(k,r) = \lim_{\sigma_x\to 0}\tilde{\tilde{R}}_0(k,r) = \tag{6.103c}$$
$$\frac{-6r^7+22r^5+22r^3-6r-3\left(r^2-1\right)^4\log\left|\frac{r-1}{r+1}\right|}{48r^3}$$

$$\tilde{\tilde{R}}_2(k,r) = \frac{\left(r^2-1\right)e^{-{\sigma_x}^2k^2\left(r^2+1\right)}}{288r^3}\Bigg\{3\left(r^2-1\right)^2\left(r^2+1\right)\left(28\log\left|\frac{r-1}{r+1}\right| - \right. \tag{6.103d}$$
$$\left.- 17e^{\frac{1}{2}P^2(r^2+1)R^2}\left(\mathrm{Ei}\left[-\tfrac{1}{2}{\sigma_x}^2k^2(r-1)^2\right] - \mathrm{Ei}\left[-\tfrac{1}{2}{\sigma_x}^2k^2(r+1)^2\right]\right)\right)$$
$$+ 56r\left(3r^4-2r^2+3\right)$$
$$- 12\left[\frac{34r}{(\sigma_x k)^2}\left(r^2+1\right)+\frac{32r}{(\sigma_x k)^4}\right]\cosh\left({\sigma_x}^2k^2r\right)$$
$$- 12\left[\frac{1}{(\sigma_x k)^2}\left(17r^4-22r^2+17\right) - \frac{34}{(\sigma_x k)^4}\left(r^2+1\right) - \frac{32}{(\sigma_x k)^6}\right]\sinh\left({\sigma_x}^2k^2r\right)\Bigg\}$$

$$\tilde{R}_2(k,r) = \lim_{\sigma_x\to 0}\tilde{\tilde{R}}_2(k,r) = \frac{\left(1-r^2\right)\left[6r^5-4r^3+6r+3\left(r^2-1\right)^2\left(r^2+1\right)\log\left|\frac{r-1}{r+1}\right|\right]}{48r^3} \tag{6.103e}$$

Note that, in the limit $\sigma_x \to 0$ we correctly recover the result of [Mat08].

$$\tilde{\tilde{Q}}_1(k,r,x) = \frac{e^{-{\sigma_x}^2k^2(2r^2-2rx+1)}}{36\left(r^2-2rx+1\right)^2}\Big\{49\left[1+3x^2+4\left(-rx+r^2x^2-rx^3\right)\right] \tag{6.104a}$$
$$-14\left[7(1+3x^2)+4\left(-4rx+4r^2x^2-10rx^3+3r^2x^4\right)\right]e^{{\sigma_x}^2k^2\left(r^2-rx\right)}$$
$$+\left[49(1+3x^2)+36r^2+4\left(-7rx-11r^2x^2-91rx^3+51r^2x^4\right)\right]e^{2{\sigma_x}^2k^2\left(r^2-rx\right)}\Big\}$$

$$\tilde{Q}_1(k,r,x) = \lim_{\sigma_x\to 0}\tilde{\tilde{Q}}_1(k,r,x) = \frac{r^2\left(x^2-1\right)^2}{\left(r^2-2rx+1\right)^2} \tag{6.104b}$$

$$\tilde{\tilde{Q}}_2(k,r,x) = \frac{r(rx-1)e^{-{\sigma_x}^2k^2\left(2r^2-2rx+1\right)}}{6\left(r^2-2rx+1\right)^2}\Big[\left(7r-21rx^2+34x^3-20x\right)e^{{\sigma_x}^2k^2(r^2-rx)}-$$
$$-\left(7r-21rx^2+28x^3-14x\right)e^{{\sigma_x}^2k^2(r^2-1)}\Big] \tag{6.104c}$$

$$\tilde{Q}_2(k,r,x) = \lim_{\sigma_x\to 0}\tilde{\tilde{Q}}_2(k,r,x) = \frac{rx\left(x^2-1\right)(rx-1)}{\left(r^2-2rx+1\right)^2} \tag{6.104d}$$

$$\tilde{\tilde{Q}}_5(k,r,x) = \frac{re^{{\sigma_x}^2k^2(-4r^2+2rx-3)}}{6\left(r^2-2rx+1\right)^2}\Big[\left(13r+14x+34r^2x^3-20r^2x-41rx^2\right)e^{{\sigma_x}^2k^2r^2}-$$
$$-\left(7r+14x+28r^2x^3-14r^2x-35rx^2\right)e^{{\sigma_x}^2k^2rx}\Big] \tag{6.104e}$$

$$\tilde{Q}_5(k,r,x) = \lim_{\sigma_x\to 0}\tilde{\tilde{Q}}_5(k,r,x) = \frac{r^2\left(x^2-1\right)(rx-1)}{\left(r^2-2rx+1\right)^2} \tag{6.104f}$$

$$\tilde{\tilde{Q}}_8(k,r,x) = \frac{re^{-{\sigma_x}^2k^2\left(2r^2-2rx+1\right)}}{3\left(r^2-2rx+1\right)}\Big[\left(7rx^2-7x\right)-\left(10rx^2-3r-7x\right)e^{{\sigma_x}^2k^2\left(r^2-rx\right)}\Big] \tag{6.104g}$$

$$\tilde{Q}_8(k,r,x) = \lim_{\sigma_x\to 0}\tilde{\tilde{Q}}_8(k,r,x) = \frac{r^2\left(1-x^2\right)}{r^2-2rx+1} \tag{6.104h}$$

6.C Calculation of Gaussian streaming functions

6.C.1 Calculation of $1+\xi_X$

First we expand the exponent which arises from the cumulant expansion theorem applied to $\langle e^{i\tilde{X}}\rangle$ up to second order in the linear power spectrum P_L

$$\sum_{N=1}^{\infty}\frac{i^N}{N!}\left\langle\tilde{X}^N_{J=0}\right\rangle_c = 1-\frac{1}{2}(\lambda_1^2+\lambda_2^2)\bar{\sigma}_R^2-\lambda_1\lambda_2\bar{\xi}_L-(\lambda_1+\lambda_2)\bar{U}_i k_i-\frac{1}{2}\bar{A}_{ij}k_ik_j \qquad (6.105)$$
$$-\frac{i}{2}(\lambda_1^2+\lambda_2^2)\bar{U}_i^{20(2)}k_i-i\lambda_1\lambda_2\bar{U}_i^{11(2)}k_i-\frac{i}{2}(\lambda_1+\lambda_2)\bar{A}_{ij}^{10}k_ik_j-$$
$$-\frac{i}{6}\bar{W}_{ijk}k_ik_jk_k+\mathcal{O}(P_L^3)\,,$$

where the Lagrangian correlators are defined as

$$\begin{aligned}
\sigma_R^2 &:= \langle\delta_1^2\rangle_c = \langle\delta_2^2\rangle_c\,, & \bar{\sigma}_R^2 &:= \langle\bar{\delta}_1^2\rangle_c = \langle\bar{\delta}_2^2\rangle_c\,,\\
\xi_L &:= \langle\delta_1\delta_2\rangle_c\,, & \bar{\xi}_L &:= \langle\bar{\delta}_1\bar{\delta}_2\rangle_c\,,\\
U_i^{mn(k)} &:= \langle\delta_1^m\delta_2^n\Delta_i^{(k)}\rangle_c\,, & \bar{U}_i^{mn(k)} &:= \langle\bar{\delta}_1^m\bar{\delta}_2^n\bar{\Delta}_i^{(k)}\rangle_c\,,\\
A_{ij}^{mn} &:= \langle\delta_1^m\delta_2^n\Delta_i\Delta_j\rangle_c\,, & \bar{A}_{ij}^{mn} &:= \langle\bar{\delta}_1^m\bar{\delta}_2^n\bar{\Delta}_i\bar{\Delta}_j\rangle_c\,,\\
W_{ijk}^{mn} &:= \langle\delta_1^m\delta_2^n\Delta_i\Delta_j\Delta_k\rangle_c & \bar{W}_{ijk}^{mn} &:= \langle\bar{\delta}_1^m\bar{\delta}_2^n\bar{\Delta}_i\bar{\Delta}_j\bar{\Delta}_k\rangle_c
\end{aligned} \qquad (6.106)$$

and we adopt the shorthand notation $U_i = U_i^{10(1)}$, $A_{ij} = A_{ij}^{00}$ and $W_{ijk} = W_{ijk}^{00}$ introduced in [CRW13] also for the barred quantities. In the following calculation we will keep this notation, such that whenever A, U or W occur they refer to the usual kernels given in [CRW13, WRW14]. In contrast, we will use $\bar{A}$, $\bar{U}$ or $\bar{W}$ for correlators arising from smoothed quantities. Plugging this expression into the exponential and keeping only the two terms which are linear in the power spectrum and have non-zero limits as $|\boldsymbol{q}|\to\infty$ exponentiated gives, see [CRW13, WRW14]

$$\bar{K}_0 = \langle e^{i\tilde{X}}\rangle = \exp\left[\sum_{N=1}^{\infty}\frac{i^N}{N!}\langle\tilde{X}^N_{J=0}\rangle_c\right] \qquad (6.107)$$

$$= e^{-\frac{1}{2}\bar{A}_{ij}k_ik_j}e^{-\frac{1}{2}(\lambda_1^2+\lambda_2^2)\bar{\sigma}_R^2}\times\Bigg\{1-\lambda_1\lambda_2\bar{\xi}_L-(\lambda_1+\lambda_2)\bar{U}_ik_i+\frac{1}{2}\lambda_1^2\lambda_2^2\bar{\xi}_L^2+ \qquad (6.108)$$
$$+\frac{1}{2}(\lambda_1+\lambda_2)^2\bar{U}_ik_i\bar{U}_jk_j+\lambda_1\lambda_2(\lambda_1+\lambda_2)\bar{\xi}_L\bar{U}_ik_i$$
$$-\frac{i}{2}(\lambda_1^2+\lambda_2^2)\bar{U}_i^{20(2)}k_i-i\lambda_1\lambda_2\bar{U}_i^{11(2)}k_i-\frac{i}{2}(\lambda_1+\lambda_2)\bar{A}_{ij}^{10}k_ik_j-$$
$$-\frac{i}{6}\bar{W}_{ijk}k_ik_jk_k+\mathcal{O}(P_L^3)\Bigg\}\,.$$

6.C.2 Calculation of v_{12}

$$\begin{aligned}\bar{K}_{1,i} &= \exp\left[\sum_{N=1}^{\infty}\frac{i^N}{N!}\langle\tilde{X}^N_{J=0}\rangle_c\right]\left[\sum_{N=0}^{\infty}\frac{i^N}{N!}\left\langle\dot{\bar{\Delta}}_i\tilde{X}^N\right\rangle_c\right] \qquad (6.109a)\\ &= e^{-\frac{1}{2}\bar{A}_{ij}k_ik_j}e^{-\frac{1}{2}(\lambda_1^2+\lambda_2^2)\bar{\sigma}_R^2}\times\Big\{i(\lambda_1+\lambda_2)\dot{\bar{U}}_i+ik_j\dot{\bar{A}}_{ji}-\frac{1}{2}(\lambda_1^2+\lambda_2^2)\dot{\bar{U}}_i^{20}-\lambda_1\lambda_2\dot{\bar{U}}_i^{11}-\\ &\quad-\frac{1}{2}k_jk_k\dot{\bar{W}}_{jki}-(\lambda_1+\lambda_2)k_j\dot{\bar{A}}^{10}_{ji}\\ &\quad-i\lambda_1\lambda_2(\lambda_1+\lambda_2)\bar{\xi}_L\dot{\bar{U}}_i-i(\lambda_1+\lambda_2)^2k_j\bar{U}_j\dot{\bar{U}}_i-\\ &\quad-i\lambda_1\lambda_2\bar{\xi}_Lk_j\dot{\bar{A}}_{ji}-i(\lambda_1+\lambda_2)k_jk_k\bar{U}_j\dot{\bar{A}}_{ki}+\mathcal{O}(P_L^3)\Big\}\,,\end{aligned}$$

where in addition to (6.106) we defined

$$\dot{\bar{U}}_i^{mn(k)} := \langle\bar{\delta}_1^m\bar{\delta}_2^n\dot{\bar{\Delta}}_i^{(k)}\rangle_c\,,\quad \dot{\bar{A}}_{ij}^{mn} := \langle\bar{\delta}_1^m\bar{\delta}_2^n\bar{\Delta}_i\dot{\bar{\Delta}}_j\rangle_c\,,\quad \dot{\bar{W}}_{ijk}^{mn} := \langle\bar{\delta}_1^m\bar{\delta}_2^n\bar{\Delta}_i\bar{\Delta}_j\dot{\bar{\Delta}}_k\rangle_c\,. \qquad (6.109b)$$

6.C.3 Calculation of σ_{12}^2

In the following we evaluate $K_{2,ij}$ defined in Eq. (6.5.3) in order to obtain an expression for $\tilde{\sigma}_{12}$ as given in Eq. (6.48c). This is done up to one-loop order such that Eq. (6.5.3) reduces to

$$K_{2,ij} := \bar{K}_{2,ij} + K^{\sigma_p}_{2,ij} + K^{\sigma_x}_{2,ij} + \mathcal{O}(P_L^3) \qquad (6.110)$$

where the different parts are

$$\begin{aligned}\bar{K}_{2,ij} &:= \exp\left[\sum_{N=1}^{\infty}\frac{i^N}{N!}\langle\tilde{X}^N_{J=0}\rangle_c\right]\Bigg[\sum_{N=0}^{\infty}\frac{i^N}{N!}\left\langle\dot{\bar{\Delta}}_i\dot{\bar{\Delta}}_j\tilde{X}^N_{J=0}\right\rangle_c+ \qquad (6.111a)\\ &\qquad+\sum_{N=0}^{\infty}\frac{i^N}{N!}\left\langle\dot{\bar{\Delta}}_i\tilde{X}^N_{J=0}\right\rangle_c\sum_{M=0}^{\infty}\frac{i^M}{M!}\left\langle\dot{\bar{\Delta}}_j\tilde{X}^M_{J=0}\right\rangle_c\Bigg]\,,\\ K^{\sigma_p}_{2,ij} &:= 2\sigma_p^2\,\exp\left[\sum_{N=1}^{\infty}\frac{i^N}{N!}\langle\tilde{X}^N_{J=0}\rangle_c\right]\sum_{N=0}^{\infty}\frac{i^N}{N!}\left\langle\tilde{X}^N_{J=0}\right\rangle_c\Bigg|_{\mathcal{O}(P_L^2)}\times\delta_{ij}\,, \qquad (6.111b)\\ K^{\sigma_x}_{2,ij} &:= K^{\sigma_x,1}_{2,ij} - K^{\sigma_x,2}_{2,ij} \qquad (6.111c)\\ K^{\sigma_x,1}_{2,ij} &:= \exp\left[\sum_{N=1}^{\infty}\frac{i^N}{N!}\langle\tilde{X}^N_{J=0}\rangle_c\right]\sum_{N=0}^{\infty}\frac{i^N}{N!}\Bigg\langle\Bigg[\frac{\overline{(1+\delta)v_iv_j}}{1+\bar{\delta}}(\boldsymbol{x}_1(\boldsymbol{q}_1))+ \qquad (6.111d)\\ &\qquad+\frac{\overline{(1+\delta)v_iv_j}}{1+\bar{\delta}}(\boldsymbol{x}_2(\boldsymbol{q}_2))\Bigg]\tilde{X}^N_{J=0}\Bigg\rangle_c\Bigg|_{\mathcal{O}(P_L^2)}\,,\\ K^{\sigma_x,2}_{2,ij} &:= \exp\left[\sum_{N=1}^{\infty}\frac{i^N}{N!}\langle\tilde{X}^N_{J=0}\rangle_c\right]\sum_{N=0}^{\infty}\frac{i^N}{N!}\Big\langle\left[\bar{v}_i\bar{v}_j(\boldsymbol{x}_1(\boldsymbol{q}_1))+\bar{v}_i\bar{v}_j(\boldsymbol{x}_2(\boldsymbol{q}_2))\right]\tilde{X}^N_{J=0}\Big\rangle_c\Big|_{\mathcal{O}(P_L^2)}\,, \qquad (6.111e)\end{aligned}$$

and $\widetilde{X}$ is given by Eq. (6.59). Note that we used the notation $v_i = \phi_{,i}/a$ for the microscopic velocity which yield the ordinary kernels for CLPT as given in [CRW13], [WRW14]. In contrast, we use $\bar{v}_i = \exp\left(\frac{1}{2}\sigma_x^2 \Delta\right)[(1+\delta)v_i]/(1+\bar{\delta})$ for the mass-weighted velocity which correspond to our modified CLPT kernels (called cgCLPT) computed for $\bar{\boldsymbol{v}}(\boldsymbol{x}(\boldsymbol{q})) = a\dot{\bar{\boldsymbol{\Psi}}}(\boldsymbol{q})$. Since some of the extra terms encoded in Eqs. (6.111) are given in Eulerian space we first have to perform a mapping to Lagrangian coordinates. This can be done according to Eq. (6.13) by using the corresponding relations (6.14) in the subsequent calculation.

6.C.3.1 σ_p^2-part (6.111b) of (6.110)

The correction term which is due to the coarse-graining with respect to momentum is easily obtained by combining (6.105) and (6.107)

$$K_{2,ij}^{\sigma_p} = 2\sigma_p^2\delta_{ij}\,\exp\left[\sum_{N=1}^{\infty}\frac{i^N}{N!}\langle\widetilde{X}_{J=0}^N\rangle_c\right]\sum_{N=0}^{\infty}\frac{i^N}{N!}\left\langle\widetilde{X}_{J=0}^N\right\rangle_c\Bigg|_{\mathcal{O}(P_L^2)} \tag{6.112a}$$

$$\begin{aligned}
&= 2\sigma_p^2\delta_{ij}\,e^{-\frac{1}{2}\bar{A}_{ij}k_ik_j}e^{-\frac{1}{2}(\lambda_1^2+\lambda_2^2)\bar{\sigma}_R^2}\times\Big\{1-2\lambda_1\lambda_2\bar{\xi}_L-2(\lambda_1+\lambda_2)\bar{U}_ik_i-\frac{1}{2}(\lambda_1^2+\lambda_2^2)\bar{\sigma}_R^2-\\
&\quad-\frac{1}{2}\bar{A}_{ij}k_ik_j+\frac{3}{2}\lambda_1^2\lambda_2^2\bar{\xi}_L^2+\frac{1}{2}\lambda_1\lambda_2(\lambda_1^2+\lambda_2^2)\bar{\xi}_L\bar{\sigma}_R^2+3\lambda_1\lambda_2(\lambda_1+\lambda_2)\bar{\xi}_L\bar{U}_ik_i+\\
&\quad+\frac{1}{2}\lambda_1\lambda_2\bar{\xi}_L\bar{A}_{ij}k_ik_j+\frac{3}{2}(\lambda_1+\lambda_2)^2\bar{U}_ik_i\bar{U}_jk_j+\\
&\quad+\frac{1}{2}(\lambda_1+\lambda_2)(\lambda_1^2+\lambda_2^2)\bar{\sigma}_R^2\bar{U}_ik_i+\frac{1}{2}(\lambda_1+\lambda_2)\bar{A}_{ij}k_ik_j\bar{U}_kk_k\\
&\quad-i(\lambda_1^2+\lambda_2^2)\bar{U}_i^{20(2)}k_i-2i\lambda_1\lambda_2\bar{U}_i^{11(2)}k_i-i(\lambda_1+\lambda_2)\bar{A}_{ij}^{10}k_ik_j-\frac{i}{3}\bar{W}_{ijk}k_ik_jk_k\Big\}\,.
\end{aligned}$$

6.C.3.2 σ_x^2 Part (6.111c) of (6.110)

The corrections to the pairwise velocity dispersion $\sigma_{12,ij}$ which are connected with the spatial coarse-graining σ_x have to be calculated by explicitly evaluating the corresponding correlators. We perform a similar calculation to the one presented as pedagogical example B4 in [CRW13] and rely on results given in [Mat08]. For convenience, the derivation was carried out by computing mixed correlators between coarse-grained density and displacements, $\bar{\delta}_L$ and $\bar{\boldsymbol{\Psi}}$, and microscopic quantities, δ_L and $\boldsymbol{\Psi}$. Since the computation is a little bit cumbersome due to the coarse-graining, we present it for the interested reader in some detail here.

First σ_x^2 part (6.111d) in (6.110) We define that $A_{(i}B_{j)} = A_iB_j + A_jB_i$. Because of the delta functions with respect to momentum in the kernels any overall smoothing factor drops out such

that $\left\langle \exp\left(\frac{1}{2}\sigma_x^2\Delta_x\right)\{v_i v_j\}\right\rangle_c = \left\langle v_i v_j\right\rangle_c$ as well as $\left\langle \exp\left(\frac{1}{2}\sigma_x^2\Delta_x\right)\{\delta v_i v_j\}\right\rangle_c = \left\langle \delta v_i v_j\right\rangle_c$.

$$\sum_{N=0}^{\infty}\frac{i^N}{N!}\left\langle\frac{\overline{(1+\delta)v_i v_j}}{1+\bar{\delta}}(\boldsymbol{x}_1(\boldsymbol{q}_1))\widetilde{X}^N_{J=0}\right\rangle_c\Bigg|_{\mathcal{O}(P_L^2)} \tag{6.113a}$$

$$= \sum_{N=0}^{\infty}\frac{i^N}{N!}\left\langle \exp\left(\tfrac{1}{2}\sigma_x^2\Delta_x\right)\{(1+\delta)v_i v_j\}\left[1-\bar{\delta}+\frac{1}{2}\bar{\delta}^2\right](\boldsymbol{x}_1(\boldsymbol{q}_1))\widetilde{X}^N_{J=0}\right\rangle_c\Bigg|_{\mathcal{O}(P_L^2)}$$

$$\begin{aligned}
&= \left\langle \exp\left(\tfrac{1}{2}\sigma_x^2\Delta_x\right)\{v_i v_j\}(\boldsymbol{x}_1)\right\rangle_c + i\left\langle \exp\left(\tfrac{1}{2}\sigma_x^2\Delta_x\right)\{v_i v_j\}(\boldsymbol{x}_1)\left[\lambda_1\bar{\delta}_{L1}+\lambda_2\bar{\delta}_{L2}+\boldsymbol{k}\cdot\bar{\boldsymbol{\Delta}}\right]\right\rangle_c\\
&+\left\langle \exp\left(\tfrac{1}{2}\sigma_x^2\Delta_x\right)\{\delta v_i v_j\}(\boldsymbol{x}_1)\right\rangle_c - \left\langle \exp\left(\tfrac{1}{2}\sigma_x^2\Delta_x\right)\{v_i v_j\}\bar{\delta}(\boldsymbol{x}_1)\right\rangle_c
\end{aligned}$$

$$\begin{aligned}
&= \left\langle\left\{a^2\dot{\Psi}_i\dot{\Psi}_j\right\}(\boldsymbol{q}_1)\right\rangle_c + i\left\langle \exp\left(\tfrac{1}{2}\sigma_x^2\Delta_q\right)\left\{a^2\dot{\Psi}_i\dot{\Psi}_j\right\}(\boldsymbol{q}_1)\left[\lambda_1\bar{\delta}_{L1}+\lambda_2\bar{\delta}_{L2}+\boldsymbol{k}\cdot\bar{\boldsymbol{\Delta}}\right]\right\rangle_c\\
&+\left\langle\left\{a^2\dot{\Psi}_i\dot{\Psi}_j(J_F^{-1}-1)\right\}(\boldsymbol{q}_1)\right\rangle_c - \left\langle \exp\left(\tfrac{1}{2}\sigma_x^2\Delta_q\right)\left\{a^2\dot{\Psi}_i\dot{\Psi}_j\right\}(\bar{J}_F^{-1}-1)(\boldsymbol{q}_1)\right\rangle_c\\
&= (afH)^2\Bigg\{\left\langle\left\{\Psi_i^{(1)}\Psi_j^{(1)}+3\Psi_{(i}^{(1)}\Psi_{j)}^{(3)}+4\Psi_i^{(2)}\Psi_j^{(2)}\right\}(\boldsymbol{q}_1)\right\rangle_c\\
&\quad+\left\langle \exp\left(\tfrac{1}{2}\sigma_x^2\Delta_q\right)\left\{2\Psi_{(i}^{(1)}\Psi_{j)}^{(2)}\right\}(\boldsymbol{q}_1)\left[i\lambda_1\bar{\delta}_L(\boldsymbol{q}_1)+i\lambda_2\bar{\delta}_L(\boldsymbol{q}_2)\right]\right\rangle_c\\
&\quad+\left\langle \exp\left(\tfrac{1}{2}\sigma_x^2\Delta_q\right)\left\{\Psi_i^{(1)}\Psi_j^{(1)}\right\}(\boldsymbol{q}_1)i\boldsymbol{k}\cdot\left(\bar{\boldsymbol{\Psi}}^{(2)}(\boldsymbol{q}_2)-\cancel{\bar{\boldsymbol{\Psi}}^{(2)}(\boldsymbol{q}_1)}\right)\right\rangle_c+\\
&\quad+\left\langle \exp\left(\tfrac{1}{2}\sigma_x^2\Delta_q\right)\left\{\Psi_i^{(1)}\Psi_j^{(1)}\right\}\cancel{\bar{\Psi}^{(2)}_{k,k}(\boldsymbol{q}_1)}\right\rangle_c\\
&\quad+\Bigg\langle \exp\left(\tfrac{1}{2}\sigma_x^2\Delta_q\right)\left\{2\Psi_{(i}^{(1)}\Psi_{j)}^{(2)}\right\}(\boldsymbol{q}_1)\underbrace{i\boldsymbol{k}\cdot\left(\bar{\boldsymbol{\Psi}}^{(1)}(\boldsymbol{q}_2)-\cancel{\bar{\boldsymbol{\Psi}}^{(1)}(\boldsymbol{q}_1)}\right)}_{-\left[\boldsymbol{\nabla}\bar{\boldsymbol{\Psi}}^{(1)}(\boldsymbol{q}_2)+\boldsymbol{\nabla}\bar{\boldsymbol{\Psi}}^{(1)}(\boldsymbol{q}_1)\right]}\Bigg\rangle_c+\\
&\quad+\left\langle \exp\left(\tfrac{1}{2}\sigma_x^2\Delta_q\right)\left\{2\Psi_{(i}^{(1)}\Psi_{j)}^{(2)}\right\}\cancel{\bar{\Psi}^{(1)}_{k,k}(\boldsymbol{q}_1)}\right\rangle_c\\
&\quad-\left\langle\left\{\Psi_i^{(1)}\Psi_j^{(1)}\Psi^{(2)}_{k,k}+2\Psi_{(i}^{(1)}\Psi_{j)}^{(2)}\Psi^{(1)}_{k,k}\right\}(\boldsymbol{q}_1)\right\rangle_c\Bigg\}
\end{aligned}$$

$$\sum_{N=0}^{\infty}\frac{i^N}{N!}\left\langle\frac{\overline{(1+\delta)v_iv_j}}{(afH)^2(1+\bar{\delta})}(\boldsymbol{x}_1(\boldsymbol{q}_1))\widetilde{X}^N_{\boldsymbol{J}=0}\right\rangle_c\Bigg|_{\mathcal{O}(P_L^2)} \tag{6.114a}$$

$$= +\int\frac{d^3k_1d^3k_2}{(2\pi)^6}e^{i(\boldsymbol{k}_1+\boldsymbol{k}_2)\cdot\boldsymbol{q}_1}\left\langle\left\{\Psi_i^{(1)}\Psi_j^{(1)}+3\Psi_{(i}^{(1)}\Psi_{j)}^{(3)}+4\Psi_i^{(2)}\Psi_j^{(2)}\right\}(\boldsymbol{k}_1,\boldsymbol{k}_2)\right\rangle_c \tag{6.114b}$$

$$+\int\frac{d^3k_1d^3k_2d^3k_3}{(2\pi)^9}\exp\left(-\tfrac{1}{2}\sigma_x^2\left[(\boldsymbol{k}_1+\boldsymbol{k}_2)^2+k_3^2\right]\right)e^{i(\boldsymbol{k}_1+\boldsymbol{k}_2)\cdot\boldsymbol{q}_1}\times$$

$$\times\left[i\lambda_1e^{i\boldsymbol{k}_3\cdot\boldsymbol{q}_1}+i\lambda_2e^{i\boldsymbol{k}_3\cdot\boldsymbol{q}_2}\right]\left\langle2\Psi_{(i}^{(1)}(\boldsymbol{k}_1)\Psi_{j)}^{(2)}(\boldsymbol{k}_2)\delta_L(\boldsymbol{k}_3)\right\rangle_c$$

$$-\int\frac{d^3k_1d^3k_2d^3k_3}{(2\pi)^9}e^{i(\boldsymbol{k}_1+\boldsymbol{k}_2+\boldsymbol{k}_3)\cdot\boldsymbol{q}_1}\left\langle\Psi_i^{(1)}(\boldsymbol{k}_1)\Psi_j^{(1)}(\boldsymbol{k}_2)i\boldsymbol{k}_3\cdot\boldsymbol{\Psi}^{(2)}(\boldsymbol{k}_3)+\right.$$

$$\left.+2\Psi_{(i}^{(1)}(\boldsymbol{k}_1)\Psi_{j)}^{(2)}(\boldsymbol{k}_2)i\boldsymbol{k}_3\cdot\boldsymbol{\Psi}^{(1)}(\boldsymbol{k}_3)\right\rangle_c$$

$$-\int\frac{d^3k_1d^3k_2d^3k_3}{(2\pi)^9}\exp\left(-\tfrac{1}{2}\sigma_x^2(\boldsymbol{k}_1+\boldsymbol{k}_2)^2\right)e^{i(\boldsymbol{k}_1+\boldsymbol{k}_2)\cdot\boldsymbol{q}_1+i\boldsymbol{k}_3\cdot\boldsymbol{q}_2}\left\langle\Psi_i^{(1)}(\boldsymbol{k}_1)\Psi_j^{(1)}(\boldsymbol{k}_2)i\boldsymbol{k}_3\cdot\bar{\boldsymbol{\Psi}}^{(2)}(\boldsymbol{k}_3)\right\rangle_c$$

$$-\int\frac{d^3k_1d^3k_2d^3k_3}{(2\pi)^9}\exp\left(-\tfrac{1}{2}\sigma_x^2(\boldsymbol{k}_1+\boldsymbol{k}_2)^2\right)e^{i(\boldsymbol{k}_1+\boldsymbol{k}_2)\cdot\boldsymbol{q}_1+i\boldsymbol{k}_3\cdot\boldsymbol{q}_2}\left\langle2\Psi_{(i}^{(1)}(\boldsymbol{k}_1)\Psi_{j)}^{(2)}(\boldsymbol{k}_2)i\boldsymbol{k}_3\cdot\bar{\boldsymbol{\Psi}}^{(1)}(\boldsymbol{k}_3)\right\rangle_c$$

$$= -\int\frac{d^3k_1}{(2\pi)^3}\left\{C_{ij}^{(11)}+3C_{ij}^{(13)}+3C_{ij}^{(31)}+4C_{ij}^{(22)}\right\}(\boldsymbol{k}_1) \tag{6.114c}$$

$$-\int\frac{d^3k_1d^3k_3}{(2\pi)^6}\exp\left(-\sigma_x^2k_3^2\right)\left[i\lambda_1+i\lambda_2e^{i\boldsymbol{k}_3\cdot(\boldsymbol{q}_2-\boldsymbol{q}_1)}\right]\left\{2C_{ij}^{(12)}+2C_{ij}^{(21)}\right\}(\boldsymbol{k}_3;\boldsymbol{k}_1,-\boldsymbol{k}_1-\boldsymbol{k}_3)$$

$$+\int\frac{d^3k_1d^3k_2}{(2\pi)^6}\left\{-(k_{1k}+k_{2k})C_{ijk}^{(112)}(\boldsymbol{k}_1,\boldsymbol{k}_2,-\boldsymbol{k}_1-\boldsymbol{k}_2)+2k_{2k}C_{(ij)k}^{(121)}(\boldsymbol{k}_1,-\boldsymbol{k}_1-\boldsymbol{k}_2,\boldsymbol{k}_2)\right\}$$

$$-\int\frac{d^3k_1d^3k_2}{(2\pi)^6}\exp\left(-\tfrac{1}{2}\sigma_x^2(\boldsymbol{k}_1+\boldsymbol{k}_2)^2\right)e^{i(\boldsymbol{k}_1+\boldsymbol{k}_2)\cdot(\boldsymbol{q}_1-\boldsymbol{q}_2)}\times$$

$$\times\left\langle i(-\boldsymbol{k}_1-\boldsymbol{k}_2)\cdot\bar{\boldsymbol{\Psi}}^{(2)}(-\boldsymbol{k}_1-\boldsymbol{k}_2)\Psi_i^{(1)}(\boldsymbol{k}_1)\Psi_j^{(1)}(\boldsymbol{k}_2)\right\rangle_c$$

$$-\int\frac{d^3k_1d^3k_3}{(2\pi)^6}\exp\left(-\tfrac{1}{2}\sigma_x^2k_3^2\right)e^{i\boldsymbol{k}_3\cdot(\boldsymbol{q}_2-\boldsymbol{q}_1)}\left\langle2i\boldsymbol{k}_3\cdot\bar{\boldsymbol{\Psi}}^{(1)}(\boldsymbol{k}_3)\Psi_{(i}^{(1)}(\boldsymbol{k}_1)\Psi_{j)}^{(2)}(-\boldsymbol{k}_1-\boldsymbol{k}_3)\right\rangle_c$$

$$
\begin{aligned}
&= + \int \frac{d^3k}{(2\pi)^3} \frac{k_i k_j}{k^4} \left\{ P_L(k) + 2\cdot 3 \cdot \frac{5}{21} R_1(k) + 4 \cdot \frac{9}{98} Q_1(k) \right\} \qquad (6.114d)\\
&\quad - \int \frac{d^3k}{(2\pi)^3} \exp\left(-\sigma_x^2 k^2\right) \left[i\lambda_1 + i\lambda_2 e^{ik\cdot(q_2-q_1)} \right] 2\cdot 2\times \\
&\qquad\qquad \times \frac{3}{14} \left[-\frac{\delta_{ij}}{k^2} R_1(k) + \frac{k_i k_j}{k^4} [R_1(k) + 2R_2(k)] \right] \\
&\quad + \int \frac{d^3k d^3p}{(2\pi)^6} \left\{ -(\boldsymbol{k}+\boldsymbol{p}) \cdot 2\boldsymbol{L}^{(2)}(\boldsymbol{k},\boldsymbol{p}) L_i^{(1)}(\boldsymbol{k}) L_j^{(1)}(\boldsymbol{p}) + 4\boldsymbol{p}\cdot \boldsymbol{L}^{(1)}(\boldsymbol{p}) L_{(i}^{(1)}(\boldsymbol{k}) L_{j)}^{(2)}(\boldsymbol{k},\boldsymbol{p}) \right\} \times \\
&\qquad\qquad \times P_L(k) P_L(p) \\
&\quad + \int \frac{d^3k d^3p}{(2\pi)^6} \exp\left(-\tfrac{1}{2}\sigma_x^2 (\boldsymbol{k}+\boldsymbol{p})^2\right) e^{i(\boldsymbol{k}+\boldsymbol{p})\cdot(\boldsymbol{q}_1-\boldsymbol{q}_2)} \times \\
&\qquad\qquad \times \left\{ -2(\boldsymbol{k}+\boldsymbol{p}) \cdot \bar{\boldsymbol{L}}^{(2)}(\boldsymbol{k},\boldsymbol{p}) L_i^{(1)}(\boldsymbol{k}) L_j^{(1)}(\boldsymbol{p}) \right\} P_L(k) P_L(p) \\
&\quad + \int \frac{d^3k d^3p}{(2\pi)^6} \exp\left(-\tfrac{1}{2}\sigma_x^2 p^2\right) e^{i\boldsymbol{p}\cdot(\boldsymbol{q}_2-\boldsymbol{q}_1)} \left\{ 4\boldsymbol{p}\cdot \bar{\boldsymbol{L}}^{(1)}(\boldsymbol{p}) L_{(i}^{(1)}(\boldsymbol{k}) L_{j)}^{(2)}(\boldsymbol{k},\boldsymbol{p}) \right\} P_L(k) P_L(p)
\end{aligned}
$$

This result for the contribution coming from $\boldsymbol{x}_1(\boldsymbol{q}_1)$ can be easily translated to the result for $\boldsymbol{x}_2(\boldsymbol{q}_2)$ by interchanging $\boldsymbol{q}_1 \leftrightarrow \boldsymbol{q}_2$ as well as $\lambda_1 \leftrightarrow \lambda_2$.

Second σ_x^2 part (6.111e) **in** (6.110)

$$
\begin{aligned}
\sum_{N=0}^{\infty} \frac{i^N}{N!} \left\langle \bar{v}_i \bar{v}_j(\boldsymbol{x}_1(\boldsymbol{q}_1)) \widetilde{X}_{\boldsymbol{J}=0}^N \right\rangle_c \Big|_{\mathcal{O}(P_L^2)} &= \sum_{N=0}^{\infty} \frac{i^N}{N!} \left\langle a^2 \dot{\bar{\Psi}}_i \dot{\bar{\Psi}}_j(\boldsymbol{q}_1) \widetilde{X}_{\boldsymbol{J}=0}^N \right\rangle_c \Big|_{\mathcal{O}(P_L^2)} \qquad (6.115a)\\
&= \left\langle a^2 \dot{\bar{\Psi}}_i \dot{\bar{\Psi}}_j(\boldsymbol{q}_1) \right\rangle_c + i \left\langle a^2 \dot{\bar{\Psi}}_i \dot{\bar{\Psi}}_j(\boldsymbol{q}_1) \left[\lambda_1 \bar{\delta}_{L1} + \lambda_2 \bar{\delta}_{L2} + \boldsymbol{k}\cdot\bar{\boldsymbol{\Delta}} \right] \right\rangle_c
\end{aligned}
$$

$$
\begin{aligned}
&\sum_{N=0}^{\infty} \frac{i^N}{N!} \left\langle \frac{\bar{v}_i \bar{v}_j(\boldsymbol{x}_1)}{(afH)^2} \widetilde{X}_{\boldsymbol{J}=0}^N \right\rangle_c \Big|_{\mathcal{O}(P_L^2)} \qquad (6.116a)\\
&= \left\langle \left[\bar{\Psi}_i^{(1)} \bar{\Psi}_j^{(1)} + 3\bar{\Psi}_{(i}^{(1)} \bar{\Psi}_{j)}^{(3)} + 4\bar{\Psi}_i^{(2)} \bar{\Psi}_j^{(2)} \right](\boldsymbol{q}_1) \right\rangle_c + \left\langle 2\bar{\Psi}_{(i}^{(1)} \bar{\Psi}_{j)}^{(2)}(\boldsymbol{q}_1) \left[i\lambda_1 \bar{\delta}_L(\boldsymbol{q}_1) + i\lambda_2 \bar{\delta}_L(\boldsymbol{q}_2) \right] \right\rangle_c \\
&+ \Big\langle \bar{\Psi}_i^{(1)} \bar{\Psi}_j^{(1)}(\boldsymbol{q}_1) \underbrace{i\boldsymbol{k}\cdot\left(\bar{\boldsymbol{\Psi}}^{(2)}(\boldsymbol{q}_2) - \bar{\boldsymbol{\Psi}}^{(2)}(\boldsymbol{q}_1) \right)}_{-i\left[\boldsymbol{\nabla}\bar{\boldsymbol{\Psi}}^{(2)}(\boldsymbol{q}_2) + \boldsymbol{\nabla}\bar{\boldsymbol{\Psi}}^{(2)}(\boldsymbol{q}_1)\right]} \Big\rangle_c + \Big\langle 2\bar{\Psi}_{(i}^{(2)} \bar{\Psi}_{j)}^{(1)}(\boldsymbol{q}_1) \underbrace{i\boldsymbol{k}\cdot\left(\bar{\boldsymbol{\Psi}}^{(1)}(\boldsymbol{q}_2) - \bar{\boldsymbol{\Psi}}^{(1)}(\boldsymbol{q}_1) \right)}_{-i\left[\boldsymbol{\nabla}\bar{\boldsymbol{\Psi}}^{(1)}(\boldsymbol{q}_2) + \boldsymbol{\nabla}\bar{\boldsymbol{\Psi}}^{(1)}(\boldsymbol{q}_1)\right]} \Big\rangle_c
\end{aligned}
$$

$$= \int \frac{d^3k_1 d^3k_2}{(2\pi)^6} e^{i(\boldsymbol{k}_1+\boldsymbol{k}_2)\cdot\boldsymbol{q}_1} \left\langle \left[\bar{\Psi}_i^{(1)} \bar{\Psi}_j^{(1)} + 3\bar{\Psi}_{(i}^{(1)} \bar{\Psi}_{j)}^{(3)} + 4\bar{\Psi}_i^{(2)} \bar{\Psi}_j^{(2)} \right] (\boldsymbol{k}_1, \boldsymbol{k}_2) \right\rangle_c \tag{6.116b}$$
$$+ \int \frac{d^3k_1 d^3k_2 d^3k_3}{(2\pi)^9} e^{i(\boldsymbol{k}_1+\boldsymbol{k}_2)\cdot\boldsymbol{q}_1} \left[i\lambda_1 e^{i\boldsymbol{k}_3\cdot\boldsymbol{q}_1} + i\lambda_2 e^{i\boldsymbol{k}_3\cdot\boldsymbol{q}_2} \right] \left\langle 2\bar{\Psi}_{(i}^{(1)}(\boldsymbol{k}_1) \bar{\Psi}_{j)}^{(2)}(\boldsymbol{k}_2) \bar{\delta}_L(\boldsymbol{k}_3) \right\rangle_c$$
$$- \int \frac{d^3k_1 d^3k_2 d^3k_3}{(2\pi)^9} e^{i(\boldsymbol{k}_1+\boldsymbol{k}_2)\cdot\boldsymbol{q}_1} \left[e^{i\boldsymbol{k}_3\cdot\boldsymbol{q}_2} + e^{i\boldsymbol{k}_3\cdot\boldsymbol{q}_1} \right] \left\langle \bar{\Psi}_i^{(1)}(\boldsymbol{k}_1) \bar{\Psi}_j^{(1)}(\boldsymbol{k}_2) i\boldsymbol{k}_3 \cdot \bar{\boldsymbol{\Psi}}^{(2)}(\boldsymbol{k}_3) \right\rangle_c$$
$$- \int \frac{d^3k_1 d^3k_2 d^3k_3}{(2\pi)^9} e^{i(\boldsymbol{k}_1+\boldsymbol{k}_2)\cdot\boldsymbol{q}_1} \left[e^{i\boldsymbol{k}_3\cdot\boldsymbol{q}_2} + e^{i\boldsymbol{k}_3\cdot\boldsymbol{q}_1} \right] \left\langle 2\bar{\Psi}_{(i}^{(2)}(\boldsymbol{k}_1) \bar{\Psi}_{j)}^{(1)}(\boldsymbol{k}_2) i\boldsymbol{k}_3 \cdot \bar{\boldsymbol{\Psi}}^{(1)}(\boldsymbol{k}_3) \right\rangle_c$$

$$= -\int \frac{d^3k_1}{(2\pi)^3} \left\{ \bar{C}_{ij}^{(11)} + 3\bar{C}_{ij}^{(13)} + 3\bar{C}_{ij}^{(31)} + 4\bar{C}_{ij}^{(22)} \right\} (\boldsymbol{k}_1) \tag{6.116c}$$
$$- \int \frac{d^3k_1 d^3k_3}{(2\pi)^6} \left[i\lambda_1 + i\lambda_2 e^{i\boldsymbol{k}_3\cdot(\boldsymbol{q}_2-\boldsymbol{q}_1)} \right] \left\{ 2\bar{C}_{ij}^{(12)} + 2\bar{C}_{ij}^{(21)} \right\} (\boldsymbol{k}_3; \boldsymbol{k}_1, -\boldsymbol{k}_1 - \boldsymbol{k}_3)$$
$$+ \int \frac{d^3k_1 d^3k_2}{(2\pi)^6} \left[e^{i(\boldsymbol{k}_1+\boldsymbol{k}_2)\cdot(\boldsymbol{q}_1-\boldsymbol{q}_2)} + 1 \right] \left\{ -(k_{1k}+k_{2k}) \bar{C}_{ijk}^{(112)} (\boldsymbol{k}_1, \boldsymbol{k}_2, -\boldsymbol{k}_1 - \boldsymbol{k}_2) \right\}$$
$$+ \int \frac{d^3k_2 d^3k_3}{(2\pi)^6} \left[e^{i\boldsymbol{k}_3\cdot(\boldsymbol{q}_2-\boldsymbol{q}_1)} + 1 \right] 2k_{3k} \bar{C}_{(ij)k}^{(211)} (-\boldsymbol{k}_2 - \boldsymbol{k}_3, \boldsymbol{k}_2, \boldsymbol{k}_3)$$

$$= \int \frac{d^3k}{(2\pi)^3} \frac{k_i k_j}{k^4} \left\{ \bar{P}_L(k) + 2\cdot 3\cdot \frac{5}{21} \bar{R}_0(k) + 4\cdot \frac{9}{98} \bar{Q}_1(k) \right\} \tag{6.116d}$$
$$- \int \frac{d^3k}{(2\pi)^3} \left[i\lambda_1 + i\lambda_2 e^{i\boldsymbol{k}\cdot(\boldsymbol{q}_2-\boldsymbol{q}_1)} \right] 2\cdot 2\cdot \frac{3}{14} \left[-\frac{\delta_{ij}}{k^2} \bar{R}_1(k) + \frac{k_i k_j}{k^4} [\bar{R}_1(k) + 2\bar{R}_2(k)] \right]$$
$$+ \int \frac{d^3k d^3p}{(2\pi)^6} \left[1 + e^{i(\boldsymbol{k}+\boldsymbol{p})\cdot(\boldsymbol{q}_1-\boldsymbol{q}_2)} \right] \left\{ -2(\boldsymbol{k}+\boldsymbol{p}) \cdot \bar{\boldsymbol{L}}^{(2)}(\boldsymbol{k}, \boldsymbol{p})\ \bar{L}_i^{(1)}(\boldsymbol{k}) \bar{L}_j^{(1)}(\boldsymbol{p}) \right\} P_L(k) P_L(p)$$
$$+ \int \frac{d^3k d^3p}{(2\pi)^6} \left[1 + e^{i\boldsymbol{p}\cdot(\boldsymbol{q}_2-\boldsymbol{q}_1)} \right] \left\{ 4\boldsymbol{p} \cdot \bar{\boldsymbol{L}}^{(1)}(\boldsymbol{p})\ \bar{L}_{(i}^{(1)}(\boldsymbol{k}) \bar{L}_{j)}^{(2)}(\boldsymbol{k}, \boldsymbol{p}) \right\} P_L(k) P_L(p)$$

$\bar{C}_{i_1\cdots i_n}$ refer to the same correlators as $C_{i_1\cdots i_n}$ defined in (6.94) but which are computed using $\bar{\Psi}$ and $\bar{\delta}_L$ instead of Ψ and δ_L. Then we write $\bar{\boldsymbol{L}}^{(n)} = \bar{\boldsymbol{S}}^{(n)} + \bar{\boldsymbol{T}}^{(n)}$ for the kernels of the coarse-grained displacement according to (6.17) and (6.18). Again, we can easily translate this calculation carried out for $\boldsymbol{x}_1(\boldsymbol{q}_1)$ to $\boldsymbol{x}_2(\boldsymbol{q}_2)$ by interchanging $\boldsymbol{q}_1 \leftrightarrow \boldsymbol{q}_2$ and $\lambda_1 \leftrightarrow \lambda_2$.

Both σ_x^2 parts (6.111c) in (6.110) Result for the extra terms due to σ_x^2, in the second step we collected the terms and used $\bar{\boldsymbol{L}}_1(\boldsymbol{p}) = \exp\left(-\frac{1}{2}\sigma_x^2 p^2\right) \boldsymbol{L}_1(\boldsymbol{p})$. Furthermore we regroup the terms and keep only terms up to $\mathcal{O}(P_L^2)$.

$$(afH)^{-2}\Bigg\{\sum_{N=0}^{\infty}\frac{i^N}{N!}\Big\langle\left[\overline{\frac{(1+\delta)v_iv_j}{1+\bar\delta}}(\boldsymbol{x}_1)+\overline{\frac{(1+\delta)v_iv_j}{1+\bar\delta}}(\boldsymbol{x}_2)\right]\widetilde{X}^N_{\boldsymbol{J}=\boldsymbol{0}}\Big\rangle_c$$
$$-\sum_{N=0}^{\infty}\frac{i^N}{N!}\Big\langle\left[\overline{\frac{(1+\delta)v_i}{1+\bar\delta}}\,\overline{\frac{(1+\delta)v_j}{1+\bar\delta}}(\boldsymbol{x}_1)+\overline{\frac{(1+\delta)v_i}{1+\bar\delta}}\,\overline{\frac{(1+\delta)v_j}{1+\bar\delta}}(\boldsymbol{x}_2)\right]\widetilde{X}^N_{\boldsymbol{J}=\boldsymbol{0}}\Big\rangle_c\Bigg\}$$

$$=\int\frac{d^3k}{(2\pi)^3}2\cdot\frac{k_ik_j}{k^4}\Big\{[P_L(k)-\bar P_L(k)]+2\cdot3\cdot\frac{5}{21}[R_1(k)-\bar R_0(k)]+$$
$$+4\cdot\frac{9}{98}[Q_1(k)-\bar Q_1(k)]\Big\}$$
$$+i(\lambda_1+\lambda_2)\int\frac{d^3k}{(2\pi)^3}\left(1+e^{i\boldsymbol{k}\cdot\boldsymbol{q}}\right)\frac{6}{7}\Big\{\frac{\delta_{ij}}{k^2}\left[\exp\left(-\sigma_x^2k^2\right)R_1(k)-\bar R_1(k)\right]$$
$$-\frac{k_ik_j}{k^4}[\exp\left(-\sigma_x^2k^2\right)[R_1(k)+2R_2(k)]-[\bar R_1(k)+2\bar R_2(k)]\Big\}$$
$$+\int\frac{d^3kd^3p}{(2\pi)^6}\Bigg\{\cos\left[\boldsymbol{k}\cdot\boldsymbol{q}\right]\left[\exp\left(-\tfrac{1}{2}\sigma_x^2(|\boldsymbol{k}-\boldsymbol{p}|^2+p^2)\right)-\exp\left(-\tfrac{1}{2}\sigma_x^2k^2\right)\right]4\boldsymbol{k}\cdot\bar{\boldsymbol{L}}^{(2)}(\boldsymbol{k}-\boldsymbol{p},\boldsymbol{p})$$
$$+4\boldsymbol{k}\cdot\left[\exp\left(-\tfrac{1}{2}\sigma_x^2(|\boldsymbol{k}-\boldsymbol{p}|^2+p^2)\right)\bar{\boldsymbol{L}}^{(2)}(\boldsymbol{k}-\boldsymbol{p},\boldsymbol{p})-\boldsymbol{L}^{(2)}(\boldsymbol{k}-\boldsymbol{p},\boldsymbol{p})\right]\Bigg\}\times$$
$$\times L_i^{(1)}(\boldsymbol{k}-\boldsymbol{p})L_j^{(1)}(\boldsymbol{p})P_L(|\boldsymbol{k}-\boldsymbol{p}|)P_L(p)$$
$$+\int\frac{d^3kd^3p}{(2\pi)^6}\Bigg\{\cos\left[\boldsymbol{p}\cdot\boldsymbol{q}\right]\Big[\exp\left(-\sigma_x^2p^2\right)L^{(2)}_{(i}(\boldsymbol{k}-\boldsymbol{p},\boldsymbol{p})-$$
$$-\exp\left(-\tfrac{1}{2}\sigma_x^2(|\boldsymbol{k}-\boldsymbol{p}|^2+p^2)\right)\cdot\bar L^{(2)}_{(i}(\boldsymbol{k}-\boldsymbol{p},\boldsymbol{p})\Big]$$
$$+\left[L^{(2)}_{(i}(\boldsymbol{k}-\boldsymbol{p},\boldsymbol{p})-\exp\left(-\tfrac{1}{2}\sigma_x^2(|\boldsymbol{k}-\boldsymbol{p}|^2+p^2)\right)\cdot\bar L^{(2)}_{(i}(\boldsymbol{k}-\boldsymbol{p},\boldsymbol{p})\right]\Bigg\}\times$$
$$\times L^{(1)}_{j)}(\boldsymbol{k}-\boldsymbol{p})\,8\boldsymbol{p}\cdot\boldsymbol{L}^{(1)}(\boldsymbol{p})P_L(|\boldsymbol{k}-\boldsymbol{p}|)P_L(p)$$

$$= \int \frac{d^3k}{(2\pi)^3} 2 \cdot \frac{k_i k_j}{k^4} \Big\{ [P_L(k) - \bar{P}_L(k)] + 2 \cdot 3 \cdot \frac{5}{21} [R_1(k) - \bar{R}_0(k)] + 4 \cdot \frac{9}{98} [Q_1(k) - \bar{Q}_1(k)] \Big\}$$

$$+ i(\lambda_1 + \lambda_2) \int \frac{d^3k}{(2\pi)^3} \left(1 + e^{i\,\boldsymbol{k}\cdot\boldsymbol{q}}\right) \frac{6}{7} \Big\{ \frac{\delta_{ij}}{k^2} \left[\exp\left(-\sigma_x^2 k^2\right) R_1(k) - \bar{R}_1(k) \right]$$

$$- \frac{k_i k_j}{k^4} [\exp\left(-\sigma_x^2 k^2\right) [R_1(k) + 2R_2(k)] - [\bar{R}_1(k) + 2\bar{R}_2(k)] \Big\}$$

$$+ \int_0^\infty \frac{dk}{4\pi^2}\, k^2 \frac{k^3}{4\pi^2} \int_0^\infty \overset{p=kr}{dr}\, r^2\, P_L(kr) \int_{-1}^1 \overset{x=\cos\angle(\boldsymbol{k},\boldsymbol{p})}{dx} \quad P_L(k\sqrt{1-2rx+r^2}) \times$$

$$\times \int_{-1}^1 \overset{\mu=\cos\angle(\boldsymbol{k},\boldsymbol{q})}{d\mu} \Big\{ \cos(kq\mu) \left[\tilde{\mathcal{Q}}_1(k,r,x)\delta_{ij} + \tilde{\mathcal{Q}}_2(k,r,x) \frac{k_i k_j}{k^2} \right] +$$

$$+ \left[\tilde{\mathcal{Q}}_3(k,r,x)\delta_{ij} + \tilde{\mathcal{Q}}_4(k,r,x) \frac{k_i k_j}{k^2} \right] \Big\} \tag{6.117a}$$

$$+ \int_0^\infty \frac{dp}{4\pi^2}\, p^2 P_L(p) \frac{p^3}{4\pi^2} \int_0^\infty \overset{k=pr}{dr}\, r^2 \int_{-1}^1 \overset{x=\cos\angle(\boldsymbol{k},\boldsymbol{p})}{dx} \quad P_L(p\sqrt{1-2rx+r^2}) \times$$

$$\times \int_{-1}^1 \overset{\mu=\cos\angle(\boldsymbol{p},\boldsymbol{q})}{d\mu} \Big\{ \cos(pq\mu) \left[\tilde{\mathfrak{Q}}_1(p,r,x)\delta_{ij} + \tilde{\mathfrak{Q}}_2(p,r,x) \frac{p_i p_j}{p^2} \right] +$$

$$+ \left[\tilde{\mathfrak{Q}}_3(p,r,x)\delta_{ij} + \tilde{\mathfrak{Q}}_4(p,r,x) \frac{p_i p_j}{p^2} \right] \Big\} \tag{6.117b}$$

We now decompose all 2-rank tensors $T_{ij} = \int d^3k\, (T_{k\delta}\, \delta_{ij} + T_{kk}\, \hat{k}_i \hat{k}_j)$ into $T_{ij} = T_{q\delta}\, \delta_{ij} + T_{qq}\, \hat{q}_i \hat{q}_j$ such that we can translate $T_{q\delta} = \int d^3k\, (T_{k\delta} + \frac{1}{2}(1-\mu^2) T_{kk})$ and $T_{qq} = \int d^3k\, (\frac{1}{2}(3\mu^2 - 1) T_{kk})$, where $\mu = \hat{\boldsymbol{k}} \cdot \hat{\boldsymbol{q}}$. Then we perform the μ-integration and use the integral relations (6.96) for the spherical Bessel functions j_0 and j_1.

$$= \int \frac{\mathrm{d}k}{2\pi^2} \cdot \frac{2}{3} \Big\{ [P_L(k) - \bar{P}_L(k)] \Big\} \delta_{ij} \tag{6.117c}$$

$$+ \int \frac{\mathrm{d}k}{2\pi^2} i(\lambda_1 + \lambda_2) \cdot \frac{6}{7} \Big\{ \left[\exp\left(-\sigma_x^2 k^2\right) R_1(k) - \bar{R}_1(k) \right] \Big(1 + j_0(kq) \Big) \delta_{ij}$$

$$- \left[\exp\left(-\sigma_x^2 k^2\right) [R_1(k) + 2R_2(k)] - [\bar{R}_1(k) + 2\bar{R}_2(k)] \right] \left(\frac{1}{3} + \frac{j_1(kq)}{kq} \right) \delta_{ij}$$

$$- \left[\exp\left(-\sigma_x^2 k^2\right) [R_1(k) + 2R_2(k)] - [\bar{R}_1(k) + 2\bar{R}_2(k)] \right] \left(j_0(kq) - 3\frac{j_1(kq)}{kq} \right) \hat{q}_i \hat{q}_j \Big\} +$$

$$
\begin{aligned}
&+\int \frac{\mathrm{d}k}{2\pi^2}\, k^2 \cdot \Bigg\{ \Big[[\mathcal{Q}_3(k)+\mathfrak{Q}_3(k)] + \frac{1}{3}[\mathcal{Q}_4(k)+\mathfrak{Q}_4(k)] + [\mathcal{Q}_1(k)+\mathfrak{Q}_1(k)]\, j_0(kq) + \\
&\quad + [\mathcal{Q}_2(k)+\mathfrak{Q}_2(k)] \left(\frac{j_1(kq)}{kq}\right) \Big] \delta_{ij} \\
&\quad + \frac{1}{k^2}\left[\frac{20}{21}[R_1(k)-\bar{R}_0(k)] + \frac{12}{49}[Q_1(k)-\bar{Q}_1(k)]\right]\delta_{ij} + \\
&\quad + [\mathcal{Q}_2(k)+\mathfrak{Q}_2(k)] \left(j_0(kq) - 3\frac{j_1(kq)}{kq}\right) \hat{q}_i \hat{q}_j \Bigg\}
\end{aligned}
$$

$$
=: K_{2,ij}^{\sigma_x(\mathrm{L})} + i(\lambda_1+\lambda_2) K_{2,ij}^{\sigma_x(b1,2)} + K_{2,ij}^{\sigma_x(b0,2)} \tag{6.117d}
$$

$$
\begin{aligned}
K_{2,ij}^{\sigma_x} &= \exp\left[\sum_{N=1}^{\infty} \frac{i^N}{N!} \langle \widetilde{X}_{J=0}^N \rangle_c\right] \Bigg\{ \sum_{N=0}^{\infty} \frac{i^N}{N!} \left\langle \left[\frac{\overline{(1+\delta)v_i v_j}}{1+\bar{\delta}}(\boldsymbol{x}_1) + \frac{\overline{(1+\delta)v_i v_j}}{1+\bar{\delta}}(\boldsymbol{x}_2) \right] \widetilde{X}_{J=0}^N \right\rangle_c \\
&\quad - \sum_{N=0}^{\infty} \frac{i^N}{N!} \left\langle \left[\frac{\overline{(1+\delta)v_i}}{1+\bar{\delta}} \frac{\overline{(1+\delta)v_j}}{1+\bar{\delta}}(\boldsymbol{x}_1) + \frac{\overline{(1+\delta)v_i}}{1+\bar{\delta}} \frac{\overline{(1+\delta)v_j}}{1+\bar{\delta}}(\boldsymbol{x}_2) \right] \widetilde{X}_{J=0}^N \right\rangle_c \Bigg\} \\
&= e^{-\frac{1}{2}K_{ij}k_i k_j} e^{-\frac{1}{2}(\lambda_1^2+\lambda_2^2)\sigma_R^2} \times \Big\{ K_{2,ij}^{\sigma_x(\mathrm{L})} + K_{2,ij}^{\sigma_x(b0,2)} + i(\lambda_1+\lambda_2) K_{2,ij}^{\sigma_x(b1,2)} - \\
&\qquad - \lambda_1\lambda_2\xi_L K_{2,ij}^{\sigma_x(\mathrm{L})} - (\lambda_1+\lambda_2) U_i^{10} k_i K_{2,ij}^{\sigma_x(\mathrm{L})} \Big\}
\end{aligned}
$$

The R and Q terms are the usual CLPT kernels from [Mat08] whereas $\bar{R}$ and $\bar{Q}$ are our corresponding cgCLPT kernels given in (6.104) and (6.103). The additional kernels, $\tilde{\mathfrak{Q}}_{1-4}$ and $\tilde{\mathcal{Q}}_{1-4}$, appearing in (6.117a) and (6.117b) were introduced in order to keep notation short. They define two other classes of functions $\mathfrak{Q}_{1-4}$ and $\mathcal{Q}_{1-4}$, besides R and Q, according to

$$
\mathcal{Q}_n(k) = \frac{k^3}{4\pi^2} \int_0^\infty dr\, P_L(kr) \int_{-1}^1 dx\, P_L(k\sqrt{1-2rx+r^2})\, \tilde{\mathcal{Q}}_n(k,r,x)\,, \tag{6.118a}
$$

$$
\mathfrak{Q}_n(k) = \frac{k^3}{4\pi^2} P_L(k) \int_0^\infty dr \int_{-1}^1 dx\, P_L(k\sqrt{1-2rx+r^2})\, \tilde{\mathfrak{Q}}_n(k,r,x)\,. \tag{6.118b}
$$

with

$$\tilde{\mathcal{Q}}_1(k,r,x) = \frac{r\left(1-x^2\right)e^{-{\sigma_x}^2k^2\left(2r^2+1\right)}}{7k^2\left(r^2-2rx+1\right)^2}\left(e^{{\sigma_x}^2k^2rx}-e^{{\sigma_x}^2k^2r^2}\right)\times \tag{6.119a}$$
$$\times\left[\left(10rx^2-3r-7x\right)e^{{\sigma_x}^2k^2r^2}-7x\left(rx-1\right)e^{{\sigma_x}^2k^2rx}\right]$$

$$\tilde{\mathcal{Q}}_2(k,r,x) = \frac{\left(3rx^2-r-2x\right)e^{-{\sigma_x}^2k^2\left(2r^2+1\right)}}{7k^2\left(r^2-2rx+1\right)^2}\left(e^{{\sigma_x}^2k^2rx}-e^{{\sigma_x}^2k^2r^2}\right)\times \tag{6.119b}$$
$$\times\left[\left(10rx^2-3r-7x\right)e^{{\sigma_x}^2k^2r^2}-7x\left(rx-1\right)e^{{\sigma_x}^2k^2rx}\right]$$

$$\tilde{\mathcal{Q}}_3(k,r,x) = \frac{r\left(1-x^2\right)e^{-{\sigma_x}^2k^2\left(2r^2+1\right)}}{7k^2\left(r^2-2rx+1\right)^2}\Big[3r\left(1-x^2\right)e^{{\sigma_x}^2k^2\left(2r^2+1\right)}+ \tag{6.119c}$$
$$+\left(10rx^2-3r-7x\right)e^{{\sigma_x}^2k^2r(r+x)}-7x\left(rx-1\right)e^{2{\sigma_x}^2k^2rx}\Big]$$

$$\tilde{\mathcal{Q}}_4(k,r,x) = \frac{\left(3rx^2-r-2x\right)e^{-{\sigma_x}^2k^2\left(2r^2+1\right)}}{7k^2\left(r^2-2rx+1\right)^2}\Big[3r\left(1-x^2\right)e^{{\sigma_x}^2k^2\left(2r^2+1\right)}+ \tag{6.119d}$$
$$+\left(10rx^2-3r-7x\right)e^{{\sigma_x}^2k^2r(r+x)}-7x\left(rx-1\right)e^{2{\sigma_x}^2k^2rx}\Big]$$

$$\tilde{\mathcal{Q}}_{1-4} \xrightarrow{\sigma_x\to 0} 0$$

$$\tilde{\mathfrak{Q}}_1(k,r,x) = -\frac{2r^4\left(1-x^2\right)e^{-{\sigma_x}^2k^2\left(r^2+2\right)}}{7k^2\left(r^2-2rx+1\right)^2}\Big[6\left(x^2-1\right)e^{{\sigma_x}^2k^2\left(r^2+1\right)}+ \tag{6.119e}$$
$$+\left(21rx-34x^2+6\right)e^{{\sigma_x}^2k^2(rx+1)}-7\left(3rx-4x^2\right)e^{2{\sigma_x}^2k^2rx}\Big]$$

$$\tilde{\mathfrak{Q}}_2(k,r,x) = \frac{2r^3e^{-{\sigma_x}^2k^2\left(r^2+2\right)}}{7k^2\left(r^2-2rx+1\right)^2}\Big[6\left(1-x^2\right)\left(3rx^2-r-2x\right)e^{{\sigma_x}^2k^2\left(r^2+1\right)} \tag{6.119f}$$
$$+\left(7r^2\left(5-9x^2\right)x+2r\left(51x^4-19x^2-4\right)-68x^3+40x\right)e^{{\sigma_x}^2k^2(rx+1)}$$
$$+7\left(r^2\left(9x^2-5\right)x+2r\left(-6x^4+x^2+1\right)+8x^3-4x\right)e^{2{\sigma_x}^2k^2rx}\Big]$$

$$\tilde{\mathfrak{Q}}_3(k,r,x) = -\frac{2r^4\left(1-x^2\right)e^{-{\sigma_x}^2k^2\left(r^2+2\right)}}{7k^2\left(r^2-2rx+1\right)^2}\Big[6\left(x^2-1\right)e^{{\sigma_x}^2k^2\left(r^2+2\right)}+ \tag{6.119g}$$
$$+\left(21rx-34x^2+6\right)e^{{\sigma_x}^2k^2(rx+1)}-7(3rx-4x^2)e^{2{\sigma_x}^2k^2rx}\Big]$$

$$\tilde{\mathfrak{Q}}_4(k,r,x) = \frac{2r^3e^{-{\sigma_x}^2k^2\left(r^2+2\right)}}{7k^2\left(r^2-2rx+1\right)^2}\Big[6\left(1-x^2\right)\left(3rx^2-r-2x\right)e^{{\sigma_x}^2k^2\left(r^2+2\right)} \tag{6.119h}$$
$$+\left(7r^2\left(5-9x^2\right)x+2r\left(51x^4-19x^2-4\right)-68x^3+40x\right)e^{{\sigma_x}^2k^2(rx+1)}$$
$$+7\left(r^2\left(9x^2-5\right)x+2r\left(-6x^4+x^2+1\right)+8x^3-4x\right)e^{2{\sigma_x}^2k^2rx}\Big]$$

$$\tilde{\mathfrak{Q}}_{1-4} \xrightarrow{\sigma_x\to 0} 0$$

Bibliography

[AAB+12] Anderson, L. ; Aubourg, E. ; Bailey, S. ; Bizyaev, D. ; Blanton, M. ; Bolton, A. S. ; Brinkmann, J. ; Brownstein, J. R. ; Burden, A. ; Cuesta, A. J. ; da Costa, L. A. N. ; Dawson, K. S. ; de Putter, R. ; Eisenstein, D. J. ; Gunn, J. E. ; Guo, H. ; Hamilton, J.-C. ; Harding, P. ; Ho, S. ; Honscheid, K. ; Kazin, E. ; Kirkby, D. ; Kneib, J.-P. ; Labatie, A. ; Loomis, C. ; Lupton, R. H. ; et al, *The clustering of galaxies in the SDSS-III Baryon Oscillation Spectroscopic Survey: baryon acoustic oscillations in the Data Release 9 spectroscopic galaxy sample*, Monthly Notices of the RAS **427**, 3435–3467 (December 2012), 1203.6594.

[ABC+06] Albrecht, A. ; Bernstein, G. ; Cahn, R. ; Freedman, W. L. ; Hewitt, J. ; Hu, W. ; Huth, J. ; Kamionkowski, M. ; Kolb, E. W. ; Knox, L. ; Mather, J. C. ; Staggs, S. ; Suntzeff, N. B., *Report of the Dark Energy Task Force*, ArXiv Astrophysics e-prints (September 2006), arXiv:astro-ph/0609591.

[ABS10] Appleby, S. A. ; Battye, R. A. ; Starobinsky, A. A., *Curing singularities in cosmological evolution of F(R) gravity*, Journal of Cosmology and Astroparticle Physics **6**, 5 (June 2010), 0909.1737.

[AC12a] Achitouv, I. E. ; Corasaniti, P. S., *Non-Gaussian halo mass function and non-spherical halo collapse: theory vs. simulations*, Journal of Cosmology and Astroparticle Physics **2**, 2 (February 2012), 1109.3196.

[AC12b] Achitouv, I. E. ; Corasaniti, P. S., *Primordial bispectrum and trispectrum contributions to the non-Gaussian excursion set halo mass function with diffusive drifting barrier*, Physical Review D **86**(8), 083011 (October 2012), 1207.4796.

[Ach12] Achitouv, I. E., *Unpublished thesis*, (2012).

[ADF10] Antonio De Felice, Shinji T., *f(R) Theories*, Living Reviews in Relativity **13**(3) (2010).

[AHK12] Abel, T. ; Hahn, O. ; Kaehler, R., *Tracing the dark matter sheet in phase space*, Monthly Notices of the RAS **427**, 61–76 (November 2012), 1111.3944.

[ARSC12] Achitouv, I. ; Rasera, Y. ; Sheth, R. K. ; Corasaniti, P. S., *Self-consistency of the Excursion Set Approach*, ArXiv e-prints (December 2012), 1212.1166.

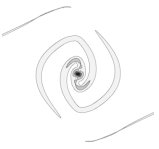

[AS01] Arriola, Enrique R. ; Soler, Juan, *A Variational Approach to the Schrödinger-Poisson System: Asymptotic Behaviour, Breathers, and Stability*, Journal of Statistical Physics **103**(5-6), 1069–1105 (2001).

[AWSH13] Angulo, Raul E. ; White, Simon D. M. ; Springel, Volker ; Henriques, Bruno, *Galaxy formation on the largest scales: The impact of astrophysics on the BAO peak*, (2013), 1311.7100.

[BAA+14] BICEP2 Collaboration ; Ade, P. A. R. ; Aikin, R. W. ; Barkats, D. ; Benton, S. J. ; Bischoff, C. A. ; Bock, J. J. ; Brevik, J. A. ; Buder, I. ; Bullock, E. ; Dowell, C. D. ; Duband, L. ; Filippini, J. P. ; Fliescher, S. ; Golwala, S. R. ; Halpern, M. ; Hasselfield, M. ; Hildebrandt, S. R. ; Hilton, G. C. ; Hristov, V. V. ; Irwin, K. D. ; Karkare, K. S. ; Kaufman, J. P. ; et al, *BICEP2 I: Detection Of B-mode Polarization at Degree Angular Scales*, ArXiv e-prints (March 2014), 1403.3985.

[Bar80] Bardeen, J. M., *Gauge-invariant cosmological perturbations*, Physical Review D **22**, 1882–1905 (October 1980).

[BBKS86] Bardeen, J. M. ; Bond, J. R. ; Kaiser, N. ; Szalay, A. S., *The statistics of peaks of Gaussian random fields*, Astrophysical Journal **304**, 15–61 (May 1986).

[BCEK91] Bond, J. R. ; Cole, S. ; Efstathiou, G. ; Kaiser, N., *Excursion set mass functions for hierarchical Gaussian fluctuations*, Astrophysical Journal **379**, 440–460 (October 1991).

[BCGS02a] Bernardeau, F. ; Colombi, S. ; Gaztañaga, E. ; Scoccimarro, R., *Large-scale structure of the Universe and cosmological perturbation theory*, Physics Reports **367**, 1–248 (September 2002), astro-ph/0112551.

[BCGS02b] Bernardeau, F. ; Colombi, S. ; Gaztañaga, E. ; Scoccimarro, R., *Large-scale structure of the Universe and cosmological perturbation theory*, Physics Reports **367**, 1–248 (September 2002), astro-ph/0112551.

[BCM94] Borgani, S. ; Coles, P. ; Moscardini, L., *Cluster correlations in the Zel'dovich approximation*, Monthly Notices of the RAS **271**, 223 (November 1994), astro-ph/9312005.

[BD05] Buchert, T. ; Domínguez, A., *Adhesive gravitational clustering*, Astronomy and Astrophysics **438**, 443–460 (August 2005), astro-ph/0502318.

[BD11] Bonvin, C. ; Durrer, R., *What galaxy surveys really measure*, Physical Review D **84**(6), 063505 (September 2011), 1105.5280.

[BDH+11] Berkhahn, F. ; Dietrich, D. ; Hofmann, S. ; Kühnel, F. ; Moyassari, P., *Island of Stability for Consistent Deformations of Einstein's Gravity*, ArXiv e-prints (June 2011), 1106.3566.

[BDS14] Baldauf, T. ; Desjacques, V. ; Seljak, U., *Velocity bias in the distribution of dark matter halos*, ArXiv e-prints (May 2014), 1405.5885.

[Ber93] Bertschinger, Edmund, *Cosmological dynamics: Course 1*, (1993), astro-ph/9503125.

[Ber12] Bertello, U., *Cosmology in the Newtonian limit*, ArXiv e-prints (March 2012), 1203.5596.

[BGK13] Blas, Diego ; Garny, Mathias ; Konstandin, Thomas, *Cosmological perturbation theory at three-loop order*, (2013), 1309.3308.

[BHMW13] Bruni, M. ; Hidalgo, J. C. ; Meures, N. ; Wands, D., *Non-Gaussian initial conditions in ΛCDM: Newtonian, relativistic and primordial contributions*, ArXiv e-prints (July 2013), 1307.1478.

[BJZ11] Borisov, A. ; Jain, B. ; Zhang, P., *Spherical Collapse in f(R) Gravity*, ArXiv e-prints (February 2011), 1102.4839.

[BM96] Bond, J. R. ; Myers, S. T., *The Peak-Patch Picture of Cosmic Catalogs. I. Algorithms*, Astrophysical Journal, Supplement **103**, 1 (March 1996).

[BM14] Baumann, D. ; McAllister, L., *Inflation and String Theory*, ArXiv e-prints (April 2014), 1404.2601.

[BMR07] Bartolo, N. ; Matarrese, S. ; Riotto, A., *CMB anisotropies at second-order II: analytical approach*, Journal of Cosmology and Astroparticle Physics **1**, 19 (January 2007), astro-ph/0610110.

[BMW94a] Buchert, T. ; Melott, A. L. ; Weiss, A. G., *Testing higher-order Lagrangian perturbation theory against numerical simulations I. Pancake models*, Astronomy and Astrophysics **288**, 349–364 (August 1994), astro-ph/9309056.

[BMW94b] Buchert, T. ; Melott, A.L. ; Weiss, A.G., *Optimized Lagrangian approximations for modeling large scale structure at nonlinear stages*, (1994), astro-ph/9412075.

[BNSZ12a] Baumann, D. ; Nicolis, A. ; Senatore, L. ; Zaldarriaga, M., *Cosmological nonlinearities as an effective fluid*, Journal of Cosmology and Astroparticle Physics **7**, 51 (July 2012), 1004.2488.

[BNSZ12b] Baumann, D. ; Nicolis, A. ; Senatore, L. ; Zaldarriaga, M., *Cosmological nonlinearities as an effective fluid*, Journal of Cosmology and Astroparticle Physics **7**, 51 (July 2012), 1004.2488.

[BNSZ12c] Baumann, Daniel ; Nicolis, Alberto ; Senatore, Leonardo ; Zaldarriaga, Matias, *Cosmological Non-Linearities as an Effective Fluid*, JCAP **1207**, 051 (2012), 1004.2488.

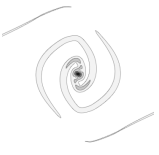

[BR11a] Brustein, R. ; Riotto, A., *Evolution Equation for Non-linear Cosmological Perturbations*, ArXiv e-prints (May 2011), 1105.4411.

[BR11b] Brustein, R. ; Riotto, A., *Evolution Equation for Non-linear Cosmological Perturbations*, JCAP **1111**, 006 (2011), 1105.4411.

[BR12] Buchert, T. ; Räsänen, S., *Backreaction in Late-Time Cosmology*, Annual Review of Nuclear and Particle Science **62**, 57–79 (November 2012), 1112.5335.

[BRS10] Brax, P. ; Rosenfeld, R. ; Steer, D. A., *Spherical collapse in chameleon models*, Journal of Cosmology and Astroparticle Physics **8**, 33 (August 2010), 1005.2051.

[BSS10] Bauer, F. ; Solà, J. ; Stefancić, H., *Dynamically avoiding fine-tuning the cosmological constant: the "Relaxed Universe"*, Journal of Cosmology and Astroparticle Physics **12**, 29 (December 2010), 1006.3944.

[BSW+09] Boylan-Kolchin, M. ; Springel, V. ; White, S. D. M. ; Jenkins, A. ; Lemson, G., *Resolving cosmic structure formation with the Millennium-II Simulation*, Monthly Notices of the RAS **398**, 1150–1164 (September 2009), 0903.3041.

[BT08] Binney, J. ; Tremaine, S., *Galactic Dynamics, chapter 4.8.3*, Princeton Series in Astrophysics, Princeton University Press, second edition, 2008.

[BTW13] Bruni, M. ; Thomas, D. B. ; Wands, D., *Computing General Relativistic effects from Newtonian N-body simulations: Frame dragging in the post-Friedmann approach*, ArXiv e-prints (June 2013), 1306.1562.

[Buc11] Buchert, T., *Toward physical cosmology: focus on inhomogeneous geometry and its non-perturbative effects*, Classical and Quantum Gravity **28**(16), 164007 (August 2011), 1103.2016.

[BvD+04] Brax, P. ; van de Bruck, C. ; Davis, A.-C. ; Khoury, J. ; Weltman, A., *Detecting dark energy in orbit: The cosmological chameleon*, Physical Review D **70**(12), 123518 (December 2004), arXiv:astro-ph/0408415.

[CA11a] Corasaniti, P. S. ; Achitouv, I., *Excursion set halo mass function and bias in a stochastic barrier model of ellipsoidal collapse*, Physical Review D **84**(2), 023009 (July 2011), 1107.1251.

[CA11b] Corasaniti, P. S. ; Achitouv, I., *Toward a Universal Formulation of the Halo Mass Function*, Physical Review Letters **106**(24), 241302 (June 2011), 1012.3468.

[Cap02] Capozziello, Salvatore, *Curvature quintessence*, Int.J.Mod.Phys. **D11**, 483–492 (2002), gr-qc/0201033.

[Car75] Cartwright, N.D., *A non-negative Wigner-type distribution*, Physica A: Statistical Mechanics and its Applications **83**(1), 210 – 212 (1975).

[Car13] Carroll, S., This over-simplistic formula for the vacuum transition amplitude was presented in the talk *Poetic Naturalism* by Sean Carroll, www.youtube.com/watch?v=xv0mKsO2goA , 2013.

[CCHO09] Cai, R.-G. ; Cao, L.-M. ; Hu, Y.-P. ; Ohta, N., *Generalized Misner-Sharp energy in f(R) gravity*, Physical Review D **80**(10), 104016 (November 2009), 0910.2387.

[CCL13] Clampitt, J. ; Cai, Y.-C. ; Li, B., *Voids in modified gravity: excursion set predictions*, Monthly Notices of the RAS **431**, 749–766 (May 2013), 1212.2216.

[CCPS11] Charmousis, C. ; Copeland, E. J. ; Padilla, A. ; Saffin, P. M., *General second order scalar-tensor theory, self tuning, and the Fab Four*, ArXiv e-prints (June 2011), 1106.2000.

[CFGS13] Carrasco, John Joseph M. ; Foreman, Simon ; Green, Daniel ; Senatore, Leonardo, *The Effective Field Theory of Large Scale Structures at Two Loops*, (2013), 1310.0464.

[CHS12] Carrasco, John Joseph M. ; Hertzberg, Mark P. ; Senatore, Leonardo, *The Effective Field Theory of Cosmological Large Scale Structures*, JHEP **1209**, 082 (2012), 1206.2926.

[CKS+12] Chatrchyan, S. ; Khachatryan, V. ; Sirunyan, A. M. ; Tumasyan, A. ; Adam, W. ; Aguilo, E. ; Bergauer, T. ; Dragicevic, M. ; Erö, J. ; Fabjan, C. ; al. et, *Observation of a new boson at a mass of 125 GeV with the CMS experiment at the LHC*, Physics Letters B **716**, 30–61 (September 2012), 1207.7235.

[CL11] Challinor, A. ; Lewis, A., *Linear power spectrum of observed source number counts*, Physical Review D **84**(4), 043516 (August 2011), 1105.5292.

[CLMP98] Catelan, P. ; Lucchin, F. ; Matarrese, S. ; Porciani, C., *The bias field of dark matter haloes*, Monthly Notices of the RAS **297**, 692–712 (July 1998), arXiv:astro-ph/9708067.

[CLP13] Carroll, S. M. ; Leichenauer, S. ; Pollack, J., *A Consistent Effective Theory of Long-Wavelength Cosmological Perturbations*, ArXiv e-prints (October 2013), 1310.2920.

[CMS93] Coles, P. ; Melott, A. L. ; Shandarin, S. F., *Testing approximations for non-linear gravitational clustering*, Monthly Notices of the RAS **260**, 765–776 (February 1993).

[CRW13] Carlson, J. ; Reid, B. ; White, M., *Convolution Lagrangian perturbation theory for biased tracers*, Monthly Notices of the RAS **429**, 1674–1685 (February 2013), 1209.0780.

[CS02] Cooray, A. ; Sheth, R., *Halo models of large scale structure*, Physics Reports **372**, 1–129 (December 2002), astro-ph/0206508.

[CS03] Coles, Peter ; Spencer, Kate, *A wave-mechanical approach to cosmic structure formation*, Mon.Not.Roy.Astron.Soc. **342**, 176 (2003), astro-ph/0212433.

[CT08] Capozziello, Salvatore ; Tsujikawa, Shinji, *Solar system and equivalence principle constraints on $f(R)$ gravity by the chameleon approach*, Phys. Rev. D **77**, 107501 (May 2008).

[CWP09] Carlson, Jordan ; White, Martin ; Padmanabhan, Nikhil, *A critical look at cosmological perturbation theory techniques*, Phys.Rev. **D80**, 043531 (2009), 0905.0479.

[CZ11] Chisari, N. E. ; Zaldarriaga, M., *Connection between Newtonian simulations and general relativity*, Physical Review D **83**(12), 123505 (June 2011), 1101.3555.

[dDH+08] de Rham, C. ; Dvali, G. ; Hofmann, S. ; Khoury, J. ; Pujolàs, O. ; Redi, M. ; Tolley, A. J., *Cascading Gravity: Extending the Dvali-Gabadadze-Porrati Model to Higher Dimension*, Physical Review Letters **100**(25), 251603 (June 2008), 0711.2072.

[DES] DES, http://www.darkenergysurvey.org/science/ .

[DFCB77] Davies, P. C. W. ; Fulling, S. A. ; Christensen, S. M. ; Bunch, T. S., *Energy-momentum tensor of a massive scalar quantum field in a Robertson-Walker universe.*, Annals of Physics **109**, 108–142 (1977).

[DG12] Dvali, G. ; Gomez, C., *Black Holes as Critical Point of Quantum Phase Transition*, ArXiv e-prints (July 2012), 1207.4059.

[DGL+14] Di Valentino, E. ; Giusarma, E. ; Lattanzi, M. ; Melchiorri, A. ; Mena, O., *Axion cold dark matter: status after Planck and BICEP2*, ArXiv e-prints (May 2014), 1405.1860.

[DHK07] Dvali, G. ; Hofmann, S. ; Khoury, J., *Degravitation of the cosmological constant and graviton width*, Physical Review D **76**(8), 084006–+ (October 2007), arXiv:hep-th/0703027.

[DM14] Dutton, A. A. ; Macciò, A. V., *Cold dark matter haloes in the Planck era: evolution of structural parameters for Einasto and NFW profiles*, ArXiv e-prints (February 2014), 1402.7073.

[dMR11a] de Simone, A. ; Maggiore, M. ; Riotto, A., *Conditional probabilities in the excursion set theory: generic barriers and non-Gaussian initial conditions*, Monthly Notices of the RAS **418**, 2403–2421 (December 2011), 1102.0046.

[dMR11b] de Simone, A. ; Maggiore, M. ; Riotto, A., *Excursion set theory for generic moving barriers and non-Gaussian initial conditions*, Monthly Notices of the RAS **412**, 2587–2602 (April 2011), 1007.1903.

[Dol85] Dolgov, A. D., *Field model with a dynamic cancellation of the cosmological constant*, ZhETF Pis ma Redaktsiiu **41**, 280–282 (March 1985).

[Dom00] Dominguez, Alvaro, *Hydrodynamic approach to the evolution of cosmological structures*, Phys.Rev. **D62**, 103501 (2000).

[DSY09] Deruelle, N. ; Sendouda, Y. ; Youssef, A., *Various Hamiltonian formulations of f(R) gravity and their canonical relationships*, Physical Review D **80**(8), 084032–+ (October 2009), 0906.4983.

[DW96] Davies, G. ; Widrow, L. M., *Test-Bed Simulations of Collisionless, Self-Gravitating Systems Using the Schr\"odinger Method*, ArXiv Astrophysics e-prints (July 1996), astro-ph/9607133.

[EB97] Ehlers, J. ; Buchert, T., *Newtonian Cosmology in Lagrangian Formulation: Foundations and Perturbation Theory*, General Relativity and Gravitation **29**, 733–764 (June 1997), arXiv:astro-ph/9609036.

[EG83] Efron, Bradley ; Gong, Gail, *A Leisurely Look at the Bootstrap, the Jackknife, and Cross-Validation*, The American Statistician **37**(1), 36–48 (February 1983).

[EHN+84] Ellis, J. ; Hagelin, J. S. ; Nanopoulos, D. V. ; Olive, K. ; Srednicki, M., *Supersymmetric relics from the big bang*, Nuclear Physics B **238**, 453–476 (June 1984).

[Ein15] Einstein, A., *Die Feldgleichungen der Gravitation*, Sitzungsberichte der Königlich Preußischen Akademie der Wissenschaften (Berlin), Seite 844-847. , 844–847 (1915).

[EK11] Emelyanov, V. ; Klinkhamer, F. R., *Vector-field model with compensated cosmological constant and radiation-dominated FRW phase*, ArXiv e-prints (August 2011), 1108.1995.

[Ell13] Ellis, J., *Summary of the Nobel symposium on Large Hadron Collider results*, Physica Scripta Volume T **158**(1), 014020 (December 2013), 1309.3549.

[EMR09] Enqvist, K. ; Mattsson, M. ; Rigopoulos, G., *Supernovae data and perturbative deviation from homogeneity*, Journal of Cosmology and Astroparticle Physics **9**, 22–+ (September 2009), 0907.4003.

[EWA+11] Eisenstein, D. J. ; Weinberg, D. H. ; Agol, E. ; Aihara, H. ; Allende Prieto, C. ; Anderson, S. F. ; Arns, J. A. ; Aubourg, É. ; Bailey, S. ; Balbinot, E. ; al. et, *SDSS-III: Massive Spectroscopic Surveys of the Distant Universe, the Milky*

Way, and Extra-Solar Planetary Systems, Astronomical Journal **142**, 72 (September 2011), 1101.1529.

[FCC+94] Fixsen, D. J. ; Cheng, E. S. ; Cottingham, D. A. ; Eplee, R. E. Jr. ; Isaacman, R. B. ; Mather, J. C. ; Meyer, S. S. ; Noerdlinger, P. D. ; Shafer, R. A. ; Weiss, R. ; Wright, E. L. ; Bennett, C. L. ; Boggess, N. W. ; Kelsall, T. ; Moseley, S. H. ; Silverberg, R. F. ; Smoot, G. F. ; Wilkinson, D. T., *Cosmic microwave background dipole spectrum measured by the COBE FIRAS instrument*, Astrophysical Journal **420**, 445–449 (January 1994).

[Fis95] Fisher, Karl B., *On the validity of the streaming model for the redshift space correlation function in the linear regime*, Astrophys.J. **448**, 494–499 (1995), astro-ph/9412081.

[Fix09] Fixsen, D. J., *The Temperature of the Cosmic Microwave Background*, Astrophysical Journal **707**, 916–920 (December 2009), 0911.1955.

[FS12] Flender, S. F. ; Schwarz, D. J., *Newtonian versus relativistic cosmology*, Physical Review D **86**(6), 063527 (September 2012), 1207.2035.

[GG72] Gunn, J. E. ; Gott, J. R. III, *On the Infall of Matter Into Clusters of Galaxies and Some Effects on Their Evolution*, Astrophysical Journal **176**, 1 (August 1972).

[GG12] Giulini, D. ; Grossardt, A., *The Schrödinger-Newton equation as a non-relativistic limit of self-gravitating Klein-Gordon and Dirac fields*, Classical and Quantum Gravity **29**(21), 215010 (November 2012), 1206.4250.

[GGRW86] Goroff, M. H. ; Grinstein, B. ; Rey, S.-J. ; Wise, M. B., *Coupling of modes of cosmological mass density fluctuations*, Astrophysical Journal **311**, 6–14 (December 1986).

[Gil68] Gilbert, I. H., *Collisional Relaxation in Stellar Systems*, Astrophysical Journal **152**, 1043 (June 1968).

[GKP10] Gasenzer, T. ; Kessler, S. ; Pawlowski, J. M., *Far-from-equilibrium quantum many-body dynamics*, European Physical Journal C **70**, 423–443 (November 2010), 1003.4163.

[GSS89] Gurbatov, S. N. ; Saichev, A. I. ; Shandarin, S. F., *The large-scale structure of the universe in the frame of the model equation of non-linear diffusion*, Monthly Notices of the RAS **236**, 385–402 (January 1989).

[Gue95] Guenther, R. L., *A Numerical Study of the Time Dependent Schroedinger Equation Coupled with Newtonian Gravity*, PhD thesis, THE UNIVERSITY OF TEXAS AT AUSTIN., 1995.

[Gun67] Gunn, J. E., *A Fundamental Limitation on the Accuracy of Angular Measurements in Observational Cosmology*, Astrophysical Journal **147**, 61 (January 1967).

[GW11] Green, S. R. ; Wald, R. M., *New framework for analyzing the effects of small scale inhomogeneities in cosmology*, Physical Review D **83**(8), 084020 (April 2011), 1011.4920.

[GW12] Green, S. R. ; Wald, R. M., *Newtonian and relativistic cosmologies*, Physical Review D **85**(6), 063512 (March 2012), 1111.2997.

[HAA14] Hahn, Oliver ; Angulo, Raul E. ; Abel, Tom, *The Properties of Cosmic Velocity Fields*, (2014), 1404.2280.

[HAK13] Hahn, O. ; Abel, T. ; Kaehler, R., *A new approach to simulating collisionless dark matter fluids*, Monthly Notices of the RAS **434**, 1171–1191 (September 2013), 1210.6652.

[He12] He, P., *Equilibrium statistical mechanics for self-gravitating systems: local ergodicity and extended Boltzmann-Gibbs/White-Narayan statistics*, Monthly Notices of the RAS **419**, 1667–1681 (January 2012), 1103.5730.

[HGH+13] Heymans, C. ; Grocutt, E. ; Heavens, A. ; Kilbinger, M. ; Kitching, T. D. ; Simpson, F. ; Benjamin, J. ; Erben, T. ; Hildebrandt, H. ; Hoekstra, H. ; Mellier, Y. ; Miller, L. ; Van Waerbeke, L. ; Brown, M. L. ; Coupon, J. ; Fu, L. ; Harnois-Déraps, J. ; Hudson, M. J. ; Kuijken, K. ; Rowe, B. ; Schrabback, T. ; Semboloni, E. ; Vafaei, S. ; Velander, M., *CFHTLenS tomographic weak lensing cosmological parameter constraints: Mitigating the impact of intrinsic galaxy alignments*, Monthly Notices of the RAS **432**, 2433–2453 (July 2013), 1303.1808.

[HHK12] Haugg, T. ; Hofmann, S. ; Kopp, M., *Newtonian N-body simulations are compatible with cosmological perturbation theory*, ArXiv e-prints (October 2012), 1211.0011.

[HHWS09] Hilbert, S. ; Hartlap, J. ; White, S. D. M. ; Schneider, P., *Ray-tracing through the Millennium Simulation: Born corrections and lens-lens coupling in cosmic shear and galaxy-galaxy lensing*, Astronomy and Astrophysics **499**, 31–43 (May 2009), 0809.5035.

[HK11] He, P. ; Kang, D.-B., *Saddle-point entropy states of equilibrated self-gravitating systems*, Monthly Notices of the RAS **414**, L21–L25 (June 2011), 1103.6121.

[Hor74] Horndeski, G. W., *Second-Order Scalar-Tensor Field Equations in a Four-Dimensional Space*, International Journal of Theoretical Physics **10**, 363–384 (September 1974).

[HS07] Hu, W. ; Sawicki, I., *Models of f(R) cosmic acceleration that evade solar system tests*, Physical Review D **76**(6), 064004–+ (September 2007), 0705.1158.

[Hu95] Hu, W., *Wandering in the Background: A CMB Explorer*, ArXiv Astrophysics e-prints (August 1995), astro-ph/9508126.

[Hus40] Husimi, Kôdi, *Some Formal Properties of the Density Matrix*, Nippon Sugaku-Buturigakkwai Kizi Dai 3 Ki **22**(4), 264–314 (1940).

[HW98] Holz, D. E. ; Wald, R. M., *New method for determining cumulative gravitational lensing effects in inhomogeneous universes*, Physical Review D **58**(6), 063501 (September 1998), arXiv:astro-ph/9708036.

[HWHS07] Hilbert, S. ; White, S. D. M. ; Hartlap, J. ; Schneider, P., *Strong lensing optical depths in a ΛCDM universe*, Monthly Notices of the RAS **382**, 121–132 (November 2007), arXiv:astro-ph/0703803.

[IW06] Ishibashi, A. ; Wald, R. M., *Can the acceleration of our universe be explained by the effects of inhomogeneities?*, Classical and Quantum Gravity **23**, 235–250 (January 2006), arXiv:gr-qc/0509108.

[Jac70] Jackson, J. C., *The dynamics of clusters of galaxies in universes NN-ith non-zero cosmological constant, and the virial theorem mass discrepancy*, Monthly Notices of the RAS **148**, 249–+ (1970).

[JB94] Jain, B. ; Bertschinger, E., *Second-order power spectrum and nonlinear evolution at high redshift*, Astrophysical Journal **431**, 495–505 (August 1994), arXiv:astro-ph/9311070.

[JB03] Jaynes, E.T. ; Bretthorst, G.L., *Probability Theory: The Logic of Science*, Cambridge University Press, 2003.

[JFW+01] Jenkins, A. ; Frenk, C. S. ; White, S. D. M. ; Colberg, J. M. ; Cole, S. ; Evrard, A. E. ; Couchman, H. M. P. ; Yoshida, N., *The mass function of dark matter haloes*, Monthly Notices of the RAS **321**, 372–384 (February 2001), arXiv:astro-ph/0005260.

[JLH09] Johnston, R. ; Lasenby, A. N. ; Hobson, M. P., *Cosmological fluid dynamics in the Schrödinger formalism*, ArXiv e-prints (April 2009), 0904.0611.

[JSW+07] Johnston, D. E. ; Sheldon, E. S. ; Wechsler, R. H. ; Rozo, E. ; Koester, B. P. ; Frieman, J. A. ; McKay, T. A. ; Evrard, A. E. ; Becker, M. R. ; Annis, J., *Cross-correlation Weak Lensing of SDSS galaxy Clusters II: Cluster Density Profiles and the Mass–Richness Relation*, ArXiv e-prints (September 2007), 0709.1159.

[JVS12] Jain, B. ; Vikram, V. ; Sakstein, J., *Astrophysical Tests of Modified Gravity: Constraints from Distance Indicators in the Nearby Universe*, ArXiv e-prints (April 2012), 1204.6044.

[KAAW13] Kopp, M. ; Appleby, S. A. ; Achitouv, I. ; Weller, J., *Spherical collapse and halo mass function in f(R) theories*, Physical Review D **88**(8), 084015 (October 2013), 1306.3233.

[Kad66] Kadanoff, L. P., *Scaling laws for ising models near T_c*, Physics **2**, 263 (1966).

[Kai87] Kaiser, N., *Clustering in real space and in redshift space*, Monthly Notices of the RAS **227**, 1–21 (July 1987).

[KBC+09] Kessler, R. ; Becker, A. C. ; Cinabro, D. ; Vanderplas, J. ; Frieman, J. A. ; Marriner, J. ; Davis, T. M. ; Dilday, B. ; Holtzman, J. ; Jha, S. W. ; Lampeitl, H. ; Sako, M. ; Smith, M. ; Zheng, C. ; Nichol, R. C. ; Bassett, B. ; Bender, R. ; Depoy, D. L. ; Doi, M. ; Elson, E. ; Filippenko, A. V. ; Foley, R. J. ; Garnavich, P. M. ; Hopp, U. ; Ihara, Y. ; Ketzeback, W. ; Kollatschny, W. ; et al, *First-Year Sloan Digital Sky Survey-II Supernova Results: Hubble Diagram and Cosmological Parameters*, Astrophysical Journal, Supplement **185**, 32–84 (November 2009), 0908.4274.

[Kli69] Klimontovich, Y. L., *REVIEW : The Statistical Theory of Non-Equilibrium Processes in a Plasma*, Journal of Plasma Physics **3**, 148 (February 1969).

[KPGD09] Kim, J. ; Park, C. ; Gott, J. R. III ; Dubinski, J., *The Horizon Run N-Body Simulation: Baryon Acoustic Oscillations and Topology of Large-scale Structure of the Universe*, Astrophysical Journal **701**, 1547–1559 (August 2009), 0812.1392.

[KPR+11] Kim, J. ; Park, C. ; Rossi, G. ; Lee, S. M. ; Gott, J. R. III, *The New Horizon Run Cosmological N-Body Simulations*, Journal of Korean Astronomical Society **44**, 217–234 (December 2011), 1112.1754.

[KS83] Klypin, A. A. ; Shandarin, S. F., *Three-dimensional numerical model of the formation of large-scale structure in the Universe*, Monthly Notices of the RAS **204**, 891–907 (September 1983).

[KS84] Kodama, H. ; Sasaki, M., *Cosmological Perturbation Theory*, Progress of Theoretical Physics Supplement **78**, 1 (1984).

[KS87] Kasai, M. ; Sasaki, M., *Number count-redshift relation in a perturbed Friedmann universe*, Modern Physics Letters A **2**, 727 (June 1987).

[KSD+11] Komatsu, E. ; Smith, K. M. ; Dunkley, J. ; Bennett, C. L. ; Gold, B. ; Hinshaw, G. ; Jarosik, N. ; Larson, D. ; Nolta, M. R. ; Page, L. ; Spergel, D. N. ; Halpern, M. ; Hill, R. S. ; Kogut, A. ; Limon, M. ; Meyer, S. S. ; Odegard, N. ; Tucker, G. S. ; Weiland, J. L. ; Wollack, E. ; Wright, E. L., *Seven-year Wilkinson Microwave Anisotropy Probe (WMAP) Observations: Cosmological Interpretation*, Astrophysical Journal, Supplement **192**, 18 (February 2011), 1001.4538.

[KUH14] Kopp, M. ; Uhlemann, C. ; Haugg, T., *Newton to Einstein - dust to dust*, Journal of Cosmology and Astroparticle Physics **3**, 18 (March 2014), 1312.3638.

[KW04a] Khoury, J. ; Weltman, A., *Chameleon cosmology*, Physical Review D **69**(4), 044026–+ (February 2004), arXiv:astro-ph/0309411.

[KW04b] Khoury, J. ; Weltman, A., *Chameleon Fields: Awaiting Surprises for Tests of Gravity in Space*, Physical Review Letters **93**(17), 171104–+ (October 2004), arXiv:astro-ph/0309300.

[LAA+11] Laureijs, R. ; Amiaux, J. ; Arduini, S. ; Augueres, J. .. ; Brinchmann, J. ; Cole, R. ; Cropper, M. ; Dabin, C. ; Duvet, L. ; Ealet, A. ; al. et, *Euclid Definition Study Report*, ArXiv e-prints (October 2011), 1110.3193.

[LCL00] Lewis, A. ; Challinor, A. ; Lasenby, A., *Efficient Computation of Cosmic Microwave Background Anisotropies in Closed Friedmann-Robertson-Walker Models*, Astrophysical Journal **538**, 473–476 (August 2000), arXiv:astro-ph/9911177.

[LE11] Li, B. ; Efstathiou, G., *An Extended Excursion Set Approach to Structure Formation in Chameleon Models*, ArXiv e-prints (October 2011), 1110.6440.

[LH11] Li, Y. ; Hu, W., *Chameleon halo modeling in f(R) gravity*, Physical Review D **84**(8), 084033 (October 2011), 1107.5120.

[Lie77] Lieb, E. H., *Existence and uniqueness of the minimizing solution of Choquard's nonlinear equation*, Studies in Applied Mathematics **57**, 93–105 (October 1977).

[LL12a] Lam, T. Y. ; Li, B., *Excursion set theory for modified gravity: correlated steps, mass functions and halo bias*, Monthly Notices of the RAS **426**, 3260–3270 (November 2012), 1205.0059.

[LL12b] Li, B. ; Lam, T. Y., *Excursion set theory for modified gravity: Eulerian versus Lagrangian environments*, Monthly Notices of the RAS **425**, 730–739 (September 2012), 1205.0058.

[LLKZ13] Lombriser, L. ; Li, B. ; Koyama, K. ; Zhao, G.-B., *Modeling halo mass functions in chameleon f(R) gravity*, ArXiv e-prints (April 2013), 1304.6395.

[LW68] Lynden-Bell, D. ; Wood, R., *The gravo-thermal catastrophe in isothermal spheres and the onset of red-giant structure for stellar systems*, Monthly Notices of the RAS **138**, 495 (1968).

[Lyn67] Lynden-Bell, D., *Statistical mechanics of violent relaxation in stellar systems*, Monthly Notices of the RAS **136**, 101 (1967).

[LZK11] Li, B. ; Zhao, G.-B. ; Koyama, K., *Halos and Voids in f(R) Gravity*, ArXiv e-prints (November 2011), 1111.2602.

[Mad27] Madelung, E., *Quantentheorie in hydrodynamischer Form*, Zeitschrift fur Physik **40**, 322–326 (March 1927).

[Mar12] Martin, J., *Everything you always wanted to know about the cosmological constant problem (but were afraid to ask)*, Comptes Rendus Physique **13**, 566–665 (July 2012), 1205.3365.

[Mat00a] Matsubara, T., *The Correlation Function in Redshift Space: General Formula with Wide-Angle Effects and Cosmological Distortions*, Astrophysical Journal **535**, 1–23 (May 2000), arXiv:astro-ph/9908056.

[Mat00b] Matsubara, T., *The Gravitational Lensing in Redshift-Space Correlation Functions of Galaxies and Quasars*, Astrophysical Journal, Letters **537**, L77–L80 (July 2000), arXiv:astro-ph/0004392.

[Mat08] Matsubara, Takahiko, *Nonlinear perturbation theory with halo bias and redshift-space distortions via the Lagrangian picture*, Phys.Rev. **D78**, 083519 (2008), 0807.1733.

[Mat12] Matsubara, T., *Deriving an accurate formula of scale-dependent bias with primordial non-Gaussianity: An application of the integrated perturbation theory*, Physical Review D **86**(6), 063518 (September 2012), 1206.0562.

[MB95] Ma, C.-P. ; Bertschinger, E., *Cosmological Perturbation Theory in the Synchronous and Conformal Newtonian Gauges*, Astrophysical Journal **455**, 7 (December 1995), arXiv:astro-ph/9506072.

[McD11] McDonald, P., *How to generate a significant effective temperature for cold dark matter, from first principles*, Journal of Cosmology and Astroparticle Physics **4**, 32 (April 2011), 0910.1002.

[MCV+11] Marulli, F. ; Carbone, C. ; Viel, M. ; Moscardini, L. ; Cimatti, A., *Effects of massive neutrinos on the large-scale structure of the Universe*, Monthly Notices of the RAS **418**, 346–356 (November 2011), 1103.0278.

[MF00] Ma, C.-P. ; Fry, J. N., *Deriving the Nonlinear Cosmological Power Spectrum and Bispectrum from Analytic Dark Matter Halo Profiles and Mass Functions*, Astrophysical Journal **543**, 503–513 (November 2000), astro-ph/0003343.

[MFB92] Mukhanov, V. F. ; Feldman, H. A. ; Brandenberger, R. H., *Theory of cosmological perturbations*, Physics Reports **215**, 203–333 (June 1992).

[MGW+13] Mana, A. ; Giannantonio, T. ; Weller, J. ; Hoyle, B. ; Hütsi, G. ; Sartoris, B., *Combining clustering and abundances of galaxy clusters to test cosmology and primordial non-Gaussianity*, Monthly Notices of the RAS **434**, 684–695 (September 2013), 1303.0287.

[MHP93] Mann, R. G. ; Heavens, A. F. ; Peacock, J. A., *The Richness Dependence of Cluster Correlations*, Monthly Notices of the RAS **263**, 798 (August 1993).

[MMM+11] Martinelli, M. ; Melchiorri, A. ; Mena, O. ; Salvatelli, V. ; Girones, Z., *Future constraints on the Hu-Sawicki modified gravity scenario*, ArXiv e-prints (September 2011), 1109.4736.

[MP07] Matarrese, Sabino ; Pietroni, Massimo, *Resumming Cosmic Perturbations*, JCAP **0706**, 026 (2007), astro-ph/0703563.

[MP13] Mercolli, Lorenzo ; Pajer, Enrico, *On the Velocity in the Effective Field Theory of Large Scale Structures*, (2013), 1307.3220.

[MPS94] Melott, A. L. ; Pellman, T. F. ; Shandarin, S. F., *Optimizing the Zeldovich Approximation*, Monthly Notices of the RAS **269**, 626 (August 1994), astro-ph/9312044.

[MPT98] Moroz, I. M. ; Penrose, R. ; Tod, P., *Spherically-symmetric solutions of the Schrödinger-Newton equations*, Classical and Quantum Gravity **15**, 2733–2742 (September 1998).

[MR10a] Maggiore, M. ; Riotto, A., *The Halo Mass Function from Excursion Set Theory. I. Gaussian Fluctuations with Non-Markovian Dependence on the Smoothing Scale*, Astrophysical Journal **711**, 907–927 (March 2010), 0903.1249.

[MR10b] Maggiore, M. ; Riotto, A., *The Halo mass function from Excursion Set Theory. II. The Diffusing Barrier*, Astrophysical Journal **717**, 515–525 (July 2010), 0903.1250.

[MSS92] Makino, N. ; Sasaki, M. ; Suto, Y., *Analytic approach to the perturbative expansion of nonlinear gravitational fluctuations in cosmological density and velocity fields*, Phys.Rev. **D46**, 585–602 (1992).

[MTW73] Misner, C. W. ; Thorne, K. S. ; Wheeler, J. A., *Gravitation*, San Francisco: W.H. Freeman and Co., 1973.

[Muk05] Mukhanov, V., *Physical Foundations of Cosmology*, November 2005.

[MW96] Mo, H. J. ; White, S. D. M., *An analytic model for the spatial clustering of dark matter haloes*, Monthly Notices of the RAS **282**, 347–361 (September 1996), astro-ph/9512127.

[MW03] Morawetz, Klaus ; Walke, Rainer, *Consequences of coarse-grained Vlasov equations*, Physica A: Statistical Mechanics and its Applications **330**(3-4), 469 – 495 (2003).

[NFW97] Navarro, J. F. ; Frenk, C. S. ; White, S. D. M., *A Universal Density Profile from Hierarchical Clustering*, Astrophysical Journal **490**, 493 (December 1997), astro-ph/9611107.

[NH12] Noh, H. ; Hwang, J.-c., *Cosmological Post-Newtonian Approximation Compared with Perturbation Theory*, Astrophysical Journal **757**, 145 (October 2012), 1206.5034.

[NS97] Nakamura, T. T. ; Suto, Y., *Strong Gravitational Lensing and Velocity Function as Tools to Probe Cosmological Parameters — Current Constraints and Future Predictions —*, Progress of Theoretical Physics **97**, 49 (January 1997), arXiv:astro-ph/9612074.

[O'H72] O'Hanlon, J., *Intermediate-Range Gravity: A Generally Covariant Model*, Physical Review Letters **29**, 137–138 (July 1972).

[OLH08] Oyaizu, H. ; Lima, M. ; Hu, W., *Nonlinear evolution of f(R) cosmologies. II. Power spectrum*, Physical Review D **78**(12), 123524 (December 2008), 0807.2462.

[OS11] Olmo, G. J. ; Sanchis-Alepuz, H., *Hamiltonian formulation of Palatini f(R) theories à la Brans-Dicke theory*, Physical Review D **83**(10), 104036 (May 2011), 1101.3403.

[PAA+13] Planck Collaboration ; Ade, P. A. R. ; Aghanim, N. ; Armitage-Caplan, C. ; Arnaud, M. ; Ashdown, M. ; Atrio-Barandela, F. ; Aumont, J. ; Baccigalupi, C. ; Banday, A. J. ; al. et, *Planck 2013 results. XVI. Cosmological parameters*, ArXiv e-prints (March 2013), 1303.5076.

[PAG+99] Perlmutter, S. ; Aldering, G. ; Goldhaber, G. ; Knop, R. A. ; Nugent, P. ; Castro, P. G. ; Deustua, S. ; Fabbro, S. ; Goobar, A. ; Groom, D. E. ; Hook, I. M. ; Kim, A. G. ; Kim, M. Y. ; Lee, J. C. ; Nunes, N. J. ; Pain, R. ; Pennypacker, C. R. ; Quimby, R. ; Lidman, C. ; Ellis, R. S. ; Irwin, M. ; McMahon, R. G. ; Ruiz-Lapuente, P. ; Walton, N. ; Schaefer, B. ; Boyle, B. J. ; Filippenko, A. V. ; Matheson, T. ; Fruchter, A. S. ; Panagia, N. ; Newberg, H. J. M. ; Couch, W. J. ; The Supernova Cosmology Project, *Measurements of Omega and Lambda from 42 High-Redshift Supernovae*, Astrophysical Journal **517**, 565–586 (June 1999), arXiv:astro-ph/9812133.

[PBS13] Puchwein, E. ; Baldi, M. ; Springel, V., *Modified Gravity-GADGET: A new code for cosmological hydrodynamical simulations of modified gravity models*, ArXiv e-prints (May 2013), 1305.2418.

[Pee67] Peebles, P. J. E., *The Gravitational Instability of the Universe*, Astrophysical Journal **147**, 859 (March 1967).

[Pee80] Peebles, P. J. E., *The large-scale structure of the universe*, 1980.

[PMLC98] Porciani, C. ; Matarrese, S. ; Lucchin, F. ; Catelan, P., *Excursion set approach to the clustering of dark matter haloes in Lagrangian space*, Monthly Notices of the RAS **298**, 1097–1112 (August 1998), astro-ph/9801290.

[PMSV12a] Pietroni, M. ; Mangano, G. ; Saviano, N. ; Viel, M., *Coarse-grained cosmological perturbation theory*, Journal of Cosmology and Astroparticle Physics **1**, 19 (January 2012), 1108.5203.

[PMSV12b] Pietroni, Massimo ; Mangano, Gianpiero ; Saviano, Ninetta ; Viel, Matteo, *Coarse-Grained Cosmological Perturbation Theory*, JCAP **1201**, 019 (2012), 1108.5203.

[Por97] Porciani, C., *Evolution of the two-point correlation function in the Zel'dovich approximation*, Monthly Notices of the RAS **290**, 639–650 (October 1997), arXiv:astro-ph/9609029.

[PQ77] Peccei, R. D. ; Quinn, H. R., *CP conservation in the presence of pseudoparticles*, Physical Review Letters **38**, 1440–1443 (June 1977).

[PS] Pan-STARRS, http://pan-starrs.ifa.hawaii.edu/public/ .

[PS74] Press, W. H. ; Schechter, P., *Formation of Galaxies and Clusters of Galaxies by Self-Similar Gravitational Condensation*, Astrophysical Journal **187**, 425–438 (February 1974).

[PS09] Pueblas, Sebastian ; Scoccimarro, Roman, *Generation of Vorticity and Velocity Dispersion by Orbit Crossing*, Phys.Rev. **D80**, 043504 (2009), 0809.4606.

[PSZ13] Porto, R. A. ; Senatore, L. ; Zaldarriaga, M., *The Lagrangian-space Effective Field Theory of Large Scale Structures*, ArXiv e-prints (November 2013), 1311.2168.

[PW65] Penzias, A. A. ; Wilson, R. W., *A Measurement of Excess Antenna Temperature at 4080 Mc/s.*, Astrophysical Journal **142**, 419–421 (July 1965).

[Ram13] Rampf, C., *Frame dragging and Eulerian frames in General Relativity*, ArXiv e-prints (July 2013), 1307.1725.

[Ras11] Rasanen, S., *Light propagation and the average expansion rate in near-FRW universes*, ArXiv e-prints (July 2011), 1107.1176.

[RB12] Rampf, C. ; Buchert, T., *Lagrangian perturbations and the matter bispectrum I: fourth-order model for non-linear clustering*, Journal of Cosmology and Astroparticle Physics **6**, 21 (June 2012), 1203.4260.

[Red01] Redner, S., *A Guide to First-Passage Processes*, October 2001.

[RFC+98] Riess, A. G. ; Filippenko, A. V. ; Challis, P. ; Clocchiatti, A. ; Diercks, A. ; Garnavich, P. M. ; Gilliland, R. L. ; Hogan, C. J. ; Jha, S. ; Kirshner, R. P. ; Leibundgut, B. ; Phillips, M. M. ; Reiss, D. ; Schmidt, B. P. ; Schommer, R. A. ;

Smith, R. C. ; Spyromilio, J. ; Stubbs, C. ; Suntzeff, N. B. ; Tonry, J., *Observational Evidence from Supernovae for an Accelerating Universe and a Cosmological Constant*, Astronomical Journal **116**, 1009–1038 (September 1998), arXiv:astro-ph/9805201.

[RMKB96] Russ, H. ; Morita, M. ; Kasai, M. ; Börner, G., *Zel'dovich-type approximation for an inhomogeneous universe in general relativity: Second-order solutions*, Physical Review D **53**, 6881–6888 (June 1996), astro-ph/9512071.

[RR13] Rampf, C. ; Rigopoulos, G., *Initial conditions for cold dark matter particles and general relativity*, Physical Review D **87**(12), 123525 (June 2013), 1305.0010.

[RSW+12] Reid, B. A. ; Samushia, L. ; White, M. ; Percival, W. J. ; Manera, M. ; Padmanabhan, N. ; Ross, A. J. ; Sánchez, A. G. ; Bailey, S. ; Bizyaev, D. ; Bolton, A. S. ; Brewington, H. ; Brinkmann, J. ; Brownstein, J. R. ; Cuesta, A. J. ; Eisenstein, D. J. ; Gunn, J. E. ; Honscheid, K. ; et al, *The clustering of galaxies in the SDSS-III Baryon Oscillation Spectroscopic Survey: measurements of the growth of structure and expansion rate at z = 0.57 from anisotropic clustering*, Monthly Notices of the RAS **426**, 2719–2737 (November 2012), 1203.6641.

[RW11] Reid, Beth A. ; White, Martin, *Towards an accurate model of the redshift space clustering of halos in the quasilinear regime*, Mon.Not.Roy.Astron.Soc. **417**, 1913–1927 (2011), 1105.4165.

[SBR+13] Schaller, M. ; Becker, C. ; Ruchayskiy, O. ; Boyarsky, A. ; Shaposhnikov, M., *A new framework for numerical simulations of structure formation*, ArXiv e-prints (October 2013), 1310.5102.

[SC06] Short, C. J. ; Coles, P., *Gravitational instability via the Schrödinger equation*, Journal of Cosmology and Astroparticle Physics **12**, 12 (December 2006), astro-ph/0605012.

[Sco00] Scoccimarro, Roman, *A new angle on gravitational clustering*, (2000), astro-ph/0008277.

[Sco04] Scoccimarro, R., *Redshift-space distortions, pairwise velocities, and nonlinearities*, Physical Review D **70**(8), 083007 (October 2004), astro-ph/0407214.

[Sex66] Sexl, R. U., *Monopole gravitational radiation*, Physics Letters **20**, 376–378 (March 1966).

[SFW06] Springel, V. ; Frenk, C. S. ; White, S. D. M., *The large-scale structure of the Universe*, Nature **440**, 1137–1144 (April 2006), astro-ph/0604561.

[SH92] Spergel, D. N. ; Hernquist, L., *Statistical mechanics of violent relaxation*, Astrophysical Journal, Letters **397**, L75–L78 (October 1992).

[SH11] Saltas, I. D. ; Hindmarsh, M., *The dynamical equivalence of modified gravity revisited*, Classical and Quantum Gravity **28**(3), 035002–+ (February 2011), 1002.1710.

[SJD13] Schmidt, F. ; Jeong, D. ; Desjacques, V., *Peak-background split, renormalization, and galaxy clustering*, Physical Review D **88**(2), 023515 (July 2013), 1212.0868.

[SK03] Szapudi, I. ; Kaiser, N., *Cosmological Perturbation Theory Using the Schrödinger Equation*, Astrophysical Journal, Letters **583**, L1–L4 (January 2003), astro-ph/0211065.

[SLOH09] Schmidt, F. ; Lima, M. ; Oyaizu, H. ; Hu, W., *Nonlinear evolution of f(R) cosmologies. III. Halo statistics*, Physical Review D **79**(8), 083518 (April 2009), 0812.0545.

[SM11] Seljak, U. ; McDonald, P., *Distribution function approach to redshift space distortions*, Journal of Cosmology and Astroparticle Physics **11**, 39 (November 2011), 1109.1888.

[SM14] Smith, R. E. ; Marian, L., *Toward optimal cluster power spectrum analysis*, ArXiv e-prints (June 2014), 1406.1800.

[SMT01] Sheth, R. K. ; Mo, H. J. ; Tormen, G., *Ellipsoidal collapse and an improved model for the number and spatial distribution of dark matter haloes*, Monthly Notices of the RAS **323**, 1–12 (May 2001), arXiv:astro-ph/9907024.

[Spi80] Spiegel, E. A., *Fluid dynamical form of the linear and nonlinear Schrödinger equations*, Physica D Nonlinear Phenomena **1**, 236–240 (June 1980).

[Sre07] Srednicki, M., *Quantum Field Theory*, January 2007.

[SRV89] Skodje, Rex T. ; Rohrs, Henry W. ; VanBuskirk, James, *Flux analysis, the correspondence principle, and the structure of quantum phase space*, Phys. Rev. A **40**, 2894–2916 (Sep 1989).

[SS91] Suto, Yasushi ; Sasaki, Misao, *Quasinonlinear theory of cosmological self-gravitating systems*, Phys. Rev. Lett. **66**, 264–267 (Jan 1991).

[ST99] Sheth, R. K. ; Tormen, G., *Large-scale bias and the peak background split*, Monthly Notices of the RAS **308**, 119–126 (September 1999), arXiv:astro-ph/9901122.

[ST02] Sheth, R. K. ; Tormen, G., *An excursion set model of hierarchical clustering: ellipsoidal collapse and the moving barrier*, Monthly Notices of the RAS **329**, 61–75 (January 2002), arXiv:astro-ph/0105113.

[Sta80] Starobinsky, A. A., *A new type of isotropic cosmological models without singularity*, Physics Letters B **91**, 99–102 (March 1980).

[Sta07] Starobinsky, A. A., *Disappearing cosmological constant in f(R) gravity*, Soviet Journal of Experimental and Theoretical Physics Letters **86**, 157–163 (October 2007), 0706.2041.

[SWJ+05] Springel, V. ; White, S. D. M. ; Jenkins, A. ; Frenk, C. S. ; Yoshida, N. ; Gao, L. ; Navarro, J. ; Thacker, R. ; Croton, D. ; Helly, J. ; Peacock, J. A. ; Cole, S. ; Thomas, P. ; Couchman, H. ; Evrard, A. ; Colberg, J. ; Pearce, F., *Simulations of the formation, evolution and clustering of galaxies and quasars*, Nature **435**, 629–636 (June 2005), astro-ph/0504097.

[SZ89] Shandarin, S. F. ; Zeldovich, Ya. B., *The large-scale structure of the universe: Turbulence, intermittency, structures in a self-gravitating medium*, Rev. Mod. Phys. **61**, 185–220 (Apr 1989).

[SZ14] Senatore, Leonardo ; Zaldarriaga, Matias, *The IR-resummed Effective Field Theory of Large Scale Structures*, (2014), 1404.5954.

[Tak89] Takahashi, K., *Distribution Functions in Classical and Quantum Mechanics*, Progress of Theoretical Physics Supplement **98**, 109–156 (1989).

[Tas11] Tassev, S. V., *The Helmholtz Hierarchy: phase space statistics of cold dark matter*, Journal of Cosmology and Astroparticle Physics **10**, 22 (October 2011), 1012.0282.

[Tas14] Tassev, S., *Lagrangian or Eulerian; real or Fourier? Not all approaches to large-scale structure are created equal*, Journal of Cosmology and Astroparticle Physics **6**, 8 (June 2014), 1311.4884.

[TB07] Takada, M. ; Bridle, S., *Probing dark energy with cluster counts and cosmic shear power spectra: including the full covariance*, New Journal of Physics **9**, 446 (December 2007), 0705.0163.

[TBW14] Thomas, D. B. ; Bruni, M. ; Wands, D., *Relativistic weak lensing from a fully non-linear cosmological density field*, ArXiv e-prints (March 2014), 1403.4947.

[Tey02] Teyssier, R., *Cosmological hydrodynamics with adaptive mesh refinement. A new high resolution code called RAMSES*, Astronomy and Astrophysics **385**, 337–364 (April 2002), astro-ph/0111367.

[TGK96] Tsuchiya, T. ; Gouda, N. ; Konishi, T., *Relaxation processes in one-dimensional self-gravitating many-body systems*, Physical Review E **53**, 2210–2216 (March 1996), astro-ph/9506018.

[Tho11] Thomson, E.A., *Schrödinger Wave-mechanics and Large Scale Structure*, University of Glasgow, 2011.

[TSM+14] Tempel, E. ; Stoica, R. S. ; Martínez, V. J. ; Liivamägi, L. J. ; Castellan, G. ; Saar, E., *Detecting filamentary pattern in the cosmic web: a catalogue of filaments for the SDSS*, Monthly Notices of the RAS **438**, 3465–3482 (March 2014), 1308.2533.

[TvJ11] Tigrak, E. ; van de Weygaert, R. ; Jones, B. J. T., *Filamentary structures of the cosmic web and the nonlinear Schrödinger type equation*, Journal of Physics Conference Series **283**(1), 012039 (February 2011).

[UHK12] Upadhye, A. ; Hu, W. ; Khoury, J., *Quantum Stability of Chameleon Field Theories*, Physical Review Letters **109**(4), 041301 (July 2012), 1204.3906.

[UKH14] Uhlemann, C. ; Kopp, M. ; Haugg, T., *Schrödinger method as N-body double and UV completion of dust*, Physical Review D **90**(12), 023517 (July 2014), 1403.5567.

[Van08] Van Acoleyen, K., *Lemaître-Tolman-Bondi solutions in the Newtonian gauge: from strong to weak fields*, Journal of Cosmology and Astroparticle Physics **10**, 28–+ (October 2008), 0808.3554.

[VSOD13] Vlah, Z. ; Seljak, U. ; Okumura, T. ; Desjacques, V., *Distribution function approach to redshift space distortions. Part V: perturbation theory applied to dark matter halos*, Journal of Cosmology and Astroparticle Physics **10**, 53 (October 2013), 1308.6294.

[WCO98] Wambsganss, J. ; Cen, R. ; Ostriker, J. P., *Testing Cosmological Models by Gravitational Lensing. I. Method and First Applications*, Astrophysical Journal **494**, 29 (February 1998).

[Wei89] Weinberg, S., *The cosmological constant problem*, Reviews of Modern Physics **61**, 1–23 (January 1989).

[Wei08] Weinberg, S., *Cosmology*, Oxford University Press, 2008.

[WG90] Weinberg, D. H. ; Gunn, J. E., *Largescale Structure and the Adhesion Approximation*, Monthly Notices of the RAS **247**, 260 (November 1990).

[WGB96] Weiss, Arno G. ; Gottlober, Stefan ; Buchert, Thomas, *Optimizing higher order Lagrangian perturbation theory for standard CDM and BSI models*, Mon.Not.Roy.Astron.Soc. **278**, 953 (1996), astro-ph/9505113.

[Whi99] White, M., editor, *Anisotropies in the CMB*, 1999.

[Whi14] White, Martin, *The Zeldovich approximation*, (2014), 1401.5466.

[Wid97] Widrow, L. M., *Modeling collisionless matter in general relativity: A new numerical technique*, Physical Review D **55**, 5997–6001 (May 1997), astro-ph/9607124.

[Wig32] Wigner, E., *On the Quantum Correction For Thermodynamic Equilibrium*, Phys. Rev. **40**, 749–759 (Jun 1932).

[Wil06] Will, Clifford M., *The Confrontation between General Relativity and Experiment*, Living Reviews in Relativity **9**(3) (2006).

[WK93] Widrow, L. M. ; Kaiser, N., *Using the Schroedinger Equation to Simulate Collisionless Matter*, Astrophysical Journal, Letters **416**, L71 (October 1993).

[WRW14] Wang, L. ; Reid, B. ; White, M., *An analytic model for redshift-space distortions*, Monthly Notices of the RAS **437**, 588–599 (January 2014), 1306.1804.

[YFZ09] Yoo, J. ; Fitzpatrick, A. L. ; Zaldarriaga, M., *New perspective on galaxy clustering as a cosmological probe: General relativistic effects*, Physical Review D **80**(8), 083514 (October 2009), 0907.0707.

[Yoo10] Yoo, J., *General relativistic description of the observed galaxy power spectrum: Do we understand what we measure?*, Physical Review D **82**(8), 083508 (October 2010), 1009.3021.

[Zel70] Zel'dovich, Y. B., *Gravitational instability: An approximate theory for large density perturbations.*, Astronomy and Astrophysics **5**, 84–89 (March 1970).

[Zwi37] Zwicky, F., *On the Masses of Nebulae and of Clusters of Nebulae*, Astrophysical Journal **86**, 217 (October 1937).